

# **A contribution on modelling deformation and residual stress in 3D polycrystals**

**A thesis submitted to The University of Manchester for the degree of PhD in the  
Faculty of Engineering and Physical Sciences**

2012

David Gonzalez

School of Materials



# Table of Contents

1	Introduction .....	17
2	Literature review .....	19
2.1	Stress operating at various length scales.....	19
2.2	Plastic deformation in metal crystals.....	21
2.2.1	Resolved shear stress and Schmid's law .....	21
2.2.2	Plastic deformation by slip .....	22
2.2.3	Existence of dislocations and types.....	23
2.2.4	Stacking fault energy (SFE) .....	24
2.2.5	Work hardening .....	25
2.2.6	Twinning.....	27
2.3	Polycrystalline Materials.....	30
2.3.1	Deformation of polycrystalline metals.....	30
2.3.2	Phase formation in metals and its relevance .....	31
2.3.3	Austenitic stainless steel.....	32
2.3.4	Aluminium oxide.....	33
2.4	Modelling of materials.....	34
2.4.1	Elastic deformation.....	35
2.4.2	Continuum plasticity .....	37
2.4.3	Constitutive laws for a crystal plasticity model.....	41
2.4.4	Models of polycrystalline deformation .....	45
2.4.5	Crystal plasticity finite element modelling (CPFEM).....	50
2.4.6	Recent approaches in CPFEM .....	54
2.5	Measuring strain by neutron diffraction.....	57
2.6	Damage mechanisms in polycrystalline materials.....	59
2.6.1	Fracture .....	59
2.6.2	Fatigue .....	61
2.6.3	Capabilities towards SCC .....	65
3	Experimental methods.....	67
4	Results and discussions .....	85
4.1	Publication 1 .....	86
4.1.1	Introduction.....	89

4.1.2	Experimental .....	92
4.1.3	Crystal plasticity model .....	96
4.1.4	Results and discussions .....	98
4.1.5	Conclusions .....	108
4.1.6	Acknowledgements .....	109
4.1.7	References associated to Publication 1 .....	110
4.2	Publication 2.....	114
4.2.1	Introduction .....	117
4.2.2	Model description.....	121
4.2.3	Results and discussions.....	129
4.2.4	Conclusions .....	145
4.2.5	References associated to Publication 2 .....	146
4.3	Publication 3.....	152
4.3.1	Introduction .....	155
4.3.2	Material & Experimental Methods .....	156
4.3.3	Results and discussion .....	159
4.3.4	Conclusions .....	162
4.3.5	Acknowledgements .....	162
4.3.6	References associated to publication 3 .....	163
4.4	Publication 4.....	166
4.4.1	Introduction .....	169
4.4.2	Experimental Details .....	172
4.4.3	Experimental Results .....	174
4.4.4	Imaged-based FEM Model .....	180
4.4.5	Validation of the FE Model by Diffraction .....	190
4.4.6	Concluding Summary .....	192
4.4.7	Acknowledgements .....	194
4.4.8	Online supplementary material .....	194
4.4.9	References associated to publication 4 .....	199
5	Conclusions and future work.....	206
5.1	Overall conclusions .....	206
5.2	Further work.....	210
5.2.1	Slip-reversal .....	210

5.2.2	Further work on grain boundary stresses .....	212
5.2.3	Fatigue and SCC.....	212
5.2.4	Further work aluminium.....	213
5.2.5	Further work alumina .....	213
6	Annexes.....	214
6.1	Annex: boundary character in SCC.....	215
6.2	Annex: Random crystal orientation assignments.....	215
6.3	Annex: averaging orientations in crystals.....	217
6.4	Supplementary research associated with publication 1.....	220
6.4.1	Pre-processing.....	220
6.4.2	Post-processing.....	222
6.4.3	Intragranular features .....	222
6.4.4	Permanent softening at the macroscale .....	223
6.5	Supplementary research associated with publication 2.....	226
6.5.1	Stresses at grain boundaries between soft and hard grains.....	227
6.5.2	Effect of excluding small grain boundaries .....	228
6.5.3	Distribution of stresses at parallel and orthogonal boundaries .....	230
6.6	Supplementary research associated with publication 3.....	232
6.6.1	Lattice rotation maps.....	232
6.6.2	Grain orientation spread .....	234
6.7	Elastic bi-crystal simulations.....	234
6.8	Submodelling using truncated octahedra.....	237
6.9	Modelling intergranular residual stress after 4 point bending.....	239
6.10	Intragranular rotations after cold-rolling stainless steel.....	242

## List of Figures

Figure 2.1. Schematic representation of variation of stress through a polycrystalline material, .....	14
Figure 2.2. Resolved shear stress on a slip system (Dunne and Petrinic, 2005) .....	15
Figure 2.3. Slip on {111} planes in FCC crystals.(Cottrell, 1953).....	18
Figure 2.4. Twin mechanism in a FCC lattice showing: a) the twinning plane and the twin direction, and b) view of the translated lattice on the (-110) plane (Shah, 2012). .....	21
Figure 2.5: Unit cell of $\alpha$ -Al <sub>2</sub> O <sub>3</sub> . A) Arrangement of Al <sup>3+</sup> ions and holes between two layers of O <sup>2-</sup> ions. Large open circles represent underlying O <sup>2-</sup> ions, small open circles represent holes, and small filled circles represent Al <sup>3+</sup> ions. The upper layer of O <sup>2-</sup> ions (not shown) are translated in $[\bar{1}0\bar{1}0]$ by the O <sup>2-</sup> ion diameter (blue arrows). b) The Al <sup>3+</sup> ions sublattice. Filled circles are Al <sup>3+</sup> ions, open circles are empty octahedral interstices (Kronberg, 1957).....	24
Figure 2.6. A) diagram demonstrating Bragg's law (Kelleher, 2006). B) diffraction patterns showing the measured peaks in IF steel (BCC structure), (Quinta da Fonseca et al., 2006).....	41
Figure 2.7. Heterogeneity of stress at Grain Boundaries (GB) for a given macroscopic stress .....	43
Figure 2.8: a) Intergranular crack (white arrows) in HCF in 304 Stainless Steel after 16,850 tested at 300 °C (Bhatti and Withers, 2008), b) Transgranular crack in LCF in 316 Stainless Steel after 5159 cycles tested at room temperature (Wang and Wang, 2005).....	45
Figure 2.9. Example of intergranular stress corrosion cracking of susceptible boundaries (smooth surfaces) and ductile failure of a bridge formed by a resistant grain boundary (rough surface, marked with an arrow). Image courtesy of D. Engelberg (University of Manchester). .....	47

Figure 4.1. Grain showing the removal of relatively small edges (a) to avoid distorted elements (marked with arrows in (b)). Grain after edge removal (c), and final mesh (d).....	123
Figure 4.2. Resulting local mesh refinement (using ABAQUS C3D10M elements) to avoid element distortion. The RVE is shown in a) whereas close-up views are shown in b), c) and d).....	124
Figure 4.3. Resulting yield strengths $\sigma_{y,(C_2C_1)}$ and $\sigma_{y,(C_2T_3)}$ as a result of the yield surface translation represented on the deviatoric plane or $\Pi$ plane (Hill, 1998). The magnitude of the backstress tensor is represented as $ \alpha $ . After compression in a transverse direction, the yield strength at $90^\circ$ to this direction (in the axial or the other transverse direction) is reduced for compression but increased for tension (red arrows), when purely kinematic hardening and no shape change are assumed. ....	126
Figure 4.4. Stress normal to boundaries versus the difference between a) the averaged plastic strain of the aggregate and the local plastic strain in the vicinity of the grain boundary; b) the plastic strains at each side of the grain boundary. All the results correspond to the unloaded state after 10% uniaxial strain. All the strains are resolved in the normal direction to the GB for comparison with Kroner approximation. The values are presented for boundaries approximately orthogonal and approximately parallel to the loading direction. ....	128
Figure 4.5. Example of a relatively small boundary (circled in white) where stresses show a much greater variability than other boundaries. ....	129
Figure 4.6. Average grain boundary stress for each grain boundary angle interval (solid squares) with the exclusion of the smallest: a) 70 boundaries (1 cohesive element each boundary), b) 109 boundaries (2 cohesive elements or less each boundary), c) 200 boundaries (4 cohesive elements or less each boundary), d) 400 boundaries (11 cohesive elements or less each boundary). Error bars show the standard error for each grain boundary angle interval.....	130

Figure 4.7. Histogram of stresses normal to boundaries whose boundary planes normal form an angle lower than 15° with the loading direction (orthogonal) in the fully anisotropic model. The results correspond to the unloaded state after 10% uniaxial strain.....131

Figure 4.8. Histogram of stresses normal to boundaries whose boundary planes normal form an angle higher than 75° with the loading direction (parallel) in the fully anisotropic model. The results correspond to the unloaded state after 10% uniaxial strain.....131

Figure 4.9. Local rotations about the grain average orientation, resolved about the X, Y and Z axes (in deg.). The rotations after annealing, subsequent deformation and the difference between these are shown in the left, central and right columns respectively. ....133

Figure 4.10. Measured diffraction blob spread by DCT versus Grain Orientation Spread (GOS) by CPFEM as loaded in compression at; a) 1.2% strain, b) 4.4% strain .....134

Figure 4.11. Elastic simulation of a bicrystal showing: a) layout of the model and b) the definition of the coordinate system employed.....135

Figure 4.12. Calculated Von Mises stress (MPa) for a bi-crystal with a misorientation of 45 degrees. ....136

Figure 4.13. Maximum Von Mises stress computed at the nodes in the vicinity of the grain boundary in a bi-crystal as a function of the misorientation angle.....137

Figure 4.14. Logitudinal stress (MPa) developed in a simulated 4 point bending test (loaded), showing: a) the boundary conditions in the global model, b) region in the global model where the submodel is placed, and c) the submodel made of 216 grains shaped as truncated octohedra. The average longitudinal stress in the global model and the submodel (~200MPa) differ from the local stresses simulated in the submodel.....138

Figure 4.15. Predicted and measured macro-scale longitudinal residual stresses in an elastic-plastically bent rectangular beam, including the extent of possible variations due to lattice orientation. The error bars show the maximum and minimum stresses for the {200} and {111} lattice planes (Smith et al., 2009). ....	140
Figure 4.16. Schematic illustration of the rolling process. Showing points of maximum compression and elastic relaxation. Relevant directions in the rolling process are shown: the normal direction (ND), the rolling direction (RD) and the transverse direction (TD).....	141
Figure 4.17. In-grain rotations (with respect to its average) as measured by EBSD and as predicted by two models with different mesh density, decomposed about the: a) X axis (TD), b) Y axis (RD) and c) Z axis (ND). The results correspond to 20 % reduction in the ND or Z direction.....	145
Figure 4.18. Strain map of the RVE resolved (a) in the rolling direction, $\varepsilon_{RD}$ , (b) in the transverse direction, $\varepsilon_{TD}$ , and (c) and in the normal direction, $\varepsilon_{ND}$ . All strains have been plotted using a colour scale in the same strain amplitude range (0.2) to compare strain heterogeneities in the 3 directions. ....	147
Figure 4.19. Strain map (resolved in the rolling direction, $\varepsilon_{RD}$ ) of three faces of the RVE, showing differences in strain bands formation for different planes. Strain bands are predicted to be more pronounced in the RD-ND plane (dashed lines). Strain ranges from 0.1 (blue) to 0.3 (red). ....	147
Figure 5.1. Stress-strain curves following reloading of cold-rolled 304 stainless steel in three different directions: rolling direction, normal direction and transverse direction. The curves show a clear difference in yield stress for different directions (especially the transverse direction). Courtesy of David Wright (University of Manchester, UK) .....	150
Figure 6.1 Left) showing the incorrectly distributed points, Right) showing the correctly distributed points (Weisstein, 2012).....	154

Figure 6.2. The upper row represents the arithmetic mean orientation when computed using quaternions and symmetry is neglected. The lower row represents the correct mean when cubic symmetry is present, which is equivalent to any of the two initial orientations.....155

Figure 6.3. Brass texture component, {144.74, 45, 270} in Bunge Euler angles is represented on the truncated cubic fundamental region in Rodrigues' space. The Brass component lies on the symmetry plane: (a) filled region and (b) transparent region. (Cho et al., 2005) .....155

Figure 6.4. The Hill Climbing procedure used in the current research to determine the grain averaged orientation.....157

## ABBREVIATIONS

ASS	Austenitic Stainless Steels
BCC	Body-Centred Cubic crystal structure
BCT	Body-Centred Tetragonal
BE	Bauschinger effect
CPFEM	Crystal Plasticity Finite Element Method
CSL	Coincidence Site Lattice
DCT	Diffraction Contrast Tomography
DDD	Discrete Dislocation Dynamics
DHD	Deep Hole Drilling
EBSD	Electron BackScatter Diffraction
EPSC	Elasto Plastic Self Consistent
FCC	Face-Centred Cubic crystal structure
FE	Finite Element
FIB	Focused Ion Beam
FWHM	Full Width Half Maximum
GB	Grain Boundary
GNDs	Geometrically Necessary Dislocations
HCF	High cycling fatigue
HCP	Hexagonal Closed Packed crystal structure
IGS	Inter Granular Stress
IGSCC	InterGranular Stress Corrosion Cracking
LCF	Low cycling fatigue
ND	Neutron Diffraction
ND	Normal Direction (cold-rolling context)
PSBs	Persistent Slip Bands
PWR	Pressurised Water Reactor
RD	Rolling Direction
RVE	Representative Volume Element

SCC	Stress Corrosion Cracking
SEM	Scanning Electron Microscope
SFE	Stacking Fault Energy
SSDs	Statistically Stored Dislocations
TD	Transverse Direction
UMAT	User MATerial

## LIST OF SYMBOLS

$\mathbf{b}$	Burger's vector
$b$	Magnitude of the Burger's vector
$E$	Young's modulus
$G$	Shear modulus
$\rho$	Dislocation density
$\mathbf{I}$	Second-order identity tensor
$\nu$	Poisson's ratio
$\boldsymbol{\sigma}$	Cauchy stress tensor
$t$	Time
$\mathbf{t}$	Surface traction vector
$\mathbf{u}$	Displacement vector field
$\mathbf{F}$	Deformation gradient
$\mathbf{L}$	Velocity gradient
$\mathbf{D}$	Rate of deformation
$\mathbf{W}$	Continuum spin
$\mathbf{E}$	Green-Lagrangian strain tensor
$\boldsymbol{\varepsilon}$	Strain tensor
$f$	Yield function
$\mathbf{x}$	Backstress tensor
$\mathbf{m}^{(\alpha)}$	Normal to the slip plane $\alpha$
$\mathbf{s}^{(\alpha)}$	Slip direction in slip system $\alpha$
$\dot{\gamma}^{(\alpha)}$	Slip rate for system $\alpha$
$g^{(\alpha)}$	Current strength for slip system $\alpha$
$\tau^{(\alpha)}$	Resolved shear stress on the slip system $\alpha$
$\dot{\boldsymbol{\sigma}}$	Material stress rate of Cauchy stress
$\nabla$	
$\boldsymbol{\sigma}$	Jaumann stress rate
$\mathbf{K}$	Global Stiffness matrix
$\mathbf{K}^e$	Element Stiffness matrix

## **ABSTRACT**

Polycrystalline materials are widely used for industrial applications. These materials are highly anisotropic with different responses under different loading conditions. This dissertation uses a crystal plasticity scheme in the finite element framework (CPFEM) to study deformation mechanisms in alumina, aluminium and stainless steel – all polycrystalline. Four research cases in this dissertation have been presented in the form of manuscripts for publication. When possible, modelling predictions have been compared against various experimental techniques such as Diffraction Contrast Tomography (DCT), Neutron Diffraction (ND) and Electron Back Scatter Diffraction (EBSD). After an introduction (Chapter 1) and a literature review (Chapter 2) on plastic deformation and modelling techniques, the methodology and results are presented and discussed (Chapters 3 and 4). Measurements of elastic strains for individual grain families (ND) and local rotations (DCT and EBSD) are compared against corresponding predictions by the model following different loading modes. Each study reveals different degrees of agreement between predictions and measurements. The individual conclusions to each study are presented in Chapter 4. Some overall conclusions and suggestions for further work are presented in Chapter 5.

## **DECLARATION**

I declare that no portion of the work referred to in the thesis has been submitted in support of an application for another degree of qualification of this or any other university or other institute of learning.

## **COPYRIGHT STATEMENT**

i. The author of this thesis (including any appendices and/or schedules to this thesis) owns certain copyright or related rights in it (the “Copyright”) and s/he has given The University of Manchester certain rights to use such Copyright, including for administrative purposes.

ii. Copies of this thesis, either in full or in extracts and whether in hard or electronic copy, may be made only in accordance with the Copyright, Designs and Patents Act 1988 (as amended) and regulations issued under it or, where appropriate, in accordance with licensing agreements which the University has from time to time. This page must form part of any such copies made.

iii. The ownership of certain Copyright, patents, designs, trademarks and other intellectual property (the “Intellectual Property”) and any reproductions of copyright works in the thesis, for example graphs and tables (“Reproductions”), which may be described in this thesis, may not be owned by the author and may be owned by third parties. Such Intellectual Property and Reproductions cannot and must not be made available for use without the prior written permission of the owner(s) of the relevant Intellectual Property and/or Reproductions.

iv. Further information on the conditions under which disclosure, publication and commercialisation of this thesis, the Copyright and any Intellectual Property and/or Reproductions described in it may take place is available in the University IP Policy (see <http://www.campus.manchester.ac.uk/medialibrary/policies/intellectual-property.pdf>), in any relevant Thesis restriction declarations deposited in the University Library, The University Library’s regulations (see <http://www.manchester.ac.uk/library/aboutus/regulations>) and in The University’s policy on presentation of Theses.

## **ACKNOWLEDGEMENTS**

Firstly, I must thank to the unconditional support from my family and friends, without it, the development of this thesis would have not been possible. Secondly, I would like to acknowledge my supervisor Prof. Phil Withers who has given me this opportunity to carry out this research as well as a top and efficient supervision. Also, I would like to grant my recognition to my co-supervisors Dr. Joao Fonseca and Prof. James Marrow, for their enormous help and guidance in my research. Invaluable discussions with Dr. Joe Kelleher have been essential for gaining much of my understanding in the early stages of my research. The generous technical help from Dr. Igor Simonovski has been a crucial tool for me to be able to obtain the results presented in this work. Mathematical discussions with Dr. Mike Keavy have provided me with much of my understanding in theory of computational methods. Last but not least, I also appreciate the help and fruitful discussions that many other researchers and former researchers from the School of Materials in Manchester (and other institutions) have offered to me at some point in my degree.

# 1 Introduction

A vast majority of the metals used in engineering applications are polycrystalline. The elastic and plastic anisotropies of the grains in the polycrystal lead to incompatibilities between grains during deformation. This implies that deformation at the microstructural scale is heterogeneous. Polycrystalline materials behave very differently at the –micro ( $\sim 10^{-10}\text{m}$ - $10^{-7}\text{m}$ ) and –meso ( $10^{-5}\text{m}$ ) scales than they do at the macroscale ( $10^{-3}\text{m}$ ) (McDowell, 2008). As a result, the local stresses, strains and rotations within each grain are heterogeneous. The stresses, strains and rotations in each grain depend not only on the orientation of that grain, but they are also affected by the constraints imposed by neighbouring grains.

Approaches to determine macroscopic resistance to yielding, fatigue or fracture have been known for many decades. However, because measuring stresses within grains is essentially impossible, there is considerable interest in modelling behaviour at different length scales (Rühle and Metallforschung, 2002, Kassner et al., 2005). Failure at the macroscale often means that only a selected region at the microscale has failed. For example, failure by fatigue initiation, SCC or fracture may happen in especially vulnerable features (e.g. grain boundaries). For example, the grain boundary character distribution has been shown to be important and useful in explaining and controlling high temperature plasticity, superplasticity and fragility in polycrystals (Watanabe, 1993). In principle, a better understanding of what microscopic character is more damaging would allow us to design better materials in the future. These include, for instance, the generation of microstructural textures with desired macroscopic elastic-plastic properties (Shaffer et al., 2010) or the generation of corrosion-resistant annealing twins.

Failure by fatigue, SCC or fracture may have in common the driving mechanism: stress. Failure by these mechanisms may happen below or above the elastic limit. Materials

often go far above the elastic limit during machining, deforming the material plastically. For example, aluminium may be extruded into a bar or a steel bar may be bent and straightened (Martinez et al., 2002). During plastic deformation stresses are introduced into the body and remain in it even when the machining process has finished (usually called residual stress). A common residual stress profile is that of a bent bar (Davies et al., 1988). Consequently, mechanical design requires that the external load is combined with the residual stresses present in the body. A major aim of this thesis is to improve understanding of deformation and the associated residual stress. This has been achieved by using a model that simulates elastic and plastic deformation of individual crystallites. For example, one aim is to improve the understanding of the effect of different combinations of grain orientations on grain boundary stresses after plastic deformation in polycrystalline materials (publication 2). When possible, corresponding predictions have been compared with experimental measurements. This is the case of publication 1, where the predicted residual strains after strain path changes are contrasted against measured strains by neutron diffraction. As an alternative to (destructive) serial sectioning techniques via EBSD (Spanos et al., 2008), experimental data from diffraction contrast tomography (DCT) has been used in this dissertation. DCT is a relatively novel technique that can map grain shapes and grain orientations in 3D to build image-based models. As DCT is non-destructive, it allows comparison with corresponding image-based models. The technique and results will be explored in publications 3 and 4.

The rest of this dissertation is structured as follows: in chapter 2 the literature review of the materials used and their deformation along with general modelling techniques are presented; chapters 3 and 4 contain the modelling methodology used, results and discussions for each independent research case (published and non-published); finally, some overall directions for further work are extracted in chapter 5.

## 2 Literature review

### 2.1 Stress operating at various length scales

It has been known for a long time that the plastic deformation of individual grains in aggregates is by no means uniform. For example, Boas and Hargreaves (1948) found great variability of hardness and strain across and within grains in a coarse-grained aluminium specimen. The length scales over which residual stresses self-equilibrate may be used to categorise them into one of three types (Withers and Bhadeshia, 2001). Type 1 stress, or macrostress, develops in the body of a component on a scale larger than the grain size of the material and acts at the macroscopic scale. Type 2 stress, or intergranular stress, is stress that varies on the scale of several grains and causes the average stress within each grain to differ from the macrostress. Type 3 residual stresses are associated with the atomic scale. One example is the residual stress field generated by a dislocation trapped in the lattice (Hull and Bacon, 1984).

Types 2 and 3 residual stresses can be classed as meso and micro-stresses whereas type 1 is called macroscale stress. In Figure 2.1, it can be seen how an averaged macroscopic stress varies when we look into a smaller scale. In this way, stresses vary from grain to grain (at the mesoscale) although the average still corresponds to the macroscopic scale (Dye et al., 2001). Similarly, stress may vary with position within a grain (at the microscale).

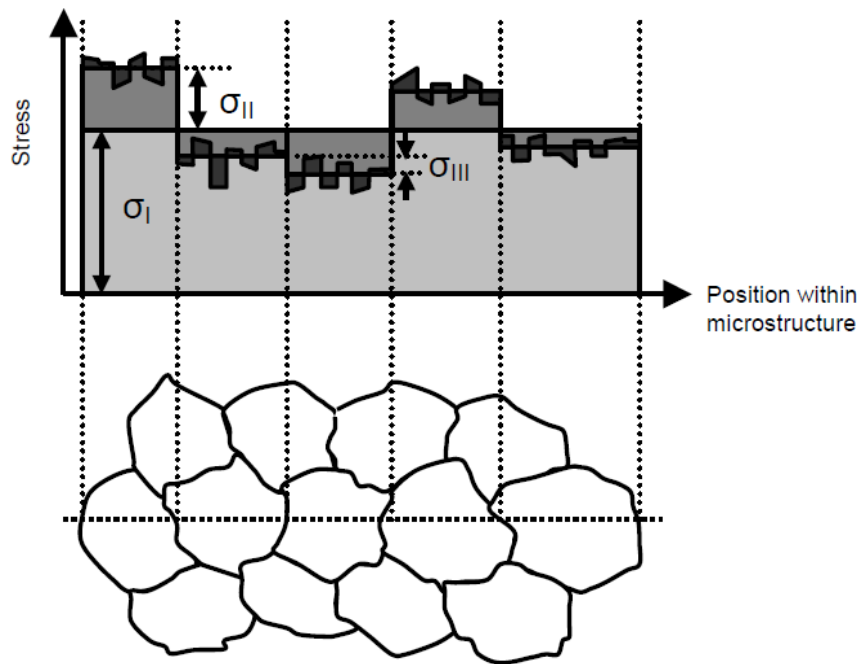


**Figure 2.1. Schematic representation of variation of stress through a polycrystalline material, showing contribution of type 1 ( $\sigma_I$ ), type 2 ( $\sigma_{II}$ ) and type 3 ( $\sigma_{III}$ ) stresses to the overall stress (Dye et al., 2001)**

A polycrystalline material that has never exceeded the elastic limit, and provided that microplasticity has not occurred, may have zero stress throughout the microstructure upon unloading. Meaning that, once the load has been removed, the average stresses (type 1), the inter-granular stresses (type 2), and the stresses within a grain (type 3) will all be zero. By contrast, if loading above the elastic limit, type II or type III stresses remain once the load is retired. In other words, residual stresses appear, indicating that plastic deformation has been put into the body. In practise even below nominal yielding some grains suffer permanent deformation as we will see in the chapter 4. Residual stress can also exist in a region always loaded within the elastic limit (Davis et al. 1988) e.g. neighbouring region to the neutral fibre in a plastically bent beam.

Stress is often associated with damage. However, residual stresses are not necessarily harmful; they can also be deliberately introduced in the body for engineering purposes.

For example, failure by stress corrosion cracking (SCC) and fatigue can be affected by the residual stress put by different welding techniques (Mochizuki, 2007). The uses of CPFEM models on damage mechanisms will be explored in section 2.6.

## 2.2 Plastic deformation in metal crystals

The stresses described in the previous section act on the material. Thus, it is of interest to gain a better physical insight on the studied material. Here we present the most common forms of plastic deformation in metal crystals.

### 2.2.1 Resolved shear stress and Schmid's law

The yield stress of a single crystal under a tensile load varies greatly with orientation. This tensile stress can be related to the shear stress that acts along the slip direction to determine the stress required to start plastic deformation (see for instance (Dunne and Petrinic, 2005)). Consider a single crystal in the shape of a rod of cross section  $A$  and an applied uniaxial tension  $\sigma$  along the tensile axis ( $\mathbf{t}$ ) in Figure 2.2.

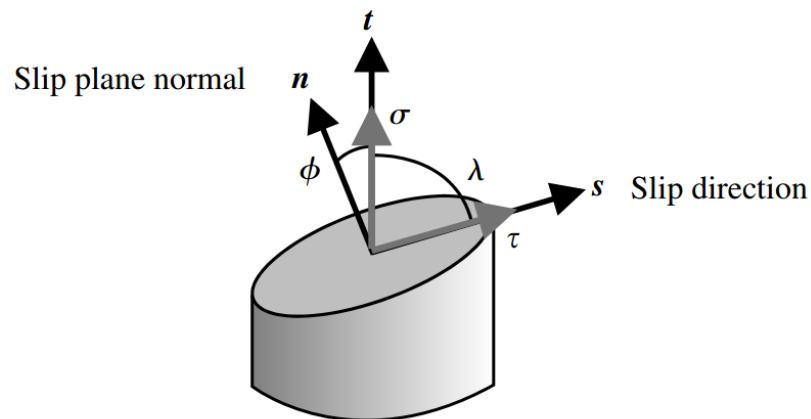


Figure 2.2. Resolved shear stress on a slip system (Dunne and Petrinic, 2005)

The Force acting in the slip direction ( $\mathbf{s}$ ) of the slip plane ( $\mathbf{n}$ ) is  $A\sigma\cos\lambda$ , defining  $\lambda$  as the angle between  $\mathbf{t}$  and  $\mathbf{s}$ . The area on which this force acts is  $A/\cos\phi$ , defining  $\phi$  as the

angle between  $\mathbf{t}$  and  $\mathbf{n}$ . Thus the *resolved shear stress* acting parallel to the slip direction may be written as:

$$\tau = (A \sigma \cos\lambda)/(A/\cos\phi) = \sigma \cos\lambda \cos\phi = \sigma (\mathbf{t}\cdot\mathbf{n}) (\mathbf{t}\cdot\mathbf{s}) \quad (\text{Eq. 2.1})$$

If we now substitute the term  $\tau$  for the critical resolved shear stress ( $\tau_{\text{critical}}$ ) we have *Schmid's law*. This critical shear stress is related to the stress required to move dislocations across the slip plane.

### 2.2.2 Plastic deformation by slip

If the resolved shear stress reaches  $\tau_{\text{critical}}$ , slip will take place in a slip system Taylor (1934). In general, the higher the temperature<sup>1</sup> and the lower the strain rate, the lower  $\tau_{\text{critical}}$ . Slip occurs in well-defined planes and directions, depending on the crystal system. Slip tends to occur in the densest planes (or close packed) and the directions in which atoms are packed closest together. For Face-Centered Cubic (FCC) crystals there are 4 possible slip planes and 3 slip directions in each plane (i.e. 12 slip systems), five of these slip systems are always independent as we will see when describing Taylor model. Although in practice it is very rare to observe 5 operating slip systems, being 2 or 3 the usual (Honeycombe, 1984). This may be partially explained by the fact that most observations have been made on the free (less constrained) surface.

In FCC metals (e.g. aluminium, copper, nickel, austenite) slip takes place on the {111} planes and the <110> directions. 2) In BCC metals (e.g. ferrite) slip can occur on {110} and/or {112} and/or {123} planes and <111> directions (Honeycombe, 1984).

---

<sup>1</sup> In this chapter we assume that thermal activation can only overcome short-range barriers, reducing the total flow stress to the contribution of the athermal component only. The athermal component of the flow stress remains almost independent of temperature. (HULL, D. & BACON, D. J. 1984. *Introduction to Dislocations*, Butterworth-Heinemann., p. 212).

### 2.2.3 Existence of dislocations and types

Frenkel as early as 1926 first estimated the theoretical shear strength assuming that slip occurs between two rows of atoms. This resulted in  $\tau_{\text{theoretical}} = Gb/2\pi a$  (Frenkel, 1926). Where  $G$  is the shear modulus,  $b$  is the magnitude of the Burgers vector ( $\mathbf{b}$ ) and  $a$  the distance between the two rows of atoms. When substituting with reasonable values of  $G$ ,  $b$  and  $a$ ,  $\tau_{\text{theoretical}}$  results in a very high shear strength. The observed values of shear strength are much lower. Orowan (1934), Taylor (1934) and Polanyi (1934) first introduced the concept of dislocation in a crystalline solid. Peierls (1940) and Nabarro (Nabarro, 1947) first gave an expression to calculate the shear stress needed to move a dislocation (*Peierls-Nabarro stress*):

$$\tau_{\text{theoretical}} = \frac{2G}{(1-\nu)} e^{-2\pi a/(b(1-\nu))} \quad (\text{Eq. 2.2})$$

where  $\nu$  is the Poisson's ratio, giving a much closer approximation to experimental observations than Frenkel's relationship. However, the presence of dislocations was not evidenced until 1950 (Honeycombe, 1984) using etching to image them, although other techniques were used to visualize them in the 1950s ((Hull and Bacon, 1984), chapter 2). Since the 1950s, TEM has become the most widely used technique for the observations of dislocations. Dislocations are present in a large number, even in annealed metals ( $\sim 10^{10}$ - $10^{12} \text{ m}^{-2}$ ), and their propagation produces slip. Each dislocation is associated with a unit of slip displacement given by the Burgers vector, which is defined more rigorously by means of Burgers circuit. The Burgers circuit defines an atomic path involving two lattice directions normal to each other. The vectorial difference in Burgers circuits for perfect and faulted lattices defines the Burgers vector. The retraction of a given atomic path (Burgers circuit) involving two lattice directions normal to each other defines the Burger vector. Thus the Burgers vector is parallel to the slip direction. In *edge dislocations* the Burgers vector is perpendicular to the dislocation line whereas in *screw dislocations* the Burgers vector (or slip direction) and

the dislocation line coincide. Loop dislocations describe a dislocation line in the form of a ring or a loop which comprises components of both: edge and screw dislocations. Dislocation loops can expand under an applied shear stress and propagate through different slip planes (e.g. {111} for FCC) that share a common slip direction (e.g. [110] in FCC). This process is called *cross slip*. In BCC metals, cross slip looks less well defined under the microscope because of the larger choice of slip planes.

#### 2.2.4 Stacking fault energy (SFE)

Stress fields in the surroundings of the dislocation core radius ( $\sim b-4b$ ) can be calculated assuming, for simplicity, isotropic elasticity. Similarly, the elastic strain energy associated to a dislocation (edge or screw) may be calculated using linear (isotropic) elasticity (Hull and Bacon, 1984). This associated elastic strain energy (excluding the dislocation core) can be approximated to  $E_{el} = \alpha Gb^2$ , resulting relatively insensitive to the character of the dislocation (screw or edge) (Hull and Bacon, 1984). This is known as *Frank's rule* and, as before,  $b$  represents the magnitude of the Burgers vector ( $\mathbf{b}$ ) and  $\alpha$  is in the range 0.5-1.

If we consider the (111) plane in a FCC crystal, one of the 3 shortest lattice vectors for slip is  $\mathbf{b}_1 = (1/2) [-110]$ . The same displacement can be achieved through the path of the two partial dislocations:  $\mathbf{b}_2 = (1/6) [-211] + \mathbf{b}_3 = (1/6) [-12-1]$  (Hull and Bacon, 1984). The latter displacement is energetically more favourable according to Frank's rule, because  $b_1^2 > b_2^2 + b_3^2$ . The stacking sequence before slip is ABCABC... whereas after slip is ABCACABC. This is shown in Figure 2.3, where the atoms in the "B" positions go to "C" positions. Such a configuration allows the partial dislocations to be at a distance  $d_0$  in the [-110] direction, creating a faulted region (not shown). The lower  $d_0$ , the higher the stacking fault energy (SFE) of the material. The addition of alloying elements significantly lowers the SFE of most metals (Venables, 1964).

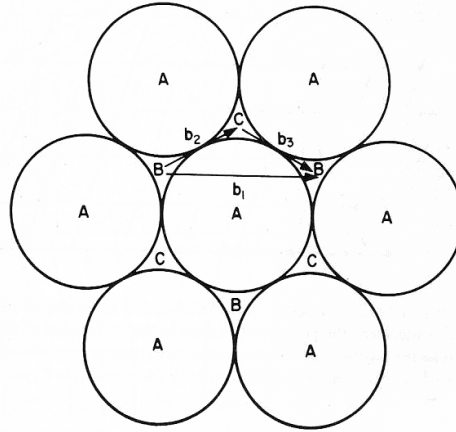


Figure 2.3. Slip on {111} planes in FCC crystals.(Cottrell, 1953)

Table 1. Stacking Fault Energy of some engineering materials (Dieter, 1988)

Metal	Austenitic Stainless Steels			Ag	Au	Cu	Ni	Al
	303	304	310					
SFE (mJm <sup>-2</sup> )	8	20	45	~25	~50	~80	~150	~200

Since they are less hindered by their short  $d_0$ , metals with high SFE often form smooth slip lines and form dislocation tangles and wall-cells substructures<sup>2</sup>. Cross-slip requires the association of partial dislocations which is relatively easier in high SFE metals (short  $d_0$ ). The SFE can also affect texture (Kocks et al., 2000) following uniaxial deformation (Honeycombe, 1984, p. 327) and cold rolling (Humphreys and Hatherly, 2004).

### 2.2.5 Work hardening

As a dislocation moves within the crystal, it finds forces exerted by point defects, other dislocations, deliberately introduced alloying elements or second phase particles<sup>3</sup>.

<sup>2</sup> TEM observations have revealed a subdivision of the cell-walls structures into geometrically necessary boundaries GNBs and incidental dislocation boundaries IDBs, each evolving by different mechanisms. (Hughes et al., 2003, Liu and Hansen, 1995)

<sup>3</sup> An obstacle in the form of a second phase particle can be overcome by leaving a dislocation loop around it (also called Orowan mechanism after his discoverer (Orowan, 1959)).

These mechanisms increase the strength of the crystal and are known as *work hardening*. The process is rather complex. For example, an edge dislocation can move out of its slip plane in a process called *climbing* which is promoted by temperature. Climbing promotes other mechanisms: cross slip for edge dislocations ((Honeycombe, 1984), p. 101); movement of jogged screw dislocations; and grain boundary sliding.

In tests on single crystals, it is usual to resolve the stress and strain onto the plane and direction of which slip occurs first. Above the critical resolved shear stress, three stages are typically well defined which can be modelled using dislocation theory ((Honeycombe, 1984), chapter 5). The flow stress ( $\tau_{\text{flow}}$ ) in Stages I and II is realistically related to the dislocation density ( $\rho$ ) as:  $\tau_{\text{flow}}=0.5Gb\rho^{1/2}$  (Ashby, 1970, Ungar et al., 1984, Mughrabi, 2006). The extent and hardening rate of the 3 stages depend on the *metal*, the *impurities*, the *temperature* and the *orientation* of the applied load. For example, the hardening rates in Stages I and II are insensitive to temperature whereas the Stage 3 hardening rate decreases with temperature. Small stages IV and V have also been reported which showed similarities with stages II and III respectively (Zehetbauer and Seumer, 1993).

#### 2.2.5.1 Stage I

In Stage I (also called *easy glide*), slip takes place on the slip system with the maximum resolved shear stress. The crystal will extend considerably with little hardening. Many tens of dislocations move over long distances ( $\sim 100\mu\text{m}$ ) forming slip lines. In FCC metals, the lower the temperature the larger the extent of stage I hardening. As deformation increases the lattice rotates and slip may begin on a second slip system with a resolved shear stress equal to that of the primary slip system. Therefore, the higher the propensity for multislip (which depends on the crystal orientation), the shorter the extent of stage I. This work hardening stage is not present in polycrystals (Hull and Bacon, 1984).

---

### **2.2.5.2 Stage II**

Secondary slip leads to strong obstacles (e.g. dislocation tangles) which can form dislocation pile-ups. New dislocations in relatively soft regions multiply by Frank-Read sources before being locked themselves. This leads to long-range stress fields, with a hardening rate about 10 times with respect to the previous stage.

### **2.2.5.3 Stage III**

In this stage the stress is so high that the lattice is partially restored by a process called *dynamic recovery* which leads to a decrease in the dislocation density. This involves annihilation of screw dislocations of opposite sign and rearrangement of edge dislocations to form low angle boundaries. Slip lines are replaced by (thicker and shorter) slip bands and the obstacles generated in stage II can be overcome by cross slip. The extent of stages II and III are dominated by low and high temperatures respectively. In metals with high SFE (i.e. easy cross slip), stage III can dominate the stress-strain curve even at medium temperatures. This is the case of pure aluminium where room temperature (293 °K) is about 0.31 times its melting temperature (limit of cold work).

### **2.2.6 Twinning**

An important deformation mechanism often associated to hexagonal metal crystals and to cubic structures is twinning. Even though the twinning mechanism is neglected in this model, it is worth describing it since, among other things, it can play an important role to prevent damage in SCC. Also, deformation twinning can create damage at the boundary in the form of microcracks (Bieler et al., 2009). Moreover, its prominent presence in twinning induced plasticity steels can improve ductility, work hardening and ultimate strength (Qin and Bhadeshia, 2008). The texture changes introduced by twins under tension in zirconium have been successfully predicted by CPFEM (Abdolvand et al., 2011).

We say there is a twin in a crystal when parts of which are oriented with respect to one another following some symmetry rule (Kelly et al., 2000, Cullity and Stock, 2001). In FCC materials, a displacement applied to the upper part of the plane (111) in the lattice produces a partial dislocation. The same displacement applied at successively higher layers parallel to (111) planes produces a twin. It is worth pointing that a partial dislocation is merely a dislocation in which the Burgers vector is a fraction of the unit cell. Note that if such vector was exactly (or a multiple of) the value of the unit cell there would be no change in orientation whilst twinning, by definition, involves a change in orientation (Kelly et al., 2000, Cullity and Stock, 2001).

In Figure 2.4, all the atoms above the mirror plane (or twinning plane) (111) (Figure 2.4a) have been translated in the twinning direction  $(1/6) [11-2]$  (Shah, 2012). The new projection of these translations on the plane (-110) is shown on Figure 2.4b. If the translation of atoms or rotation of the lattice happened again about another mirror plane parallel to the first, the original orientation would appear again, forming a twinned region (Figure 2.4b).

Notice that both before and after the translation all the atoms stay on the (-110) plane since no distortion of the unit rectangular cell projected in (-110) plane is observed. Unlike slip, twinning is directional. Accordingly, when reversing the direction of the Burgers vector to  $(1/6) [-1-12]$ , the translated atoms sit (uncomfortably) on top of the (111) plane (hydrostatic axis view). An alternative diagram showing this can be found in ((Oliver, 2004), p. 43-45). For BCC the twin plane is usually {112} and the twinning shear is in the  $\langle 111 \rangle$  direction. Twins in FCC and BCC metals are usually narrow in contrast to those in HCP metals which are thicker (Hosford 2005).

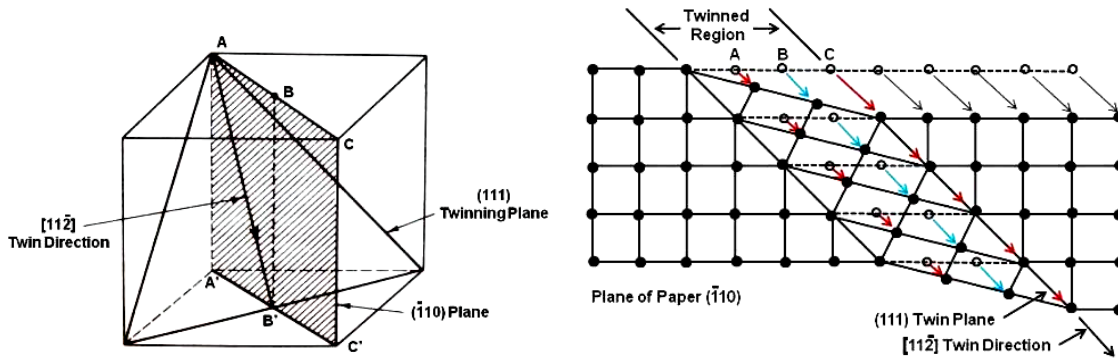


Figure 2.4. Twin mechanism in a FCC lattice showing: a) the twinning plane and the twin direction, and b) view of the translated lattice on the  $(-110)$  plane (Shah, 2012).

Twins can be created in two ways: *annealing twinning* and *deformation twinning* (Kelly et al., 2000, Cullity and Stock, 2001). Annealing twinning occurs during grain growth on cooling after heating a cold worked specimen. Annealing twins occur in an effort to accommodate the overall energy balance across its boundaries. As a consequence, stored energy from dislocations can be relieved through heating, along with that releasing of energy, twinning appears. *Deformation twinning* follows plastic deformation i.e. the crystal prefers to accommodate the imposed shear deformation by twinning. In general, the lower the temperature and the higher the strain rate, the higher the tendency to deform by twinning. Metals with low SFE (such as austenitic stainless steels) tend to deform relatively more by twinning (Honeycombe, 1984), presumable because other “less catastrophic” modes are hindered by their high  $d_0$ .

It is not always clear whether a twin was formed by growth or shear. However, there is a tendency for annealing twins to present a larger twinned region (wider bands) crossing the grain throughout. Twins by plastic deformation are usually rather narrow and often discontinue somewhere inside the grain. Nevertheless, once a twin has formed it is believed they behave similarly regardless of the cause for forming (Kelly et al., 2000)

## 2.3 Polycrystalline Materials

Here we examine the chemistry, structure and behaviour of some of the polycrystalline materials that are widely used in industry. Namely, we are interested in the materials modelled in this dissertation: austenitic stainless steels, aluminium and alumina. Aluminium, however, is not further discussed here because some relevant points have been previously addressed about this metal (*work hardening* section) and some others are examined in publication 3.

### 2.3.1 Deformation of polycrystalline metals

The mechanisms discussed in section 2.2 largely apply for polycrystals. However there are some differences such as the absence of stage I. Further, the grain boundaries have an impact on the response of the polycrystal. Near the boundaries, where constraints are greatest, more slip systems have been seen active than in the centre of grains, being this observation more pronounced in large grains (Hirth, 1972).

Another mechanism that could contribute on plastic deformation is sliding along grain boundaries; however this is thought not to be significant for temperatures below 50% the melting temperature ( $T_m$ ) (Honeycombe, 1984). For the purpose of simplification, this is neglected in this research.

Plastic deformation can also, by itself, promote new phases in the material. This is the case of martensite (Varma et al., 1994), usually referred to as *deformation induced martensite*. Martensite is formed as a result of lack of diffusion of the atoms of carbon, avoiding the formation of cementite and getting them trapped in the unit cell forming a body centred tetragonal structure (BCT). This could be fatal, since martensite is very brittle. Nevertheless martensite is largely used in industry when the designing conditions require a high level of hardness.

### ***2.3.2 Phase formation in metals and its relevance***

Although this research focuses primarily on single phase polycrystalline aggregates, second phase particles usually coexist in the aggregate. An anisotropic polycrystalline aggregate effectively contains as many phases as orientations. Second phase particles essentially involve a more pronounced anisotropy and a great effect, for example, in the internal stress redistribution or the Bauschinger effect. Internal stresses may also arise due to a phase transformation itself. Modelling results and neutron diffraction measurements of two phase metals have shown the large stresses developed for different phases (Oliver et al., 2004).

An example of the phase transformation in plain carbon steel is presented. Plain carbon steel is an interstitial solid solution of carbon (normally less than 1% wt.) in iron (Callister, 2006). Plain carbon steels are made of the combination of one or two out of the four solid phases which presence, in percentages, varies depending on the temperature and the percentage of Carbon according to the lever rule. The solid phases are  $\alpha$  ferrite (BCC), austenite (FCC),  $\delta$  ferrite (BCC) and cementite (orthorhombic crystal structure of 12 Fe atoms and 4 C atoms). The relative amount of these phases obtained upon cooling of austenite depends on the rate of cooling. Namely, pearlite or bainite are obtained when performing a slow or medium cooling rate respectively.

### ***2.3.3 Austenitic stainless steel***

Ferrous alloys are especially important in engineering because of their abundance on earth and their relatively economical fabrication (Callister, 2006). The principal disadvantage of many ferrous alloys is their susceptibility to corrosion. Stainless steels are iron based alloys containing at least 11% wt. of chromium, enhancing their resistance to corrosion (e.g. (Lozano-Perez et al., 2009)). They achieve this resistance by forming a surface-adherent layer of  $\text{Cr}_2\text{O}_3$  rather than  $\text{Fe}_2\text{O}_3$  (rust) which does not adhere adequately to the surface due to the volume changing associated with its

formation. Stainless steels are divided into three classes on the basis of the predominant phase constituent of the microstructure: austenitic, martensitic and ferritic.

Austenitic stainless steels (Grade 316) has been studied in publications 1 and 2. Austenite (FCC) can exist at room temperature when stabilizing elements are added (mainly nickel and manganese, (Raghavan, 2006)). This alloy is called austenitic stainless steel. The chemical compositions of the popular 304L and 316L austenitic stainless steel are shown in Table 2 and Table 3 respectively (Raquet et al., 2006). The low carbon contents of these steels reduce the susceptibility to sensitization during high temperature applications including welding.

**Table 2. Chemical composition of 304L. (Raquet et al., 2006).**

<b>304L</b>	<b>C</b>	<b>Cr</b>	<b>Ni</b>	<b>Mo</b>	<b>Mn</b>	<b>Si</b>	<b>P</b>	<b>S</b>	<b>N</b>
<b>Wt %</b>	0.026	19.23	9.45	0.24	1.49	0.52	0.027	0.002	0.064

**Table 3. Chemical composition of 316L. (Raquet et al., 2006).**

<b>316L</b>	<b>C</b>	<b>Cr</b>	<b>Ni</b>	<b>Mo</b>	<b>Mn</b>	<b>Si</b>	<b>P</b>	<b>S</b>	<b>N</b>
<b>Wt %</b>	0.027	17.2	12.15	2.34	1.76	0.48	0.23	0.001	0.064

Molybdenum is often added as it improves the resistance against SCC (Shibata, 1983, Karaminezhaad et al., 2006). On the other hand, molybdenum content in stainless steels can promote low temperature embrittlement (Kain et al., 2004), suggesting the use of 304 Type (rather than 316 Type) in nuclear reactors. There are other elements that can be added to austenitic stainless steels. For example, niobium is often added in modern steels such as pipeline steels (cca. 0.06% Nb) to mitigate both: thermal sensitisation (Schweitzer, 2010; Mcguire, 2008) and irradiation damage (Ahmedabadi et al., 2011). In both cases, damage is caused by the migration of chromium. In thermal sensitisation, the free atoms of chromium in the lattice combine with carbon to form chromium carbides at the boundary. This effect leaves a lack of chromium in the vicinity of the grain boundary (GB) making this region more exposed to corrosion. In this case, Nb

combines with carbon to stop the formation of chromium carbides. In irradiation damage, vacancies and dislocations tend to propagate near the GB. Atoms of chromium are somewhat ejected by the incoming lattice defects. The role of Nb is, in this case, to stop the propagation of lattice defects from the core of the grain to the GB.

### 2.3.4 Aluminium oxide

Alpha alumina ( $\text{Al}_2\text{O}_3$ ), as most ceramic materials, is brittle ( $K_{Ic} \sim 4 \text{ MPa}/\text{m}^{1/2}$ ), stiff ( $E \sim 393 \text{ GPa}$ ), strong (Flexural strength: 275-700<sup>4</sup>MPa) and has a mixed ionic (63%)–covalent (27%) atomic bonding (Callister, 2006). Although alumina has a trigonal structure (R-3c), the oxygen ions nearly form a hexagon (Figure 2.5a). For this reason, it is usually described as ABAB stacking of oxygen planes along the c axis with Al ions in 2/3 of the octahedral interstitial positions as seen in Figure 2.5.

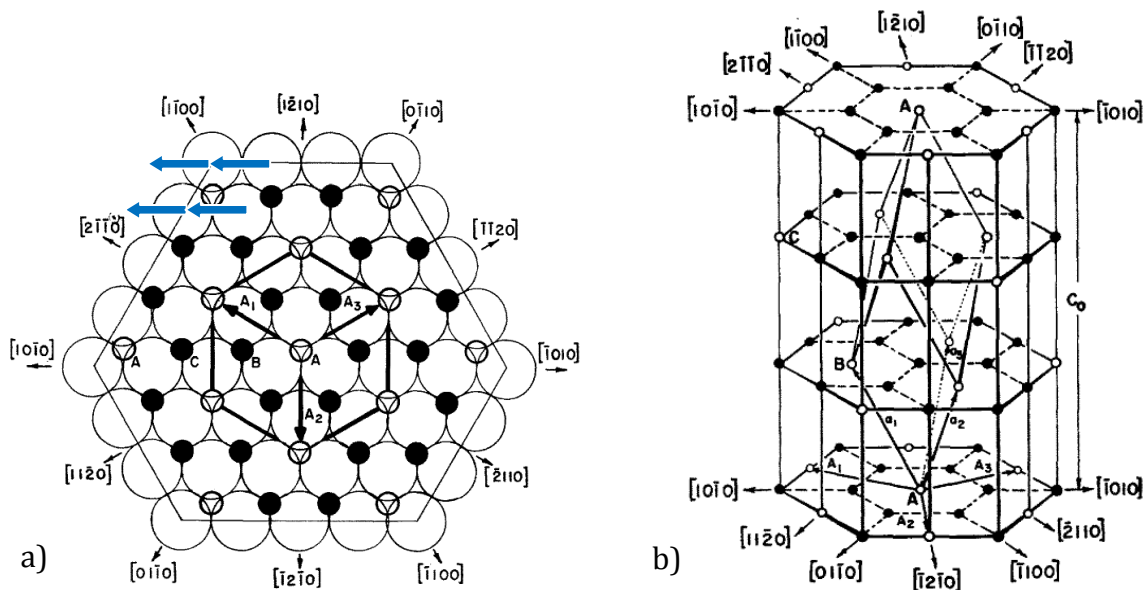


**Figure 2.5: Unit cell of  $\alpha$ - $\text{Al}_2\text{O}_3$ . A) Arrangement of  $\text{Al}^{3+}$  ions and holes between two layers of  $\text{O}^{2-}$  ions. Large open circles represent underlying  $\text{O}^{2-}$  ions, small open circles represent holes, and small filled circles represent  $\text{Al}^{3+}$  ions. The upper layer of  $\text{O}^{2-}$  ions (not shown) are translated in  $[\text{10}\bar{1}\text{0}]$  by the  $\text{O}^{2-}$  ion diameter (blue arrows). b) The  $\text{Al}^{3+}$  ions sublattice. Filled circles are  $\text{Al}^{3+}$  ions, open circles are empty octahedral interstices (Kronberg, 1957).**

<sup>4</sup> Flexural strength according to ASTM Standard C1161. "Standard Test Method for Flexural Strength of Advanced Ceramics at Ambient Temperature"

## 2.4 Modelling of materials

Cottrell (1953) classed hardening as a “spectacular phenomenon” and probably the last problem to be solved by dislocation theory. Unfortunately, his statement still largely remains valid (Humphreys and Hatherly, 2004), although some unified theories have been proposed (Brown, 2003). In the past decades, increasingly high power of computers has enabled atomistic simulations ( $\sim 10^{-10}\text{m}$ ). Yet, computers can only model about  $0.1\mu\text{m}$  while a small grain size in metals is about  $10\mu\text{m}$ . These can be coupled with discrete dislocation mechanics to model larger amount of material (Shilkrot et al., 2004). A defect in the atomic arrangement can then be detected at the boundary and “converted” to a well-defined dislocations interacting in a continuum elastic medium and vice versa. The dislocation can travel in the continuum medium over a long distance which is often the case of ductile metals. This model captured the critical stress intensity factor (material opening toughness) at the crack tip in a single crystal of hexagonal Al, even when using a small number of atoms. Much of the recent work in modelling plasticity at the micro scale ( $\sim 10^{-10}\text{m}$ - $10^{-7}\text{m}$ ) has been compiled (McDowell, 2008), emphasizing the limiting computational power at modelling these scales.

Deformation via slip solving simultaneously the linear momentum balance and a (thermodynamically consistent) slip evolution equation has been claimed to predict dislocation patterning (Yalcinkaya et al., 2011). In such approach three participating stress contributions can be distinguished: 1) the conventional resolved stress, 2) the modified stress characteristic of the strain gradient plasticity (considering size effects) and 3) and the stress that emanates from a non-convex free energy function. The use of such a function and the strong coupling (unlike weak coupling in phase field models) between deformation and the evolution of plastic slip are seen, in such work, as keys for patterning prediction. Yet validation would involve numerous thin-foil electron micrographs. Polycrystal plasticity ( $\sim 10^{-5}\text{m}$ ), also called crystal plasticity, is sufficient for many applications such as predicting texture (Needleman and Asaro, 1985), formability of sheets, etc. In this chapter attention will be paid to this group. Many of

the recent simulations using crystal plasticity have been reviewed by Roters et al. (2010). We will also present the constitutive laws of continuum plasticity ( $10^{-3}\text{m}$ ), due to its relevance to industrial applications (e.g. fracture, fatigue, etc) for decades.

### 2.4.1 Elastic deformation

The generalized Hooke's law at any small volume of material may be given as:

$$\sigma_{ij} = C_{ijkl} \varepsilon_{kl} \quad (\text{Eq. 2.3})$$

The 81 components of the fourth rank tensor ( $C_{ijkl}$ ) may be reduced to 36 because of the symmetries of the Cauchy stress tensor ( $\sigma_{ij} = \sigma_{ji} \Rightarrow C_{ijkl} = C_{jikl}$ ) and the infinitesimal strain tensor ( $\varepsilon_{kl} = \varepsilon_{lk} \Rightarrow C_{ijkl} = C_{ijlk}$ ). These symmetries are called the minor symmetries of the stiffness tensor  $C_{ijkl}$ .

Further, the components of  $C_{ijkl}$  can be given as a strain energy function,  $W(\mathbf{E})$ , (Teodosiu, 1982), where  $\mathbf{E}$  is the Green-Lagrangian strain tensor.

$$C_{ijkl} = \frac{\partial^2 W(\mathbf{E})}{\partial E_{ij} \partial E_{kl}}, \text{ or if we assume small strains: } C_{ijkl} = \frac{\partial^2 W(\boldsymbol{\varepsilon})}{\partial \varepsilon_{ij} \partial \varepsilon_{kl}} \quad (\text{Eq. 2.4})$$

The arbitrariness of the order of differentiation implies that  $C_{ijkl} = C_{klij}$ , reducing the total number of independent constants to 21. These symmetries are called the major symmetries of the stiffness tensor  $C_{ijkl}$ .

For simplicity, Hooke's law is usually given in Voigt notation: by  $\sigma_i = C_{ij} \varepsilon_j$  ( $i, j=1, 2, \dots, 6$ ), as explained by Nye (1985). Note that the terms  $\varepsilon_4$ ,  $\varepsilon_5$  and  $\varepsilon_6$  represents the engineering shear strain components. If the shear components of the strain tensor are used, these should enter Hooke's law by doubling their values. Note that, if using Abaqus FE package,

the output is always in terms of the engineering shear strain components.

It is possible to resolve the directional stiffness in a particular direction (Oliver, 2004, Wong and Dawson, 2010), as done in section 4.2.

In the case of cubic crystal structures, symmetric relationships are applied (Nye 1985), giving:  $C_{11}=C_{22}=C_{33}$ ,  $C_{12}=C_{21}=C_{13}=C_{31}=C_{23}=C_{32}$  and  $C_{44}=C_{55}=C_{66}$ , for any other term  $C_{ij}=0$ . Thus the terms are reduced to 3 independent constants:  $C_{11}$ ,  $C_{12}$  and  $C_{44}$ . In the case of isotropic elasticity, the stiffness tensor can be reduced to two independent terms (Young modulus and Poisson ratio).

## ***2.4.2 Continuum plasticity***

This theory (Hill, 1998), since it was first published by Hill in 1950, has been widely used in modelling metal process forming (Szczepinski, 1979) or fracture. In this dissertation, we also use it in publication 2. Although its basic concepts are presented here, greater details can be found in the literature (Hill, 1998, Dunne and Petrinic, 2005).

### **2.4.2.1 Yield function**

Tresca and Von Mises are perhaps the best known yielding criteria. These criteria have been used for about a century in structural integrity and mechanical design in order to keep the material under its elastic limit. The Von Mises equivalent stress is defined by:

$$\sigma_e = \left( \frac{3}{2} \boldsymbol{\sigma}' : \boldsymbol{\sigma}' \right)^{1/2} = J(\boldsymbol{\sigma}') \quad (\text{Eq. 2.5})$$

where  $\boldsymbol{\sigma}'$  represents the deviatoric stress tensor, namely:

$$\boldsymbol{\sigma}' = \boldsymbol{\sigma} - \frac{1}{3} \text{Tr}(\boldsymbol{\sigma}) \mathbf{I} \quad (\text{Eq. 2.6})$$

$\boldsymbol{\sigma}$  is the general stress state at an infinitesimal point in the material, “Tr” is the trace of its matrix representation and  $\mathbf{I}$  is the identity tensor. The term on the right represents the hydrostatic stress and it has no effect on yielding. From now on, function  $J$  may be used because of its similarity with the second stress invariant.

We can now write a yield function that relates the Von Mises equivalent stress and the uniaxial material strength ( $\sigma_y$ ) as:

$$f = \sigma_e - \sigma_y \quad (\text{Eq. 2.7})$$

Therefore the material would not yield if  $f$  is less than zero under this criterion. Such function in general defines a cylinder in stress space which is a 3D yield surface. The axis of this cylinder is the hydrostatic axis ( $\sigma_1 = \sigma_2 = \sigma_3$ ). For plane stress this yield surface becomes a 2D ellipse when projected on the plane of stress.

#### 2.4.2.2 How does the material deform when it has reached yielding?

We have given so far a yield function that determines whether or not yielding occurs. The normality hypothesis of plasticity states that the increment in the plastic strain tensor occurs in a direction normal to the yield surface at the load point. In Eq. 2.8, the direction of plastic flow is given by  $\partial f / \partial \boldsymbol{\sigma}$ .

$$d\boldsymbol{\epsilon}^p = d\lambda \frac{\partial f}{\partial \boldsymbol{\sigma}} \quad \text{or} \quad \dot{\boldsymbol{\epsilon}}^p = \dot{\lambda} \frac{\partial f}{\partial \boldsymbol{\sigma}} \quad (\text{Eq. 2.8})$$

The term  $d\lambda$  is called the plastic multiplier and is related to the magnitude of the plastic deformation away from the yield surface which, for a material that yields according to the Von Mises criterion, it turns out to be simply equal to the rate of equivalent plastic strain,  $\dot{p}$ . However,  $\dot{p}$  is still unknown but can be found using the consistency

condition. Then using Hook's law and the additive decomposition of total strain into elastic plus plastic<sup>5</sup>, we can solve  $\dot{p}$  as a function of the elastic constants,  $\partial f / \partial \boldsymbol{\sigma}$  and  $\partial f / \partial p$ .

The yield function, as seen above, varies depending on the type of hardening considered: kinematic hardening, isotropic hardening or both. This function has to be implemented into the formula by differentiating over the stress  $\partial f / \partial \boldsymbol{\sigma}$ , term that will provide with a vector defining the direction of the plastic strain increment.

Moreover, the yield function may evolve depending on the current state of the material. This is the case of material hardening. In order to get a better physical insight about these changes of  $f$ , we will first introduce isotropic and kinematic hardening.

#### 2.4.2.3 Isotropic hardening

At some point in which plastic deformation has occurred, the stress required for yielding ( $\sigma_y$ ) it is no longer constant and this is precisely the term in the yielding function that varies depending on the hardness. When the expansion of the yield surface is uniform in all directions in stress space, the hardening is referred to as isotropic. The amount of expansion depends on the accumulated plastic strain,  $p$ :

$$\sigma_y(p) = \sigma_{y0} + r(p) \quad (\text{Eq. 2.9})$$

the term  $\sigma_{y0}$  is the initial yield stress. The term  $r(p)$  is referred to as the isotropic hardening function. Consequently, the yield function becomes:

$$f = \sigma_e - \sigma_y(p) \quad (\text{Eq. 2.10})$$

Finally, the plastic deformation increment can be calculated using Eq. 2.8. In order to find  $p$ , it is now necessary to integrate  $\dot{p}$  over the time increment.

---

<sup>5</sup> Assuming that elastic strains are small

#### 2.4.2.4 Kinematic hardening

Considering uniquely isotropic hardening leads to very large elastic regions on reverse loading which disagrees with experiments. In fact a much smaller region is expected if the load was to be reversed; this is called the Bauschinger effect (Bauschinger, 1881, Bauschinger, 1886). Such effect can be captured through the incorporation of kinematic hardening. This is equivalent to the translation of the yield surface<sup>6</sup> by  $\mathbf{x}$  which is called often back stress and it is a tensor unlike the scalar value “ $r$ ” in isotropic hardening. The explanation at the microstructure level of the Bauschinger effect deals with the dislocation theory and is discussed in publication 1. With kinematic hardening the yield function may be modified by using  $(\boldsymbol{\sigma}' - \mathbf{x}')$  in place of  $\boldsymbol{\sigma}$ . Using linear Prager (1956) hardening:

$$f = \left( \frac{3}{2} (\boldsymbol{\sigma}' - \mathbf{x}') : (\boldsymbol{\sigma}' - \mathbf{x}') \right)^{1/2} - \sigma_y \quad (\text{Eq. 2.11})$$

When kinematic hardening is modelled, the plastic multiplier also results a function of the backstress which is a function of the plastic strain increment itself. In reality, kinematic and isotropic hardenings are combined to define the entire hardening of the material. The reader is referred to the book by Dunne and Petrinic (2005) for details on the form of the plastic multiplier.

#### 2.4.2.5 Combined hardening

We have considered non time-dependent plasticity so far. In reality the rate of deformation affects the stress-strain relationships. This implies another change in the stress-strain relationship (or *viscous stress*) where a rate-dependent deformation function is introduced<sup>7</sup>. This adds up to the total stress associated in the deformation, in a similar way as  $r(p)$  does in isotropic hardening.

<sup>6</sup> Some details about this translation will be seen in more detail in section 4.1.4

<sup>7</sup> Similar hardening and rate-dependence will be seen in more detail when modelling slip (section 2.4.3), yet these mechanisms occur at different length scales.

For a von mises material, the plastic multiplier ( $d\lambda$ ) equals the increment of effective plastic strain ( $\dot{p}$ ). Combining effects of isotropic and kinematic hardening and viscous stress by viscoplasticity under uniaxial perfect plasticity the plastic multiplier becomes:

$$d\lambda = \dot{p} = \left( \frac{J(\boldsymbol{\sigma}' - \mathbf{x}') - r - \sigma_y}{K} \right)^{1/m} \quad (\text{Eq. 2.12})$$

where  $K$  and  $m$  are constants associated to viscoplasticity. The term  $\partial f / \partial \boldsymbol{\sigma}$  turns out to be:

$$\frac{\partial f}{\partial \boldsymbol{\sigma}} = \frac{3}{2} \frac{\boldsymbol{\sigma}' - \mathbf{x}'}{J(\boldsymbol{\sigma}' - \mathbf{x}')} \quad (\text{Eq. 2.13})$$

Finally, substituting these two terms into equation Eq. 2.8:

$$d\boldsymbol{\varepsilon}^p = \frac{3}{2} \left( \frac{J(\boldsymbol{\sigma}' - \mathbf{x}') - r - \sigma_y}{K} \right)^{1/m} \frac{\boldsymbol{\sigma}' - \mathbf{x}'}{J(\boldsymbol{\sigma}' - \mathbf{x}')} \quad (\text{Eq. 2.14})$$

### ***2.4.3 Constitutive laws for a crystal plasticity model***

Plastic flow in a single crystal is anisotropic, and cannot be adequately modelled using the constitutive equations for continuum plasticity. Instead, a slip-based constitutive law can be used (Asaro and Rice, 1977, Asaro, 1983). These constitutive equations are capable of modelling the rotations of individual grains in a polycrystal, and hence to predict the evolution of texture (Pi et al., 2008) as well as the elastic and plastic deformation. Here we are describing the basic steps in the ABAQUS material subroutine used in this dissertation (Huang, 1991) to model deformation by slip. The subroutine describes the material behaviour of a single crystal or in other words; the response in incremental stress that the subroutine returns for an assumed (small or large) total

displacement. The material subroutine also provides the material Jacobian matrix  $\partial\Delta\boldsymbol{\sigma}/\partial\Delta\boldsymbol{\varepsilon}$  for building the global stiffness matrix, assuming small elastic strains. The differentiation of the second order tensor  $\partial\Delta\boldsymbol{\sigma}$  with respect to the second order tensor  $\partial\Delta\boldsymbol{\varepsilon}$  gives a the fourth order tensor. Thus, because of the symmetries of  $\boldsymbol{\sigma}$  and  $\boldsymbol{\varepsilon}$  (see section 2.4.1), the material Jacobian will be composed of 36 components for a fully three-dimensional problem.

1<sup>st</sup>) Determine the velocity gradient ( $\mathbf{L}$ ): to define the spatial rate of change of the velocity since we are dealing with a rate-dependent model.

$$\mathbf{L} = \dot{\mathbf{F}}\mathbf{F}^{-1} \quad (\text{Eq. 2.15})$$

Where  $\mathbf{F}$  and  $\dot{\mathbf{F}}$  are the deformation gradient and its rate. Both are assumed to be known from the imposed deformation of the current time increment. At a given time increment and at a given Newton-Raphson iteration, the residual values (from Newton-Raphson procedure) would update the displacements and these would update  $\mathbf{F}$  and  $\dot{\mathbf{F}}$ .

The deformation gradient consists of both elastic and plastic terms related as follows according to the *multiplicative decomposition*:

$$\mathbf{F} = \mathbf{F}^e\mathbf{F}^p \quad (\text{Eq. 2.16})$$

where  $\mathbf{F}^p$  corresponds to an intermediate configuration where only plastic shear has occurred whereas in  $\mathbf{F}^e$  denotes stretching and rotation of the lattice. Elastic properties are assumed to be unaffected by slip leaving the dependence of stress solely on  $\mathbf{F}^e$

2<sup>nd</sup>) Decomposition of  $\mathbf{L}$  into  $\mathbf{D}$  (rate of deformation) and  $\mathbf{W}$  (continuum spin) given by the symmetric and anti-symmetric tensors of  $\mathbf{L}$  respectively. As a consequence of the

elastic-plastic decomposition in the previous step and assuming small elastic stretches, each of these tensors can be decomposed into an elastic and a plastic part as follows:

$$\mathbf{D} = \text{sym}(\mathbf{L}) = \frac{1}{2}(\mathbf{L} + \mathbf{L}^T) = \mathbf{D}^e + \mathbf{D}^p \quad (\text{Eq. 2.17})$$

$$\mathbf{W} = \text{asym}(\mathbf{L}) = \frac{1}{2}(\mathbf{L} - \mathbf{L}^T) = \mathbf{W}^e + \mathbf{W}^p \quad (\text{Eq. 2.18})$$

For simplicity, here we assume  $\mathbf{W}^p = 0$ , so the continuum spin,  $\mathbf{W}$ , will be directly assigned to a rotation of the elastic domain.

3<sup>rd</sup>) Calculate the plastic deformation component of the stretching:  $\mathbf{D}^p$  which will be the sum of the deformation of all active slips systems at that integration point:

$$\mathbf{D}^p = \sum_{\alpha} \dot{\gamma}^{(\alpha)} \mathbf{s}^{(\alpha)} \mathbf{m}^{(\alpha)} \quad (\text{Eq. 2.19})$$

Where for the slip system  $\alpha$ ,  $\mathbf{m}^{(\alpha)}$  is the vector normal to the slip plane and  $\mathbf{s}^{(\alpha)}$  is the vector defining the slip direction. The slipping rate for that slip system is defined by  $\dot{\gamma}^{(\alpha)}$ . Obviously, only planes with  $\dot{\gamma}^{(\alpha)} > 0$  will contribute to the deformation. (this is a similar criterion to the yielding function for continuum plasticity). The slipping rate  $\dot{\gamma}^{(\alpha)}$  depends on the current resolved shear stress ( $\tau^{(\alpha)}$ ), current strength ( $g^{(\alpha)}$ ) and cumulative shear strain ( $\gamma^{(\alpha)}$ ) of the slip system  $\alpha$ . These variables are explained further in publication 2. The values of such variables in the previous time increment can serve as an initial guess for the first global Newton-Raphson iteration (step 5 of finite element section). For subsequent global Newton-Raphson iterations, the new stresses calculated in the previous iteration would serve to calculate new guesses of  $\tau^{(\alpha)}$ ,  $g^{(\alpha)}$  and  $\gamma^{(\alpha)}$ . In practice, it is possible to use an *incremental integration scheme* in an effort to find a better initial guess for such plastic parameters (data card number 20 in the UMAT used (Huang, 1991). The subroutine allows two means to find such initial values: by a *linear increment formulation* or using a *non-linear increment formulation*. In the *linear increment formulation*, a simple Euler time integration scheme or a linear

interpolation within the time increment are possible. In the *non-linear increment formulation* scheme, a Newton-Raphson iteration within the subroutine is employed, using the *linear increment formulation* as an initial guess. In the present work, the *linear increment formulation* approach is used. Further discussions about these methodologies can be found elsewhere (Abdolvand, 2012).

4<sup>th</sup>) Determine the rate of elastic deformation  $\mathbf{D}^e$

This is a rather simple step assuming small elastic strains since we know the total rate of deformation imposed  $\mathbf{D}$ , hence:

$$\mathbf{D}^e = \mathbf{D} - \mathbf{D}^p \quad (\text{Eq. 2.20})$$

5<sup>th</sup> Determine the stress rate in the material (global) coordinates: First, we consider the rate of stress due solely to the rate of elastic deformation  $\mathbf{D}^e$  using Hook's law as if rotations never occurred by assuming co-rotational axes that rotate with the crystal lattice. For a general case where the material is elastically anisotropic, the *Jaumann stress rate* ( $\overset{\nabla}{\boldsymbol{\sigma}}$ ) becomes:

$$\overset{\nabla}{\boldsymbol{\sigma}} = \mathbf{L} : \mathbf{D}^e \quad (\text{Eq. 2.21})$$

Where here  $\mathbf{L}$  is the tensor of elastic moduli (Nemat-Nasser, 2004). This expression represents the double contraction of rank-fourth tensor ( $\mathbf{L}$ ) with rank two tensor  $\mathbf{D}^e$ , giving a rank two tensor, as explained by Dunne and Petrinic (2005). Whereas the rate of deformation  $\mathbf{D}$  is objective, the continuum spin  $\mathbf{W}$  is not. This means that a variation of the continuum spin (combined with the presence of any rate of deformation) will affect the *material stress rate of Cauchy stress* ( $\overset{\nabla}{\boldsymbol{\sigma}}$ ) in the global reference and hence a correction must be applied to make it objective. The stress rate of the material therefore depends on both: the previously defined Jauman stress rate and the total continuum spin:

$$\dot{\boldsymbol{\sigma}} = \overset{\nabla}{\boldsymbol{\sigma}} + \mathbf{W}\boldsymbol{\sigma} - \boldsymbol{\sigma}\mathbf{W} \quad (\text{Eq. 2.22})$$

Naturally, the step-dependent variables in the iteration need to be updated at the end of each time increment. If using the large deformation option in Abaqus software (2006), the *material stress rate* is automatically calculated from the *Jaumann stress rate* by the software.

#### 2.4.3.1 Differences and similarities to the continuum plasticity method

This procedure of relating imposed strains and associated stress in the crystals is similar to that used to define continuum plasticity. In fact the procedure holds if we replace the 3<sup>rd</sup> step for the plastic deformation component of the stretching ( $\mathbf{D}^p$ ) for this model. For example, we could use the combined isotropic and kinematic hardening and viscoplasticity seen in Eq. 2.8 <sup>8</sup>:

$$\mathbf{D}^p = \frac{3}{2} \left( \frac{J(\boldsymbol{\sigma}' - \mathbf{x}) - r - \sigma_y}{K} \right)^{1/m} \frac{\boldsymbol{\sigma}' - \mathbf{x}}{J(\boldsymbol{\sigma}' - \mathbf{x})} \quad (\text{Eq. 2.23})$$

To conclude, note that the backstress itself depends upon strain, showing in this way the incremental time nature of plasticity.

### 2.4.4 Models of polycrystalline deformation

#### 2.4.4.1 Deformation and displacement gradients by slip

For simple shear or slip,  $\gamma$ , on the plane where shear deformation occurs as the reference frame, we have:

---

<sup>8</sup> Note the equivalency between the rate of deformation ( $\mathbf{D}^p$ ) and the plastic strain rate ( $\dot{\boldsymbol{\epsilon}}^p$ ). If small elastic strains are assumed, an additive rate of deformation decomposition is possible (4<sup>th</sup> step in section 2.4.3). Under such assumption, the rate of stretch ( $\mathbf{D}^p$ ) can be approximated to the plastic strain rate ( $\dot{\boldsymbol{\epsilon}}$ ) (Abaqus Documentation, Inc., 2006), where the classical decomposition ( $\dot{\boldsymbol{\epsilon}} = \dot{\boldsymbol{\epsilon}}^{el} + \dot{\boldsymbol{\epsilon}}^p$ ) still holds.

$$\mathbf{F}_{\text{sh}} = \begin{pmatrix} 1 & 0 & \gamma \\ 0 & 1 & 0 \\ 0 & 0 & 1 \end{pmatrix} \quad (\text{Eq. 2.24})$$

It is convenient to describe this in terms of the *displacement gradient* ( $\nabla \mathbf{u} = \partial \mathbf{u} / \partial \mathbf{X}$ ) which represents the partial differentiation of the displacement vector with respect to the global or *material coordinates* ( $\mathbf{X}$ ). The displacement gradient and the deformation gradient on the shear plane are related as:

$$\nabla \mathbf{u}_{\text{sh}} = \mathbf{F}_{\text{sh}} - \mathbf{I} \quad (\text{Eq. 2.25})$$

where  $\mathbf{I}$  is the second-order identity tensor. Ignoring second-order terms, the *Green-Lagrange strain tensor* or simply the *large strain tensor* becomes:

$$\mathbf{E}_{\text{sh}} = \frac{1}{2} (\nabla \mathbf{u}_{\text{sh}} + (\nabla \mathbf{u}_{\text{sh}})^T) \quad (\text{Eq. 2.26})$$

Assuming small displacements, the Green-Lagrangian description (global or *material coordinates*) and the Eulerian description (current or *spatial coordinates*) are approximately equal ( $\mathbf{E}_{\text{sh}} \approx \boldsymbol{\varepsilon}_{\text{sh}}$ ). Moreover, Eq. 2.26 implies that the displacement gradient can be split into their symmetric and anti-symmetric parts, representing the shear strain ( $\boldsymbol{\varepsilon}_{\text{sh}}$ ) and the rotation ( $\boldsymbol{\omega}_{\text{sh}}$ ):

$$\nabla \mathbf{u}_{\text{sh}} = \boldsymbol{\varepsilon}_{\text{sh}} + \boldsymbol{\omega}_{\text{sh}} \quad (\text{Eq. 2.27})$$

or

$$\begin{pmatrix} 0 & 0 & \gamma \\ 0 & 0 & 0 \\ 0 & 0 & 0 \end{pmatrix} = \begin{pmatrix} 0 & 0 & \gamma/2 \\ 0 & 0 & 0 \\ \gamma/2 & 0 & 0 \end{pmatrix} + \begin{pmatrix} 0 & 0 & \gamma/2 \\ 0 & 0 & 0 \\ -\gamma/2 & 0 & 0 \end{pmatrix} \quad (\text{Eq. 2.28})$$

Alternatively, the *polar decomposition theorem* can be used to obtain the rotation  $\mathbf{R}_{sh}$  and the stretch  $\mathbf{U}_{sh}$  from the deformation gradient using little algebra ((Dunne and Petrinic, 2005), p. 57). Again, if small displacements are assumed and second-order terms ignored ( $\gamma^2 \sim 0$ ), it can be easily shown that  $\mathbf{R}_{sh} = \boldsymbol{\omega}_{sh}$  and  $\mathbf{U}_{sh} = \boldsymbol{\epsilon}_{sh}$ .

#### 2.4.4.2 Sachs model

Sachs, as early as 1928, proposed a plastic polycrystalline model to determine the yield stress under uniaxial tension (Sachs, 1928). An important simplification has been done by assuming one slip system, namely that with the highest Schmid's factor, to become active. As grains are differently oriented, stress and strain discontinuities at GBs will appear. This contradicts equilibrium, which states that the variation of stress is smooth. By implementing a hardening law, the Sachs model may also be used to predict a plastic flow curve (Clausen, 1997).

#### 2.4.4.3 Taylor model

In 1938, Taylor proposed another model to determine the yield stress under uniaxial tension (Taylor, 1938). In this case, Taylor assumed that all the grains undergo the same amount of deformation for a given overall deformation. Some details on this model are presented, as it is still relevant in modelling single crystal plasticity, such as tool machining (Demir, 2008). The macroscopic incremental plastic strain tensor for uniaxial loading ( $\sigma_{11}$ ) in the 1-axis is given by:

$$\mathbf{d}\boldsymbol{\epsilon}^p = \begin{pmatrix} d\epsilon_{11}^p & 0 & 0 \\ 0 & -\frac{1}{2}d\epsilon_{11}^p & 0 \\ 0 & 0 & -\frac{1}{2}d\epsilon_{11}^p \end{pmatrix} \quad (\text{Eq. 2.29})$$

Note that the trace of  $d\boldsymbol{\varepsilon}^p$  equals zero, this reflects the incompressibility condition. The macroscopic work done is:

$$dw = \sigma_{11} d\varepsilon_{11}^p \quad (\text{Eq. 2.30})$$

Von Mises (Von Mises, 1928) demonstrated in 1928 that 5 independent strain components (shear deformations by slip in our case) are sufficient to create any desired change in deformation. In the case of FCC metals, five independent slip systems are assumed to be active out of 12 possible for a given deformation. Based on this criterion, Taylor assumed that the 5 active slip systems are those which require least work. The work done by the active slip systems in all the differently oriented grains is given by:

$$dw = \sum_{\alpha} \tau^{\alpha} d\gamma^{\alpha} \quad (\text{Eq. 2.31})$$

Where  $\tau^{\alpha}$  and  $\gamma^{\alpha}$  are the shear stress and the shear strain for the slip system  $\alpha$ . Taylor further assumed that the critical shear stress is identical for all slip systems ( $\tau^{\alpha} = \tau^c$ ).

Equating Eq. 2.30 and Eq. 2.31, we can then write:

$$\frac{\sigma_{11}}{\tau^c} = \frac{\sum d\gamma^{\alpha}}{d\varepsilon_{11}^p} = m \quad (\text{Eq. 2.32})$$

The number  $m$  relates the uniaxial yield stress with the critical resolved shear stress. Using Sachs and Taylor models, the calculated  $m$  for FCC polycrystals are 2.24 (Sachs, 1928) and 3.06 (Taylor, 1938) respectively. These represent the lower and upper limits, analogous to Reuss (1929) (uniform stress) and Voigt (1889) (uniform strain) models for determining the average elastic stiffness in an elastic polycrystalline aggregate.

Once the shear strain is known in each system, the crystal rotations, if needed, can be calculated for Sachs and Taylor models. This can be done incrementally using Eq. 2.28. Despite his age, Taylor model can simulate texture in largely deformed Al polycrystals as successfully as modern crystal plasticity models such as CPFEM (Pi et al., 2008).

#### 2.4.4.4 Elasto Plastic Self Consistent (EPSC)

Another relevant approach is described here due to the important validation work that has been done using this model using neutron diffraction: Elasto Plastic Self Consistent (EPSC) model. This model is based in the well-known work by Eshelby (1957). In his paper Eshelby proposes a model to determine the stress and strain fields due to an eigenstrain in an ellipsoidal inclusion embedded in an infinite matrix. The three basic steps include: “imaginary cutting” the inclusion from the matrix (allowing free transformation); “straining” the inclusion to achieve its original shape; and “weld back” by applying forces of opposite sign in the surrounding matrix. Eshelby demonstrated that the stress and strain are uniform within an ellipsoidal inclusion. Many researchers were inspired by his work over the following decades. Eshelby’s work assumes the ellipsoidal inclusion embedded in an homogeneous medium. However, the theory becomes more powerful when the inclusion and the matrix are allowed to have a different stiffness. This is called the *equivalent inclusion method* (Clyne and Withers, 1995) and can be applied to a wide range of problems because the equations of the ellipsoid, when approximating it to a plate or a fibre, still hold.

The self-consistent model was proposed to tackle problems where a matrix does not exist i.e. polycrystalline aggregates (Kröner, 1958). The averaged elastic modulus of an aggregate containing many differently oriented anisotropic inclusions can be calculated via iteration, because it depends on the estimated modulus itself. Hill proposed an initial estimate as the arithmetic average of the Reuss (1929) (uniform stress) and Voigt (1889) (uniform strain) elastic moduli averages.

An important breakthrough in polycrystal plasticity can be achieved by “upgrading” the (elastic) self-consistent model through modelling of slip (Kröner, 1961). Elasto Plastic Self Consistent (EPSC) model considers an ellipsoidal inclusion in a surrounding medium which has the average properties of the entire polycrystal. Since the properties of the medium derive from the average response of all grains, these are computed by iteration. In this case, elastic isotropy is assumed. The anisotropy arises from the

compliance caused by slip for plastically deformed grains, quantified by the *instantaneous moduli*. The slip rate in each slip system is determined from the current slip system strength which increases with slip via a hardening matrix. For grains where plasticity has not occurred yet, the instantaneous moduli equal the elastic stiffnesses. An averaged instantaneous moduli is initially estimated and updated with each iteration until the difference between its successive values is small enough to be neglected. Having determined the self-consistent instantaneous stiffness, a small strain increment is prescribed, and the stress and strain states of the individual crystals are updated.

This approach, unlike CPFEM, does not fully simulate the effect of neighbours. Usually, elastic anisotropy is also neglected when using this approach. However, it becomes of interest due to its cost efficiency (relatively low time required for simulations) and good experimental validation results (Daymond et al., 2000, Daymond, 2005, Oliver et al., 2004).

#### ***2.4.5 Crystal plasticity finite element modelling (CPFEM)***

The pioneer compilation by Zienkiewicz (1977) describes the FE methodology in mathematical rigor whereas practical engineering examples can be found elsewhere (Benham et al., 1996). Here attention is paid to what concerns the implicit implementation of the crystal plasticity approach used in this research.

Time-independent elastic problems can usually be solved using a *linear finite element approach*. Meaning that only one increment is needed to obtain the final solution. However, contact between elements presenting different material properties is highly non-linear thus *non-linear finite element approach* is required, as used in publication 4. Continuum plasticity, as seen earlier, is another example of non-linear finite element approach. In general, such approach is needed when the material properties are a function of the current stress (Crisfield, 1996). Its solving involves an iterative process which is described in this section.

### 2.4.5.1 Steps in non-linear implicit

We present here the general steps to be followed by a non-linear implicit finite element analysis assuming large (plastic) deformations. These steps, as well as the stiffness matrix  $\mathbf{K}$ , can be found either by the virtual work principle (Abaqus Documentation, Inc., 2006; Keavy, 2008) or the variational principle (Fagan, 1992; Buchanan, 1995). Although explicit implementation must be used for high discontinuity problems (e.g. impact), in this work the solution is smooth with time. Moreover, explicit implementation may become numerically unstable thus a much smaller time increment is required.

1. An initial displacement increment is guessed for all the nodes on a basis of the previous displacements. The strain rates are calculated at each Gauss point from the velocity gradient, which is a function of the mentioned assumed displacement.

2. The material subroutine is called (step 1 to 5 of previous section) to calculate the stress rates using the strain rates calculated in step 1. Still for each Gauss point, the material Jacobian tensor is calculated.

3. The stiffness matrix of the element is given by:

$$\mathbf{K}^e = \int_{V^e} \mathbf{B}^T \mathbf{D} \mathbf{B} d(\text{vol}) \quad (\text{Eq. 2.33})$$

Where  $\mathbf{D}$  is the material Jacobian. In the case of a purely elastic element, this would simply be the elastic moduli (fourth rank tensor). The matrix  $\mathbf{B}$  represents the kinetics in the element and relates the strains with the displacements. The matrix  $\mathbf{B}$  depends on the *shape functions* which are used to describe the displacement at any point within the element from the displacement at the element nodes (Zienkiewicz, 1977). The shape functions comprise a very important and wide subject in finite element analysis but they are out of the scope of this work. It is of interest to mention that in the case of large deformations, the matrix  $\mathbf{B}$  is also a function of the displacements ( $\mathbf{B} = \mathbf{B}(\mathbf{u})$ ).

In order to interconnect these elements to each other, an assembly matrix is created in the basis of the geometry of the problem to be solved e.g. node 1 of element 2 might be connected to node 2 of element 1 but not to node 1 of element 1.

The stiffness tensor of the whole model is assembled using the Jacobian of each integration point.

$$\mathbf{K} = \int_V \mathbf{B}^T \mathbf{D} \mathbf{B} d(\text{vol}) \quad (\text{Eq. 2.34})$$

4. Equilibrium is checked using the known external loads at nodes ( $\mathbf{f}$ ), the previously calculated assembled stiffness matrix and the assumed displacements ( $\mathbf{u}$ ). The residual forces are:

$$\mathbf{F}_R(\mathbf{u}) = \mathbf{K}\mathbf{u} - \mathbf{f} \quad (\text{Eq. 2.35})$$

In the case of other forces acting on nodes such as body forces or those arising from initial strains or initial stresses, these would be added to  $\mathbf{f}$ <sup>9</sup>. In practise, if the stress rates are known, it is easier to integrate them over the time increment to obtain the stress to give the residual forces as (Bonet and Wood, 1997):

$$\mathbf{F}_R(\mathbf{u}) = \int_V \mathbf{B}^T \boldsymbol{\sigma} d(\text{vol}) - \mathbf{f} \quad (\text{Eq. 2.36})$$

Since we are essentially dealing with a static problem, the target for the residual forces  $\mathbf{F}_R(\mathbf{u})$  is zero. If equilibrium occurs according to a certain convergence criterion (e.g.  $\mathbf{F}_R(\mathbf{u})$  approaches zero) then the step solution ends here and the supposed displacements in step 1 and the new stress rates calculated in step 2 are assumed valid. At this stage, the solver is ready for the next increment assuming the “new” stresses now as “old” ones. The solver now jumps to step 6. If such criterion reveals no convergence, the solver jumps to step 5.

---

<sup>9</sup> In the case of large total deformations:  $\mathbf{f} = \mathbf{f}(\mathbf{u})$

5. A further iteration is needed (from steps 1 to 4) but now assuming “new” displacements. This is done using the residual forces function:

$$\delta \mathbf{u} = - \left[ \frac{\partial \mathbf{F}_R(\mathbf{u})}{\partial(\mathbf{u})} \right]^{-1} \mathbf{F}_R(\mathbf{u}) \quad \text{or} \quad \delta \mathbf{u} = - [\nabla \mathbf{F}_R(\mathbf{u})]^{-1} \mathbf{F}_R(\mathbf{u}) \quad (\text{Eq. 2.37})$$

The current displacements are updated by adding the change of displacements,  $\delta \mathbf{u}$ , according to the Newton-Raphson iterative process. This will result in a better displacement guess.

In general, the initial guess for the unknown  $\mathbf{u}$  in the assembled system can be the previous or an extrapolated value. For the first iteration of the first increment,  $\mathbf{u}$  can generally be set to zero because  $\mathbf{f}$  (in Eq. 2.36) will not be zero and the global system material Jacobian ( $\partial \mathbf{F}_R(\mathbf{u}) / \partial(\mathbf{u})$ ) is not zero. This would provide with non-zero values in Eq. 2.37 to update the displacements with a better guess.

6. Once such iteration (from steps 1 to 5) has finished, the “new” stress rates computed from the displacements assumed are considered as valid. In the event that a large number of iterations from steps 1 to 5 did not meet the equilibrium criterion, a shorter time increment would be assumed. The velocity gradient would be recalculated and it would be needed to go to step 1.

#### 2.4.5.2 Coupling in FEM

A major concern of multiscale modelling is how to link computations at these various length scales together. A straight forward mean to achieve this is by *one-way coupling*, in which the boundary conditions are passed through from a component level simulation to another. For example, it is possible to model the stress state near the crack tip or at some point in a bent bar (section 4.4.2). This model is called the global model in Abaqus software. The displacement field at a smaller simulation window within this model can be passed on to an assembly of anisotropic crystals. This model is called the sub-model in Abaqus software. This in principle changes the geometry of the

global model, but in practice, the change is small enough to be negligible since a large number of randomly oriented crystals would result in an isotropic behaviour at the macroscale. Thus, there is no need to iterate.

Alternatively, the iteration between the two simulations can be taken into account. In the example above, this means Sub-modelling results need to be incorporated into the global model. When the input of one physics analysis depends on the results from another analysis, the analyses are *fully coupled*. This may be achieved by assembling all the physics fields as finite-element equations in one matrix. Meaning that properties of the submodel are incorporated into the global model as a mathematical relationship. This makes the stiffness matrix more complicated and the most computationally intensive.

### ***2.4.6 Recent approaches in CPFEM***

#### *2.4.6.1.1 Modelling the Hall-Petch effect*

Nye (1953) first thought that the curvature of the lattice can be accommodated by an introduction of a density of dislocations. These dislocations are referred to as geometrically necessary dislocations (GNDs) which differ from the randomly introduced dislocations or statistically stored dislocations (SSDs). Both SSDs and GNDs accumulate in single crystals during straining. Hardening is assumed to arise from the addition of SSDs and GNDs. Strain spatial gradients (with distance), which typically build up near interfaces, are responsible for GNDs (Ashby, 1970) and, thereby, increase the slip resistance.

Recent studies aim to capture the Hall-Petch effect in order to explain the effect of the grain size on hardness: “the smaller the harder”. The main contribution of such studies is the consideration of GNDs as an extra contribution to hardening. Since GND are believed to arise from the strain gradients, it is possible to predict different aggregate responses for different grain sizes.

Fleck and co-authors (1994) conducted experiments on polycrystals that confirmed the strain gradient hardening. This finding fits with the Hall-Petch effect found in polycrystals since, for a given deformation field within a polycrystal, the shorter the length scale the higher strain gradients. They further proposed that hardening arises from the addition of dislocation densities of SSDs and GNDs.

The density of GNDs is related to the net Burgers vector associated with crystallographic slip that produces plastic strain incompatibility. Nye's dislocation density tensor (1953), defined as  $\alpha = \text{curl } \mathbf{F}^p$ , is a measure of the plastic strain incompatibility (or the number of GNDs). Years after, Kroner (1960) first established an equivalency between elastic and plastic strain tensors and gave the dislocation tensor as a function of the elastic tensor and the lattice rotation. Based on this principle, the elastic part of the deformation gradient, as determined by high resolution EBSD (Electron Backscatter Diffraction), can be used to estimate the density of GNDs. (Britton et al., 2009).

Busso and co-authors (2000) first implemented the theory of strain gradient plasticity into a finite element model. Using this theory, some Hall-Petch effect has been shown through the introduction of GNDs (Abrivard et al., 2007). Further, in-grain heterogeneity of accumulated plastic strain correlated visually with in-grain heterogeneity of rotations when only SSDs were considered. A grain that presented a high heterogeneity of rotations showed relatively large accumulation of GNDs. Later, (Liang and Dunne, 2009) showed some agreement between simulated and measured GNDs at the interface of a plastically deformed aluminium bi-crystal. They also showed some effect of the GNDs on lattice rotations at the interface. Size-dependent models tend to predict higher stresses near the GB due to the high degree of deformation heterogeneity at the boundary.

Kroner (2001) has suggested some pathways for development of dislocation density models. For instance, models were reported to only incorporate dislocations of one

sign, whilst it is well known that the presence of both signs explains the hardening and softening of materials. In this respect, some progress has recently been done by modelling the signs of screw and edge dislocation densities (Alankar et al., 2009), yet validations of such results remain difficult. Kroner also emphasized that the motion of atoms during plastic deformation is extremely discontinuous and might not be valid for continuum mechanics. In his article, Kroner suggests a continuum theory through molecular dynamics (principles of molecular dynamics can be found in (Arsenault et al., 1988), page 47) and statistical physics as a way forward. An adequate model should be able to reproduce the random dislocation networks formed in the aggregate.

The local dislocation density has been modelled in BCC metals (Ma et al., 2007) as well as FCC metals (Ma et al., 2006). In both cases, the hardening was modelled by the energy associated with edge (forest cutting process) and screw (Peierls energy barrier) dislocation densities at the local level. While the Peierls mechanism dominates in BCC metals, the forest dislocation density dominates the hardening in FCC. Although activation of slip systems was captured, agreement in strain predictions between simulations and experiments is generally poor. This study also aimed to capture the slip transmission across the boundary by taking into account an energy barrier parameter that varies as a function of the GB angle and misorientation between grains. For this purpose, the geometry of the boundary was represented by a boundary finite element. It was shown that the calculated misorientation across the boundary was influenced by the boundary finite element constants. Adjusting such constants can be sufficient to reproduce the measured misorientations.

Some approaches try to capture the Hall-Petch effect by assigning a higher hardening rate to an exterior phase around the GB of an arbitrary thickness (Meyers et al., 2002). However, unlike strain gradients theory, this approach does not describe a smooth transition of GNDs across the grain.

#### 2.4.6.1.2 Thermo-dynamical approaches

In the recent years, considerable attention has been paid into the search of thermodynamical formulations for crystal plasticity (McDowell, 2008). These are based in the fundamental inequality which contains the first and second principles of thermodynamics. The fundamental inequality delivers thermodynamical balance, including stress, rate of deformation, entropy, internal free energy, temperature and heat flux. A free energy function can be introduced into such inequality (Lemaitre and Chaboche, 1994). The free energy function is a function of a reduced set of state variables associated to thermoelastic and inelastic deformation. The variables that enter the latter set have been proposed differently by several authors in crystal plasticity. For example, Gurtin (2002) suggested the free energy being dependent on the dislocation density tensor ( $\mathbf{G}$ ). In this way, the standard elastic strain-energy is augmented by a *defect energy*, in consistency with classical dislocation theory (Hull and Bacon, 1984). The manner in which  $\mathbf{G}$  enters the free energy function has later been discussed by Archaya (2008). Alternatively, the free energy function has been assumed to depend on the gradient of the plastic slip (Yalcinkaya et al., 2011). Slip activity, stress and the back-stresses can then be calculated. Only a few practical CPFEM simulations have been performed to date following such procedure, yet in 1D elements (Yalcinkaya et al., 2011).

## 2.5 Measuring strain by neutron diffraction

The principle of diffraction is based on the well-known Bragg's law:  $\sin\theta = \lambda/2d$  where  $d$  is the spacing between atoms in the lattice arranged in imaginary planes (Cullity and Stock, 2001) (see Figure 2.6a). For a given crystal structure, each lattice plane has an associated angle at which the diffraction peak occurs. This angle is determined by the formula. The variation of the diffraction angle of such peak is precisely what is related to the  $d$  spacing parameter and hence, to the elastic strain stored in the lattice in a given direction. Modern measurement facilities can record several diffraction peaks at the

same time thus differently oriented grains within the gauge volume for a given direction. Some measurement facilities even let record other sections of the diffraction cone, allowing experimental measurement of texture.

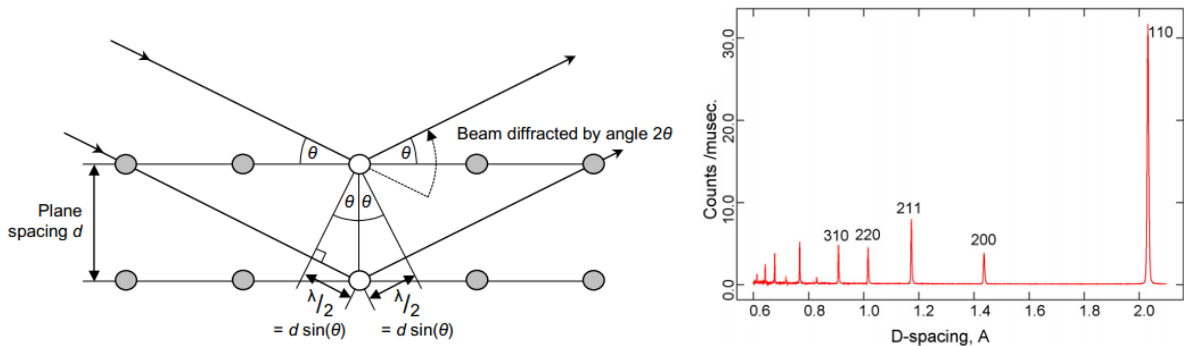


**Figure 2.6. A) diagram demonstrating Bragg's law (Kelleher, 2006). B) diffraction patterns showing the measured peaks in IF steel (BCC structure), (Quinta da Fonseca et al., 2006).**

Diffraction by high power X-Rays (generated in synchrotron facilities) allows strain analyses at a depth to study the bulk material properties rather than conventional X-Rays where only surface measurements are possible. Neutron diffraction allows even deeper measurements (several tens of mm underneath the surface) due to their lack of electrical charge and thus the weak interaction with other atoms in the lattice, although the resolution is not as good as that for high energy X-Rays.

Different length scale residual stresses can be measured by diffraction. Consider a diffraction intensity diagram showing the different diffraction peaks for different crystallographic planes (Figure 2.6b): 1) Type I stresses alone would move all peaks in the same direction (left or right) 2) Type II stresses would move some peaks left and some right by different amount.

The magnitude of the relative shifts of individual peaks is expected to be related to the maximum Inter Granular Stress (IGS) in the material, although in reality, IGS may vary locally since diffraction only measures the average strains over many grains 3) Type III stress makes the peak wider keeping the area constant. This peak widening can be due

to either: spreading of the different peaks due to the difference of stress in the different grains contributing in the diffraction (IGS) or due to the lattice defects and dislocation density making each diffraction peak wider. 4) Additionally, a change in texture would changes the area of each peak.

In FCC metals, 200 and 111 diffraction peaks are elastically softest and stiffest in the loading direction (Korsunsky et al, 2004). As a result,  $\langle 111 \rangle // LD$  grains have been shown to carry more load and yield earlier (Wang 2005), despite having the highest yield strength. These experimental results agree with predictions from EPSC (Korsunsky et al., 2004). This shows evidence of, apart from the presence of IGS, certain families of grains yielding before than others and likely some of them yielding even in the elastic regime. Average stiffness between 111 and 200 peaks has been experimentally found in 311 peaks in FCC polycrystals (Daymond, 2005). Measurements of individual peaks in hexagonal materials (Ti-6Al-4V alloy) is also possible, yielding a good agreement with finite element simulations (Song et al., 2008).

## **2.6 Damage mechanisms in polycrystalline materials**

There is a number of damage mechanisms where CPFEM can be useful such as fracture, stress corrosion cracking or fatigue. These are discussed in this section.

### **2.6.1 Fracture**

#### **2.6.1.1 Macroscale**

In 1913, Inglis found an expression to relate the average tensile stress to the local stress at the head of a crack tip in a homogeneous (amorphous) material (Inglis, 1913). Such higher local stress is associated with a release of elastic strain in the solid as the crack grows. Years later, Griffith (1921) postulated that the crack will grow if this energy is higher than the energy needed to create the new (crack) surface. The surface energy can be adjusted to allow a small amount of plasticity. In these materials, *the stress*

*intensity factor*, which is related to the crack length and the external load, can be compared directly to the material toughness. In fully elastic-plastic materials, the numerical difficulties involved in computing the stress close to a crack tip makes inadequate the calculation of stress intensity factor. In 1968, Rice showed that the J-integral could be used to post-process the energy release rate (Rice, 1968) in a continuum plasticity model (section 2.4.2), and this can be compared to the material fracture toughness (Riveros, 2006). Nowadays, many structural integrity assessments rely on the assumptions of Inglis and Griffith (for brittle materials) and Rice (for elastic-plastic materials).

### 2.6.1.2 Meso and microscale

The local variability of the maximum tensile stresses within the microstructure is of special concern since this drives brittle fracture Figure 2.7. The variability of intergranular stresses is studied in publications 1 and 2.

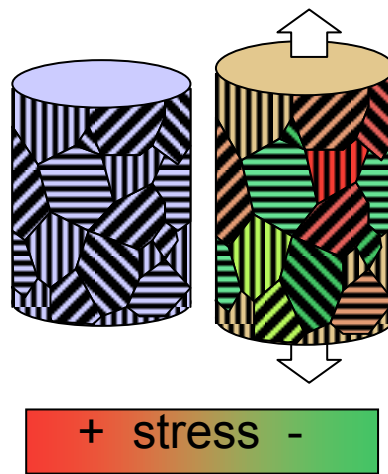


**Figure 2.1. Heterogeneity of stress at Grain Boundaries (GB) for a given macroscopic stress**

The combination of CPFEM modeling with a fracture initiation parameter has been shown promising at evaluating damage at boundaries in a TiAl polycrystal (Bieler et al., 2009). The damaged boundary of a reconstructed microstructure had a high fracture

initiation parameter (*fip*) value, indicating that multiple types of imperfect slip transfer were possible, leaving residual dislocation content at the boundary. In this case microcracks developed where neither the stress nor the strain was large, indicating that a high strain energy did not cause fracture.

Finally, it is worth noting that transgranular brittle fracture is also possible. For example, BCC crystals at low temperatures tend to crack along defined crystallographic planes (cleavage), propagating rapidly since these planes possess low surface energy (Honeycombe, 1984).

### **2.6.2 Fatigue**

Failure by fatigue is estimated to comprise approximately 90% of all the metallic materials failures (Callister, 2006). Although fatigue is not dealt with in this research, it is a field where crystal plasticity has been claimed as useful (McDowell and Dunne, 2010). Some basic concepts and directions are presented here.

#### **2.6.2.1 Fatigue in individual FCC crystals**

As discussed previously, modelling of microscopic features within grains are still difficult. A brief insight of the microstructure evolution under cycling and a CPFEM approach are presented here.

It is well established that plastic strains are necessary for the inducement of fatigue fracture in ductile single crystals (Suresh, 1998). Usually shear strain-stress tests involving fixed amplitudes of plastic strains in crystals oriented for single slips are conducted. Such tests reveal an initial rapid hardening. Eventually the stress is no further altered by the cycling (saturation stress), which depends on the crystal orientation (Wang et al., 2001). The dislocation substructures in the crystal can be related to the variation of the saturation shear stress with the imposed plastic strain. These substructures include veins, labyrinth structures, dislocation cells and persistent

slip bands (PSBs). PSBs appear at low fixed plastic strains and eventually cover the whole crystal volume at higher fixed plastic strains. PSB are composed of a large number of slip planes forming a flat lamellar structure and spanning the whole cross section of the single crystal thus reaching the GB. In CPFEM, slip softening properties can be assigned to bands within grains with typical observed values of thickness and wavelength in, for instance, a Ti-6Al-4V alloy (Zhang et al., 2010).

Further, PSBs are divided by walls and channels, each having very different dislocation densities (Suresh, 1998). Therefore, as flow stresses may vary accordingly, internal stresses may appear, behaving effectively as different phases. Mughrabi (Mughrabi, 1983) first proposed a composite model to study such stress effects.

### **2.6.2.2 Fatigue cracks in polycrystals**

The relative number of cycles to crack initiation and crack propagation depend on the material and testing conditions (Callister, 2006). Initiation depends on features such as crystallographic orientations (Taylor 1999), triple points, inclusions (Dunne et al 2007 - Experimental and computational studies of low cycle fatigue crack nucleation in a polycrystal) as well as on the interaction of PSBs with GBs (Zhang and Wang 2008). Once a stable crack has nucleated, it then initially propagates very slowly and, in polycrystalline metals, along crystallographic planes of high shear stress (stage I propagation). Eventually, a second propagation stage (stage II) takes over, wherein the crack extension rate increases dramaticall (Callister, 2006).

The fatigue regime can influence the mode of the crack in polycrystals. Figure 2.8 shows an intergranular crack in High Cycling Fatigue (HCF) and a transgranular crack in Low Cycling Fatigue (LCF) where the crack seems to present little susceptibility to the GB.

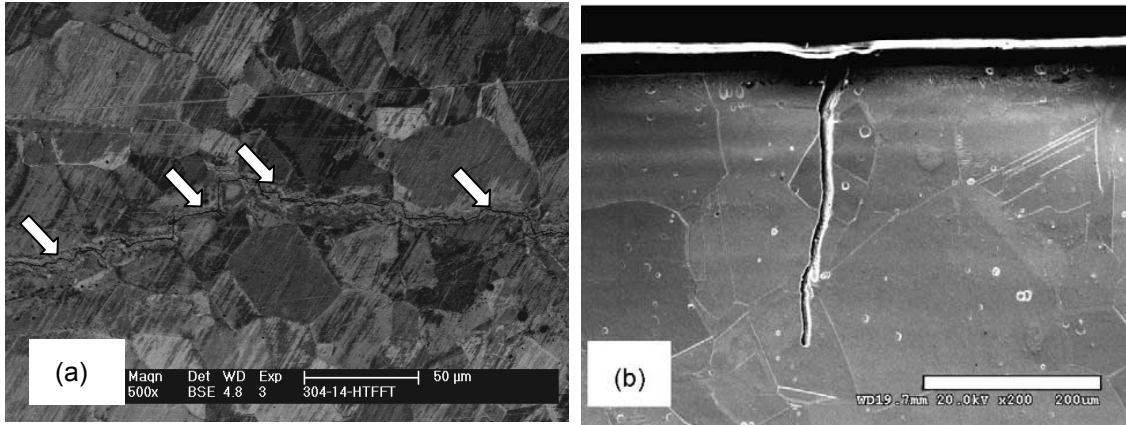


**Figure 2.8: a) Intergranular crack (white arrows) in HCF in 304 Stainless Steel after 16,850 tested at 300 °C (Bhatti and Withers, 2008), b) Transgranular crack in LCF in 316 Stainless Steel after 5159 cycles tested at room temperature (Wang and Wang, 2005)**

### 2.6.2.3 Impact of stress and deformation

Elber (1970) showed that fatigue cracks could remain closed even when subjected to cyclic tensile loads. Plastic deformation (e.g. bending) can introduce a compressive residual stress that promotes crack closure. This can be checked by measuring the crack propagation rate as a function of number of cycles (Kelleher et al., 2010) or by measuring the reduction of compressive lattice strains by ND. If this residual stress was previously preventing the growth of a crack, then it is possible that a crack will initiate and grow once the residual stress disappears. Surface treatments, such as peening, are often performed in order to introduce average in-plane compressive residual stress near the surface. This can improve (or sometimes worsen) in cyclic bending tests (Mochizuki, 2007, Fathallah et al., 2003). Peening, however, is difficult to model due to the high strain rates, the high total plastic strains involved or even the deformation induced martensite (Smith et al., 2009).

At the mesoscale, difference of stresses for different grains may control the initiation in fatigue life in polycrystalline samples (Song et al., 2008). In LCF, IGS stays constant after a few cycles until the initiation of the crack (Wang and Wang, 2005). ND measurements (Korsunsky et al., 2004), have revealed that {200} grain families show a high hysteresis

cycle while {111} show a virtually elastic cycle, being the latter more likely to fail (Taylor et al., 1999). These deformation anisotropies within the polycrystal during cycling, inspire the exploration of the CPFEM capabilities presented in the next section.

#### 2.6.2.4 Length scales of fatigue modelling

At the *macroscale*, there is a large stage of linear relationship between  $\log(\Delta K)$  and  $\log(da/dN)$  as Paris<sup>10</sup> determined for a number of alloys in the HCF regime (Callister, 2006). At the *microscale*, prediction of dislocation structures such as cells or PSBs are in early stages according to a recent review paper (Dunne 2010). At the *mesoscale*, CPFEM can be used to model the role of microstructure on the driving forces for fatigue initiation, particularly in HCF where cyclic plastic deformation is highly heterogeneous. For example, CPFEM can be used to predict life-limiting scenarios within a RVE of grains (Zhang et al., 2010).

In the HCF regime, Dang Van (1993) postulated that infinite fatigue life (fatigue limit) corresponds to elastic response occurring on every crystallographic plane, relating damage with the dissipated energy. The energy per saturated cycle could be considered as a constant to be multiplied by the number of cycles. Thus such approach can be easily extended to complex loading paths as opposed to classical criteria based on variables such as maximum stresses, plastic strain range, total strain range (Korsunsky et al., 2007). CPFEM shows promise at predicting crack initiation by the locations of most intense energy dissipation by slip (Korsunsky et al., 2007) or simply by accumulated plastic slip (Manonukul and Dunne, 2004). The experimentally observed nucleation sites have been predicted as the regions of highest accumulated slip (Dunne et al., 2007). Criteria combining stress components with the cumulative plastic slip are also possible (McDowell and Dunne, 2010).

---

<sup>10</sup>  $\Delta K$  and  $da/dN$  represent the stress intensity range and crack growth rate respectively.

### ***2.6.3 Capabilities towards SCC***

Some materials in some environments subjected to stress may suffer SCC. SCC predictions often rely on fracture mechanics at the macroscale. The stress intensity factor limit in an environment is lower than the critical material's  $K_{Ic}$  (opening mode) (Anderson, 2005). The reduction of  $K_{Ic}$  depends on the alloy and the SCC environment.

Inter-laboratory studies using nominally identical material-environment combinations have revealed a high degree of scatter between the obtained values of  $K_{ISCC}$  (Dietzel and Turnbull, 2007). In this regard, the boundary character can play a role on the boundary resistance to SCC (Marrow et al., 2006, King et al., 2008). These findings are summarized in annex 6.1.

An example is given in Figure 2.9, where crack bridges are formed by non-sensitised boundaries around which the crack has deviated (annealing twins ( $\Sigma 3$ )). In contrast to the brittle failure of the sensitised boundaries, these bridges deform plastically before ultimate rupture.

Figure 2.7 shows that stresses between grains (or intergranular stresses) vary for different grain boundaries. Since the stress corrosion cracks are largely intergranular, there is an interest in modelling stresses at boundaries. For example, in publication 2 we seek for combinations of grains that may lead to high stresses at the boundary in virtually generated microstructures.

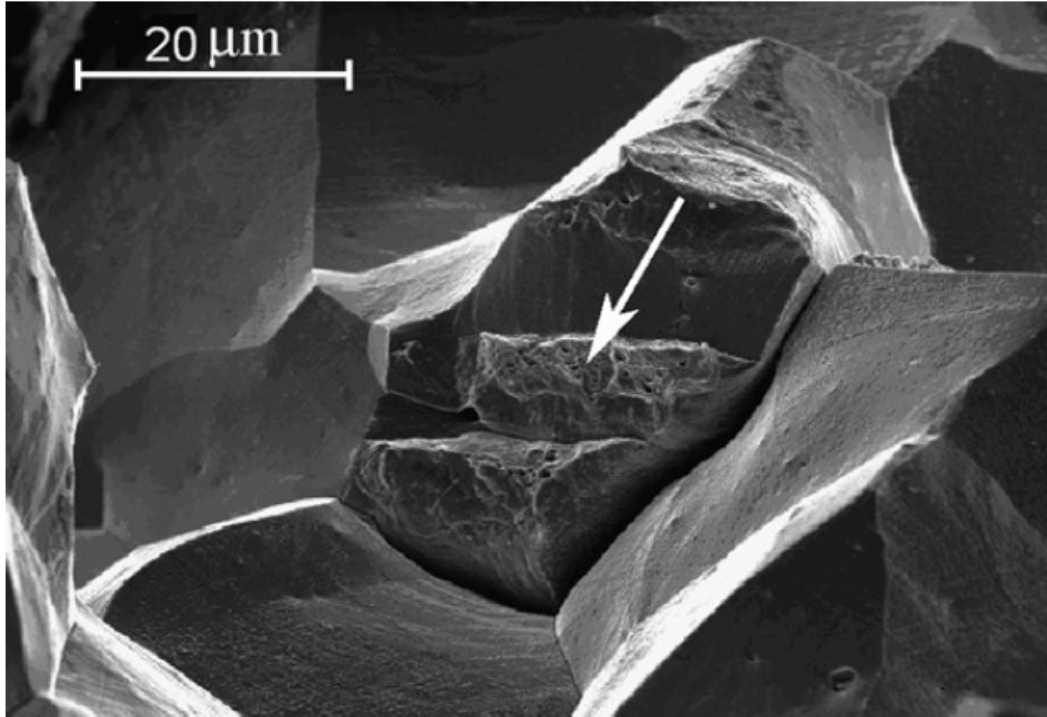


**Figure 2.9.** Example of intergranular stress corrosion cracking of susceptible boundaries (smooth surfaces) and ductile failure of a bridge formed by a resistant grain boundary (rough surface, marked with an arrow). Image courtesy of D. Engelberg (University of Manchester).

Alternatively, a stress corrosion crack can be imported into a 3D CPFEM model (Simonovski and Cizelj, 2012, Simonovski and Cizelj, 2011b). This allows evaluation of the role of boundary stress on cracking when coupled with the findings of susceptible boundaries (annex 6.1). The calculated boundary stresses are, of course, an approximation since the model does not capture certain effects. For example, different mechanisms occurring at the boundary (dislocation pile-ups or GNDs) may substantially increase the local stresses (Kamaya et al., 2005).

## **3 Experimental methods**

The majority of the experimental and modelling techniques are described in each (self-consistent) publication. Further experimental methods not included in the publications are presented in the supplementary research associated to each publication. The experimental methods used in additional research cases are also presented in the next chapter. In addition, the pre-processing methodology used for the initial random grain orientation assignment is described in section 6.2. The post-processing methodology used for averaging lattice rotations, taking into account the crystal symmetry, is described in section 6.3. As the material presented in these annexes are used in a number of occasions in the remaining of the dissertation.

## 4 Results and discussions

This chapter is structured in the form of four publications. Supplementary research material associated to these publications will be presented in annexes 6.4, 6.5 and 6.6. The experimental methods, discussions and results are presented individually in each research case. In publication 1: *“Macro and Intergranular stress responses of austenitic stainless steel to 90° strain path changes”*, results of elastic strains for individual grain families by neutron diffraction following strain path changes are compared to those predicted by CPFEM. Publication 2: *“Modelling the effect of elastic and plastic anisotropies on stresses at grain boundaries”*, is a virtual study where the relative impact of crystal anisotropies on grain boundary stresses is examined. Special attention is paid to the unloaded state because of its relevance to SCC. In publication 3: *“Modelling and measurement of plastic deformation and grain rotation in 3D at the grain-to-grain level”*, the lattice rotations in a reconstructed aluminium polycrystal have been measured (by Diffraction Contrast Tomography (DCT)) and predicted (by CPFEM). In publication 4: *“Three-dimensional observation and image-based modelling of thermal strains in polycrystalline alumina”*, the stresses at boundaries in a reconstructed (by DCT) aluminium oxide polycrystal have been calculated. Diffraction images have been measured and predicted via post-processing.

Additional research material to these publications has been performed. This will be presented in annexes 6.7, 6.8, 6.9 and 6.10. The corresponding experimental methods, discussions and results are presented individually in each of these annexes for each research case.

## 4.1 Publication 1

### **Macro and Intergranular stress responses of austenitic stainless steel to 90° strain path changes**

D. Gonzalez, J.F. Kelleher, J. Quinta da Fonseca, P.J. Withers

Materials Science and Engineering: A, Volume 546, 1 June 2012, Pages 263–271

In this publication the idea of stress-strain measurements in perpendicular directions to the pre-strain was proposed by J.F. Kelleher and supervised by P. Withers. The corresponding experimental results were performed by J.F. Kelleher and myself. Some comments in the paper about the neutron diffraction technique used were edited by Joao Fonseca. The Voronoi geometry was created by Zoran Petric and I. Simonovski (Petric, 2010) whereas the rest of the pre-processing (meshing, material properties calibration, random orientation assignment, boundary conditions...etc) and all the post-processing was done by myself.

**BEGIN OF PUBLICATION 1**

**Macro and Intergranular stress responses of austenitic stainless steel to 90° strain path changes**

D. Gonzalez<sup>1\*</sup>, J.F. Kelleher<sup>2</sup>, J. Quinta da Fonseca<sup>1</sup>, P.J. Withers<sup>1</sup>

<sup>1</sup> School of Materials, Univ. of Manchester, Grosvenor St., Manchester, M1 7HS, UK.

<sup>2</sup> ISIS Pulsed Neutron & Muon Source, RAL, Didcot, OX11 0QX, UK

\*Corresponding author:

david.gonzalez@postgrad.manchester.ac.uk

Mobile number: 00447961684966

Strain path history can play a crucial role in sensitising/desensitising metals to various damage mechanisms and yet little work has been done to quantify and understand how intergranular strains change upon path changes, or their effect on the macroscopic behaviour. Here we have measured, by neutron diffraction, and modelled, by crystal plasticity finite elements, the stress-strain responses of 316L stainless steel over three different 90° strain paths using an assembled microstructure of randomly oriented crystallites. The measurements show a clear Bauschinger effect on reloading that is only partially captured by the model. Further, measurements of the elastic response of different  $\{hkl\}$  grain families revealed an even earlier onset of yield for strain paths reloaded in compression while a strain path reloaded in tension showed good agreement with corresponding predictions. Finally, we propose that the study of strain path effects provides a more rigorous test of crystal plasticity models than conventional in situ diffraction studies of uniaxial loading.

Keywords: neutron scattering, finite element method, austenite, residual stresses, crystal plasticity, hardening

### **4.1.1 Introduction**

The purpose of this paper is to contribute to our understanding of the mechanical response to non-monotonic strain paths at the granular level. In practice it is rare for metals to be deformation processed to final shape without some form of strain path change having taken place at some stage; either at 180° (e.g. tension compression) or 90° (say tension perpendicular to a prior tensile strain) or at some arbitrary angle. However most of our understanding of the deformation of polycrystalline metals has been acquired on the basis of uniaxial deformation, with limited attention focused on strain reversals (180°). Consequently relatively little is known about the development of intergranular and intragranular stresses and heterogeneities as a function of complex (non 180°) strain paths.

This gap in our knowledge base is of concern because strain history can play a crucial role in sensitising/desensitising metals to various damage mechanisms. For example, prior strain path can influence stress corrosion cracking [1], most probably due, at least in part, to the inter-granular stress (IGS) acting between grains, while a reduction in the critical crack tip opening displacement (COTD) has been observed in pipe-line steels after tensile and compressive pre-strain, the effect being most severe for compressive pre-strain [2]. Similarly, a few percent of pre-strain was found to promote strain-induced ductile-brittle transition and a high compressive pre-strain found to accelerate fatigue-crack initiation and growth [2]. Further, several studies conducted under high temperature PWR environments have demonstrated the importance of strain path on cracking, for example: Couvant et al. [3] found that the complex strain paths can promote the intergranular crack initiation in 304L steels as well as 316L steels [4], while the influence of loading orientation on crack growth rates has been shown in cold-rolled Alloy 600 [5] and 304 stainless steel [6].

In general, any amount of plastic deformation in a material changes the stress required for further deformation. Typically, plastic strain increases the stress required for

continued deformation in the same direction (i.e. strain hardening occurs), but the yield stress in other directions may be affected in more subtle ways. In particular, if the sign of the applied load is reversed after plastic deformation, the yield stress in the opposite direction may be reduced. This is the 'Bauschinger effect' (BE), named after its discoverer, which has been known for over a hundred years [7]. The Bauschinger effect can originate at two length scales, namely at the inter- and intra-granular levels.

In polycrystalline metals heterogeneous yielding leads to intergranular stresses (IGS), sometimes referred to as mean stresses, between crystallographic families [8,9], or between different phases [10-12], which will remain upon unloading. For certain grain families (sometimes called soft grains) these mean (back) stresses will add to the applied stress upon reverse loading leading to premature yield whereas in other (hard) grains they will be of opposite sign and oppose it.

At the intra-granular level (or microscale), several mechanisms contribute to the heterogeneous nature of deformation that can facilitate slip upon load reversal [13]. These could be pile-up dislocations present at obstacles [14-16] such as vacancies, dislocation tangles, small second-phase particles [17], Lomer-Cottrell locks [18,19], or twins [20]. Similarly, cells and walls within grains may also behave as distinct regions within the crystals, generating long-range internal or mean stresses that act similarly to the IGS [21].

Mathematically the directionality of hardening is often described by isotropic and kinematic hardening components. The former describes hardening that exhibits no directionality and thus it does not contribute to strain path effects. For a single phase this is equivalent to saying that dislocations once created are equally difficult to move in all directions. The latter describes hardening that is strain path dependent; this could be at the intra granular or intergranular level as discussed above.

The macroscopic flow curve has traditionally been the primary means of characterising metal deformation. These macroscopic measurements can be compared with Crystal

Plasticity Finite Element Modelling (CPFEM) which simulates the deformation of an aggregate of grains [22-24]. The macroscopic BE in sheet metal has been captured by straightforward [25] and sophisticated empirical models [26]. At the grain scale, a model considering easier slip upon reversal has been incorporated to capture the Bauschinger effect observed in cycled single crystals of copper [27]. Stress-strain hysteresis loops and the evolution of resolved shear stress amplitude versus resolved plastic shear strain amplitude were also captured by the model. Miller and McDowell [28] used a Taylor model to predict compression-followed-by-torsion under large strains (>50%). This model only partially captured the experimentally observed textural softening during torsion, probably due to the over constraints assumed in Taylor model. Sophisticated multiscale models that incorporate dislocation-based reversal mechanisms have been used to successfully capture the strain path changes in uniaxial loading of polycrystals at the macroscale [29,30]. In 1965, Wilson [31] found a relationship between the residual stress and the permanent softening in two phase steels using X-ray diffraction. Years later, the residual stress was demonstrated to approach the same limiting value in forward and reverse loading with this limiting value dependent on the amount of pre-strain [11,32].

Over the last 15 years, neutron diffraction has been used to measure the evolution of lattice strain for individual grain families (or mesoscopic behaviour) under plastic deformation of initially unstrained samples [33-35]. For uniaxial loading, such measurements showed a good agreement with elastic intergranular strains predicted by CPFEM. Moreover, correlations between the broadening of the Bragg peaks and the evolution of the system strength have been demonstrated [36]. In addition the lattice strain response to 180° (tension-compression) path changes has been studied by neutron diffraction [8],[37]. However, we are not aware of any studies looking at 90° path changes. This is perhaps a pity because it may provide a more critical test of such models.

Here the goal is to compare CPFEM predictions with neutron diffraction measurements of intergranular strain for 90° strain path changes. In our study the pre-strains applied

do not exceed 4%, since texture has been found not to change significantly up to about 8% strain [38].

## 4.1.2 Experimental

### 4.1.2.1 Material, sampling and loading paths

316L stainless steel (composition summarised in Table 1) was annealed for about 10 hours at 1050°C, in an effort to obtain a more homogeneous microstructure giving an average grain size of 65µm Figure 1. The neutron diffraction spectra revealed low texture and an absence of second phases such as martensite or ferrite.

**Table 1 . Chemical composition in % of the AISI 316L stainless steel used in the present work.**

316L	C	Cr	Ni	Mo	Mn	Si	P	S	N
Wt %	0.02	16.7	10.1	2.04	1.57	0.53	0.03	0.02	0.04
	3							6	8

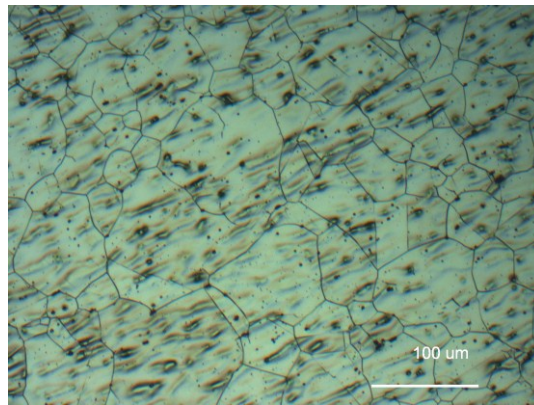


**Figure 1. Micrograph of the recrystallised austenite after 1050 °C annealing in the studied 316L stainless steel.**

Figure 2a shows the sample design developed to achieve multiaxial strain paths. Both tensile and compressive loads can be applied in the longitudinal direction via threaded sample ends. The gauge length of each sample was machined to a square cross-section. Compression can thus also be applied to the flat faces of the gauge length in either one, or both, of the two transverse directions by means of contacting alumina platens (used

due to its relative transparency to neutrons.). For this work, the platens were coated with copper grease to prevent the expected Poisson expansion being constrained by friction. A range of plastic strain states could thus be introduced although with the restriction that tension can only be applied along one axis.

Diffraction measurements were made for three samples during the second loading stage, each deformed following a different strain path ( $C_2C_1$ ,  $T_3C_1$  and  $C_2T_3$  - see Figure 2b). In each of the three strain paths studied, the pre-strain was approximately 1.5% and the total deformations during the *in-situ* measurement are about 3%. Lattice strains have been measured both *axial* and *transverse* to the loading direction.

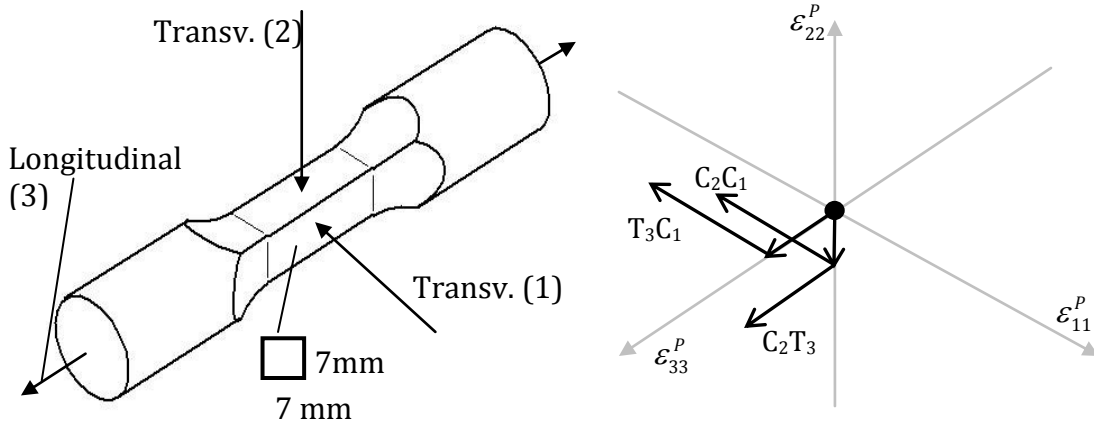


**Figure 2. a) The sample design allows three distinct 90° strain path changes shown in (b), namely compression-compression ( $C_2C_1$ ), tension-compression ( $T_3C_1$ ) and compression-tension ( $C_2T_3$ ). For sake of clarity, only the longitudinal components of plastic strain are shown.**

Conventionally, the Bauschinger Effect (BE) describes the reduction in yield strength when the direction of loading is completely reversed (180°). In our case the strain paths are different by 90°; in order to quantify this “reversibility” in the strain paths, Schmitt [39,40] introduced the scalar parameter ( $\alpha$ ):

$$\alpha = \frac{\boldsymbol{\epsilon}^P : \boldsymbol{\epsilon}}{(\boldsymbol{\epsilon}^P : \boldsymbol{\epsilon}^P)^{1/2}(\boldsymbol{\epsilon} : \boldsymbol{\epsilon})^{1/2}} \quad \text{eq. 1}$$

Where  $\varepsilon^p$  is the tensor corresponding to the plastic pre-strain and  $\varepsilon$  the tensor representing the plastic part of the subsequent deformation. The  $\alpha$  parameter quantifies *the magnitude of a change of strain path* upon reloading with;

$\alpha = -1$  indicating that subsequent straining is in the opposite sense to pre-straining (conventional BE);

$\alpha = +1$  indicating that subsequent straining is in the same sense as pre-straining;

$\alpha = 0$  indicating that subsequent straining is at  $54.7^\circ$  to uniaxial pre-straining.

Substituting the plasticity tensors for our strain paths into equation 3, the  $\alpha$  values for  $C_2C_1$ ,  $C_2T_3$  and  $T_2C_1$  are -0.5, 0.5 and 0.5 respectively. Of these, the  $C_2C_1$  strain path is closest to “complete reversibility” ( $\alpha = -1$ ).

#### 4.1.2.2 Neutron diffraction measurements

Neutron diffraction is a versatile probe of the elastic strain state: it is sufficiently penetrating to provide a volume average, yet selectively measures only those grains which have a common crystallographic direction normal to the diffracting planes. Our measurements were carried out at the ENGIN-X time-of-flight diffractometer at the ISIS spallation neutron source. Two detector banks were employed, each situated opposite the other so as to make a  $90^\circ$  angle with the incoming neutron beam ( $2\theta$ ) in the horizontal plane. In this way, the strain within the gauge volume ( $4 \times 4 \times 4 \text{ mm}^3$ ) can be measured in the direction of applied load and at  $90^\circ$  to it (i.e. also measuring in the direction of Poisson straining). Each diffraction peak in the time-of-flight spectrum represents a different family of grain orientations  $\{hkl\}$ . The loading test was undertaken in situ, providing neutron strain measurements for each level of sample deformation. The strain was held constant while each neutron measurement was made in order to minimize creep relaxation effects; even though some additional plastic straining occurred over the  $\sim 10$  minutes required to acquire each measurement point.

The interplanar spacing for an  $(hkl)$  peak,  $d_{hkl}$ , can be calculated as a function of the measured time of flight and Bragg angle  $2\theta$  of the detector [41]. The average strain for grains  $\{hkl\}$  oriented for diffraction may then be found as

$$\varepsilon_{hkl} = \frac{d_{hkl} - d_{0hkl}}{d_{0hkl}} \quad \text{eq. 2}$$

where  $d_{0hkl}$  is the lattice spacing for the same  $hkl$  peak in the unstressed state. Ideally,  $d_{0hkl}$  would be measured from an unloaded sample on the same instrument at a similar time, so that any change in the measured lattice spacing could be directly attributed to strain and not any instrumental or sample artefacts. However, the samples measured here had all been pre-strained off-line. A single value of  $a_0$  was determined for an unstrained sample using a Rietveld refinement of the entire diffraction spectrum. Individual  $d_{0hkl}$  were determined from  $a_0$  using:

$$d_{0hkl} = \frac{a_0}{\sqrt{h^2 + k^2 + l^2}} \quad \text{eq. 3}$$

Finally, some instrumental and electronic artefacts had to be accounted for in order to achieve the required strain accuracy. An ideal instrument should show a linear, unvarying relation between the time-of-flight value for each  $hkl$  peak and the corresponding d-spacing value. However, a small quadratic term had to be included in the calibration, and a different relation was derived for each sample to allow for long-term drift of instrument parameters. The quadratic part of the calibration was derived by exploiting the fact that different order crystallographic reflections from the same plane (e.g. 111 and 222 peaks) must have identical strains for any intergranular stress state. The  $d_{hkl}$  values found in this way were used to find strains with equation (1) where it was verified that higher order  $hkl$  peaks each showed the same behaviour as the corresponding lower order peak.

### 4.1.3 Crystal plasticity model

A UMAT subroutine has been implemented in ABAQUS to describe the slip-restricted elasto visco-plastic material behaviour of each crystal inside a polycrystalline aggregate of material [42]. Random orientations have been assigned to each individual grain following the procedure described in [43]. Here we model a *representative volume element* (RVE) comprising 199 grains.

#### 4.1.3.1 Modelled geometry and meshing

A given displacement was applied as a boundary condition to one face of the RVE. The other opposite face was fixed by a boundary condition restricting displacement only in the direction of the applied displacement. Each grain was linked to its neighbours through a surface constraint i.e. nodes belonging to the boundary surface of one grain evolve with interpolated displacements and rotations from the boundary surface of the second grain. The experimental and modelled strain rates were assumed to be approximately  $2 \times 10^{-6} \text{ s}^{-1}$  for loading steps and  $2 \times 10^{-5} \text{ s}^{-1}$  for unloading. These strain rates fall within the set of strain rates previously measured and simulated by CPFEM where good agreement was found [24].

3D Voronoi tessellation [45] was used to produce a random virtual microstructure that mimics the presence of real microstructure features, including a range of grain sizes, grain shapes, and crystallographic orientations. We investigated meshing the RVE using both C3D4<sup>11</sup> linear interpolation elements (Figure 3) and C3D10M<sup>1</sup> quadratic interpolation elements. In an effort to achieve similar computational cost, the quadratic element mesh (16,783 elements) was substantially coarser than the linear element mesh (228,946 elements). This resulted in some (quadratic) elements being too distorted when meshing a region containing relatively small edges. To overcome this, we firstly merged some small edges together (always preserving the GB) and refined the mesh near GBs with 3 edges. Since both meshes gave almost identical results, only the linearly interpolated elements are reported here.

---

<sup>11</sup> Details regarding the formulation can be found in [46].

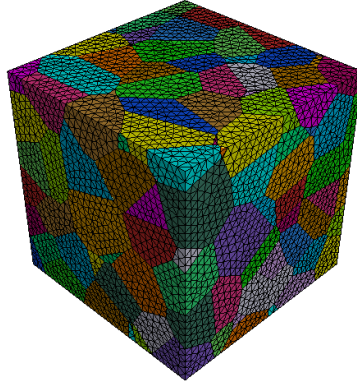


**Figure 3. Mesh used to simulate microstructure of 199 randomly oriented grains using linear interpolation elements.**

#### 4.1.3.2 Constitutive laws

The single crystal parameters required for the crystal plasticity constitutive laws used in the model cannot be obtained directly from an experiment on a polycrystal. Instead, it is common practice to calibrate the model using the macroscopic stress-strain curve (Figure 4c). The parameters obtained this way are given in Table 2.

**Table 2. Constants used in the present work. The elastic constants ( $C_{11}$ ,  $C_{12}$  and  $C_{44}$ ) and other parameters used in the model [44].**

$C_{11}$	$C_{12}$	$C_{44}$	$n$	$\dot{\alpha}$	$h_0$	$\tau_s$	$\tau_0$
(GPa)	(GPa)	(GPa)			(MPa)	(MPa)	(MPa)
204.6	137.7	126.2	55	0.001	675	175	90

The slip rate of each individual crystallographic slip system is a function of the current strength of the slip system, which increases as deformation proceeds. We assume that flow on one slip system causes hardening on all slip systems to the same extent. Hardening on each slip system is directionally independent hence the model assumes isotropic hardening at the crystal level and is strain rate sensitive. The present model was first proposed by Hill and Rice [47] in its rate-independent form and updated by D.

Peirce and co-authors [48] for elasto-visco plastic deformation by slip. The parameters used to match the tensile stress strain curves between the modelled aggregate and the solution annealed 316L steel samples are given in Table 2. Further detail regarding the constitutive laws and examples of the implementation can be found elsewhere [49,50].

#### **4.1.3.3 Extracting the response of {hkl} grain families**

Six simulations using different random grain orientation sets were studied and found to show negligible differences in the uniaxial macro stress-strain curve. This suggests that, from a macroscopic point of view, the RVE contained sufficient grains. Since diffraction is grain orientation selective only correctly oriented grains contribute to each diffraction peak. A post-processing tool was incorporated to calculate elastic strains averaged only over those grains oriented so as to contribute to a given {hkl} diffraction peak. All grains oriented within 8 degrees of the exact diffraction condition were included: this is comparable to the angular discrimination of the detector used for the neutron diffraction experiment.

### ***4.1.4 Results and discussions***

#### **4.1.4.1 Macroscopic stress-strain curves**

The macroscopic stress-strain curves predicted by CPFEM for the three strain paths are shown in Figure 4 alongside the experimentally measured ones. The differences in the initial elastic slopes during pre-straining in compression can probably be attributed to displacement resulting from initial sample re-alignment and expulsion of lubricant between the sample and the hydraulic press. The associated yield stresses (at 0.2% permanent strain), which are not sensitive to these effects, are presented in Table 3.

**Table 3. Yield stresses (at 0.2% permanent strain) extracted from the predicted and measured stress-strain curves for the three different strain paths. Note the model was calibrated on the basis of the tensile yield curve T<sub>2</sub>**

Strain path	$\alpha$	Pre-strain (%)	Initial Forward Yield ( $\pm 10$ MPa)		Reloaded Yield ( $\pm 10$ MPa)	
			Model	Experiment	Model	Experiment
C <sub>2</sub> C <sub>1</sub>	-0.5	1.3	-210	-200	-270	-200
C <sub>2</sub> T <sub>3</sub>	0.5	1.5	210	225	270	240
T <sub>2</sub> C <sub>1</sub>	0.5	1.6	-210	-210	-270	-240

It is clear from both the model and the experiments that on changing the strain path, yielding initiates due to transient softening before the current yield point for continued forward loading, though this effect is more pronounced for the experimental curves. The fact that the 0.2% yield point on reloading is lowest for C<sub>2</sub>C<sub>1</sub> may relate to its being a more drastic strain path change, as quantified by the  $\alpha$  parameter.

It is also clear from Figure 4 that only for C<sub>2</sub>T<sub>3</sub> is there any significant Bauschinger-style permanent lowering of the yield stress ( $\sim 30$ MPa). These observations are consistent with those of [51] who found only a very small permanent BE after 1.5% pre-strain for 316L, but significant transient softening. The Bauschinger effect (BE) seems to be controlled by the amount of piled-up dislocations against the obstacles during the pre-strain. Low stacking fault energy (SFE) [16], the presence of particles [52], or alloying elements [53] would enhance this effect. It is also well known that the transient softening region and permanent softening increase with the amount of pre-strain. Therefore the small permanent softening is not unexpected given the low SFE and the small pre-strain applied.

$C_2T_3$  and  $T_3C_1$  are equivalent strain paths (in terms of  $\alpha$ ), but their reverse straining responses are different. A small transient hardening region can be seen for the  $C_2T_3$  strain path before significant permanent softening. However, a larger transient region can be seen for the  $T_3C_1$  strain path, with no permanent softening. It remains unclear why this happens but analysis of other samples pre-strained to a similar extent confirmed this behaviour. It is possible that, due to poor lubrication, an effective biaxial (rather than an ideal uniaxial) stress state occurs in tests where the compression is applied upon reloading ( $T_3C_1$  and  $C_2C_1$ ). This would leave an extended transient hardening region for these strain paths, as opposed to the permanent softening observed for  $C_2T_3$ . Of course, the corresponding predictions are not sensitive to this anisotropy.

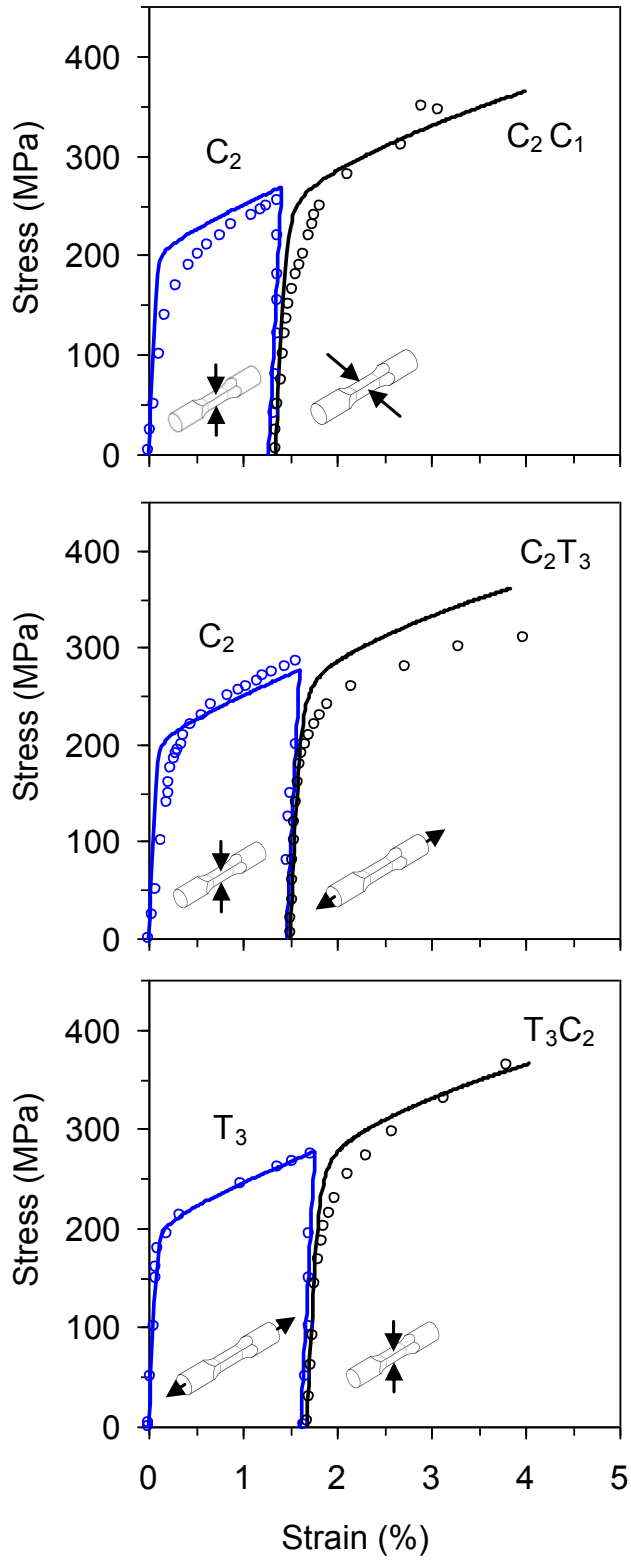
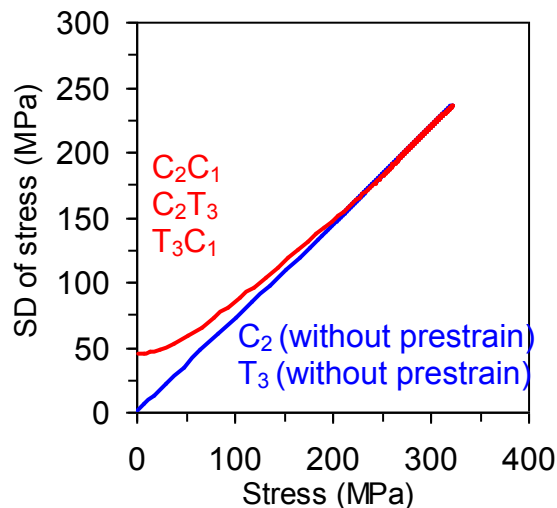


Figure 4 Measured stress strain data (points) and CPFEM simulations (continuous lines) for the three different strain paths.

#### 4.1.4.2 Intergranular mean stresses

Intergranular mean stresses arise naturally from the heterogeneous flow predicted by the CPFEM model at the grain scale some of which assist reverse flow (back-stresses) while those in other grain families hinder it. What is clear from Figure 4 is that the local grain to grain residual stresses accumulated during pre-straining do initiate microyielding on reloading at stresses well below that required for continued forward loading (see also the discussion in 4.3.2) – if not quite to the same extent as that observed by experiment. However the fact that this effect exhausts at about 0.5% strain rather than give rise to a permanent softening is because the strains developed on pre-strain are soon replaced by strains characteristic of the new strain path. It is noteworthy that the predicted spread of IGS as demonstrated in Figure 5 behaves similarly. It can be seen that soon after reloading ( $\sim 250$ MPa) the spread for the pre-strained sample matches that developed by simple uniaxial tension or compression. This is consistent with neutron diffraction results of uniaxial path changes in two phase steels [11].



**Figure 5. Predicted scatter of IGS between different grains (quantified as the standard deviation of the grain-averaged stresses) versus the applied load for the three studied strain paths. Note that the spread for the pre-strained samples (initially  $\sim 50$ MPa) approaches that of the uniaxial strain ( $C_2$  or  $T_2$ ) at a load of about 250MPa regardless of the strain path.**

### 4.1.4.3 Individual grain family responses

#### 4.1.4.3.1 Intergranular stresses upon uniaxial tensile loading

The *in-situ* measured and predicted elastic strains for different  $\{hkl\}$  families under uniaxial tension of a non pre-strained sample are shown in Figure 6. As in previous work there is good agreement between modelled and measured strains [33].

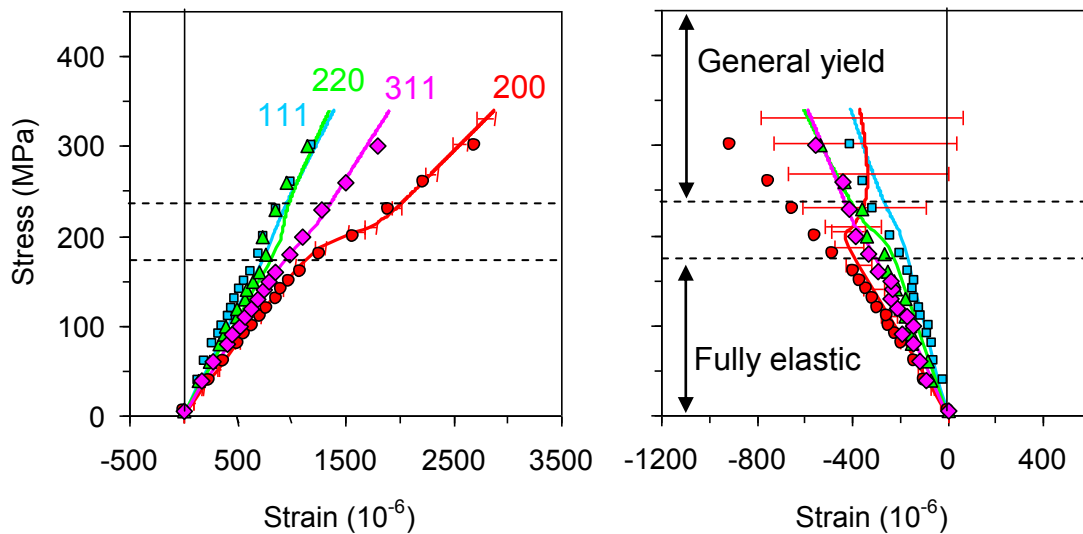


**Figure 6. Measured (data points) and predicted (continuous line) elastic strains for axial tension to 2.5% total elongation a) in the direction of loading; b) in the perpendicular to loading for four  $\{hkl\}$  grain families during tension. The predictions are the average strain of six equivalent random orientation (RPV) sets is presented in all cases. The error bars correspond to the difference between the extreme 200 predictions for over the 6 representative models.**

Below 170MPa, the sample is fully elastic; above 230MPa it is fully plastic. The region between these two represents the elastic-plastic transition with certain grain families deforming plastically while others deform elastically. The crystal elastic constants define the response under the fully elastic regime, while both the elastic crystal constants and the Schmid's factor of the crystallographic family define the fully plastic

region. Work by Wong and Dawson [54] has concluded that the single crystal elastic properties have a negligible effect in fully developed plasticity when the Young's modulus is kept constant. This negligible effect of elastic anisotropy in fully developed plasticity has also been confirmed at stresses calculated directly at grain boundaries [43].

We found that upon changing the set of random grains used to represent the polycrystal that in contrast to the insensitivity of the macroscopic response, the predicted elastic strains were quite sensitive to the grain set probably because only small numbers of the 199 grains in the RPV contribute to a given diffraction peak response. Consequently, results averaged over six different equivalent random orientation sets are presented in Figure 6-9 and the error bars in Figure 6 represent the extreme values of over 6 sets. The variation was found to vary with  $\{hkl\}$  being much larger in the transverse direction than the axial with the transverse 200 peak exhibiting the largest variation. This is in agreement with CPFEM predictions of deformation of ferrite (BCC), where the in-plane rotation angle around the transverse measurement direction for grains giving rise to axial 200 and 110 peaks was found to have a great effect [17]. In the present FCC study this was not seen for the transverse 220 peak. It is clear, however, that *local texture* of the diffracting grains has a great impact on the measured and predicted 200 peaks. This probably explains the better agreement observed for the axial as against the transverse lattice strain data, as has been observed previously [34].

#### 4.1.4.3.2 *Intergranular stresses upon strain path change*

The  $hkl$  peaks responses for reloading for the three strain path changes  $C_2C_1$ ,  $T_3C_1$  and  $C_2T_3$  are shown in Figure 7, Figure 8 and Figure 9 respectively assuming zero lattice strain prior to the *pre-strain*. It is clear from Figure 7a for  $C_2C_1$  that upon re-loading the initial gradients observed experimentally differ from those predicted for elastic loading, but are closer to those predicted once yielding has begun. This suggests that microyielding commences essentially from the onset of re-loading, possibly even having already started towards the end of unloading from the pre-straining (not shown).

Further, we can see that general yielding is predicted to occur at approximately -260MPa which is between those for the axial (-270MPa) and transverse (-250MPa) inferred from the experimental curves in Fig.7.

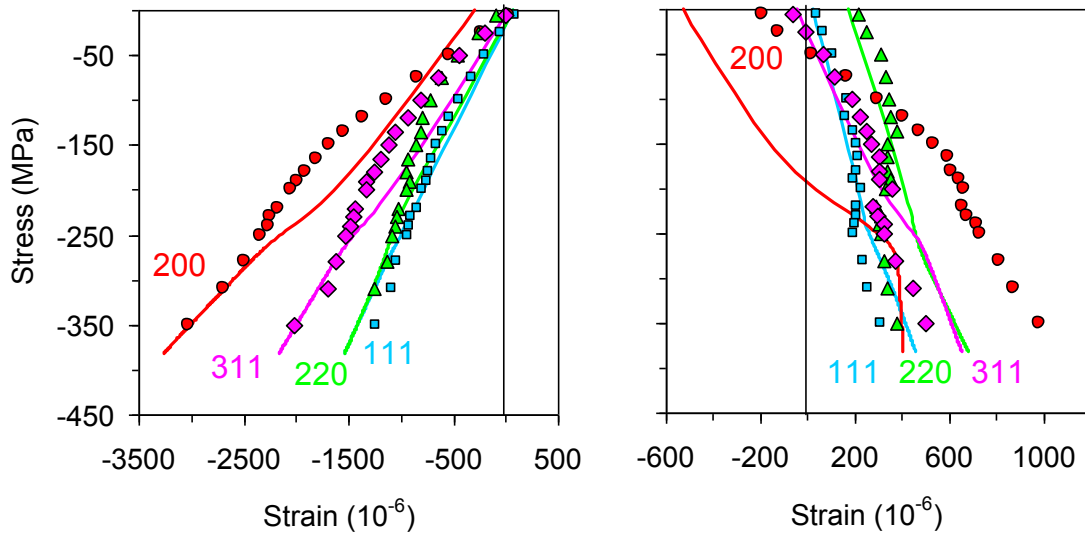


**Figure 7. Measured data points and predicted (continuous line) elastic strains: a) in the direction of loading; b) in the perpendicular to loading of four grain families during compression after compression in the perpendicular direction to the test ( $C_2C_1$ ).**

The reloading response for  $C_2T_3$  is shown in Figure 8. The measured and predicted elastic strains for most of the peaks are in good agreement for this strain path. The most noticeable difference is the offset due to incorrect prediction of the intergranular residual stresses incurred in forward loading, especially for the 200 peak measured in the transverse direction (Figure 8b). The onset of micro-yielding ( $\sim 190$ MPa) is reasonably well captured, as is the onset of general yielding at around 260MPa.

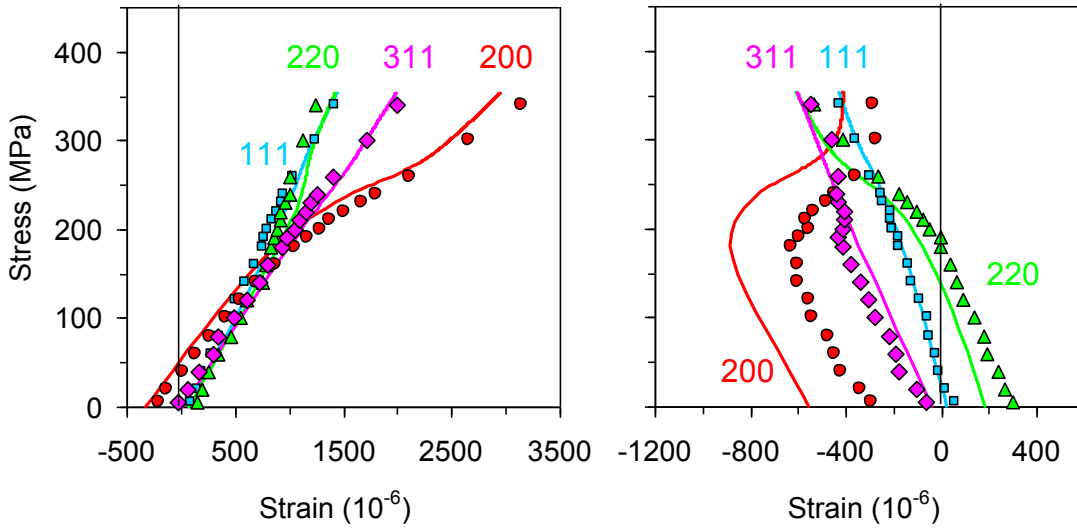


**Figure 8. Measured data points and predicted (continuous line) elastic strains: a) in the direction of loading; b) in the perpendicular to loading of four grain families during tension after compression in the perpendicular direction to the test ( $C_2T_3$ ).**

For  $T_2C_1$  (Figure 9), the lattice strain responses suggest micro-yielding at -50MPa with general yielding at around -270MPa in contrast to the model which predicts values of -170 and -290MPa respectively. This difference between predictions and simulations is again consistent with the macroscopic measurements and is similar to that observed for the  $C_2C_1$  strain path.

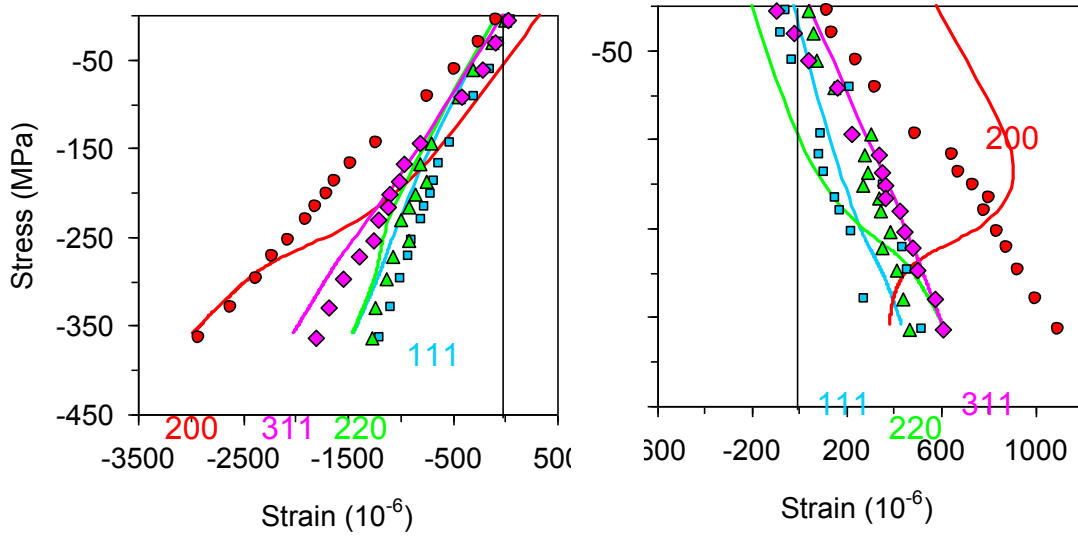


**Figure 9. Measured data points and predicted (continuous line) elastic strains: a) in the direction of loading; b) in the perpendicular to loading of four grain families during compression after tension in the perpendicular direction to the test ( $T_2C_1$ ).**

In general, the measured and predicted lattice strain curves, shown in Figures 6 to 9, reveal considerable differences. Some of these differences arise from two contributing (scattering) factors in each grain in Bragg condition: its neighbourhood and its rotation about the measurement direction. Therefore, the averaged measured and averaged predicted strains may differ from one representative volume to another. In addition, strain-induced martensite is typically reported only for higher strains (>5%) for 316 [55]; if present here, this phase would also contribute to the lattice strains and the Bauschinger effect.

**Table 4. Reloaded yield values extracted from the predicted and modelled lattice strain curves for the three different strain paths.**

Strain path	$\alpha$	Pre-strain (%)	Micro-yield ( $\pm 10$ MPa)		General Yield ( $\pm 10$ MPa)	
			Model	Experiment	Model	Experiment
$C_2C_1$	-0.5	1.3	-180	0	-260	-270
$C_2T_3$	0.5	1.5	190	150	270	260
$T_2C_1$	0.5	1.6	-170	-50	-290	-270

From the changes in slopes of the elastic strains we can conclude that in the experiment micro-yielding occurs much earlier than the model predictions in  $C_2C_1$  and  $T_3C_1$  samples. This tendency for earlier than predicted microyielding upon path change is consistent with previous work [37] where earlier than predicted micro-yielding was observed for 200 peaks under uniaxial tension-compression in 316L austenitic stainless steel. Such experiments showed a larger yielding transition (difference between microyield and general yield). This yielding transition was better captured by the incorporation of kinematic hardening at the grain level [8].

Overall, we can conclude that the macroscopic 0.2% yield stress determined from the stress-strain curve, with or without pre-strain, lies close to, but below, the point at which all grain families are under general yield. Additionally, for  $C_2C_1$  macroyield occurred earlier than for other strain paths while microyielding occurred much earlier. These effects are attributed to greater strain path change (lower  $\alpha$ ).

#### **4.1.5 Conclusions**

Three different 90° strain path changes have been studied giving rise to the following observations.

- 1) Transient softening upon changing strain path was observed both in the model and in the experiments. This arises at least in part from the different residual stresses introduced in each grain family during pre-straining.
- 2) Only in the case of  $C_2T_3$  was any significant permanent softening observed. Low levels of permanent softening are consistent with previous work on single phase stainless steels.
- 3) Modelling results show that intergranular strains are introduced in the pre-strain but these soon become over-written by intergranular strains characteristic of the reloading such that no permanent softening is predicted.
- 4) While the slopes for the different  $\{hkl\}$  families were well predicted for elastic loading, the onset of microyielding was found to occur generally earlier than

predicted by the CPFÉ model especially for the samples reloaded in compression. By contrast, the occurrence of general yielding was in much closer agreement corresponding well with the onset of macroscopic yielding in the stress-strain curves. This early activation of microyielding between the  $\{hkl\}$  families relative to that predicted has been observed previously for other strain path changes [37].

- 5) The current model does not include an inherent Bauschinger style permanent softening in the constitutive laws governing slip. It is quite possible that this would need to be invoked to explain any permanent softening encountered for larger pre-strains.
- 6) At least for compressive reloading, the onset of microyielding between the lattice plane families occurs almost immediately in contrast to the model. This probably explains why the corresponding macrostress curves appear to show greater transient softening effects than for  $C_2T_3$ . Because of its more severe strain path change (lower  $\alpha$ ), these effects are more noticeable for  $C_2C_1$  than  $T_3C_1$ .
- 7) Studying the grain behaviours by diffraction during strain path changes would appear to be a more rigorous test of crystal plasticity models compared to monolithic straining.

#### ***4.1.6 Acknowledgements***

The authors would like to thank the ISIS Pulsed Neutron & Muon Source for providing beam on the ENGIN-X instrument (experiments RB910522 and RB920469), and Shu Yan Zhang for experimental support. Dr. Igor Simonovski (Institute for energy, The Netherlands) and Dr. Zoran Petric (Jozef Stefan Institute, Slovenia) are also gratefully acknowledged for providing the 3D Voronoi geometry. Finally, we thank Professor Peter Bate for his useful advice.

#### **4.1.7 References associated to Publication 1**

- [1] C. García, F. Martín, P.D. Tiedra, J.A. Heredero, M.L. Aparicio, *Corros. Sci.* 43 (2001) 1519-1539.
- [2] N. Hagiwara, T. Masuda, N. Oguchi, *J. Pressure Vessel Technol.* 123 (2001) 355-361.
- [3] T. Couvant, L. Legras, F. Vaillant, J.M. Boursier, Y. Rouillon, in: *Eurocorr 2004*, Nice, France, 2004.
- [4] T. Couvant, L. Legras, A. Herbelin, A. Musienko, Q. Vertenelle, G. Ilevbare, D. Delafosse, G. Cailletaud, J. Hickling, in: *14th International Conference on Environmental Degradation of Materials in Nuclear Power System*, Virginia Beach, Virginia, USA, 2009.
- [5] W.C. Moshier, C.M. Brown, *Corrosion* 56 (2000) 307-320.
- [6] D. Tice, J. Stairmand, N. Platts, in: *Serco Presentation*, Toronto, 2007.
- [7] J. Bauschinger, *Civiling N.F.* 27 (1881) 289–348.
- [8] T. Lorentzen, M.R. Daymond, B. Clausen, C.N. Tomé, *Acta Mater.* 50 (2002) 1627-1638.
- [9] B. Clausen, T. Lorentzen, T. Leffers, *Acta Mater.* 46 (1998) 3087-3098.
- [10] O.B. Pedersen, *Acta Metall.* 31 (1983) 1795-1808.
- [11] P.B. Prangnell, T. Downes, P.J. Withers, T. Lorentzen, *Mater. Sci. Eng., A* 197 (1995) 215-221.
- [12] L.M. Brown, D.R. Clarke, *Acta Metall.* 23 (1975) 821-830.
- [13] O.B. Pedersen, L.M. Brown, W.M. Stobbs, *Acta Metall.* 29 (1981) 1843-1850.
- [14] E. Orowan, *Causes and Effects of Internal Stresses*, Elsevier Publishing Company, New York, 1959.
- [15] A. Abel, H. Muir, *Philosophical Magazine* 26 (1972) 489.
- [16] I. Gokyu, T. Kishi, H. Wada, *Japan Inst. Metals* 34 (1970) 154-160.
- [17] E.C. Oliver, M.R. Daymond, P.J. Withers, *Acta Mater.* 52 (2004) 1937-1951.
- [18] D. Hull, D.J. Bacon, *Introduction to Dislocations*, Butterworth-Heinemann, 2001.
- [19] R.W.K. Honeycombe, *The Plastic Deformation of Metals*, 1984.
- [20] K. Spencer, K.T. Conlon, Y. Bréchet, J.D. Embury, *Mats. Sci. Tech.* 25 (2009) 18-28.

- [21] H. Mughrabi, T. Ungár, W. Kienle, M. Wilkens, *Philosophical Magazine A* 53 (1986) 793.
- [22] S. Quilici, G. Cailletaud, *Comput. Mater. Sci.* 16 (1999) 383-390.
- [23] P. Bate, 357 (1999) 1589-1601.
- [24] O. Diard, S. Leclereq, G. Rousselier, G. Cailletaud, *Int. J. of Plas.* 21 (2005) 691-722.
- [25] Z. Tan, C. Magnusson, B. Persson, *Mater. Sci. Eng., A-structural Materials Properties Microstructure and Processing* 183 (1994) 31-38.
- [26] L.M. Geng, R.H. Wagoner, *International Journal of Mechanical Sciences* 44 (2002) 123-148.
- [27] B. Xu, Y. Jiang, *Int. J. of Plas.* 20 (2004) 2161-2178.
- [28] M.P. Miller, D.L. McDowell, *Int. J. of Plas.* 12 (1996) 875-902.
- [29] I.J. Beyerlein, C.N. Tomé, *Int. J. of Plas.* 23 (2007) 640-664.
- [30] E.M. Viatkina, W.A.M. Brekelmans, M.G.D. Geers, *Int. J. of Sol. and Str.* 44 (2007) 6030-6054.
- [31] D.V. Wilson, *Acta Metall.* 13 (1965) 807-814.
- [32] D.V. Wilson, P.S. Bate, *Acta Metall.* 34 (1986) 1107-1120.
- [33] B. Clausen, T. Lorentzen, M.A.M. Bourke, M.R. Daymond, *Mater. Sci. Eng., A* 259 (1999) 17-24.
- [34] J. Quinta da Fonseca, E.C. Oliver, P.S. Bate, P.J. Withers, *Mater. Sci. Eng., A* 437 (2006) 26-32.
- [35] M.R. Daymond, *Materials Science Forum* 495-497 (2005) 1019-1024.
- [36] P.R. Dawson, D.E. Boyce, R.B. Rogge, *Materials Science and Engineering: A* 399 (2005) 13-25.
- [37] A. Korsunsky, K. Jarnes, M. Daymond, *Engineering Fracture Mechanics* 71 (2004) 805-812.
- [38] A. Ma, F. Roters, D. Raabe, *Comput. Mater. Sci.* 39 (2007) 91-95.
- [39] J.H. Schmitt, E. Aernoudt, B. Baudelet, *Materials Science and Engineering* 75 (1985) 13-20.
- [40] J.H. Schmitt, E.L. Shen, J.L. Raphanel, *Int. J. of Plas.* 10 (1994) 535-551.

- [41] A. Lodini, M. Fitzpatrick, eds., *Analysis of Residual Stress by Diffraction Using Neutron and Synchrotron Radiation*, CRC Press, 2003.
- [42] Y. Huang, *A User-material Subroutine Incorporating Single Crystal Plasticity in the ABAQUS Finite Element Program*, Mech Report178, Division of Engineering and Applied Sciences, Harvard University, Cambridge, Massachusetts, 1991.
- [43] D. Gonzalez, I. Simonovski, P.J. Withers, J. Quinta da Fonseca, *Unpublished Results* (n.d.).
- [44] H. Ledbetter, *Physica Status Solidi A-Applied Research* 85 (1984) 89-96.
- [45] Z. Petric, *Generating 3D Voronoi Tessellations for Material Modeling*, Jozef Stefan Institute. Tech. report, 2010.
- [46] ABAQUS, Inc., *ABAQUS Documentation*, Providence, Rhode Island, 2006.
- [47] R. Hill, J.R. Rice, *J. of the Mech. and Phy. of Solids* 20 (1972) 401-413.
- [48] D. Peirce, R.J. Asaro, A. Needleman, *Acta Metall.* 31 (1983) 1951-1976.
- [49] H. Pi, J. Han, C. Zhang, A.K. Tieu, Z. Jiang, *Journal of University of Science and Technology Beijing, Mineral, Metallurgy, Material* 15 (2008) 43-47.
- [50] I. Simonovski, L. Cizelj, *Comput. Mater. Sci.* 50 (2011) 1606-1618.
- [51] M. Choteau, P. Quaegebeur, S. Degallaix, *Comptes Rendus De l'Académie Des Sciences - Series IIB - Mechanics* 328 (2000) 451-456.
- [52] J.D. Atkinson, L.M. Brown, W.M. Stobbs, *Phil. Mag.* 30 (1974) 1247-1280.
- [53] A. Abel, H. Muir, *Phil. Mag.* 27 (1973) 585-594.
- [54] S.L. Wong, P.R. Dawson, *Acta Mater.* 58 (2010) 1658-1678.
- [55] S.K. Varma, J. Kalyanam, L.E. Murr, V. Srinivas, *Journal of Materials Science Letters*. 13 (1994) 107-111.

**END OF PUBLICATION 1**

## 4.2 Publication 2

### **Modelling the effect of elastic and plastic anisotropies on stresses at grain boundaries**

D. Gonzalez, I. Simonovski, P.J. Withers, J. Quinta da Fonseca

Publication submitted to Int. J. of Plasticity on the 30/05/2012

In this publication the idea of investigating the effect of elastic and plastic anisotropies were proposed and supervised by Joao Fonseca. The 3D Voronoi geometry and mesh (including the inserted cohesive elements) were created by I. Simonovski (Simonovski and Cizelj, 2011a) whereas the rest of the pre-processing (material properties calibration, random orientation assignment, boundary conditions...etc) and all the post-processing was done by myself.

**BEGIN OF PUBLICATION 2**

## **Modelling the effect of elastic and plastic anisotropies on stresses at grain boundaries**

D. Gonzalez<sup>1\*</sup>, I. Simonovski<sup>2</sup>, P.J. Withers<sup>1</sup> and J. Quinta da Fonseca<sup>1</sup>

<sup>1</sup> School of Materials, Univ. of Manchester, Grosvenor St., Manchester, M1 7HS, UK.

<sup>2</sup> Institute for Energy, P.O. Box 2, Petten, NL-1755 ZG, The Netherlands

\*Corresponding author:

david.gonzalez@postgrad.manchester.ac.uk

Mobile number: 00447961684966

Postal address: School of Materials, University of Manchester,  
Manchester, M13 9PL,

United Kingdom

### **Abstract**

It is believed that intergranular stresses play a significant role in failure processes, such as stress corrosion cracking (SCC) and fatigue cracking. In deformed cubic metals, intergranular stresses arise solely from the plastic and elastic anisotropies of the individual grains. In this work, stresses normal to the grain boundaries in deformed stainless steel have been calculated using crystal plasticity finite element modelling (CPFEM). The calculations show that, at strains larger than 0.5% and under load, the stress at grain boundaries is dominated by the effect of plastic anisotropy rather than elastic anisotropy. Upon unloading, plastic misfit still fully dominates the heterogeneity of normal stresses and its insensitive to the angle between the boundary normal and the preloaded direction. The effects of mesh density and size of boundaries on normal stresses are also studied. Special attention has been focused on examining what conditions give rise to large grain boundary stresses. Our results suggest that the magnitudes of the residual grain boundary stress predicted is not highly correlated to

the amount of plastic strain in the vicinity of the boundary and whether it is higher or lower than the average plastic strain. In other words, a soft-hard grain combination does not imply high tensile (nor compressive) residual stress normal to its boundary. The results are similar if instead of comparing the plastic strain near neighbours, we compare the plastic strain in the grain to the average plastic strain.

**Keywords:**

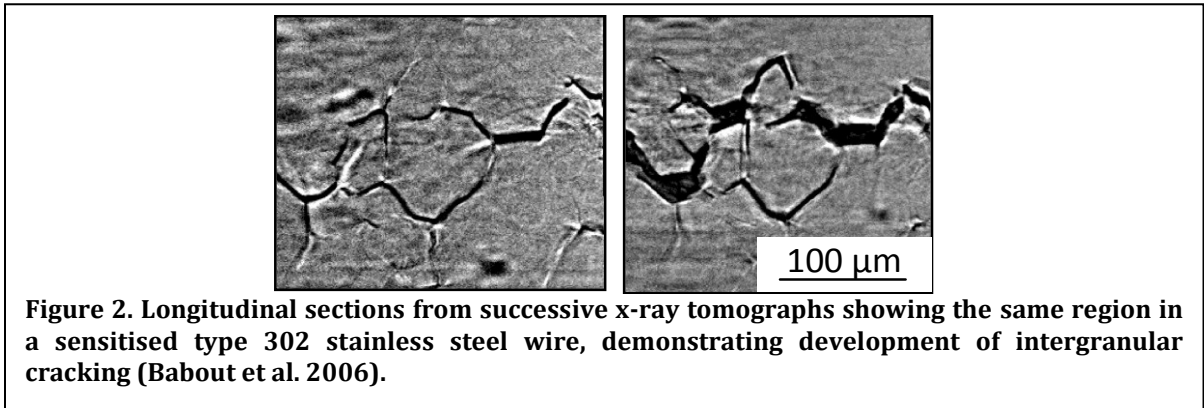
- A. grain boundaries
- B. anisotropic material
- B. polycrystalline material
- C. finite elements
- C. boundary elements

***4.2.1 Introduction***

Intergranular stresses are believed to be important for a range of grain boundary (GB) related failure mechanisms. For example, the brittle intergranular fracture of alumina can be related to the normal grain boundary stresses generated by the anisotropy in elastic constants (Marrow et al., 2011). Failure by stress corrosion cracking (SCC) in stainless steel often occurs intergranularly as illustrated in Figure 1 by Babout et al. (2006). The reasons for this are complex, but, the magnitude of stress normal to the grain boundary is likely to be one of the contributing factors for intergranular cracking (Palumbo et al., 1991). Similarly, grain boundaries have been demonstrated to have an impact on the initiation of fatigue cracks in polycrystals (Sangid et al., 2011). In such cases, measuring the stresses at grain boundaries in the bulk is very difficult experimentally, if not altogether impossible, although some hope has recently raised with high resolution EBSD techniques (Gardner et al., 2010). Consequently, there is considerable interest in modelling deformation at the grain scale and using these models to give estimates of local stresses at the microstructural level. At this scale, isotropic material models no longer apply and the inherent plastic and elastic

anisotropy of crystals must be taken into account. One way of achieving this is to use the Finite Element Method (FEM) with appropriate single crystal plasticity laws. Such models can be used to successfully predict the evolution of the lattice strains during uniaxial tensile loading in stainless steels (Clausen et al., 1999) and to study the impact of single crystal elastic anisotropy on the lattice strains during the elastic-plastic transition (Clausen et al., 1998). Further, crystal plasticity models have been used to predict the dislocation density across the boundary of a deformed aluminium bi-crystal (Liang and Dunne, 2009) as determined experimentally (Sun et al., 2000). The strengthening effect of grain boundaries has also been modelled using size-dependent constitutive laws (Lim et al., 2011). However, only in a few cases has crystal plasticity FEM been used to predict stresses right at the boundary (Diard et al., 2002; Diard et al., 2005), perhaps due to the difficulty in measuring them.

In this article, we present the results of a systematic study on the development of normal stresses at grain boundaries during, and subsequent to, uniaxial deformation. The unloaded state is of particular interest due to the enhancing effect that prior deformation has on SCC and fatigue susceptibility (Mochizuki, 2007). Our study has two main aims: to determine the relative importance of elastic and plastic anisotropy on the development of grain boundary stresses and to determine whether the magnitude of the stresses can be correlated with the amount of plastic deformation in the grains that neighbour the boundary. In this line, intergranular damage has been correlated to the deformation incompatibility (Bieler et al., 2009) and the amount of plastic strain in neighbouring grains (Couvant et al., 2009). Here the emphasis is on the stresses acting normal to the grain boundaries, as these are probably the most relevant in the context of IGSCC.



In annealed metals, stresses at grain boundaries are likely to be relatively small, especially in those with a cubic crystal structure and which therefore have no thermal expansion anisotropy. When deformed, however, the magnitude of these stresses increases due to the mechanical anisotropy of individual grains. During uniaxial deformation, the magnitude of the stresses normal to the boundary depends on three major factors: boundary orientation with respect to the loading direction, elastic mismatches caused by the anisotropy single crystal elastic constants (Fallahi and Ataei, 2010) and plastic strain misfit caused by single crystal plastic anisotropy.

- 1) *Boundary orientation with respect to the loading direction.* The resolved stress at the grain boundary depends strongly on the angle of the grain boundary plane with the loading direction.
- 2) *Elastic mismatches caused by single crystal elastic anisotropy.* Most metals exhibit elastic anisotropy at the single crystal level. During deformation of a polycrystalline aggregate, this anisotropy causes the strain and stress within each grain to differ from their macroscopic average (Sauzay, 2007). As a consequence, deformation incompatibilities develop between neighbouring grains with different crystallographic orientations, giving rise to stresses at the grain boundaries. If deformation is purely elastic, these stresses disappear on unloading.
- 3) *Misfit caused by plastic anisotropy.* If plastic deformation occurs by crystallographic slip, then the stress at which individual grains deform plastically will depend on the

crystallographic orientation of the grains. Grain orientation will determine how many slip systems are activated and how easily they are activated in response to a given constraint. Some grains are therefore “harder” than average and others “softer” in certain directions. As in the elastic strain case, this plastic anisotropy leads to incompatibilities between neighbouring grains, with associated grain boundary stresses.

Whilst the metal is being plastically deformed and therefore is under applied stress, elastic and plastic anisotropy modulate the grain boundary orientation effect. After unloading, however, the grain boundary residual stresses are determined by the mechanical anisotropy of the material alone. The development of grain boundary stress was predicted in (HCP) zirconium following uniaxial deformation using CPFEM (Diard et al., 2005), accounting for both elastic and plastic anisotropy. Unsurprisingly, they found that the distribution of normal grain boundary stresses becomes increasingly wider as macroscopic deformation progresses. However, the study could not find any correlation between the magnitude of the grain boundary stress and the characteristics of the grains defining the boundary.

Here we follow a similar methodology to distinguish the effects of elastic and plastic anisotropy on the magnitude of the stress calculated at grain boundaries in (FCC) stainless steel. Because of its assumed importance on intergranular cracking, only normal stresses are considered. Four cases are studied: elastic isotropy with plastic isotropy (model EI-PI), elastic anisotropy with plastic isotropy (model EA-PI), elastic isotropy with plastic anisotropy (model EI-PA) and elastic anisotropy with plastic anisotropy (model EA-PA) or fully anisotropic. We are interested in both the stress development during loading and on the residual stresses after load removal (unloaded state). The loaded case will provide us with information on how the anisotropy affects the stresses on grain boundaries during service. The study of the unloaded case will be relevant to intergranular stresses introduced by the previously introduced deformation or cold work which has a significant impact in development of damage and on stress corrosion crack susceptibility (García et al., 2001; Singh et al., 2003). Finally, we have

paid special attention to the high stresses developed at small grain boundaries, how these change with the mesh refinement and the effect of their exclusion.

### 4.2.2 Model description

In crystal plasticity finite element modelling (CPFEM), a finite element mesh is used to represent the grain structure. Grains are therefore represented by one or more elements. In single-phase polycrystals, the material properties are the same for all grains and grains are defined simply by their orientation. CPFEM models have been used to study stresses in aggregates by several authors (Barbe et al., 2001a; Barbe et al., 2001b; Bate, 1999; Kalidindi et al., 1992; Sarma and Dawson, 1996). They have been validated at the -macro and -meso scales by strain-stress curves (Diard et al., 2005; Quilici and Cailletaud, 1999) and diffraction techniques (Lorentzen et al., 2002; Quinta da Fonseca et al., 2006; Song et al., 2008). The model used here was first introduced by Hill & Rice (1972) in its rate-independent form and updated (Peirce et al., 1983) into the current elasto-viscoplastic formulation.

#### 4.2.2.1 Crystal plasticity constitutive laws

In our case we have used a UMAT subroutine (Huang, 1991) that has been implemented in ABAQUS to describe the slip-restricted elasto-viscoplastic material behaviour of each crystal. It is described only in essence here; more details and examples of implementation can be found in (Pi et al., 2008; Qian et al., 2010; Simonovski et al., 2007). The plastic part of the velocity gradient is assumed to be the summation of the slip rates of each active slip system,  $(\alpha)$ , considering the Schmid tensor in the evaluated Gauss point. The slip rate  $\dot{\gamma}^{(\alpha)}$  is defined as:

$$\dot{\gamma}^{(\alpha)} = \dot{a}^{(\alpha)} \left( \frac{\tau^{(\alpha)}}{g^{(\alpha)}} \right) \left| \frac{\tau^{(\alpha)}}{g^{(\alpha)}} \right|^{n-1} \quad (1)$$

In equation (1)  $\tau^{(\alpha)}$  represents the resolved shear stress acting on the considered slip system,  $g^{(\alpha)}$  the current strength,  $\dot{a}^{(\alpha)}$  the reference strain rate and  $n$  the strain rate

sensitivity. In the limit, as  $n$  approaches infinity, this power law approaches that of a rate independent material.

For coplanar systems, the ratio of latent hardening to self-hardening is close to unity, whereas for non-coplanar systems the range 1.0-1.4 seems to encompass much of the experimental data (Kocks, 1970). We assume that flow on one slip system causes hardening on all slip systems to the same extent (isotropic hardening), meaning that all terms of the hardening matrix ( $h_{\alpha\beta}$ ) are equal. Therefore, the current strength,  $g^{(\alpha)}$ , of a slip system, ( $\alpha$ ), is directly related to the slip rate of each active slip system and a parameter called slip hardening moduli ( $h_{\alpha\alpha}$ ) described by Peirce et al. (1982) as follows:

$$h_{\alpha\alpha} = h_0 \sec h^2 \left( \frac{h_0 \gamma}{\tau_s - \tau_0} \right), \sec h = 1 / \cosh \quad (2)$$

Where  $h_0$  is the initial hardening modulus,  $\tau_s$  is a hardening sensitivity parameter,  $\tau_0$  represents the initial critical resolved shear stress. Cumulative slip is represented by  $\gamma$  and it is defined as:

$$\gamma = \sum_{\alpha} \int_0^t |\dot{\gamma}^{(\alpha)}| dt \quad (3)$$

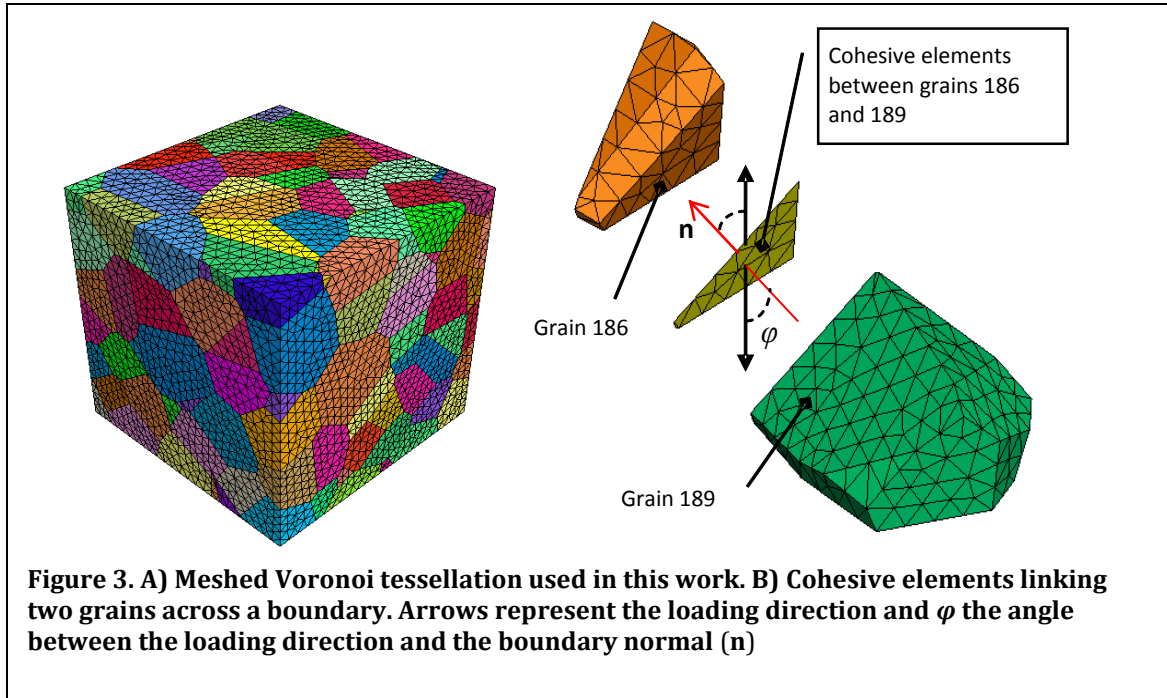
Although explicit implementation has been reported to perform better for large models (Harewood and McHugh, 2007), implicit implementation has been used for simplicity in the calibration of the model since stability checks are not needed, allowing a much larger time increment. Checks are done by definition in each increment.

#### 4.2.2.2 Meshing the grains

Real microstructures are complex, comprising a range of grain sizes, grain shapes, crystallographic orientations, and orientations of the grain boundary plane relative to the loading direction. 3D Voronoi tessellation has been extensively used over the last

decade (Barbe et al., 2001a; Barbe et al., 2001b; Diard et al., 2005; Quilici and Cailletaud, 1999) since it produces a random virtual microstructure that captures some of these features. A virtual Voronoi microstructure needs to be meshed with individual elements for calculation with crystal plasticity finite element method (CPFEM). Since features such as small grains and small edges are present in real microstructures, the aggregate was generated without a repulsion distance function. This function ensures that the distance between any two random Voronoi seeds is above a limit resulting in a more homogeneous grain volume distribution. However, by not using a repulsion distance function we can probe the effects of differences in grain boundary size. The special behaviour exhibited by small boundaries is discussed later. Quey and colleagues (2011) have recently used an algorithm called “regularization” (implemented in a free (open-source) software package) to remove these small entities (edges and faces) that can lead to numerical issues. This work revealed a small effect of regularization on the grain size distribution.

The 3D Voronoi tessellation, shown in Figure 2, was used to generate an aggregate composed of 199 grains and 1016 grain boundaries (Petric, 2010). This ensures a broad range of random grain boundary orientations with respect to the loading direction suitable for statistical analysis in the present study.



We found that linear elements allow longer time increments than quadratic ones. Therefore simulations to relatively large deformations (10%) were possible at a reasonable computational cost. Linear interpolation elements are, in general, less accurate than quadratic, meaning that more linear elements are needed compared to quadratic elements. A good balance between computational cost and mechanical response was found with tetragonal linear elements C3D4<sup>12</sup>. This was determined by finding the point at which the stress-strain response became independent of mesh density. Although C3D4 elements can suffer from shear locking, becoming overly stiff under bending moments (ABAQUS, 2006), and more accurate results may be obtained by using quadratic C3D10M, these could not be used in this work since the number of nodes (i.e. 6) at their triangular faces differs from the number of nodes (i.e. 3) at the triangular faces of the cohesive elements used here (COH3D6). Nevertheless, the solid C3D4 elements gave similar results to the solid C3D10M elements. Further, the possible high in-plane shear strains introduced by possible shear locking at the linear cohesive elements are unlikely to affect the out-plane stresses (studied in this work). Therefore,

<sup>12</sup> The element names used in the present work refer to Abaqus elements. Details in the formulation can be found elsewhere (ABAQUS, I., 2006. ABAQUS Documentation, Providence, Rhode Island.).

we are confident that the main conclusions of this work are not affected by the use of linear elements. The resulting mesh comprised 148000 C3D4 elements and 22921 cohesive elements. We assigned a random orientation to each grain whose first axis is based on the *sphere point picking* method (Weisstein, 2012). This method defines a vector from the sphere's centre to a strictly random point on the surface of the sphere. The second axis is defined by a vector perpendicular to the first axis with origin in the sphere's centre and ending in a random point between 0 and  $2\pi$ . The third axis is defined by the cross product of the other two axes.

### **4.2.2.3 Meshing and constitutive laws of the interface**

#### *4.2.2.3.1 Choice of suitable elements*

Our aim is to study the effects of elastic and plastic anisotropies on the magnitude of the predicted grain boundaries stresses. In order to quantify stresses accurately at the grain boundary, Gauss points need to be placed directly at the interface. Standard solid elements do not usually contain Gauss points at the faces of the elements. However, this can be achieved in two ways: 1) by placing Gauss points at the element faces (Diard et al., 2002; Diard et al., 2005), 2) by inserting elements between the grains that do not significantly alter the mechanical response of the aggregate (Simonovski and Cizelj, 2011). The latter approach was used here firstly because suitable elements are available in ABAQUS (ABAQUS, 2006) and secondly, because they allow for the incorporation of cracking which may be useful in the future.

3D elements are required to calculate out-of-plane stresses between 3D grains. The elements need to be sufficiently thin so that their integration points are essentially positioned at the boundary. In theory, the resolution of the computation of the inserted element increases as their grain boundary normal dimension approaches zero. In practise, this causes computational errors (e.g. overly distorted elements) when using classic 3D elements such as C3D20R. Cohesive elements (COH3D6) allow virtual thickness assignment, avoiding computational singularities.

#### 4.2.2.3.2 *Implementation of cohesive elements*

The cohesive elements (COH3D6) comprise 6 nodes and 3 Gauss points. They were assigned the properties of bulk 316 stainless steel ( $E = 200$  GPa,  $\nu = 0.3$ ). Further detail regarding cohesive element behaviour can be found elsewhere (ABAQUS, 2006). Note that the cohesive elements, as shown in Figure 2b, are planar, matching in-plane nodes of the element with nodes of adjacent C3D4 elements. The nominal thickness was chosen to be relatively very small, namely  $10^{-5}$  the size of the Voronoi cube (Figure 2), in an effort to ensure that the mechanical response of the aggregate was not affected by the boundaries. This is several orders of magnitude smaller than the average grain size of the aggregate in Figure 2.

#### 4.2.2.4 **Boundary conditions**

The aggregate shown in Figure 2 comprises a few hundred grains, which is sufficient to ensure that the macroscopic response does not depend too heavily on the details of the grain structure. According to this assumption, homogeneous stress or strain fields can be imposed as boundary conditions in the normal direction to the external boundaries of the aggregate. We constrained axial displacements to be zero over the bottom face and imposed the desired constant axial displacement across the nodes on the top face. This allowed bulk Poisson contraction of the side-faces. Such boundary conditions would introduce unrealistic stresses in the grains proximate to the constrained surfaces because of their anisotropy. In practise, full coupling may be addressed by embedding the RVE in a (finite) matrix of isotropic material with the average properties. This would better accommodate stress and strain fields around “hard” or “soft” grains positioned on the constrained surface. However, this would involve a considerable increase of computational cost due to the extra number of matrix-elements required to match the mesh of the RVE. A compromise was found by averaging the predicted boundary stresses over several simulations using each a different (equivalent) random set of crystal orientations.

#### 4.2.2.5 Fitting to the macroscopic response

The elastic anisotropy of single crystals is well documented (Nye, 1985). 316 stainless steel is face centred cubic and as such has the single crystal elastic constants given in table 1. Our calculations give the stiffest direction to be  $\langle 111 \rangle$  at 308 GPa and the most compliant  $\langle 100 \rangle$  at 91.7 GPa in close agreement with Wong et al. (2010). Austenite has a relatively high elastic anisotropy when compared to other cubic metals such as aluminium, nickel and ferrite (Sauzay, 2007). The single crystal directional elastic modulus surface for austenite is shown in Figure 3.

**Table 1. Constants used in the present work. The elastic constants ( $C_{11}$ ,  $C_{12}$  and  $C_{44}$ ) were obtained from the literature (Ledbetter, 1984).**

$C_{11}$ (GPa)	$C_{12}$ (GPa)	$C_{44}$ (GPa)	$n$	$\dot{a}$	$h_0$ (MPa)	$\tau_s$ (MPa)	$\tau_0$ (MPa)
204.6	137.7	126.2	55	0.001	675	175	90

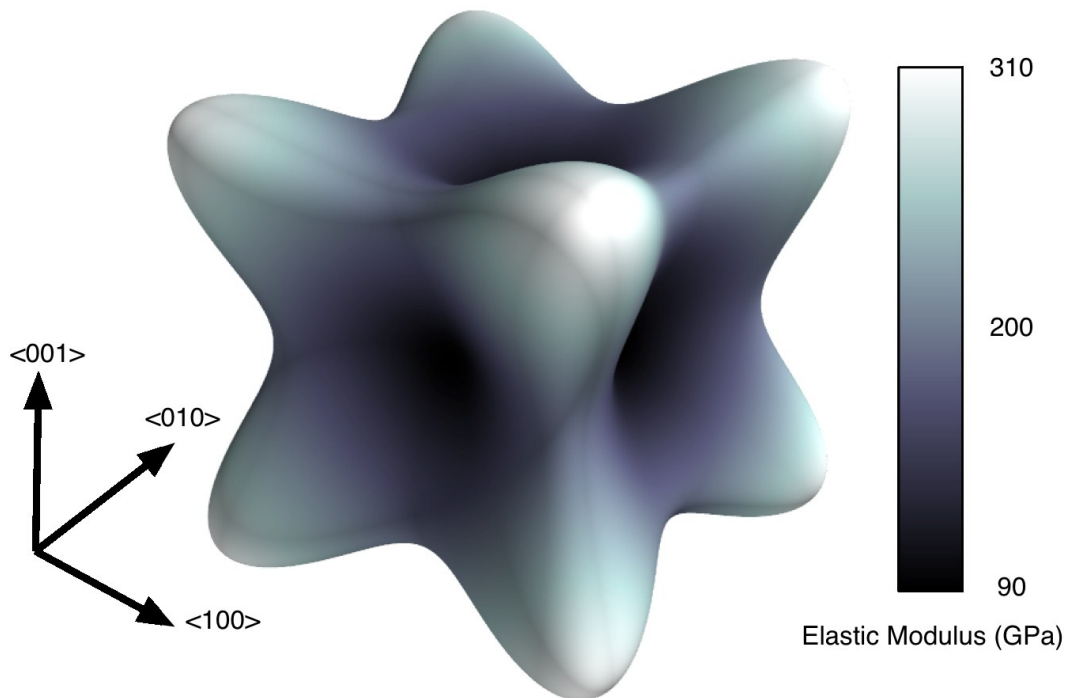
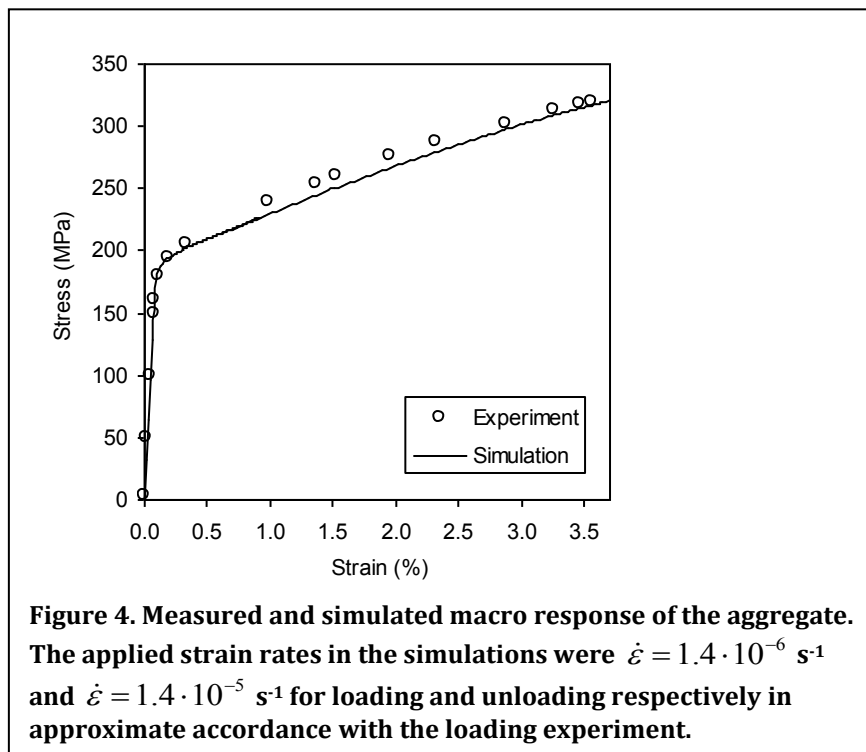


**Figure 3 Single crystal directional elastic modulus surface for austenite, showing the stiffness dependence on the direction of loading.**

In contrast to the elastic properties, the plastic single crystal parameters required by the constitutive laws used in the model are not readily obtained experimentally. Instead, it is common practise to calibrate the model parameters by fitting the predicted deformation to the macroscopic stress-strain curve. Figure 4 shows the experimental and simulated curves obtained using parameters shown in Table 1. The behaviour of the aggregate was also validated by comparing the predicted average response for differently oriented grains with those measured by neutron diffraction showing good agreement (Gonzalez et al. 2012). Details about the neutron diffraction technique can be found elsewhere (Clausen et al., 1999; Oliver et al., 2004; Quinta da Fonseca et al., 2006).



For the two models with elastic isotropy, the bulk elastic constants ( $E = 200 \text{ GPa}$ ,  $\nu = 0.3$ ) were used. For the two models having plastic isotropy, the plastic response was chosen to match the response of the experimental stress strain curve in Figure 4. The macro response of the model was slightly affected by different sets of crystallographic

orientations. On the other hand, small changes to the thickness and elastic properties of the cohesive elements did not change the predicted stress-strain curve in a discernible way.

### 4.2.3 Results and discussions

#### 4.2.3.1 Variability of normal grain boundary stresses

We performed several bi-crystal simulations within the fully elastic region that served as a motivation for the study of polycrystalline materials. Our preliminary results show that, as crystallographic misorientation increases from 0 to ~60 degrees, the mean Von Mises stresses increases up to 80% at Gauss points in the vicinity of the grain boundaries due solely to elastic anisotropy.

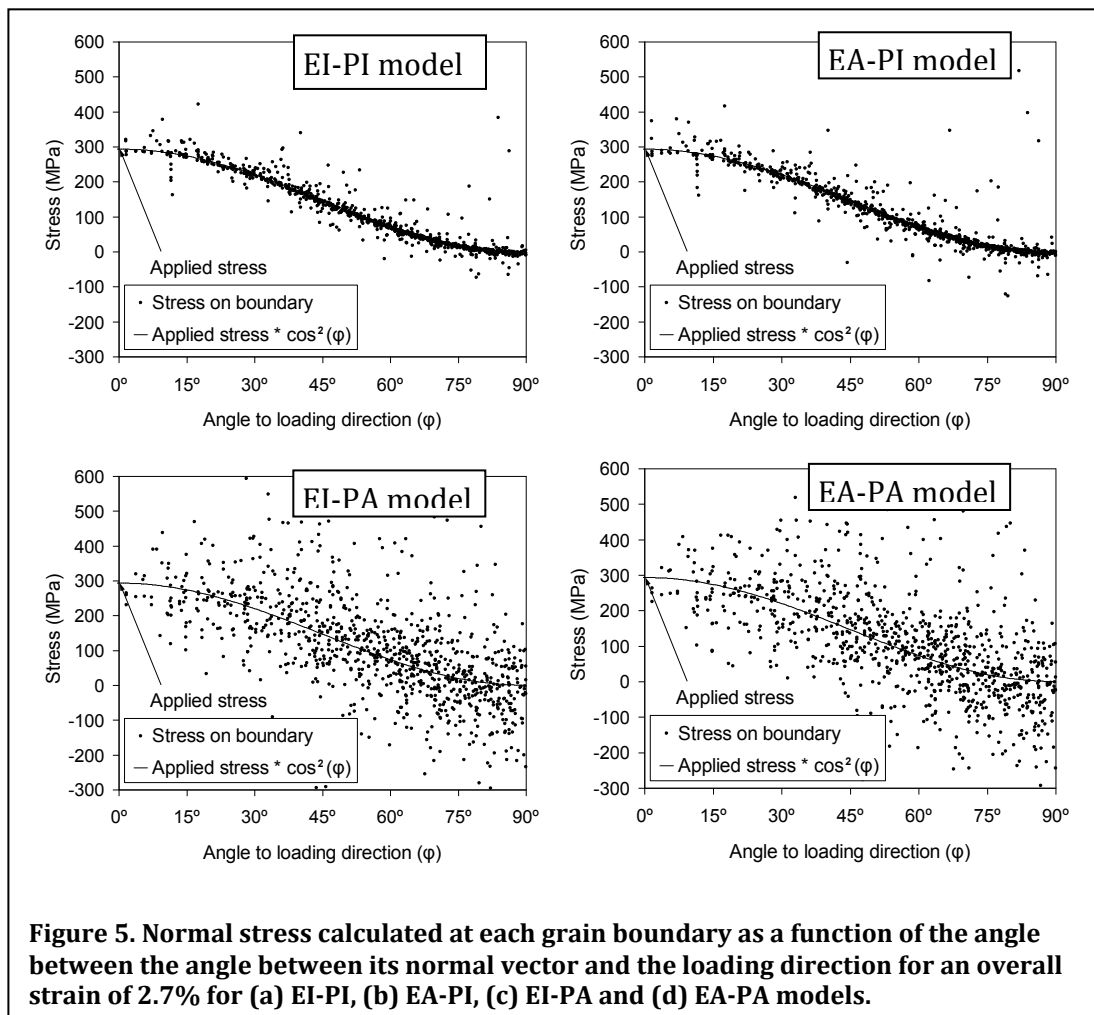
During uniaxial loading of an ideal uniformly stressed isotropic polycrystalline material, the normal stress across a grain boundary should vary with  $\cos^2(\varphi)$  (Zavatsky 2012) where  $\varphi$  the angle between the grain boundary normal and the loading direction. The aim of our work is to study the perturbation to the homogeneous value caused by elastic and plastic anisotropy. To do this, we use the standard deviation ( $S$ ) around the expected macrostress,  $\sigma_{macro}$ :

$$S = \left[ \frac{1}{n} \sum_n (\sigma_{GB} - \sigma_{macro})^2 \right]^{1/2} \quad (4)$$

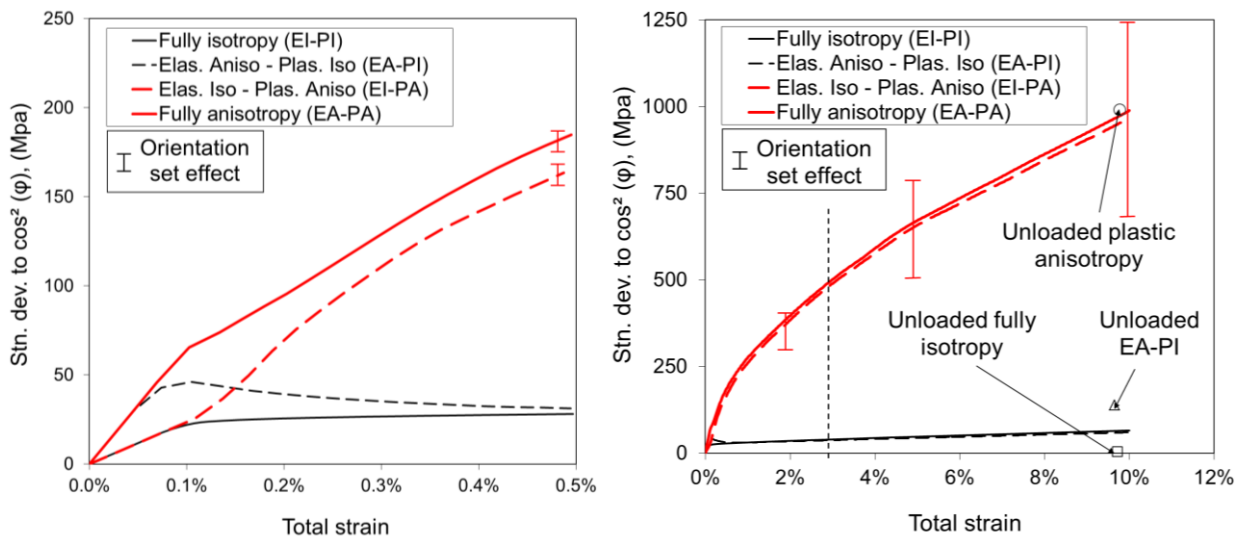
where  $\sigma_{GB}$  represents the mean boundary stress (i.e. the average stress for all elements in the grain facet, weighted by the triangular element area) and  $n$  is the total number of (flat) boundaries.

Figure 5 shows the normal stress on each grain boundary, at 2.7% total strain for the fully isotropic model (model EI-PI), the elastically anisotropic model (EA-PI), the plastically anisotropic model (EI-PA) and the fully anisotropic model (EA-PA), each

compared against the continuum  $\varphi$  expectation. In the first case, full isotropy is assumed, meaning that the normal stress at each boundary should fall on the  $\varphi$  line. However, it can be seen that some boundaries deviate significantly from this value. These boundaries were found to be relatively small, containing only a few cohesive elements. Possible reasons for this effect and the consequences of excluding small boundaries are discussed later in the paper. The variations on such boundaries are likely to arise from numerical issues giving a standard deviation away from the continuum result of  $S \sim 40\text{MPa}$ . Using a finer mesh reduced this scatter but could not remove it completely. Therefore, the scatter in the fully isotropic case can be regarded as the uncertainty in the model predictions at this strain. It is clear by comparing Figure 5a-b with Figure 5c-d that the variability is much larger ( $S \sim 470\text{MPa}$ ), when the grains are allowed to deform anisotropically according to crystal slip.



The evolution of variability in normal grain boundary stresses during the elastic and plastic straining is easily shown in Figure 6. It is clear that while the FE model does predict some grain boundary variability in the elastically anisotropic model, this is much smaller (<30MPa up to 10% strain) than for the plastically anisotropic models. It can be reduced by increasing mesh refinement but this leads to significantly higher computational costs and therefore a compromise was made resulting in a standard deviation of about 10% of the mean applied stress.



**Figure 6. The variability in grain boundary stress (standard deviation) for each model a) at low strains, b) at larger strains. The early stage of deformation marked by the dashed box on the right plot is expanded in the left plot. Data plotted in Figure 5 come from the simulations at 2.7% strain (vertical dashed line). The variability on grain boundary stress upon unloading after 10% strain is also shown in (b). The spread in the variability according to the 4 initial equivalently-random set of grain orientations chosen is indicated by the error bars.**

It is clear from Figure 6(a) that elastic anisotropy (model EA-PI) increases the boundary to boundary variability, but really only until the proportional (elastic) limit for the plastically isotropic model is reached. Appropriately EA-PA matches EA-PI and EI-PA matches EI-PI up until the proportional limit ( $\sim 0.1\%$ ) is exceeded, since there is little plastic deformation until this point.

With the onset of plasticity the anisotropic nature of crystalline slip is much more of an influence on the grain boundary stress than the elastic anisotropy, such that from about 0.1% plastic strain the effect of elastic anisotropy is relatively minor for stainless steel although it does appear to contribute about 20MPa to the variability irrespective of the strain for the fully anisotropic model compared to that which assumes only elastic isotropy. The standard deviation of the variation in grain boundary stress becomes larger than the applied stress at relatively low levels of plastic strain.

The unloaded state is also shown for all models after 10% strain in Figure 6b. For the completely isotropic model there is a reduction of variability upon unloading. Conversely, there is a small increase in variability for the other models. It can be noticed, however, an increase of  $S$  for models with any kind of anisotropy upon unloading. It is intuitive to attribute this to the fact that unloading is dominated by the elastic anisotropic response. However, as we will discuss later, this effect was found to arise from the heterogeneities found in very small boundaries. The cohesive zone properties made no difference to the results before the proportional limit. Afterwards, they made only little difference when it was kept thin and within a reasonable stiffness range.

These results are in agreement with recent work by Wong and Dawson (2010) who investigated the effect of elastic anisotropy on the evolution of the average response of crystals belonging to different crystallographic fibres. Several sets of cubic single crystal elastic constants were calculated while keeping the average Young's modulus and average Poisson's ratio unchanged. It was found that, in fully developed plasticity, the stress distribution of grains within fibres was independent of the single crystal elastic constants. CPFEM modelling has also been used to evaluate the effect of elastic properties on the evolution of stress and total strain (Bieler et al., 2009). This work showed that, after about 1% strain, the stress and strain field gradients were similar regardless of the elastic properties. The dominance of plastic anisotropy over elastic anisotropy on stress is very clear. This suggests that, in some cases, elastic anisotropy can be neglected in these kinds of computations. When the stresses at boundaries for total

strains above 0.5% are of interest, isotropic elasticity can be assumed. This would simplify the computation of the Jaumann stress rate, since this depends on the elastic part of the rate of deformation ( $\mathbf{D}_e$ ). The resulting computational cost saving would make possible simulations of aggregates with a larger number of grains.

#### **4.2.3.2 Grain orientation statistics**

Although the simulated volume contains randomly oriented grains, the stresses at the boundaries change for sets computed for different random grain orientations since the number of grains in the polycrystal is relatively small. The standard error arising from four different equivalent sets of random orientations is displayed as an error bar in Figure 6. Unsurprisingly, the spread varies much more for the crystal plasticity models ( $\sim\pm 25\%$  of the variability) than for the plastically isotropic ones.

#### **4.2.3.3 Grain boundary size and mesh density effects**

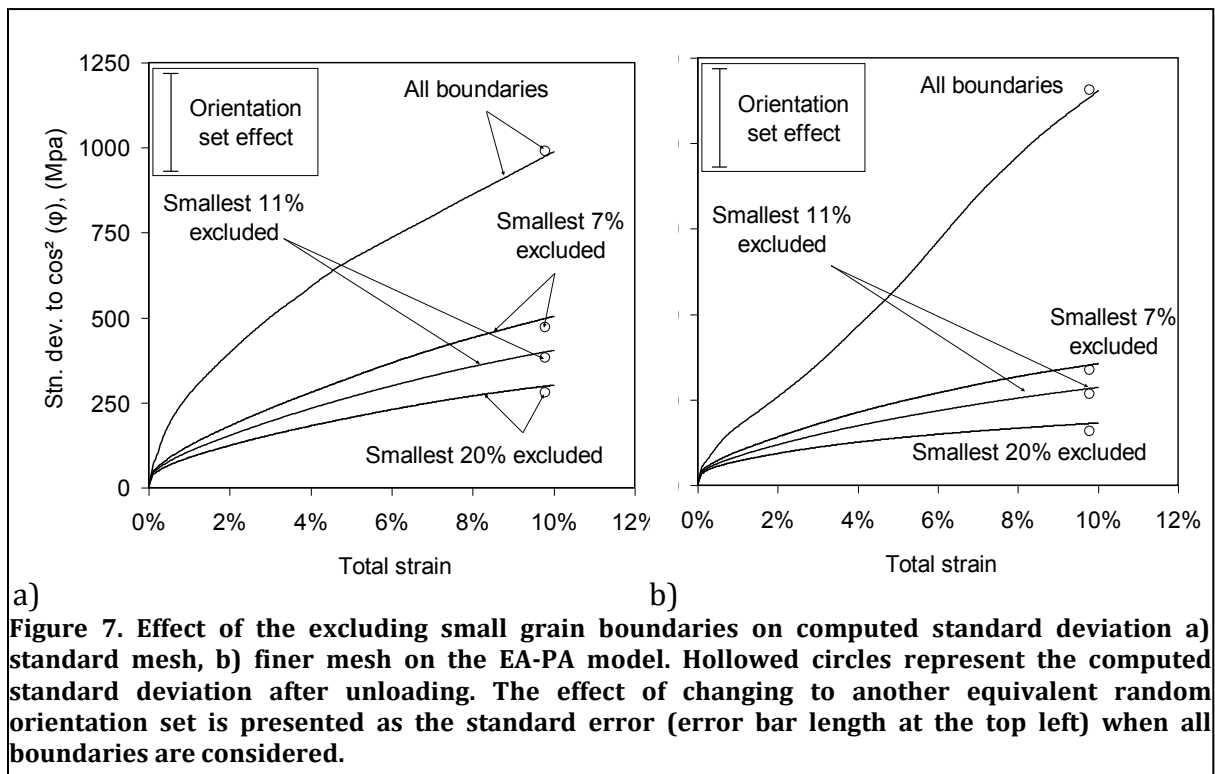
It was found that the consideration of small boundaries had a great impact on the computed standard deviations. The number of cohesive elements forming a boundary is proportional to its area. Figure 2b illustrates a boundary composed of 24 cohesive elements. However, 70 grain boundaries in the aggregate (7% of the total number of boundaries) have only 1 cohesive element, 130 grain boundaries (11% of the total) have 2 cohesive elements or less and 200 grain boundaries (20% of the total) contain 5 cohesive elements or less. Figure 7a shows the variability in grain boundary normal stress computed for the fully anisotropic model when different small grain boundaries are excluded. It is clear that small GBs have the highest variability of normal stress. This was also observed, but to a lesser extent, when only elastic anisotropy was considered for strains below the proportional limit (Marrow et al., 2011). In order to further investigate the behaviour of boundaries formed by one element only, the previously presented simulations were repeated with a finer mesh comprising 545002 C3D4 elements and 58912 cohesive elements. The number of grain boundaries with only one element dropped from 70 to 43 and the results are shown in Figure 7b. While there are slight differences between the curves, the overall results are largely the same: including small boundaries gives the largest variation in normal stress, regardless of the mesh

refinement of the boundary and its vicinity. The variability for the grain boundaries for the EI-PI and EA-PI models is reduced by approximately 30% on using a finer mesh (not shown). For the EA-PA model, mesh refinement reduces the variability when very small boundaries are excluded (smallest 7%). However, when these boundaries are also included (all GBs included) the variability increases disproportionately after 4% strain regardless of the mesh density. It was observed that, at this point, some single-element boundaries presented extremely high stress magnitudes (i.e. about 60 times the standard deviation), leading to the overall disproportionate increase of variability.

The high variability of stresses calculated at the small boundaries is somewhat surprising in our work, since the constitutive laws of the crystals are not size dependent. However, numerical and physical effects are possible. Numerically, this may be attributed to the limited number of elements conforming the mesh. Physically, this may be attributed to the stress concentrators arising from different geometries of the grains. Consider two elliptical grains of the same area embedded in a matrix, each grain having different elliptic eccentricities. If both embedded grains had a very low stiffness (or effectively a hole), then the stress at the boundary of the highly eccentric grain is higher near the low local radius of curvature (Griffith 1921). If we were to approximate each elliptical grain with a polygon of a fixed number of lines (e.g. 8) then the regions with the higher local radii of curvature would best fit using shorter lines (Weisstein, 2012). Therefore, the smallest lines (or boundaries) of the octagons (or grains) would concentrate the highest stresses.

Close inspection of the stress distribution across grain boundary faces revealed that stresses are always much higher at the edges (the line along which three 3D grains meet) as can be seen in Figure 8. It is not unexpected that grain boundary edges should have the highest stresses; they represent regions in the polycrystals where at least 3 grains meet and where, therefore, incompatibility stresses should be highest. In this regard, recent work has shown that near triple junctions, the influence of a third grain induces severe oscillations of the stress tensor, reflecting a singularity (Kanjarla et al., 2010). Furthermore, different cohesive elements meet at these edges, which in itself

could give rise to the observed stress concentration. Whatever the reason for the higher stresses, the contribution of the edges to the average grain boundary stresses is proportionally higher for small boundaries and therefore they show extreme stress values. This effect is practically insensitive to mesh refinement. However, since it only affects the regions near the boundary edges (Figure 8), it is reasonable to ignore these small boundaries and their corresponding extreme stress values. This was the approach employed in the next sections, which deal with the effect of grain boundary orientation and the effect of local plasticity on grain boundary stresses.



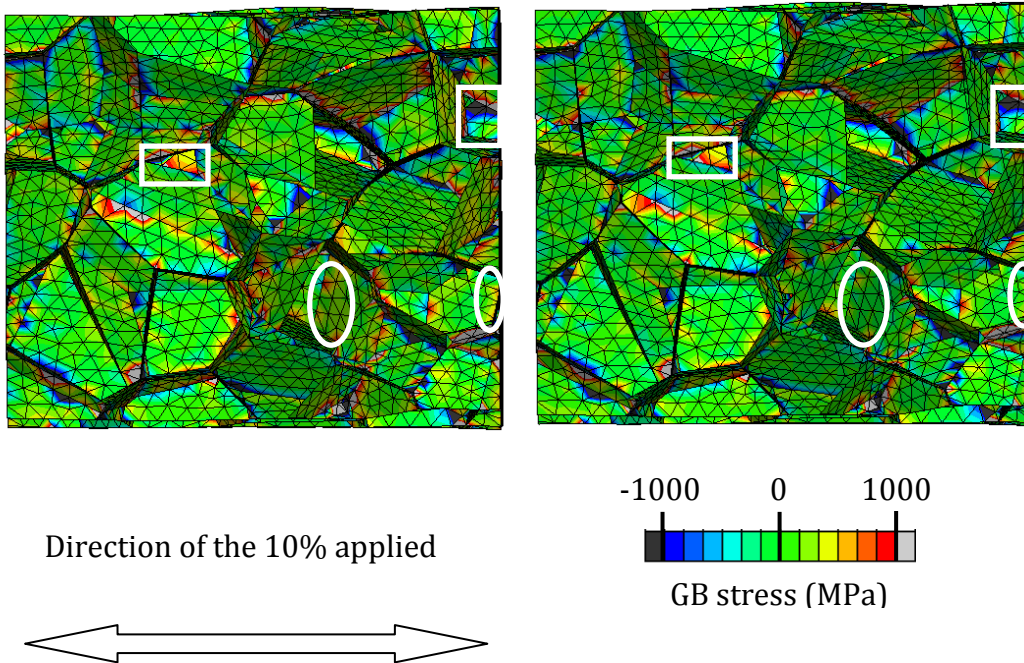


**Figure 8. Stresses normal to the boundary elements for the EA-PA model: (a) at 10% strain, (b) after unloading. Maximum and minimum stresses tend to occur in elements in contact with boundary edges while inner areas of the GB show less extreme values. Small GBs (marked in white squares) generally show a very high stress variability. The white ellipses spot differences before and after unloading. Note that the figure represents a cut-through view of the (flat) grain boundaries which leaves some partially sectioned out-plane boundaries (darker regions)**

#### 4.2.3.4 Distribution of stress normal to boundaries upon unloading

Until now, grain boundary stresses have been considered mainly during loading. The unloaded state is of particular interest since it has been suggested that these grain boundary residual stresses have an impact on degradation mechanisms such as SCC. It has been reported that, following pre-straining, cracking susceptibility is direction dependent (Moshier and Brown, 2000; Tice et al., 2007). This is consistent with work on damage nucleation in nickel alloys (Dyson et al., 1976), where it is proposed that damage nucleation is anisotropic. There is therefore an interest in determining whether the spread in stresses observed is also anisotropic.

It has also been reported that cracking often occurs at boundaries separating grains that are heavily plastically deformed from those in which deformation is mostly elastic (Couvant et al., 2009). In some cases large local strains can help relax local stresses (e.g. favourable slip near grain boundaries) preventing damage, whereas in other cases heterogeneous deformation can lead to stress concentrations and even damage nucleation (Bieler et al., 2009). Therefore, we are interested in whether the stresses are highest at the boundaries separating “hard” and “soft” grains.

### *4.2.3.4.1 Effect of grain boundary angle on stresses at grain boundaries*

We showed earlier that, in an anisotropic material, the spread in grain boundary stresses is mostly a consequence of plastic anisotropy. However the distribution of stresses were not analysed in detail. Figure 5 shows the normal stress on each grain boundary as a function of the angle  $\varphi$ . The unloaded state is now divided in 6 intervals of  $15^\circ$  depending on the angle  $\varphi$ . The standard deviations of each interval are shown in Figure 9a. The results from simulations containing five sets of random orientations were used to calculate the values of each interval. In order insure statistical significance, each interval contains at least 30 grain boundaries, from each orientation set. The total deviation in each angle range is reduced with the increasing exclusion of small grain boundaries (Figure 9b). This can also be seen in Figure 7, where the computed standard deviations become smaller as the percentage of exclusion increases.

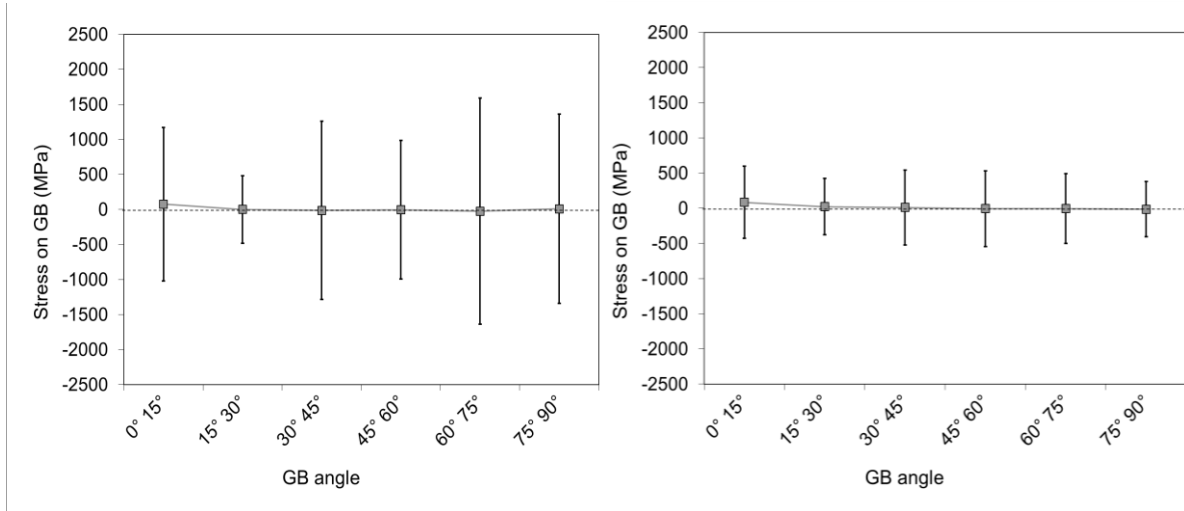


**Figure 9. Average grain boundary residual stress for each grain boundary angle interval (solid squares) after 10% strain when a) all boundaries are included, and b) when (small) boundaries composed of only one cohesive element are excluded. Error bars show the standard error for each grain boundary angle interval.**

Figure 9 shows that the average stress for each 15° interval is approximately zero. The error bars in that figure represent, for each interval, the standard deviation of the distribution of the stresses normal to each boundary. The distributions of stresses within these intervals are not symmetric when all GBs are included (Figure 9a). However, when boundaries comprised of only one cohesive element are excluded (Figure 9b), the dispersion becomes more uniform for each interval. Therefore, no clear trend of these standard errors can be inferred.

Previous 3D bi-crystal simulations showed the influence of the grain boundary orientation (relative to the loading direction) on the strain and stress distributions (Sarma and Radhakrishnan, 2008). These results show that, in the absence of a precipitate, higher stress values are seen along certain boundaries depending on both grain orientation and the angle  $\varphi$ . Furthermore, 2D modelling work results show a clear influence of the angle  $\varphi$  on the stress in neighbouring “hard” grains, with a particular “rogue” combination causing significantly higher stresses (Dunne et al., 2007).

Our results complete such findings by statistically analysing the effect of the angle  $\varphi$  on the stress distribution using a 3D aggregate with numerous boundaries following deformation and unloading. If the angle  $\varphi$  were to have an effect on the stress distribution, the mean stress or the standard error (or a combination of both) would differ from some intervals to others in Figure 9. This applies for, in particular, high values of  $\varphi$ , where the predicted stress in previous work is higher (Dunne et al., 2007). Therefore, we conclude that, following preloading, a boundary is not statistically more likely to present higher or extreme values of stress by simply considering the angle  $\varphi$  when the boundary is embedded in a 3D polycrystal. Furthermore, we are just as likely to find boundaries under tensile residual stress as we are to find boundaries in residual compression, regardless of boundary orientation.

#### 4.2.3.4.2 *Stresses at grain boundaries between soft and hard grains*

Since it is clear that plastic anisotropy is the main source of grain boundary stresses, it is reasonable to assume stresses will be highest on boundaries separating grains with the biggest difference in the amount of plastic strain, that is, the grain boundaries separating “hard” and “soft” grains. In this section, we present results that seek a relationship between and stresses at boundaries and plastic deformation in neighbouring grains.

In their article on the effects of pre-straining on creep damage, Dyson et al. (1976) use a result by Kröner (1961) to try to explain why grain boundaries parallel to the preloading direction are more damaged than those perpendicular to it. Kröner established a correlation between the boundary stress and the amount of plastic strain. We recall that the internal stress,  $\sigma_{ij}$ , in any small volume of the aggregate was given by Kröner as:

$$\sigma_{ij} \propto (\bar{\varepsilon}_{ij} - \varepsilon_{ij}) \quad (8)$$

where  $\bar{\varepsilon}_{ij}$  is the average deviatoric plastic strain and  $\varepsilon_{ij}$  is the local deviatoric plastic strain. This expression is based on the capability of relating all strain and stress

components within, and immediately outside, an ellipsoidal inclusion embedded in an infinite homogeneous medium through imaginary cutting, straining and welding operations (Eshelby, 1957). Consider tension applied on the medium where a grain is softer than the average. Then, near a boundary orthogonal to the loading direction  $\varepsilon_{ij} > \bar{\varepsilon}_{ij}$  and the stress normal to the boundary will be compressive. On the other hand, if the boundary is parallel to the loading direction  $\varepsilon_{ij} < \bar{\varepsilon}_{ij}$  and the stress normal to the boundary will be tensile. The normal stresses in the plastically harder grains will, of course, be of reverse sign. Therefore, using this approach, the difference between the average and local plastic strains is expected to reveal the sign (tension or compression) and relative magnitude of the stress normal to the boundary.

The constraints on each grain in our aggregate are more complex since there are different grain shapes, neighbourhoods and orientations. However, because our models provide values for stress and strain at each integration point we can study this effect locally and in a statistical manner. It has been observed that stress corrosion cracks are often found on boundaries separating a heavily deformed grain from one with hardly any deformation (Couvant et al., 2009). There is some debate as to whether this is a consequence of the difference in dislocation density in neighbouring grains or of the residual stresses generated between the two misfitting grains. We are therefore interested whether the residual stress at grain boundaries can be correlated to the difference between plastic strain in the neighbouring grains. To achieve this, we propose to use the equivalent plastic strain ( $p$ ) as a measure of the amount of plastic deformation in the neighbouring grains. We define  $p$  as:

$$p = \left( \frac{2}{3} \boldsymbol{\varepsilon}^{pl} : \boldsymbol{\varepsilon}^{pl} \right)^{\frac{1}{2}} \quad (9)$$

where  $\boldsymbol{\varepsilon}^{pl}$  is the accumulated plastic strain tensor throughout the simulation time. For each grain, we have averaged all the values of  $p$  at each Gauss point weighting by the Gauss point volume. Although the concept of equivalent strain is not entirely appropriate in a crystal plasticity framework, it is a convenient way of reducing the

deviatoric strain tensor to a scalar value that can be easily compared for neighbouring grains. Our results (not shown) showed a good correlation between the grain-averaged  $p$  and the grain-averaged cumulative slip (Eq. 3).

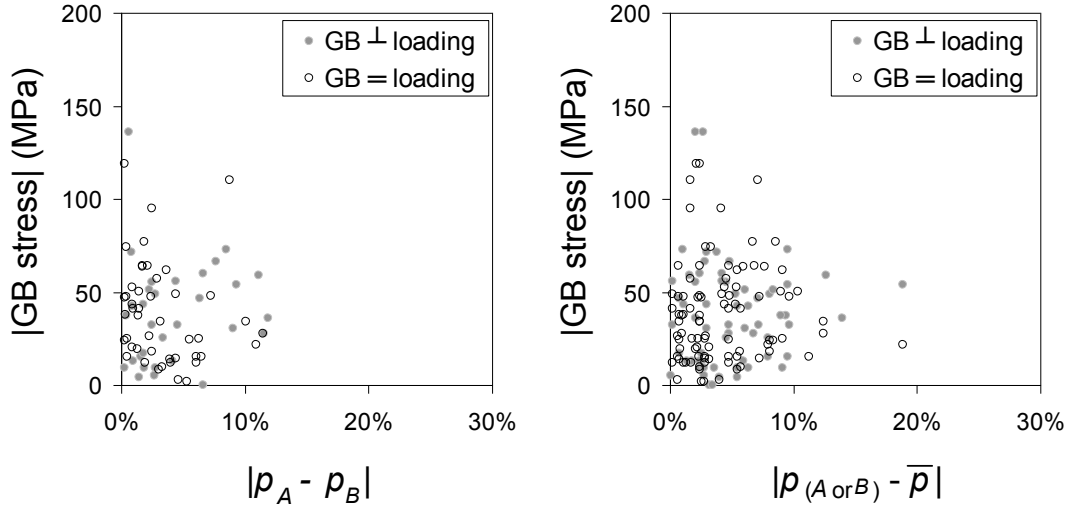


**Figure 10. Absolute residual stress (after unloading) normal to boundaries versus the absolute difference between a) the equivalent plastic strain ( $p$ ) of each adjacent grain to the boundary; b) the equivalent plastic strain of one adjacent grain to the boundary and the averaged plastic strain of the aggregate. The results are presented for boundaries with  $\varphi$  lower than  $30^\circ$  (considered orthogonal) boundaries with  $\varphi$  higher than  $75^\circ$  (considered parallel).**

Figure 10a shows the difference of equivalent plastic strain ( $p$ ) between adjacent grains versus the stresses normal to their boundary, an indication of the extent to which neighbouring grains form a “hard-soft” combination. Figure 10b shows the difference of equivalent plastic strain ( $p$ ) between one adjacent grain and the aggregate-averaged equivalent strain versus the stresses normal to their boundary, giving an indication to which extent the grain is “softer” or “harder” than average. Each boundary has two adjacent grains and therefore produces two values in the horizontal axis in Figure 10b. Only the 20 percent largest GBs ( $>120$  Gauss points) have been considered to avoid the high stresses characteristic of small boundaries. In addition, the relatively extreme Gauss point stress values ( $\bar{\sigma}_{GB} \pm 1000\text{MPa}$ ) in the edges of these boundaries have been neglected on averaging the boundary stress. For clarity, boundaries are divided into

two sets: boundaries parallel to the loading direction, defined as those with  $\varphi > 75^\circ$ , and orthogonal boundaries, with  $\varphi < 30^\circ$ .

As it can be seen in Figure 10a, the grain boundary residual stresses range from 0 to about 140 MPa, whereas the differences in effective plastic strain range from 0 to just over 10%. There is no strong correlation between the magnitude of grain boundary residual stresses and the difference in equivalent plastic strain in neighbouring grains. Grain pairs with larger differences in plastic strain seem to have larger grain boundary stresses, however there is at least one boundary ( $\sim |140|$  MPa) separating grains with the same plastic strain. Therefore, although a large difference in plastic strain seems to increase grain boundary stresses, it is not a necessary condition. Our results imply that, using our definition, a “hard-soft” grain combination is no more likely to cause higher grain boundary residual stresses than any other combination. The results are similar if instead of comparing the plastic strain of near neighbours, we compare the plastic strain in the grain to the average plastic strain, as can be seen in Figure 10b, which shows the absolute values of the grain boundary stresses. However, it is important to note that these stresses average to zero, which indicates that the stresses are as likely to be compressive as they are to be tensile.

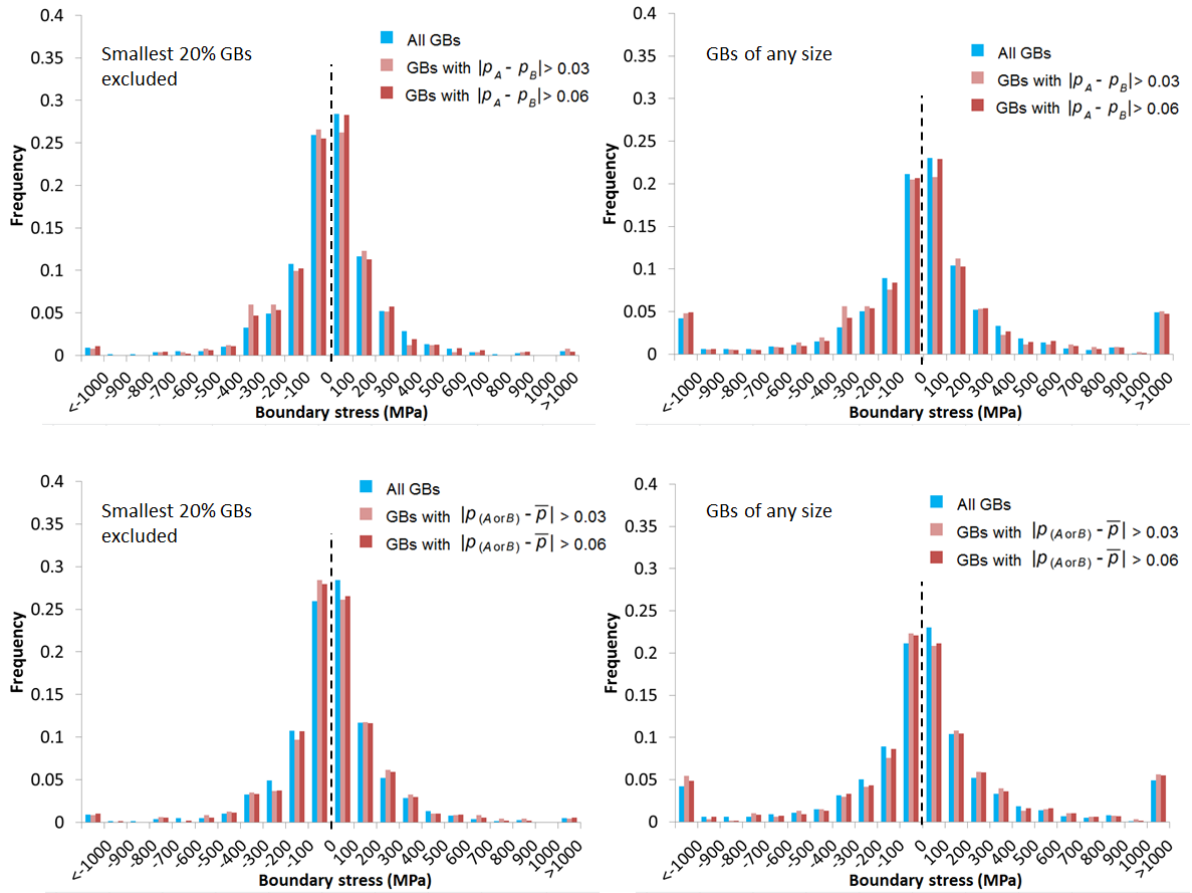


**Figure 11. Distribution of residual boundary stresses. The histograms show the effect of the high absolute difference between the (a and b) equivalent plastic strain ( $p$ ) of each adjacent grain to the boundary; (c and d) the equivalent plastic strain of one adjacent grain to the boundary and the averaged plastic strain of the aggregate. The histograms also show the high boundary stress variability introduced by small boundaries (b and d) as studied in previous sections.**

The results largely remain the same if we consider boundaries of any orientation as well as the high stress values calculated at Gauss points near the boundary edges and (Figure 11). Boundaries separating grains with high difference in plastic deformation do not tend to develop higher tensile (or compressive) stresses. As previously shown, the results are similar if we compare the plastic strain in the grain to the average plastic strain. Further, these findings are unaltered by the high boundary stress variability introduced by small boundaries.

These results are somehow counterintuitive. One could reasonably expect that, since the origin of the residual grain boundary stresses is the misfit caused by anisotropic plasticity, the larger the difference in plastic strain between neighbouring grains, the larger the stresses across the boundary separating them. Although this is probably valid for the bi-crystal case, our results show that, in a polycrystal, the stresses redistribute in such a way that it becomes impossible to predict their magnitude solely from the amount of plastic deformation near the boundary or the difference either side of it. This is consistent with previous CPFEM results using cycled polycrystals. The neighbouring crystallographic orientations were found to have a great impact on the stresses within grains (Turkmen et al., 2002) and on the crack tip opening displacement (Simonovski et al., 2007). Besides, plastic strain is well known to localize along bands which expand across several grains whereas stresses tend to localize into individual grains. This is to say that the stresses at the grain boundary depend not only on the misfits generated by plastic anisotropy but on how they are accommodated by the grains in the neighbourhood of the grain boundary of interest. This finding has implications for the understanding of intergranular SCC in cold worked material and, in particular, the observation that grain boundaries separating a heavily deformed grain and an undeformed or lightly deformed grain are more susceptible to cracking. Our results suggest that this higher susceptibility is probably not due to the intergranular residual stresses developed during cold working, since these can be compressive as well as tensile and their magnitude depends on how the stress redistributes over a wider neighbourhood.

Interestingly, previous work using finite element crystal plasticity (Diard et al., 2005) also failed to relate grain boundary stress to other grain boundary characteristics such as misorientation and slip incompatibility. It is important to remember that, although crystal plasticity finite element modelling captures some features of the deformation at the microscale, it fails to capture other features, like the heterogeneous nature of deformation within grains and the slip localization (typically called slip bands) characteristic of low stacking fault energy metals like stainless steel. It is likely that these features give rise to stresses at grain boundaries that cannot be predicted with

the current crystal plasticity modelling approaches but which play a role during stress corrosion cracking.

#### ***4.2.4 Conclusions***

Crystal plasticity finite element modelling using cohesive elements in the grain boundary regions have been incorporated in order to calculate normal stresses at grain boundaries generated by elastic and plastic anisotropy during deformation and following unloading. This has enabled us to examine a number of factors that might be expected to give rise to large grain boundary stresses.

Our results show that, after 0.5% applied strain, stresses normal to grain boundaries introduced by plastic anisotropy dominate over the normal stresses introduced by elastic anisotropy. This was unaffected by mesh density. Small boundaries were found to have much higher absolute stresses (whether tensile or compressive) than larger boundaries. This was attributed to the high stresses predicted at grain boundary edges (or triple junctions). Generally, mesh refinement mitigated this effect, except when the smallest GBs were considered.

Following unloading, the standard deviation of residual grain boundary stresses was only slightly decreased and was found to be independent of grain boundary orientation.

The magnitudes of the residual grain boundary stresses predicted is unrelated to the amount of plastic strain in the vicinity of the boundary and whether it was higher or lower than the average plastic strain. In other words, in a plastically deformed polycrystal, a soft-hard grain combination does not imply high residual stress normal to its boundary.

#### **4.2.5 References associated to Publication 2**

- ABAQUS, I., 2006. ABAQUS Documentation, Providence, Rhode Island.
- Babout, L., Marrow, T.J., Engelberg, D., Withers, P.J., 2006. X-ray microtomographic observation of intergranular stress corrosion cracking in sensitised austenitic stainless steel. *Mater. Sci. Technol.* 22, 1068-1075.
- Barbe, F., Decker, L., Jeulin, D., Cailletaud, G., 2001a. Intergranular and intragranular behavior of polycrystalline aggregates. Part 1: F.E. model. *Int. J. of Plas.* 17, 513-536.
- Barbe, F., Forest, S., Cailletaud, G., 2001b. Intergranular and intragranular behavior of polycrystalline aggregates. Part 2: Results. *Int. J. of Plas.* 17, 537-563.
- Bate, P., 1999. Modelling deformation microstructure with the crystal plasticity finite-element method. 357, 1589-1601.
- Bieler, T.R., Eisenlohr, P., Roters, F., Kumar, D., Mason, D.E., Crimp, M.A., Raabe, D., 2009. The role of heterogeneous deformation on damage nucleation at grain boundaries in single phase metals. *Int. J. of Plas.* 25, 1655-1683.
- Clausen, B., Lorentzen, T., Bourke, M.A.M., Daymond, M.R., 1999. Lattice strain evolution during uniaxial tensile loading of stainless steel. *Materials Science and Engineering A* 259, 17-24.
- Clausen, B., Lorentzen, T., Leffers, T., 1998. Self-consistent modelling of the plastic deformation of FCC polycrystals and its implications for diffraction measurements of internal stresses. *Acta Materialia* 46, 3087-3098.
- Couvant, T., Legras, L., Herbelin, A., Musienko, A., Vertenelle, Q., Ilevbare, G., Delafosse, D., Cailletaud, G., Hickling, J., 2009. Development of understanding of the interaction between localized deformation and SCC of austenitic stainless steels exposed to primary PWR environment, Virginia Beach, Virginia, USA.
- Diard, O., Leclercq, S., Rousselier, G., Cailletaud, G., 2002. Distribution of normal stress at grain boundaries in multicrystals: application to an intergranular damage modeling. *Comput. Mater. Sci.* 25, 73-84.
- Diard, O., Leclercq, S., Rousselier, G., Cailletaud, G., 2005. Evaluation of finite element based analysis of 3D multicrystalline aggregates plasticity - Application to crystal

plasticity model identification and the study of stress and strain fields near grain boundaries. *Int. J. of Plas.* 21, 691-722.

Dunne, F.P.E., Walker, A., Rugg, D., 2007. A systematic study of hcp crystal orientation and morphology effects in polycrystal deformation and fatigue. *Proceedings of the Royal Society A: Mathematical, Physical and Engineering Sciences* 463, 1467-1489.

Dyson, B.F., Loveday, M.S., Rodgers, M.J., 1976. Grain Boundary Cavitation Under Various States of Applied Stress. *Proceedings of the Royal Society of London. A. Mathematical and Physical Sciences* 349, 245-259.

Eshelby, J.D., 1957. The Determination of the Elastic Field of an Ellipsoidal Inclusion, and Related Problems. *Proceedings of the Royal Society of London. Series A. Mathematical and Physical Sciences* 241, 376-396.

Fallahi, A. & Ataee, A. 2010. Effects of crystal orientation on stress distribution near the triple junction in a tricrystal  $\gamma$ -TiAl. *Materials Science and Engineering: A*, 527, 4576-4581.

García, C., Martín, F., Tiedra, P.D., Heredero, J.A., Aparicio, M.L., 2001. Effects of prior cold work and sensitization heat treatment on chloride stress corrosion cracking in type 304 stainless steels. *Corrosion Science* 43, 1519-1539.

Gardner, C.J., Adams, B.L., Basinger, J., Fullwood, D.T., 2010. EBSD-based continuum dislocation microscopy. *International Journal of Plasticity* 26, 1234-1247

Gonzalez, D., Kelleher, J.F., Quinta da Fonseca, J., Withers, P.J., 2012. Macro and intergranular stress responses of austenitic stainless steel to 90° strain path changes. *Materials Science and Engineering: A* 546, 263-271.

Gonzalez, D. A contribution on modelling deformation and residual stress in deformed 3D polycrystals. PhD Thesis 2012.

Harewood, F.J., McHugh, P.E., 2007. Comparison of the implicit and explicit finite element methods using crystal plasticity. *Comput. Mater. Sci.* 39, 481-494.

Hill, R., Rice, J.R., 1972. Constitutive analysis of elastic-plastic crystals at arbitrary strain. *J. of the Mech. and Phy. of Solids* 20, 401-413.

Huang, Y., 1991. A user-material subroutine incorporating single crystal plasticity in the ABAQUS finite element program, Mech Report 178, Division of Engineering and Applied Sciences, Harvard University, Cambridge, Massachusetts.

- Kalidindi, S.R., Bronkhorst, C.A., Anand, L., 1992. Crystallographic texture evolution in bulk deformation processing of FCC metals. *Journal of the Mechanics and Physics of Solids* 40, 537-569.
- Kanjarla, A.K., Van Houtte, P., Delannay, L., 2010. Assessment of plastic heterogeneity in grain interaction models using crystal plasticity finite element method. *Int. J. of Plas.* 26, 1220-1233.
- Kocks, U. F., Relation between polycrystal deformation and single-crystal deformation. *Metall. Trans.* 1, 1121 (1970)
- Kröner, E., 1961. Zur plastischen verformung des vielkristalls. *Acta Metallurgica* 9, 155-161.
- Ledbetter, H.M., 1984. Monocrystal Polycrystal Elastic-Constants Of A Stainless-Steel. *Physica Status Solidi A-Applied Research* 85, 89-96.
- Liang, H., Dunne, F.P.E., 2009. GND accumulation in bi-crystal deformation: Crystal plasticity analysis and comparison with experiments. *Int. J. of Mech. Sci.* 51, 326-333.
- Lim, H., Lee, M.G., Kim, J.H., Adams, B.L., Wagoner, R.H., 2011. Simulation of polycrystal deformation with grain and grain boundary effects. *International Journal of Plasticity* 27, 1328-1354.
- Lorentzen, T., Daymond, M.R., Clausen, B., Tomé, C.N., 2002. Lattice strain evolution during cyclic loading of stainless steel. *Acta Mater.* 50, 1627-1638.
- Marrow, T.J., Gonzalez, D., Aswad, M., Quinta da Fonseca, J., Withers, P.J., 2011. In-situ observation and modelling of intergranular cracking in polycrystalline alumina. *Key Engineering Materials* 465, 560-563.
- Mochizuki, M., 2007. Control of welding residual stress for ensuring integrity against fatigue and stress-corrosion cracking. *Nucl. Eng. Des.* 237, 107-123.
- Moshier, W.C., Brown, C.M., 2000. Effect of cold work and processing orientation on stress corrosion cracking behavior of alloy 600. *CORROSION* 56, 307-320.
- Nye, J.F., 1985. *Physical Properties of Crystals: Their Representation by Tensors and Matrices.* Oxford University Press, USA.
- Oliver, E.C., Daymond, M.R., Withers, P.J., 2004. Interphase and intergranular stress generation in carbon steels. *Acta Mater.* 52, 1937-1951.

- Palumbo, G., King, P.J., Aust, K.T., Erb, U., Lichtenberger, P.C., 1991. Grain boundary design and control for intergranular stress-corrosion resistance. *Scripta Metallurgica et Materialia* 25, 1775-1780.
- Peirce, D., Asaro, R.J., Needleman, A., 1982. An analysis of nonuniform and localized deformation in ductile single crystals. *Acta Metallurgica* 30, 1087-1119.
- Peirce, D., Asaro, R.J., Needleman, A., 1983. Material rate dependence and localized deformation in crystalline solids. *Acta Metall.* 31, 1951-1976.
- Petric, Z., 2010. Generating 3D Voronoi tessellations for material modeling. Jozef Stefan Institute. Tech. report.
- Pi, H., Han, J., Zhang, C., Tieu, A.K., Jiang, Z., 2008. Modeling uniaxial tensile deformation of polycrystalline Al using CPFEM. *Journal of University of Science and Technology Beijing, Mineral, Metallurgy, Material* 15, 43-47.
- Qian, J., Zhang, Y., Wang, W., Lewis, A.C., Qidwai, M.A.S., Geltmacher, A.B., 2010. Quality improvement of non-manifold hexahedral meshes for critical feature determination of microstructure materials. *International Journal for Numerical Methods in Engineering* 82, 1406-1423.
- Quey R., Dawson P.R. and Barbe F., 2011. Large-scale 3D random polycrystals for the finite element method: Generation, meshing and remeshing. *Computer Methods in Applied Mechanics and Engineering* 200, 1729–1745
- Quilici, S., Cailletaud, G., 1999. FE simulation of macro-, meso- and micro-scales in polycrystalline plasticity. *Comput. Mater. Sci.* 16, 383-390.
- Quinta da Fonseca, J., Oliver, E.C., Bate, P.S., Withers, P.J., 2006. Evolution of intergranular stresses during in situ straining of IF steel with different grain sizes. *Materials Science and Engineering: A* 437, 26-32.
- Sangid, M.D., Maier, H.J., Sehitoglu, H., 2011. The role of grain boundaries on fatigue crack initiation – An energy approach. *International Journal of Plasticity* 27, 801-821.
- Sarma, G.B., Dawson, P.R., 1996. Texture predictions using a polycrystal plasticity model incorporating neighbor interactions. *Int. J. of Plas.* 12, 1023-1054.
- Sarma, G.B., Radhakrishnan, B., 2008. Modeling the effect of microstructural features on the nucleation of creep cavities. *Materials Science and Engineering: A* 494, 92-102.

- Sauzay, M., 2007. Cubic elasticity and stress distribution at the free surface of polycrystals. *Acta Mater.* 55, 1193-1202.
- Simonovski, I., Cizelj, L., 2011. Automatic parallel generation of finite element meshes for complex spatial structures. *Comput. Mater. Sci.* 50, 1606-1618.
- Simonovski, I., Cizelj, L., 2007. The influence of grains' crystallographic orientations on advancing short crack. *Int. J. of Fatigue* 29, 2005-2014.
- Singh, R., Chattoraj, I., Kumar, A., Ravikumar, B., Dey, P., 2003. The effects of cold working on sensitization and intergranular corrosion behavior of AISI 304 stainless steel. *Metallurgical and Materials Transactions A* 34, 2441-2447.
- Song, X., Zhang, S.Y., Dini, D., Korsunsky, A.M., 2008. Inter-granular residual stresses in polycrystalline aggregates: finite element modelling and diffraction post-processing. *Stress evaluation in materials using neutrons and synchrotron radiation* 571-572, 271-276.
- Sun, S., Adams, B.L., King, W.E., 2000. Observations of lattice curvature near the interface of a deformed aluminium bicrystal. *Philosophical Magazine A* 80, 9-9.
- Tice, D., Stairmand, J., Platts, N., 2007. Crack Growth Testing of Cold-Worked Type 304 Stainless Steel in PWR Primary Coolant, Toronto.
- Turkmen, H.S., Dawson, P.R., Miller, M.P., 2002. The evolution of crystalline stresses of a polycrystalline metal during cyclic loading. *Int. J. of Plas.* 18, 941-969.
- Weisstein, E.W., 2012. Drawing an Ellipse Using Circles and Lines. Wolfram Demonstrations Project -- from Wolfram MathWorld.
- Weisstein, E.W., 2012. Sphere Point Picking -- from Wolfram MathWorld.
- Wong, S.L., Dawson, P.R., 2010. Influence of directional strength-to-stiffness on the elastic-plastic transition of fcc polycrystals under uniaxial tensile loading. *Acta Mater.* 58, 1658-1678.
- Zavatsky, A.B., Stress and Strain, Lecture 5. <http://www.eng.ox.ac.uk>

**END OF PUBLICATION 2**

### 4.3 Publication 3

**Modelling and measurement of plastic deformation and grain rotation in 3D at the grain-to-grain level**

D. Gonzalez, I. Simonovski, P.J. Withers and J. Quinta da Fonseca

Proceedings of the 1st World Congress on Integrated Computational Materials Engineering (ICME) 2011, p107-112

In this publication the idea of the comparison between the DCT data and the 3D model was proposed and supervised by Joao Fonseca. The corresponding experimental results were performed by a working team in ESRF (including myself) led by Andrew King. The Python scripts used to create the geometry (.sat files) from the DCT data (binary file) were developed by I. Simonovski whereas the rest of the pre-processing (Amira simplification and correction, Abaqus model import, meshing, material properties calibration, real orientation assignment, boundary conditions...etc) and all the post-processing was done by myself.

**BEGIN OF PUBLICATION 3**

**MODELLING AND MEASUREMENT OF PLASTIC DEFORMATION AND GRAIN ROTATION IN 3D AT  
THE GRAIN-TO-GRAIN LEVEL**

David Gonzalez<sup>1</sup>, Andrew King<sup>2</sup>, Igor Simonovski<sup>3</sup>, João Quinta da Fonseca<sup>1</sup>, Philip J.  
Withers<sup>1</sup>

<sup>1</sup>School of Materials, University of Manchester, Grosvenor St., Manchester, M1 7HS, UK.

<sup>2</sup>ESRF, Polygone Scientifique Louis Néel, 6 rue Jules Horowitz, Grenoble, 38000, France.

<sup>3</sup>Institute for Energy, P.O. Box 2, Petten, NL-1755 ZG, The Netherlands

Keywords: Image-based model, Texture, Plastic deformation, Aluminium

**Abstract**

The deformation of a polycrystalline sample of aluminium at the microstructural scale was studied by a combination of computational modelling and synchrotron X-ray diffraction contrast tomography (DCT). DCT was used to map the 3D grain arrangement in a polycrystal. This was the basis of a microstructurally faithful mesh for crystal plasticity finite element modelling (CPFEM). The sample was then monitored by DCT during incremental uniaxial compression. Changes in the diffracted spots during deformation were interpreted in terms of crystal re-orientation and orientation spread within grains. Reorientation within grains of  $\sim \pm 1^\circ$  has been observed after 1.2% compressive strain and alongside considerable grain-to-grain variation in reorientation relative to that expected according to simple crystal plasticity models. The CPFEM results showed similar grain-to-grain variations, indicating that the local geometry is important in determining the level of heterogeneity in deformation at this scale. However, on a grain-to-grain basis, agreement is relatively poor. Possible reasons for the observed differences are discussed.

### ***4.3.1 Introduction***

Plastic deformation in polycrystalline materials is heterogeneous at the microstructural scale. It has been suggested that strain localisation at this scale is important in determining the fundamental processes responsible for failure in fatigue [1] and environmental assisted cracking [2]. In some cases large local strains can help relax local stresses (e.g. favourable slip near grain boundaries) preventing damage, whereas in other cases heterogeneous deformation can lead to stress concentrations and even damage nucleation [3]. There is therefore a need to understand and model the deformation of metals at the microstructural scale.

When deformed in isolation, the mechanical behavior of a grain is simply related to its orientation, but in a polycrystal the deformation is further influenced by its shape, size, and the constraint of neighboring grains. As a consequence, it is not possible to compare the results from deformation models to results from experiments without a complete description of the microstructure. Consequently, while surface techniques such as electron back scattered diffraction (EBSD) can provide spatially resolved measurements of lattice rotation during straining [2], they cannot be directly compared to results from polycrystalline deformation models such as Crystal Plasticity Finite Element Models (CPFEM) [4] because there is no information regarding sub-surface grains before deformation. The only way to obtain this information is by destructive sectioning [5], which of course precludes further deformation.

Synchrotron X-ray diffraction makes it possible to study individual grains in the bulk [6]. Diffraction Contrast Tomography (DCT) has recently become established as a technique for mapping polycrystalline microstructures in 3D [7, 8]. Since DCT is non-destructive, diffraction measurements during deformation are possible. We have used DCT to fully map the grain geometries and orientations of an aluminium sample as a function of deformation. This has enabled us to build a microstructurally-faithful crystal plasticity model and to compare its deformation directly with experimental 3D

observations. To the best of our knowledge, this is the first side-by-side experiment vs model comparison for a real 3D microstructure that includes a full description of the local neighbourhoods.

### ***4.3.2 Material & Experimental Methods***

**Material:** We have studied a high purity aluminium (0.1% Mg) sample because of its low elastic anisotropy, almost perfect plasticity and high stacking fault energy (SFE). Traditionally, texture has been poorly captured by CPFEMs for low SFE FCC metals [9], in part due to the occurrence of twinning which is difficult to account for. Moreover, in high SFE metals obstacles to dislocations can be readily by-passed, in line with the idealised behaviour assumed by CPFEM.

**Diffraction Contrast Tomography:** The experimental arrangement is similar to that used for absorption contrast tomography. The sample is illuminated by a parallel, monochromatic x-ray beam. A high resolution 2D detector placed close behind the sample records simultaneously radiographs (projections) of the sample and diffraction spots arising from grains oriented for Bragg diffraction. During rotation of the sample through 360°, many diffraction spots are observed from each grain. Diffraction spots are assigned to grains according to a range of geometrical criteria and the grain orientations reconstructed from the diffraction events. Grain shapes are reconstructed from the diffraction spots using a 3D ART algorithm [10]. More details about the DCT technique can be found elsewhere [11, 12].

A material comprising perfect grains would give diffraction spots that are spread over only 1-2 projections. However, distortion of the crystal lattice means diffraction spots arising from a grain smear out over many successive projections (scanning angle,  $\theta$ ). We refer to these 3D objects as “diffraction blobs”. Their spread in  $\theta$  can be used to give a measure of the misorientation spread within a grain [6]. Each blob can be summed in the two detector directions resulting in a profile of intensity as a function of  $\theta$ . The

profile can then be fit using a Gaussian function. The observations are corrected for the Lorentz factor (blobs with a scattering vector that is close to the rotation axis spread over more images). After this correction, the average angular blob spread gives a scalar measure of the grain mosaicity [6]. Each grain comprises many diffraction blobs. To get a single value representative of the grain, we have averaged the blob values of the middle 50%. This discards outliers, reducing the effect of bad data points. Since the grains for the undeformed sample showed distortion (probably due to residual strain during grain growth), the blob values have been normalized by their initial value. During deformation the intensity within a blob does not spread out uniformly, but instead sub-structures are often observed within a blob. We have used an algorithm that estimates the misorientation as a function of position within a grain based on the observed diffraction blobs [13]. The algorithm can consider both the full elastic strain tensor and the rotation at each point. In this measurement, because of the low yield stress the elastic strain was neglected, and only the three components of rotation determined.

DCT scans of the ( $\varnothing$  1 mm x 1.5 mm) cylindrical sample in its undeformed state revealed the grain size to be around 160  $\mu\text{m}$  (Fig.1). As shown in Figure 2, the sample has a significant  $\langle 100 \rangle$  texture. Grain distortion may mean that the DCT algorithms may fail to identify certain grains in later deformation steps. In this work, only grains whose orientations are available in all loading steps have been considered. Unfortunately it was not possible to measure the precise compressive strains at which DCT was carried out. Consequently, we have averaged the known angle of the average grain rotations for the two loaded steps ( $0.43^\circ$  and  $1.30^\circ$ ). We then calculated from the model the strains at which these average grain rotations are achieved (1.2% and 4.4%) which accord well with the loads applied.

**CPFEM Model:** The sample reconstructed by DCT had  $284 \times 284 \times 176$  voxels. This volume was imported into Amira™ to reconstruct the grain boundaries. The number of these surfaces was 2,067,409. Since this would require too many elements for CPFEM computation, the surface geometry was simplified to 9,994 surfaces. These faces were

used to create the grains in ABAQUS software (using 3D10M elements) via a Python script [14]. Each grain was linked to its neighbours by merging the nodes. The total number of grains, elements, nodes and Gauss points of the model were 117; 31,490; 93,699 and 125,960 respectively (Figure 1).

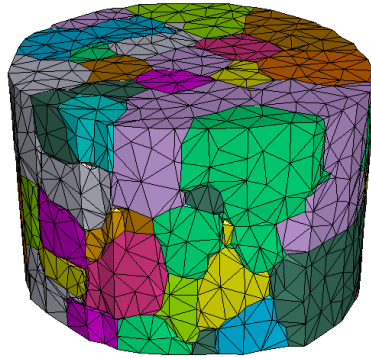


**Figure 1. Mesh built from 3D grains measured by DCT on 1mm diameter sample.**

The base of the sample was constrained only in the loading direction and a compressive displacement applied to nodes on the opposite face. A UMAT subroutine [15] has been implemented in ABAQUS to simulate the behaviour of each grain. This subroutine assumes elasto visco-plasticity where plasticity is treated uniquely via slip [16], [17]. We assume isotropic hardening which is to say that flow on one slip system causes the same hardening on all slip systems. The UMAT parameters used in Table 1 were used to adjust the macroscopic stress-strain curve of the model to that of the experiment.

**Table 1. UMAT parameters used in the present work**

$C_{11}$ (GPa)	$C_{12}$ (GPa)	$C_{44}$ (GPa)	$n$	$\dot{\epsilon}$	$h_0$ (MPa)	$\tau_s$ (MPa)	$\tau_0$ (MPa)
108.2	62.16	28.3	55	0.001	260	18	9.6

Average grain rotations were calculated using quaternion algebra [18]. We have used the Grain Orientation Spread (GOS) to quantify the average misorientation within a grain, enabling comparison with experimental results. GOS is defined as the arithmetic mean of the minimum misorientation angles of local points when the reference is taken as the average orientation of the grain [19]. Finally, we have used quaternions to

compute local misorientation angles from the grain average orientation about each axis [20] for direct comparison with experiment.

### 4.3.3 Results and discussion

**Grain Rotations:** The crystal directions parallel to the compression axis for the CPFEM model and experiment are presented in Figure 2. In aluminium it is well known that a  $\langle 110 \rangle$  fibre texture develops following compression [21]. Further, rotation of the crystal directions away from  $\langle 100 \rangle$  and  $\langle 111 \rangle$  poles is usually reported while rotations near  $\langle 114 \rangle$  are hindered. These trends, marked by arrows in Fig 2, are weakly evident in the DCT data. Both model and measurements show grain-to-grain deviations from the Taylor model predictions, which assume homogenous plastic deformation due to grain-to-grain interactions. Although the predicted rotations have the correct magnitude, the grain trajectories only agree for some grains being marginally better near the  $\langle 100 \rangle$  pole than elsewhere. The overall lack of correlation grain-for-grain may be attributable to microstructural features that are neglected by the model. For example, deformation bands [23] and dislocation boundaries aligned with one of the  $\{111\}$  planes [24] have been reported in lightly deformed aluminum crystals.

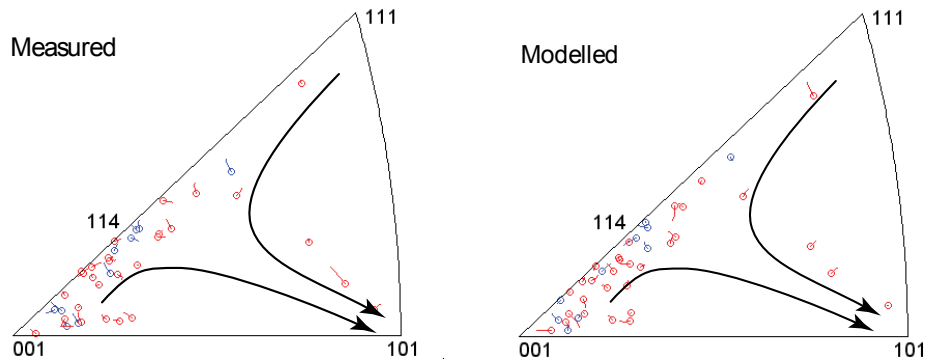


**Figure 2. The crystal directions parallel to the compression axis after 0, 1.2% and 4.4% strain; a) measured by DCT, b) modelled by CPFEM. The circles represent 4.4% strain. Surface contacting grains (red) and bulk grains (blue). Only those grains where data is available for all three loading steps are shown.**

**Orientation spread:** GOS results for each grain from CPFEM correlate with the average equivalent plastic strain and the accumulated slip (not shown here). The GOS and the experimental blob spread, quantified as the normalized FWHM of the Gaussian fit are weakly correlated. That reasonable correlation is seen when they are normalized by the volume of the grain (Figure 3), suggesting that spread increases with grain size for both model and measurement. In this respect mosaicity has been reported elsewhere to strongly correlate with the grain area in 2D measurements [18, 22]. Further this correlation of mosaicity with grain volume has also been observed in steels heated above the austenite transition temperature, which might be expected to be in an undeformed state [20]. Unsurprisingly spread increases with plastic strain. For both loading steps bulk grains show a higher spread than surface grains (GOS and normalized FWHM), probably due to the higher constraints imposed by their neighbors.

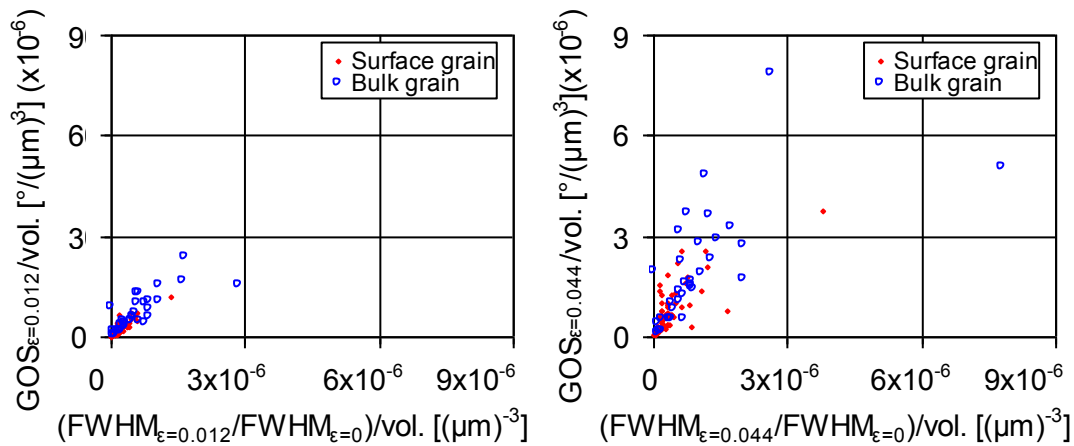


**Figure 3. Normalized diffraction blob spread (FWHM of the Gaussian fit) measured by DCT versus Grain Orientation Spread (GOS) by CPFEM as loaded in compression to; a) 1.2% strain, b) 4.4% strain**

**Local Rotations:** The intragranular rotations mapped over a cross-section through the sample at about 1/3 of the cylinder height for the experiment and model are presented in Figure 4. These results represent the intermediate loading step (1.2% strain), since the less deformed diffracted spots are easier to process. Again, some intragranular

rotations were measured prior to loading. In Figure 4, we have subtracted these from the final rotations.

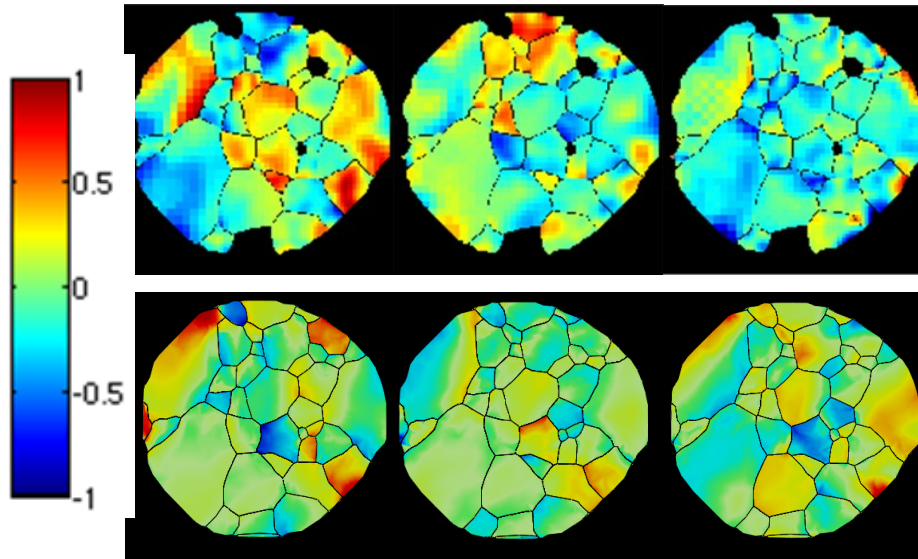


**Figure 4. Intragranular rotations (°) about X, Y and Z axes; above) based on the observed diffraction spots, below) calculated from CPFEM after 1.2% strain**

The experimental results show substantial grain-to-grain variation in both the magnitudes of the local rotations and in the local, intragranular gradients of deformation. The spreads of the local lattice rotations predicted by the model agrees well with those observed, but the predicted intragranular variations are smoother and lower in magnitude. Since the model is micro structurally faithful, one might expect to see good agreement on a grain-to-grain basis. By contrast, we find poor relatively poor agreement. Interestingly, the patterns of lattice rotation often match well with those observed but are either the wrong sign or magnitude.

There are several possible reasons for this lack of agreement. The analysis of the experimental diffraction data ignores elastic distortions, which might be a significant source of error, since elastic strains can also cause changes in contrast. Although the alloy is extremely soft, the low elastic stiffness of aluminium means that elastic strains will be large even if stresses are low. The procedure is now being extended to include elastic distortion effects. The material model used is also very simple and it is likely

that it cannot capture well the results of multiple slip and the associated recovery that is known to occur in aluminium [19, 20]. It is also not clear whether the mesh density is sufficiently high to capture local variations faithfully. A sensitivity study on mesh density will shed some light on this issue. Furthermore, the boundary conditions employed in the model are likely to be somewhat different to those in the experiment. It is indeed very difficult to deform such a small sample in an idealised manner.

#### ***4.3.4 Conclusions***

DCT has been used both to map the 3D arrangement in a polycrystal and to study the evolution of crystal re-orientation and orientation spread within grains with compressive deformation. A CPFE model has been constructed with the same initial polycrystal arrangement. In both cases reorientation of the grains by  $\sim \pm 1^\circ$  has been observed after 1.2% strain. In both cases, considerable grain-to-grain variation in reorientation under compressive deformation has been observed relative to the overall expected reorientation (Fig.2). This is presumably due in part to the effect of local neighbours. Some grains show good agreement between model and experiments, others much less so. This may be due to intragranular heterogeneities in deformation not accounted for in the model, or to oversimplifications in the analysis of the diffracted data. Nevertheless, this work shows that DCT can provide unique data for comparison with crystal plasticity deformation models. Although these initial results allow only limited insight into the effectiveness of the models, it is clear that the methodology has significant promise and we believe it will play an important role in the validation and development of future crystal plasticity models.

#### ***4.3.5 Acknowledgements***

The authors thank Alexei Bytchkov (instrument scientist in ID11, ESRF) for his support.

### 4.3.6 References associated to publication 3

- [1] Z. Zhang, Z. Wang, *Prog. Mater. Sci.*, 53, (7) (2008) 1027-1099.
- [2] T. Couvant et al., “Development of understanding of the interaction between localized deformation and SCC of austenitic stainless steels exposed to primary PWR environment,”, in *14th International Conference on Environmental Degradation of Materials in Nuclear Power System*, Virginia Beach, Virginia, USA, 2009.
- [3] T. R. Bieler et al., *Int. J. of Plas.*, 25, (9) (2009) 1655-1683.
- [4] J. Q. da Fonseca et al., *Materials Science and Engineering: A*, 437, (1) (2006) 26-32.
- [5] A. Musienko et al., *Acta Mater.*, 55, (12) (2007) 4121-4136.
- [6] H. F. Poulsen et al., *Acta Mater.*, 51, (13) (2003) 3821-3830.
- [7] A. King et al., *Science*, 321, (5887) (2008) 382-385.
- [8] M. Herbig et al., *Acta Mater.*, 59, (2) (2011) 590 - 601.
- [9] P. Van Houtte, *Acta Metal.*, 26, (4) (1978) 591 - 604.
- [10] R. Gordon, R. Bender, G. T. Herman, *J. Theoretical Biology*, 29, (3) (1970) 471-481.
- [11] G. Johnson et al., *J. of App. Crystall.*, 41, (2) (2008) 310-318.
- [12] W. Ludwig et al., *Review of Scientific Instruments*, 80, (3) (2009).033905
- [13] A. King et al., “Grain mapping by diffraction contrast tomography: extending the technique to sub-grain information”, in *Proc. of the 31st Riso Int. Symp. on Materials Science*, Technical University of Denmark, 2010.
- [14] I. Simonovski, L. Cizelj, *Computational Materials Science*, 50, (5) (2011) 1606-1618.
- [15] Y. Huang, *A user-material subroutine incorporating single crystal plasticity in the ABAQUS finite element program, Mech Report178*,. Division of Engineering and Applied Sciences, Harvard University, Cambridge, Massachusetts, 1991.
- [16] R. Hill, J. R. Rice, *J. of the Mech. and Phy. of Solids*, 20, (6) (1972) 401-413.
- [17] D. Peirce, R. J. Asaro, A. Needleman, *Acta Metall.*, 31, (12) (1983) 1951-1976.
- [18] W. He, W. Ma, W. Pantleon, *Materials Science and Engineering A*, 494, (1) (2008) 21-27.

- [19] A. J. Schwartz, M. Kumar, *Electron Backscatter Diffraction in Materials Science*, Springer, 2009.
- [20] W. Pantleon, *Scr. Mater.*, 58, (11) (2008) 994-997.
- [21] F. J. Humphreys and M. Hatherly, *Recrystallization and related annealing phenomena*, Elsevier, 2004.
- [22] M. Kamaya, A. J. Wilkinson, and J. M. Titchmarsh, *Nuclear Engineering and Design*, 235, (6) (2005) 713 - 725.
- [23] R. W. K. Honeycombe, *The Plastic Deformation of Metals*,. 1984.
- [24] W. Pantleon et al., *Materials Science and Engineering A*, 387 (2004) 339-342.

**END OF PUBLICATION 3**

## 4.4 Publication 4

### **Three-dimensional observation and image-based modelling of thermal strains in polycrystalline alumina**

D. Gonzalez, A. King, M. Mostafavi, P. Reischig, S. Rolland du Roscoat, W. Ludwig,  
J. Quinta da Fonseca, P.J. Withers, T.J. Marrow

Publication submitted to Acta Materialia on the 30/05/2012

In this publication the idea of the comparison between the DCT data and the 3D model was proposed and supervised by James Marrow. The corresponding experimental results were performed by a working team in ESRF led by Andrew King. The digital volume correlation (DVC) studies were carried out by Mahamoud Mostafavi. The Python scripts used to create the geometry (.sat files) from the DCT data (binary file) were programmed by I. Simonovski whereas the rest of the pre-processing (Amira simplification and correction, Abaqus model import, element assignment, material properties calibration, real orientation assignment, boundary conditions...etc) and all the post-processing was done by myself.

**BEGIN OF PUBLICATION 4**

## **Three-dimensional observation and image-based modelling of thermal strains in polycrystalline alumina**

**Authors**, D. Gonzalez<sup>1</sup>, A. King<sup>2</sup>, M. Mostafavi<sup>3</sup>, P. Reischig<sup>2</sup>, S. Rolland du Roscoat<sup>2,4</sup>, W. Ludwig<sup>5</sup>,

J. Quinta da Fonseca<sup>1</sup>, P.J. Withers<sup>1</sup>, T.J. Marrow<sup>3</sup>

**Affiliations**

<sup>1</sup> School of Materials, University of Manchester, Grosvenor St., Manchester, M1 7HS, UK

<sup>2</sup> ESRF, Polygone Scientifique Louis Néel, 6 rue Jules Horowitz, Grenoble, 38000, France

<sup>3</sup> Department of Materials, University of Oxford, Parks Rd, OX1 3PH, UK

<sup>4</sup>Laboratoire 3S-R, Université Joseph Fourier, Grenoble, 38041, France

<sup>5</sup> GEMPPM-MATEIS, INSA de Lyon, France

**Keywords:** Alumina, Diffraction Contrast Tomography, Synchrotron X-ray Residual Stress, Image-based modelling

### **Abstract**

Diffraction Contrast Tomography (DCT) with synchrotron X-rays was used to map the three-dimensional microstructure of alumina; each grain boundary of this coarse grain size ceramic was characterised by its physical orientation and the crystal misorientation of the adjacent grains. The microstructure of alumina was sufficiently well described by DCT to produce a microstructurally representative image-based finite element model comprising approximately 400 grains. Grain boundary cohesive elements were used to calculate the local thermal stresses acting on each grain boundary arising from the crystal anisotropy. The bulk properties of the model were tested by digital volume correlation analysis of computed tomography (CT) images of the elastic deformation of the sample under load; Poisson's ratio was obtained. The model simulations showed the average intergranular stress to be influenced by the

orientation of the grain boundary plane relative to the basal planes of the adjacent grains. Boundaries to which at least one of the basal planes was closely aligned tended to develop higher tensile stress; these boundaries were predicted to have a tendency for intergranular fracture. The predicted effect of crystal lattice strains and rotations on diffraction, due to the modelled thermal stresses, showed general agreement with the observed X-ray diffraction images of individual grains.

#### ***4.4.1 Introduction***

The physical properties of polycrystalline materials depend on the aggregate behaviour of their constituent crystal grains, and may be affected strongly by their interfaces. Certain grain boundaries (GB) in metals are particularly resistant to stress corrosion cracking [1], for instance. The strength of polycrystalline ceramics such as alumina may be affected by intergranular cracks, which are caused by residual stresses arising from the crystalline anisotropy of thermal expansion and elasticity [2]. The three-dimensional distribution of grain boundary structures and the grain morphology determine the residual stresses, and thus influence the tendency for intergranular fracture. As the underlying deformation is essentially elastic, such systems are well suited to numerical simulation of the interactions between individual crystals. The purpose of such models is to guide the optimisation of microstructure; in the case of polycrystalline alumina the aim would be to control the proportion of boundaries that develop significant tensile internal stresses, ultimately improving strength.

In single-phase non-cubic crystal ceramics, intergranular microcracks may occur on cooling from the fabrication temperature due to the strains of thermal expansion and elastic anisotropy [3]. Grain-to-grain misorientation has been proposed as a means of controlling grain boundary stress [4], supported by observations of cracks at such boundaries in a coarse alumina [2]. Commonly, grain-to-grain misorientations are defined using the coincidence site lattice (CSL) description, but this neglects the grain boundary plane. A more complete description of the boundary, which is important in determining its structure and energy, involves five degrees of freedom; three to define the grain-to-grain misorientation and two to define the grain boundary plane [5, 6].

Direct measurements of intergranular crack nuclei in a fine grained alumina, identified by in-situ measurements of crack opening displacements under load using digital image correlation [7], showed that these were associated with grain boundaries that were aligned close to basal plane. A simple model was proposed that predicted higher tensile stresses developed for larger grains having grain boundary facets close to the basal plane; grain-to-grain misorientation and boundary facet orientation were both found to be important.

The grain boundary plane populations may be altered in some materials [8] by appropriate processing, usually referred to as grain boundary engineering (GBE) [9, 10]; the aim being to maximize the proportion of GB with desirable properties. For example, in austenitic stainless steels, maximising the population of coherent twin boundaries through thermo-mechanical processing may improve intergranular stress corrosion cracking resistance [11]. For ceramics, altering the dopants and sintering temperature can change the grain boundary plane distributions [12]. For instance, additions of silica to alumina sintered at 1400°C increased the abundance of basal plane faceted GBs [13]. Such processing might be used to improve the strength of ceramics, but guidance is needed from modelling on the desirable GB population characteristics, and also the achievable effects.

A number of different models using abstract representations of the microstructure have been developed. Two-dimensional approaches (e.g. [14-16]) have described approximately the crack path, the sensitivity to stress state and the statistics of failure, for example. More realistic three-dimensional (3D) simulations of polycrystalline assemblages have, until lately, been impractical due to computing limitations. However, progress has been made with constitutive models [17], and recent simulations used 3D tessellation to approach more realistic microstructures [18]. Image-based modelling (e.g. [19-21]) is an alternative approach in which a 3D reconstruction of the actual microstructure including crystallographic orientation provides the input for 3D Finite Element model simulations. Such data can be obtained by serial sectioning (for instance by incremental focussed ion beam milling and electron backscatter diffraction

analysis [22-27]), but this is destructive. Serial sectioning only provides surface information on residual stress or strain states, which may not be representative of the 3D distribution that existed prior to sectioning.

Experimental measurements are essential to validate and refine modelling approaches. To date, this has generally employed bulk measurements derived from the average behaviour of the microstructure, or by extracting the average response of particular grain families by neutron or X-ray diffraction [28-31]. However, techniques are now available for non-destructive three-dimensional local characterisation of microstructure [32-35] that can be used to develop new models and help to validate their outputs. Recently, the internal strains in grains of metals [36] and ferroelectric ceramics [37] have been characterised by three-dimensional X-ray diffraction (3DXRD). Here, the related technique of diffraction contrast tomography (DCT) [34] has been applied to polycrystalline alumina. DCT allows grain shapes and orientations in three-dimensional volumes of over one thousand grains to be characterised, provided the sample fulfils certain conditions on grain size, mosaicity and texture [38-40]. It has the advantage of a simple experimental set-up and speed of data acquisition compared to other techniques, and can be easily combined with computed tomography to study simultaneously the 3D development of damage [39].

In this paper, DCT using synchrotron X-rays has been employed to map the three-dimensional microstructure of polycrystalline alumina, a coarse grain size ceramic, in order to fully characterise each grain boundary. The local thermal stresses from crystal anisotropy were calculated using an image-based finite element model, generated from the three-dimensional data. The bulk properties of the model were tested by measurement of the bulk elastic properties of the sample, using digital volume correlation analysis of computed tomography (CT) datasets. The crystal lattice strains and rotations obtained by the model are tested by comparison of the observed diffraction from individual grains with predicted diffraction images. The aims were to determine whether the three-dimensional microstructure was sufficiently well described to produce a microstructural-representative model of a polycrystalline

aggregate, and to obtain guidance on the nature of undesirable grain boundary structures in polycrystalline alumina. Image-based FE models are computationally intensive, but simulated large scale approximations of microstructure (e.g. Voronoi [21]) may use the insights obtained here to investigate the beneficial effects of alterations in the grain boundary population on the frequency and distribution of cracking, and hence component reliability.

#### **4.4.2 Experimental Details**

The principles of DCT have been presented elsewhere [34, 40], and only a brief description is provided here. The experimental arrangement is similar to that of absorption contrast tomography, with the sample illuminated by a parallel, monochromatic X-ray beam. A high-resolution 2D detector, placed close behind the sample, records radiographs and also the projected diffraction spots arising from grains oriented to satisfy the Bragg diffraction. During the 360° sample rotation, multiple diffraction images are observed from all grains. Post-processing assigns the diffraction spots to grains according to a range of geometrical criteria. The grain orientations and positions within the sample are inferred from the geometry of the diffraction events, and 3D grain shapes are reconstructed using the diffraction images as grain projections. Due to overlap of diffraction spots, DCT is limited currently to samples containing less than a few thousand grains, so polycrystalline alumina with a nominal grain size of 80 to 100 µm was used in this work. This was the same material as studied in reference [2], prepared using Magnesia doped (500 ppm) Al<sub>2</sub>O<sub>3</sub> powder (Sumitomo 23AKP 3000, 99.995% pure, particle size 0.6 mm, Tokyo, Japan).

A rectangular sample (4 mm × 0.7 mm × 0.7 mm) was examined on beamline ID11 at the European Synchrotron Radiation Facility (ESRF) (Figure 1). A monochromatic beam ( $E = 40$  keV), produced by a Laue-Laue monochromator (bandwidth  $\Delta E/E \sim 10^{-3}$ ), illuminated the sample. This provided sufficient flux for a counting time of one second per image, and a complete DCT scan with continuous rotation in 0.05° increments was recorded in less than 2.5 hours. The selected optics gave an effective projected image pixel size of 1.8 µm. The minimum sample to detector distance, limited by the

diameter of the miniature loading rig, was approximately 8 mm. Hence with the maximum diffraction angle  $2\theta$  of between  $13^\circ$  and  $18^\circ$ , the first 6 or 7 families of diffracting planes were sampled, giving around 25 diffraction images per grain. This was sufficient for the algebraic reconstruction of 3D grain shape. After mapping of a volume of the unloaded sample by DCT, a series of absorption tomograms were recorded at increasing loads (55, 80, 120, 170 N) in order to observe the development of intergranular cracking. The sample failed catastrophically under load, shortly after the scan at 170 N.

The reconstructed absorption contrast CT datasets (each  $500 \times 500 \times 200$  voxels; a voxel is the 3D analogue of a pixel) were analysed by Digital Volume Correlation (DVC), using the LA Vision Davis 8.0 software [41]. The initial correlating patch size was  $128 \times 128 \times 128$  voxels, followed by  $64 \times 64 \times 64$  voxels, each with 50% overlap and 3 passes. The objective of this analysis was to measure the bulk deformation of the specimen, and determine any misalignment of loading. The relatively large patch size was necessary due to the paucity of contrast-inducing features in the microstructure.

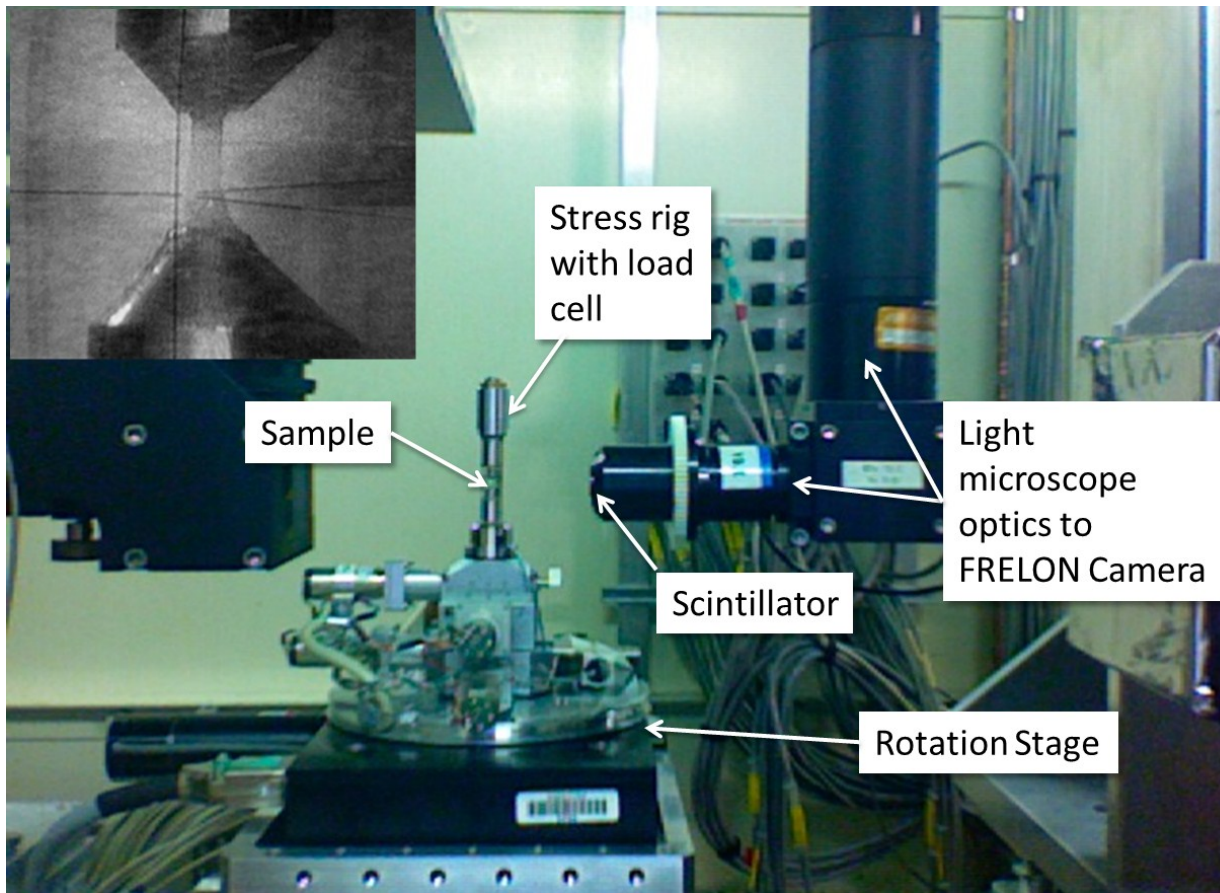


**Figure 1:** Experimental arrangement for Diffraction Contrast Tomography and Computed Tomography on beam line ID11 at ESRF. The compressive loading cell is positioned on the rotation stage. The sample to camera distance was reduced to 8 mm for the actual observation. The inset optical image (top left) shows the sample observed between the anvils of the compressive loading stage.

### ***4.4.3 Experimental Results***

#### **4.4.3.1 Three-Dimensional Reconstruction of Microstructure**

A typical projected diffraction image is shown in Figure 2. Most spots appear in one or two successive images as the sample is rotated, so the angular spread is up to 0.1 degrees. This is of the order expected when the Lorentz factor (i.e. the expected effect of spread in wavelength and lattice parameter) is taken into account. One spot from a large grain is highlighted in Figure 2; this grain is oriented such that the scattering vector is close to the sample rotation axis, and this exaggerates the angular spread in the diffraction images. Its variation in appearance while rotated through  $0.75^\circ$  shows

its edges and centre differently satisfy the diffracting condition. Some degree of angular spread within grains is generally detected in DCT of metallic samples [37], arising from misorientation gradients due to dislocations (i.e. mosaicity). Plastic deformation is not anticipated during the processing of the alumina ceramic, and the observed spreads may be due to a combination of the Lorentz factor and lattice distortions from thermal stresses. Summing the consecutive diffraction spot images minimised the effect of this angular spread on the process of grain shape reconstruction.

A 2D slice through the reconstructed 3D grain volume is shown in Figure 3a, overlaid with the absorption contrast tomographic reconstruction, showing the larger intergranular pores. The sample was slightly larger than the beam size, so both reconstructions show the region of interest of the sample that remained within the field of view during sample rotation. Figure 3b shows the results of post-processing to form a space-filling structure by 3D morphological dilation of the reconstructed grains. The DCT reconstruction process tends to systematically underestimate the size of reconstructed grains, since the segmentation of diffraction spots in the process tends to clip their edges and so reduce the reconstructed grain size. To produce a space filling map, a morphological dilatation is required. The maximum dilation applied was 18  $\mu\text{m}$ , with less being sufficient in many regions. The dilation process consists of eliminating the gap between two parallel grain surfaces, and does not significantly alter the reconstructed plane and grain shapes. A small error ( $\sim 3 \mu\text{m}$ ) has been found in comparisons of a similarly dilated microstructure with a grain boundaries decorated by a second precipitated phase in a beta titanium alloy [40]. The pores generally coincide with the identified grain boundary triple points, which is consistent with the expected intergranular nature of porosity [2]. The three-dimensional visualization of the central volume of the sample in Figure 3c contains approximately 400 grains. The effect of compressive load is illustrated in Figure 4. The development of intergranular damage, observed at 170 N, correlates well with the grain boundaries detected by DCT. These observations support the reliability of the reconstructed three-dimensional grain shapes [40].

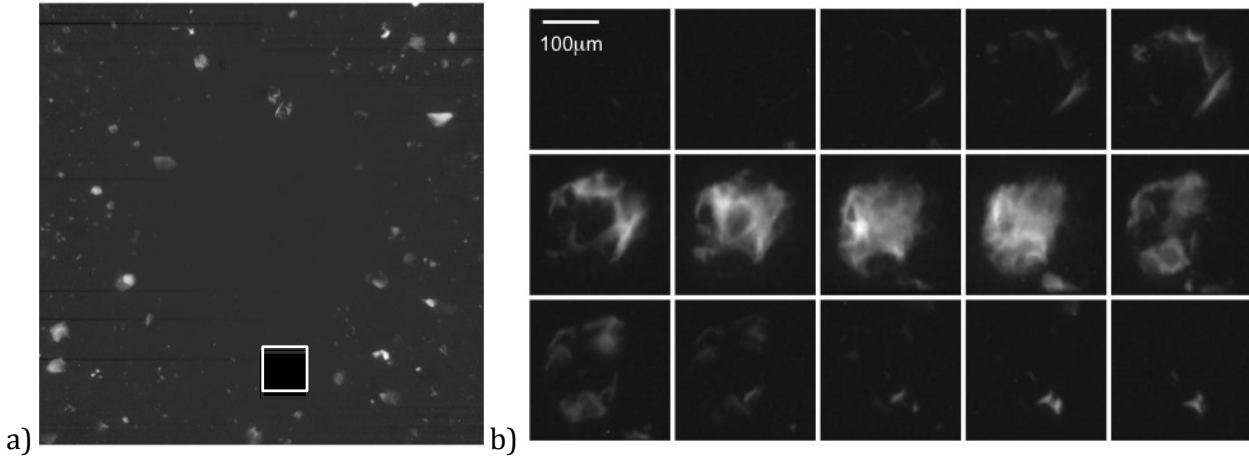


**Figure 2: Projection diffraction images showing, a) diffraction spots obtained for the sample, after background correction and removal of the central transmitted image, b) the variation in appearance of the diffraction spot shown boxed in (a) at rotation intervals of  $0.05^\circ$  (top left to bottom right)**

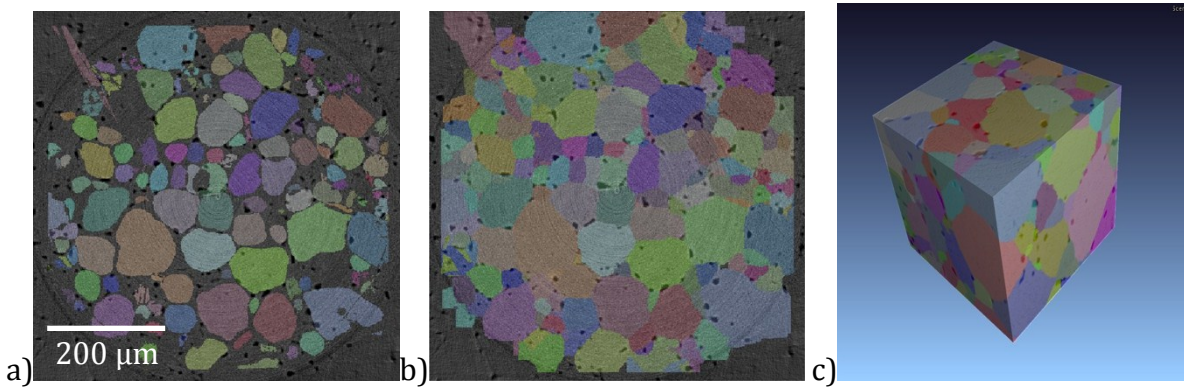


**Figure 3: Diffraction contrast tomography; a) reconstructed 2D slice showing initial reconstructed grains, superposed on CT image of microstructure, b) the same 2D slice after 3D grain dilation c) 3D volume of the microstructure, cropped from the centre of the sample, after grain dilation. DCT and CT images are superposed to show the pores.**

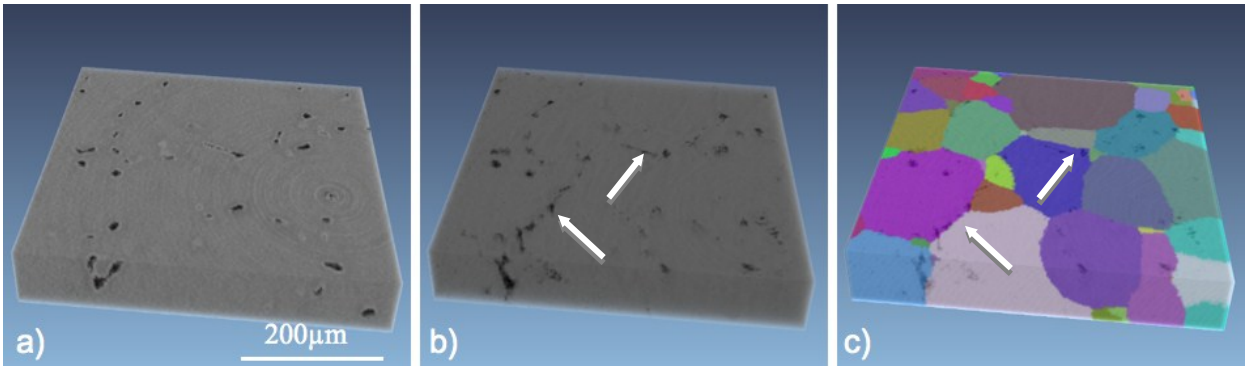


**Figure 4:** a) CT image of a region of interest before loading, b) the same volume at a load of 170 N (~350 MPa), c) comparison of the microstructure obtained by DCT and the CT image at 170 N. (picture from reference [42]). Intergranular damage is indicated by arrows in (b) and (c).

#### 4.4.3.2 Grain Boundary Plane Structures

The full five-parameter description of GB structure [43] can be inferred from the DCT observations [39]. The simplest analysis fits a plane to the interface between each pair of adjoining grains. The plane normal is defined relative to the crystal axes of the adjacent grains; hence every interface produces two plane normals in crystallographic coordinates. These normals can be plotted using a stereographic projection to show the distribution of grain boundary planes referred to the crystallographic axes. Figure 5(a) shows the frequency of occurrence of GB planes. The total number of grains analysed is not very high (886), and confidence in the determination of the GB plane by DCT is estimated to be of the order of  $5^\circ$  to  $10^\circ$  [39], so some care should be taken in the interpretation of these plots. Figure 5(b) shows the same data, weighted according to grain boundary area. The application of the R-3c symmetry to the data in figure 5(c) aids the visual detection of more frequent sets of planes; its effect is analogous to plotting the full dataset within a standard triangle of the stereographic projection. The distributions in Figure 5 are scaled relative to random distribution of poles; symmetry has been applied to a random distribution in Figure 5(c), leading to a non-uniform background against which the data are scaled.

In an annealed microstructure, the GB facets are expected to be those with low energy. Transmission electron microscopy observations of facet planes from pores within sapphire ( $\alpha$ -alumina) crystals [44] show these to be the low energy basal (C) (0001),

rhombohedral (R)  $\{01\bar{1}2\}$ , prismatic (A)  $\{11\bar{2}0\}$ , pyramidal (P)  $\{11\bar{2}3\}$ , and structural rhombohedral (S)  $\{01\bar{1}1\}$  planes. The prismatic (M)  $\{01\bar{1}0\}$  is also a low energy plane, but has not been observed to form facets [44]. The locations of these poles are shown in Figure 5, indicating some prevalence for the basal (C), rhombohedral (R), and structural rhombohedral (S) planes in the measured GB plane distribution. The paucity of GBs close to the prismatic (M) planes is quite noticeable, although the data do not show any clear preference for pyramidal (P) planes. The observation of characteristic poles is not sensitive to weighting by GB area, nor selection of the larger boundaries. Consequently, the grain shapes obtained by DCT are broadly consistent with the expected planes for faceted grains with the alumina crystal structure.

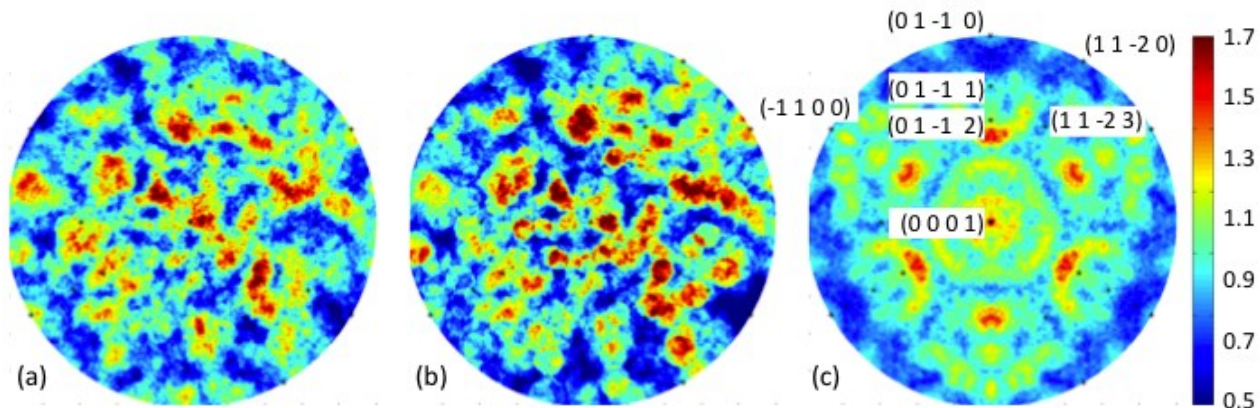


**Figure 5: Stereographic projection of the distribution of poles (relative to a random distribution) (left) for all the GB planes, (middle) weighted by the area of the GB plane and (right) weighted by the area of the GB plane with trigonal symmetry applied R-3c.**

#### 4.4.3.3 Digital Volume Correlation

The DVC analysis was performed primarily to check the uniformity of compressive loading. It used the reconstructed CT volume obtained at a compressive load of 55 N ( $\sim 110$  MPa) as a reference; this was correlated with the CT volumes at loads of 80 N and 120 N ( $\sim 160$  and  $\sim 245$  MPa), mapping their relative displacements. Correlation with the volume at 170 N ( $\sim 350$  MPa) was poor, with a high level of noise. Strains may be obtained by the local gradients of displacement, to extract a distribution of local

strain values. Alternatively, the net displacements across the dimensions of the sample can be used to obtain the net strain in the sample, thereby treating it as a strain gauge. The maps of the axial displacement across the imaged volume at its top and bottom (Figure 6a and b) show that the sample tilted as the load was applied. The displacement measurement error is approximately  $5.2 \times 10^{-2} \mu\text{m}$  (i.e.  $\sim 0.03$  voxels); this was estimated as the standard error between the measured values and a second order 3D polynomial fit to the axial displacements. It is the same value as the expected error in displacement measurement with a good quality image for the analysis window size ( $64 \times 64 \times 64$  voxels) [45]. A map of the net axial strain was obtained from the displacement differences measured across the height (0.36 mm) of the imaged volume (Figure 6c). The calculated strain error, based on the displacement error, is  $0.15 \times 10^{-3}$ . The average strains in the axial and orthogonal directions are given in Table 1, with the derived Poisson's ratio. Young's modulus was obtained by assuming the axial load was applied uniformly across the sample cross-section.

The measured Poisson's ratio, between 0.22 and 0.24, is reasonably close to the expected value of 0.27 [46], indicating that DVC of the CT data measures the sample displacements sufficiently well. The measured Young's modulus does not agree with the expected value of 400 GPa [47], and the deviation from the expected value increases with applied load. The strains in the sample (Figure 6c), which are significant compared to the magnitude of the measurement uncertainty of the net axial strains, show that the sample is flexing due to uneven loading or barrelling. The axial strain to one side of the sample therefore becomes progressively more tensile, by approximately  $0.5$  to  $1 \times 10^{-3}$ , as the compressive load increases from 55 N to 120 N. The deviation between the measured and expected Young's modulus (Table 1) is therefore due to the non-uniform axial stress, which is neglected in its measurement.

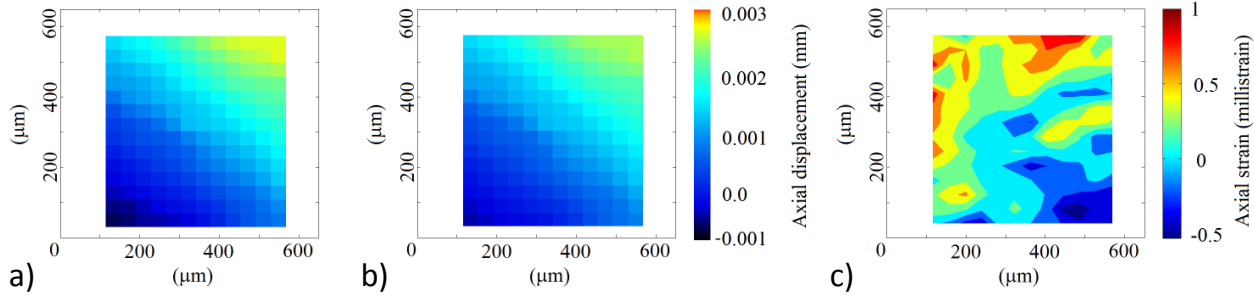


**Figure 6:** DVC analysis of the deformation of the CT volume between -55 and -120 N; a) axial displacements at the top of the volume, b) axial displacements at the bottom of the volume, c) axial strain due to difference between a) and b) over the observed gauge length of 0.36 mm.

**Table 1:** Strains and elastic moduli, obtained by DVC analysis of CT data at 80 and 120 N compressive loads (relative to data at 55 N compressive load). The values are the averages obtained from using displacement vectors with an image analysis patch of 64 voxels with 50% overlap. The uncertainties are the standard deviation.

Relative Compressive Load (N)	Relative Nominal Stress (MPa)	Axial Strain ( $\times 10^{-3}$ )	Orthogonal Strain ( $\times 10^{-3}$ )	Young's Modulus (GPa)	Poisson's ratio
-25	-51	-0.113 $\pm 0.007$	0.025 $\pm 0.003$	464 $\pm 59$	0.23 $\pm 0.04$
-65	-133	-0.270 $\pm 0.011$	0.066 $\pm 0.003$	493 $\pm 40$	0.24 $\pm 0.02$

#### 4.4.4 Imaged-based FEM Model

##### 4.4.4.1 FE Mesh Generation

The procedure for creating a finite element mesh from DCT data for image-based modelling is described in [21], and so only a summary is presented here. The DCT grain shapes and grain orientations were imported into the Amira<sup>13</sup> software package and segmented to reconstruct surfaces that form the grain boundaries (Figure 7a and b). Each voxel in the DCT dataset is labelled with its corresponding grain number; a voxel with label  $n$  is assigned to grain number  $n$ . The total numbers of crystallographic

<sup>13</sup> Amira 5.2.1 <<http://www.amiravis.com/>>

orientations, grains and grain boundaries between adjacent grains (i.e. grain facets) were 886, 1048 and 5725 respectively. Intersection errors were detected and manually repaired by slight adjustments to the corresponding interfaces. A number of separated regions that had the same voxel label were observed; these might be connected regions of the same grain that had been separated by deficiencies in the observations and reconstruction. For simplicity these were treated as separated grains of the same orientation. After segmentation, there were approximately 8,220,000 triangles defining the multifaceted GBs (e.g. Figure 7c). This number is impractical for FEM computation, so was decreased to approximately 275,000 using surface simplification (Figure 7d) (using standard algorithms in the Amira software), before creating the grains in the ABAQUS FE software<sup>14</sup> using a Python script [21] (Figure 7e). The average number of triangles per grain facet was 39. The grains were meshed using solid ABAQUS C3D4 elements [48]. Finally, an assembly of cohesive elements linking the grains was generated in order to be able to extract grain boundary stresses from the model; further details of the cohesive elements are given in section 4.3.

#### 4.4.4.2 Geometrical Distribution of Grains

The statistics for grain volume, number of facets per grain and facet area are summarised in Figure 8. The 162 smallest grains all having fewer than 600 voxels are excluded from the statistics in Figure 8a; these small grains have the same orientation as nearby larger grains, but are unconnected to them, and as noted earlier may be reconstruction artefacts. Grains in contact with the surface of the reconstructed volume (432 in total) were also excluded. The mean values for the remaining 454 grains are approximately 158,000  $\mu\text{m}^3$  per grain, 12.4 facets per grain, and 1140  $\mu\text{m}^2$  per facet. Experimental data in the literature for describing the three-dimensional grain shapes are limited. Mean numbers of facets per grain are reported to be 12.5, 11.8, 12.9, 13.7 and 14 for an Al-Sn alloy, a  $\beta$ -brass, nickel-base superalloy [27], a  $\beta$ -titanium alloy [23] and a stainless steel respectively [6] which are broadly consistent with the 12.4 facets per grain obtained here. For a slowly cooled  $\beta$ -brass ingot [49], the number of facets per grain increased from 8 to 40 as grain size increased from 2 to 12 mm. A

---

<sup>14</sup> Simulia, Abaqus/Standard 6.6-1 <<http://www.simulia.com/>>

similar trend is observed here (Figure 8b), with larger grains having more facets. Previous studies on  $\beta$ -titanium alloy have reported also grains containing up to 40 facets per grain [23]. These comparisons show that the reconstructed grain assembly is consistent with realistic microstructures.

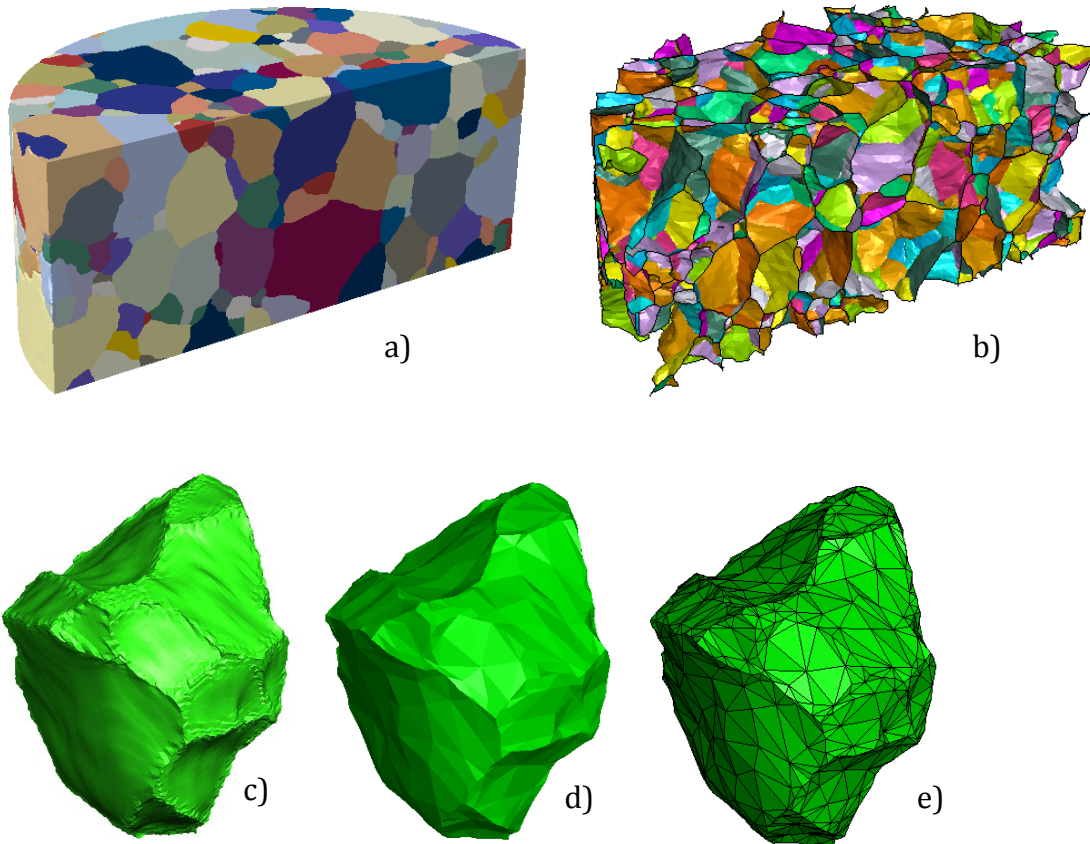
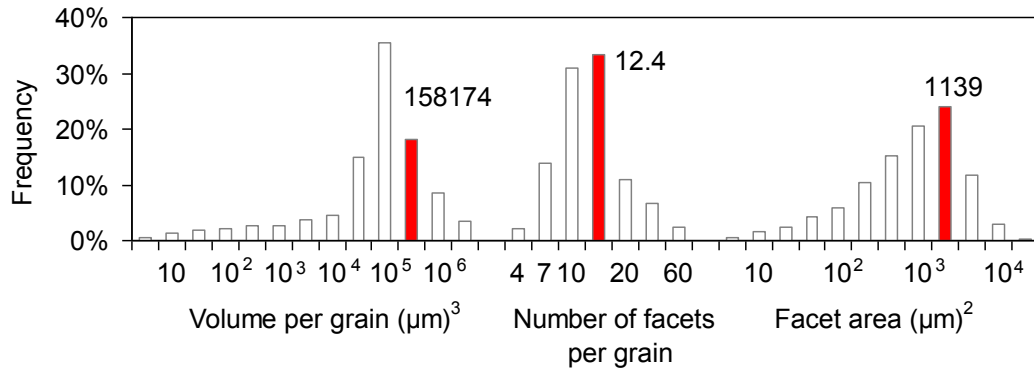
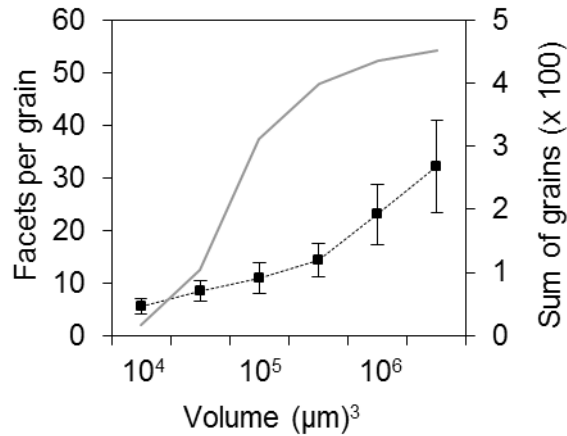


**Figure 7: The finite element model; a) reconstructed grains comprising the polycrystalline aggregate, b) cohesive elements used to link grains. The different grains in a) and different grain boundaries in b) are randomly coloured for clarity. A typical grain showing c) surface before simplification, d) surface after simplification and e) FE mesh (black lines) after surface simplification.**



a)



b)

**Figure 8: Data for the grain assembly in the Finite Element model: a) histograms showing the volume per grain, number of facets and facet area (excluding grains connected to the surface); the mean average values are labelled.), b) the number of facets per grain as a function of grain size; the cumulative number of grains (continuous line) with increasing volume is on the secondary axis.**

#### 4.4.4.3 Modelling of Intergranular Thermal Stresses

A cooling cycle from a stress-free state at 1900°C to room temperature was imposed on the FE model in 10 steps. No mechanical load was applied. Cooling was done incrementally since although the material behaviour is treated as linear elastic, non-linear effects might arise from the contact behaviour of grains. The elastic stiffness constants were:  $C_{11}=496.8$  GPa,  $C_{12}=163.6$  GPa,  $C_{13}=110.9$  GPa,  $C_{33}=498.1$  GPa and

$C_{44} = 147.4$  GPa [47], as in reference [2]. Although alumina is trigonal (space group R-3c), hexagonal symmetry was assumed by setting to zero the small component of the stiffness matrix  $C_{14} = -23.5$  MPa. The single crystal thermal expansion coefficients were  $\alpha_{11} = \alpha_{22} = 8.62 \times 10^{-6} \text{ K}^{-1}$  and  $\alpha_{33} = 9.38 \times 10^{-6} \text{ K}^{-1}$  [50]. The thermal and elastic properties were assumed to be temperature independent. Gauss points, placed directly at the GB through the use of cohesive elements [48], were used to find the interface stresses. For this ABAQUS COH3D6 elements having 6 nodes and 3 Gauss points were used. At each Gauss point, stress and strain are related through the stiffness matrix  $\mathbf{K}$  via linear elasticity. The assumed stress vector contains only one normal and two shear components. Elastic isotropy was assumed at the grain boundaries;  $\mathbf{K}$  is therefore a diagonal  $3 \times 3$  matrix. The numbers of solid elements, cohesive elements, Gauss points and nodes were  $1.0 \times 10^6$ ,  $2.2 \times 10^5$ ,  $4.8 \times 10^6$  and  $3.3 \times 10^5$  respectively. The cohesive element thickness was  $1.8 \mu\text{m}$ , approximately 50 times thinner than the average grain size, so as to minimize their effect on properties. The interface elements had a Young's modulus ( $E = 400$  GPa) and Poisson's ratio ( $\nu = 0.27$ ), representative of the polycrystalline properties at room temperature [46]. The model sensitivity to the properties of the interface elements was tested by a set of simulations, varying the interface elastic modulus from 210 GPa (Young's modulus of polycrystalline alumina at  $1400^\circ\text{C}$  [46]) to 2100 GPa, with little or no effect on the calculated GB stresses. Although it would have been desirable to test the effects of mesh refinement to demonstrate convergence, it was not possible to run a more refined mesh on the available computing resource, and a more coarse mesh would have led to the loss of some boundaries. The bulk elastic properties of the model were obtained by applying a uniform compressive axial displacement to develop a stress of 350 MPa. The average axial and orthogonal strains were used to obtain Young's modulus and Poisson's ratio of 377 GPa and 0.23. Comparison with literature values [46] for Young's modulus and Poisson's ratio, and also the DVC data for Poisson's ratio (Table 1) shows reasonable agreement, indicating that the sample contains sufficient grains to be representative of polycrystalline alumina.

The objective of the modelling work was to determine the intergranular stresses, and their relationship to the local microstructure. A typical result (Figure 9) for the stresses within two grains and at their boundary shows significant spatial variation. For instance, although the stress along segment AB varies relatively smoothly with distance to the boundary, the stress at point M, where AB intersects the boundary, is lower than the mean boundary stress (i.e. the average stress for all elements in the GB facet, weighted by the triangular element area). This is a consequence of the relatively high stress around the grain boundary margins, indicating a significant effect of the grain junctions (i.e. triple points). This pattern is typical of other grains.

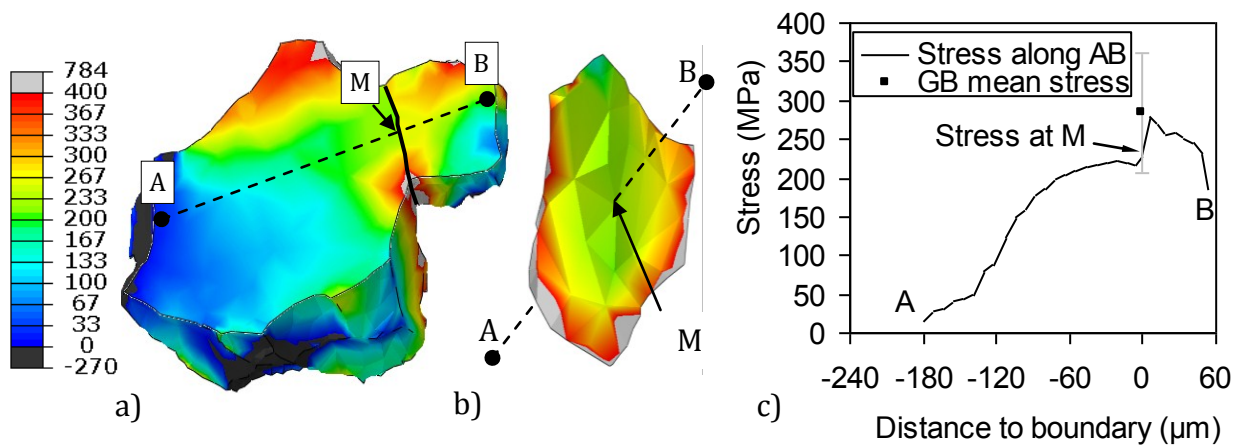


**Figure 9: An example of thermal stresses developed between and within grains. Component of stress (MPa) normal to the grain boundary (i.e. in the direction AB) as a) a stress map for two grains sharing the (mean tensilely stressed) boundary , b) normal stress across the grain boundary , and c) variation in stress along the line AB compared with the mean and standard error of stress calculated across the boundary – see (b).**

The dependence of the GB area on the GB stress is plotted in Figure 10a, showing no clear trend. The relatively small GBs (area < 1000 μm<sup>2</sup>) comprise over 50% of the total number, and unsurprisingly show the larger variation. Previous experimental work on coarse-grained alumina [2] reported that 4 out of the 5 cracked grain boundaries that were observed exhibited a high degree of grain-to-grain misorientation. The average normal stresses obtained at a GB as a function of the misorientation between the [0001] poles of adjacent grains are shown in Figure 10b. No significant sensitivity to grain-to-

grain misorientation is observed. The crystal grain-to-grain misorientation angle therefore appears to be an insufficient indicator of GB stress in the model predictions.

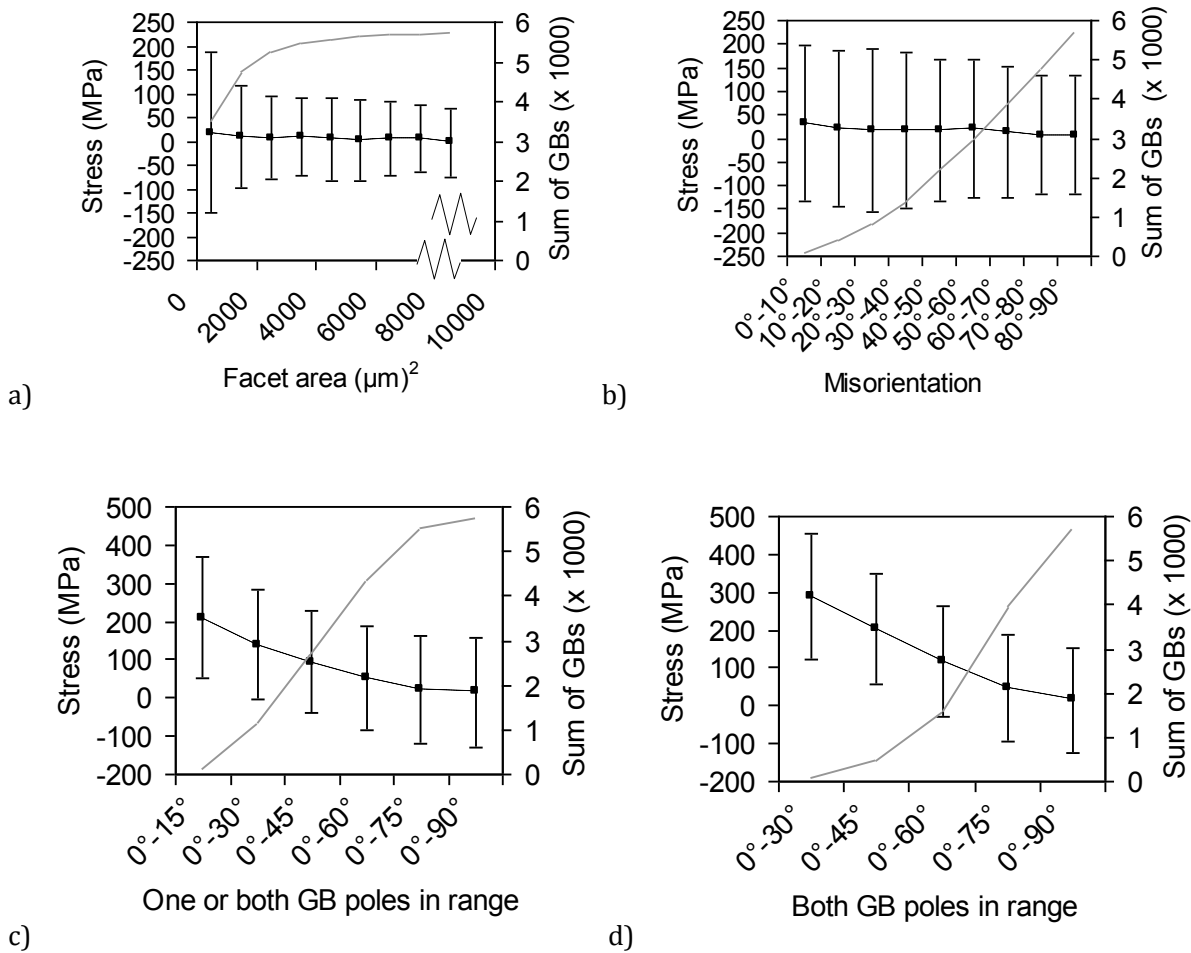


**Figure 10: Mean normal stress at grain boundaries as a function of: a) the boundary area, b) the grain-to-grain misorientation angle, c) the angle formed between the crystal basal plane [0001] pole and the GB facet pole for at least one of the GB facet poles, and d) both GB facet poles below the threshold range. The scatter bars show the grain to grain facet variation. The secondary axes (continuous grey line) show the cumulative number of boundaries.**

The effect of grain orientation relative to the grain boundary plane was examined. Here the vector normal to a GB defines the local GB pole. The GB pole angle is defined as the angle between the basal plane normal of one of the neighbouring grains and the GB pole: if a GB is close to the basal plane, the angle will be zero. As the pole approaches

the  $c$  axis, the thermal expansion coefficient in the direction of the pole approaches  $\alpha_{33}$ , which is the maximum value. Each GB is a curved surface in 3D space, and the FE model approximates the surfaces between grains by a set of triangular elements, as shown in Figure 9b. To obtain a representative average orientation of each GB, a weighted average orientation was calculated, where the weight is proportional to the triangle area. This reduced the effects of smaller regions, which tend to be at the boundary edges.

The data have been binned into a set of increasing angular ranges, each containing at least 92 GBs (Figure 10c). The normal stresses are found to decrease with increasing angle, with the effect more marked in cases where both poles are close to the  $c$  axis; stresses at boundaries that are close to the basal plane in *both* grains are thus considerably more tensile, compared to those with at least one such grain. These are the boundaries between the grains that contract most relative to the boundary plane. This is consistent with experimental observations of cracked boundaries in a fine-grained polycrystalline alumina [51], and suggests the image-based FE model of the grain aggregate is sufficiently representative of the microstructure to predict the development of average intergranular thermal stresses.

Inspection of the tomography images identified at least 21 cracked boundaries in the sample that was loaded in compression to 350 MPa (Figure 11a); no cracks were resolved at lower loads. The cracks tended to be aligned orthogonally to the applied compressive stress (Figure 13b). The average GB pole angle of these boundaries was  $55^\circ$  with 14 GBs presenting at least one GB pole higher than  $60^\circ$ . In order to investigate the stresses at these boundaries, the FE model was used to predict their normal stresses after cooling and with the sample loaded uniformly in compression (350 MPa) (Figure 11c). With thermal loading alone, the average stress for both the total grain boundary population and the cracked boundary population was close to zero. The cracked boundaries do not appear to present higher tensile stresses than the general population after cooling. With uniform compressive load of 350 MPa applied, the normal stresses of the cracked boundaries tended to become more tensile relative to

the general population due to grain-to-grain interactions, although their developed tensile stresses are not large. Most other boundaries become compressively loaded, increasingly so the nearer their plane normal to the compressive loading axis. However, the cracked boundaries are clearly located towards with the region where the axial strain was measured to become increasingly tensile as the sample was loaded (Figure 11b and d). This suggests that bending flexure of the sample quite strongly influences intergranular fracture in this experiment, and so further examination of the stresses on the cracked boundaries was not attempted. However, this analysis shows that in principal, an examination of the cracked boundaries might lead to a criterion for intergranular fracture, such as a critical tensile stress, in an experiment with well-defined loading. DVC analysis of the displacement fields would provide the full 3D boundary conditions for the FE model.

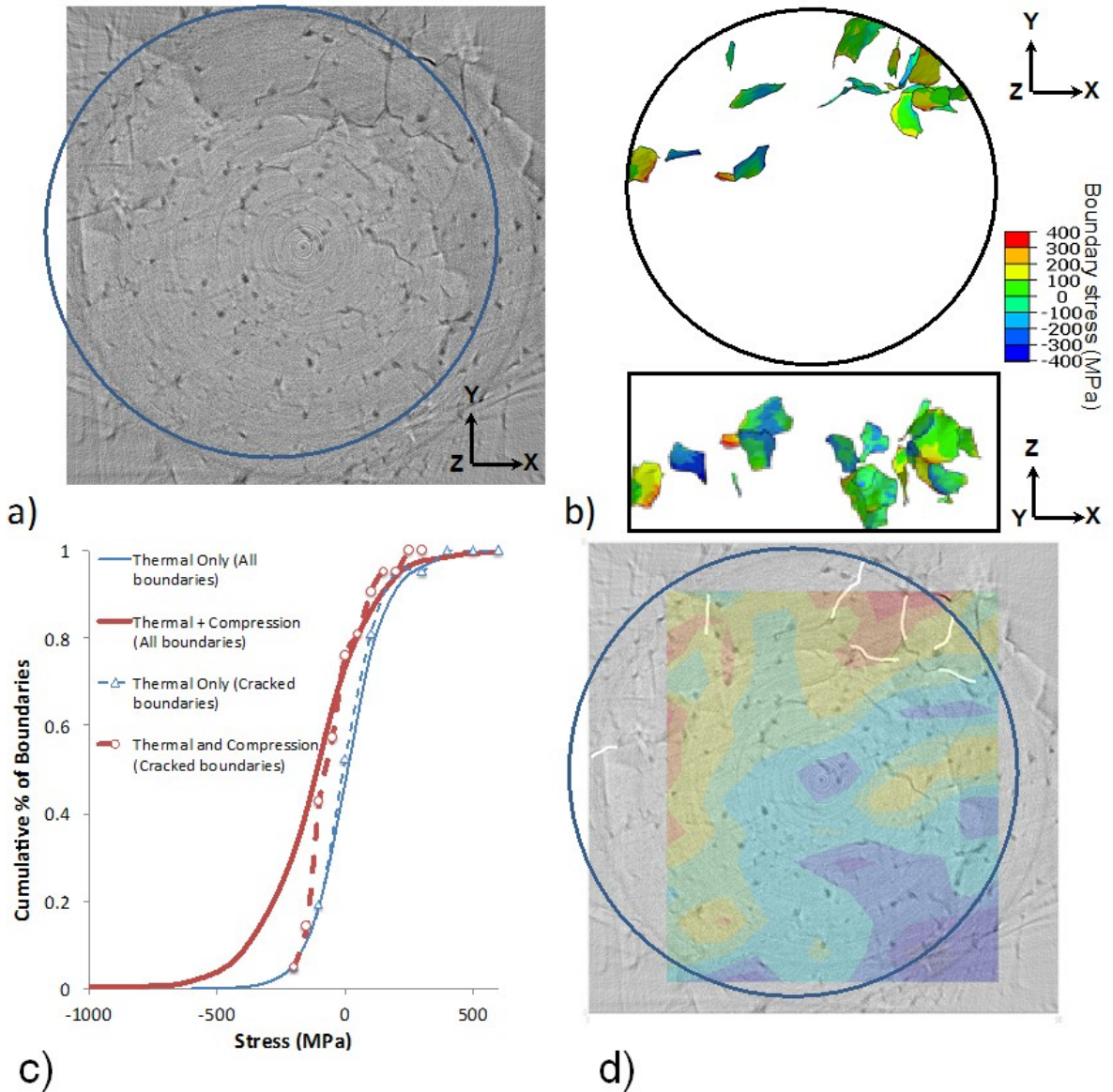


**Figure 11: Characterisation of cracked boundaries: a) a section of the tomography data at 170 N, showing intergranular cracking, b) visualisation of the cracked grain boundaries in the model and their calculated thermal stresses; the cracks are visualised in the x-y and x-z plane, c) the cumulative frequency distribution for the mean normal stress on all boundaries and cracked boundaries, with thermal stresses and with a uniform compressive stress of 350 MPa, d) The traces of the cracked boundaries in the same section of the tomography data are superposed with axial strain map (see Figure 6 for scale). The circle in each case identifies the boundary of the FE model in the x-y plane; this was constructed from the DCT data of an unloaded sample and does not bound the CT data at 170 N in (a) due to sample movement.**

#### 4.4.5 Validation of the FE Model by Diffraction

The FE model predicts significant thermal strains within grains leading to local lattice distortion. For example, a typical grain (Figure 12) experiences an average lattice rotation of  $0.16^\circ$  (calculated by quaternions [52]), but also has a spread of rotation of approximately  $0.15^\circ$  due to the thermal strains within in the grain. Synchrotron X-rays are highly monochromatic, so the Bragg diffraction condition is satisfied only over a small angular range of crystal orientation (described by the Lorentz factor). The observation that grains pass gradually through the Bragg condition (Figure 2 is an extreme example) may be explained by the range of thermal strain-induced lattice rotations (e.g.  $0.15^\circ$ ). By simulating the effect of these distortions on diffraction, a direct grain-by-grain comparison was therefore done to test the validity of the FE model.

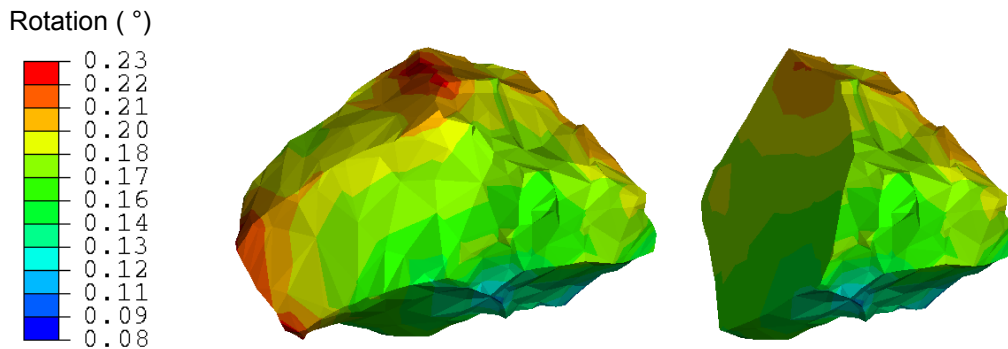


**Figure 12: Rotation of individual elements in a grain from the initial orientation due to thermal strains: a) map of the grain surface b) cut-view of the same grain.**

The elastic strains and lattice rotations obtained at the nodal positions of the elements within the grains in the FE model were used to predict the diffraction images for each grain. Assuming kinematical diffraction, the diffraction images are simulated by superposition of the diffracted intensity from each 3D element. To do this, each element is assigned an average lattice rotation and strain from the output of the FEM model. Functions describing the position of the diffracted intensity (in image coordinates  $x$  and  $y$ , and sample rotation  $\omega$ ) are then calculated for each grain for the average grain orientation and the selected diffracting planes. Linear approximation, using coefficients from the partial derivatives of these functions with respect to the components of lattice

rotation and elastic strain, provides a computationally efficient means to calculate the effect of element strain and lattice rotation on the distribution of diffracted intensity. A separate diffraction image is thus obtained for each grain as a function of  $\omega$  in steps of  $0.05^\circ$ ; their diffracted intensities are summed and the local value relative to the average lattice rotation presented in a 2D image with an arbitrary scale to exclude outlier points. The predicted diffraction images are then compared to the experimental observations. An example for one grain in one diffracting condition is given in Figure 13 (a and b). Further examples and explanations of the methodology are given in the online supplementary material. The agreement between the predicted and observed diffraction images is fairly good; the model captures the general patterns of intensity, although there are differences in the detail.

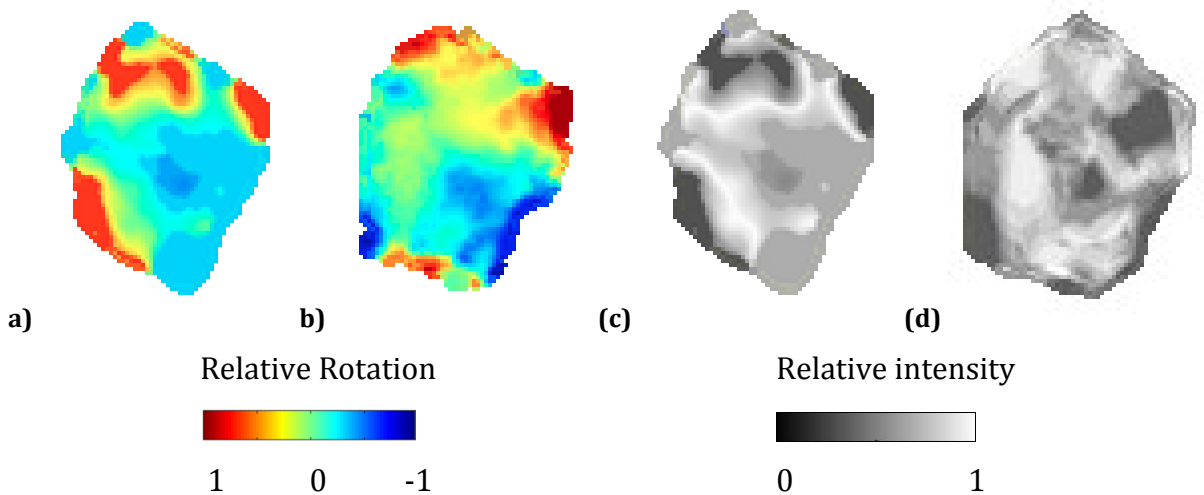


**Figure 13: An example of the comparisons between measured and predicted diffraction image intensity; a) measured, b) prediction considering local strains and lattice rotation, c) measured (same as (a), scaled in relative intensity to remove sign), d) prediction considering lattice rotation only. Data for  $(2\bar{1}\bar{1}3)$  diffraction in grain 3. Further examples are given in the online supplementary material.**

The relative importance of dilational strains (i.e. tension or compression) and shear strains (which are associated with lattice rotations) was investigated by post-processing to predict diffraction images using only the local misorientation angles [54] relative to the grain average orientation that was obtained using quaternions [52]. Only

the rotation component about the sample rotation axis was considered. The intensity change with  $\omega$ , relative to the Bragg condition, was described by a Gaussian function with an arbitrary standard deviation of  $0.05^\circ$ . An experimental and predicted diffraction image pair is shown in Figure 13 (c and d). The predicted diffraction image was obtained by summing the set of images with rotation about the Bragg condition, as before. While some features are captured, the agreement is worse than generally obtained when the elastic strains were included, indicating the dilational elastic strains contribute significantly to diffraction. Varying the Gaussian standard deviation between  $0.02^\circ$  and  $0.08^\circ$  did not significantly affect the patterns of intensity, and an examination of the effect of lattice rotations about the diffraction plane did not improve the agreement with experiment. Further examples are given in the online supplementary material.

The broad agreement between the experimental and predicted diffraction images supports the general validity of the thermal stresses predicted by the image-based Finite Element model. We attribute the most significant cause of error to the inevitable approximations in grain shape in the creation of the model from the experimental DCT data. Errors may also arise from neglect of stress redistribution following intergranular cracking during cooling. However tomography did not reveal significant levels of cracking, so this may not be important here. However, intergranular porosity was observed and this has not been treated in the model. The effects of plasticity were also neglected, since thermal strains would not have developed to a significant magnitude at the temperature where plasticity could occur in alumina. However, any plasticity that did develop at high temperature may contribute to local lattice distortions [53].

#### ***4.4.6 Concluding Summary***

Diffraction contrast tomography (DCT) has been applied to a coarse grain size polycrystalline alumina to obtain experimental 3D data on the shape and crystallographic orientation of each detected grain in a volume comprising many grains. Comparison with computed absorption tomography observations of intergranular porosity and cracking, the latter induced by compressive loading of the unconstrained

sample, provides confidence in the inferred grain boundary locations. The grain boundary planes are also consistent with the expected preferences for low-energy facets in alumina. The DCT data are judged to provide a good description of the three-dimensional microstructure.

An image-based Finite Element model of the microstructure, with cohesive elements at the grain boundaries to extract grain boundary stresses, has been constructed from the DCT data. The grain orientations were used to implement the anisotropic crystal elastic stiffness constants and thermal expansion coefficients. The bulk elastic properties of the model were consistent with those of polycrystalline alumina, and also agreed with the experimental observations of Poisson's ratio obtained by digital volume correlation of tomographic images obtained under in-situ loading.

Using the Finite Element model it was possible to simulate the effects of cooling from elevated temperature (i.e. sintering temperature) on strains at grain boundaries and within grains. We found that the largest thermal tensile stresses develop for boundaries where one or both adjacent grains have their basal plane closely aligned to the grain boundary plane. Higher tensile stresses are apparent when both grains have such orientation. The average grain boundary stresses were insensitive to the relative grain-to-grain crystal misorientation and volume of adjacent grains, suggesting these are secondary factors. It was not possible to use tomographic observations of intergranular cracking under load to obtain an intergranular failure criterion, principally due to experimental uncertainty caused by the alignment of loading and the resulting flexure of the sample.

A spread of the diffraction angle was observed for individual grains, indicative of significant lattice rotations. These are similar in magnitude and distribution with those predicted by FE. Alternative simulations showed that the tensile and compressive elastic strains contribute significantly to diffraction; this supports the validity of the image-based Finite Element model to predict intergranular stress.

In conclusion, the three-dimensional microstructure of alumina has been sufficiently well measured by diffraction contrast tomography to produce a microstructurally-representative model of a polycrystalline aggregate and its thermally induced residual stresses. Future developments of this approach might use in-situ tomographic observations, with well-defined mechanical loading quantified by digital volume correlation, to obtain an intergranular fracture criterion as a function of grain boundary structure. The relationships between grain and grain boundary orientations and grain boundary stress might also be implemented within Voronoi-type approximations of microstructures to investigate the sensitivity of the grain boundary structure distribution on the development of intergranular cracking.

#### ***4.4.7 Acknowledgements***

The authors gratefully acknowledge I. Simonovski (Institute for Energy, The Netherlands) for generous contributions with the FE pre-processing methodology, and S.G. Yousef (Technical University, Darmstadt, Germany) for providing the alumina used in this study. The beam time on ID11 was provided by ESRF under experiment MA-157, and we appreciate the helpful support of the beamline scientists. We also thank G. Johnson (University of Manchester) and A.A. Kahn (Pakistan Institute of Nuclear Science and Technology) for their assistance with the experiment.

#### ***4.4.8 Online supplementary material***

##### **4.4.8.1 Additional validation research**

In Figure 13(a) we presented the calculated and predicted diffraction image for one diffraction condition of one grain (grain 3 in the dataset). The diffraction images corresponding to all the observed diffraction conditions of this grain are shown in Figure 14; a total of 64 diffraction image pairs. Visual examination shows the general agreement is reasonably good, with about half of the pairs showing similar patterns of relative rotation ( $\omega$ ). According to the author's visual criterion, examples of good and bad agreement are enclosed in blue and red respectively.

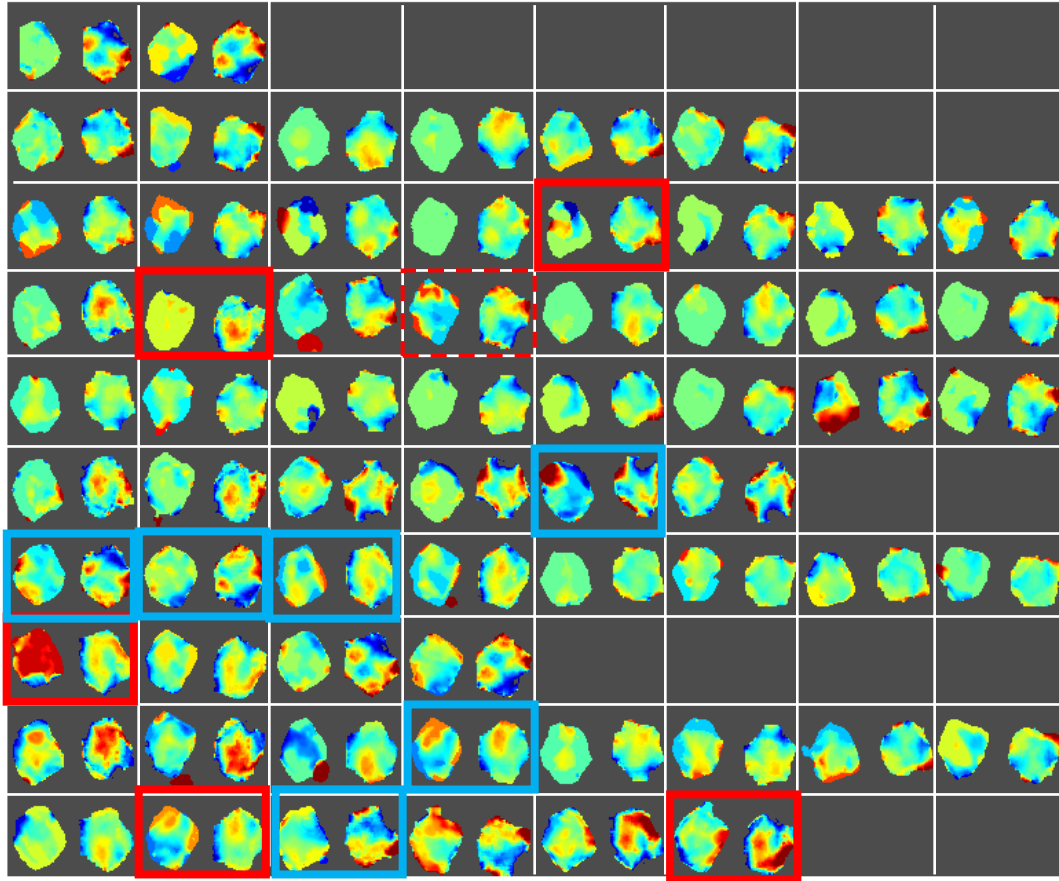


**Figure 14:** Pairs of measured (left) and predicted (right) diffraction images for one grain (grain 3). Results are presented in a relative scale values of  $\omega$  (■1, ■-1). Rows from top to bottom represent the diffraction conditions for the following families of planes:  $\{0\ 1\ -1\ 2\}$ ,  $\{1\ 0\ -1\ 4\}$ ,  $\{1\ 1\ -2\ 0\}$ ,  $\{1\ 1\ -2\ 3\}$ ,  $\{1\ 1\ -2\ 3\}$ ,  $\{1\ 1\ -2\ 3\}$ ,  $\{0\ 2\ -2\ 4\}$ ,  $\{0\ 2\ -2\ 4\}$ ,  $\{1\ 1\ -2\ 6\}$  and  $\{1\ 1\ -2\ 6\}$ . The pair shown in Figure 13 is highlighted.

A more detailed comparison of the measured and predicted diffraction images in terms of relative rotation ( $\omega$ ) and diffracted intensity (as in Figure 13) is shown in Figure 15. As shown in Figure 13, the agreement is considerably worse than when the elastic strains were excluded (columns 1 and 2 in Figure 15), demonstrating that these contribute significantly to the observed diffraction effects.

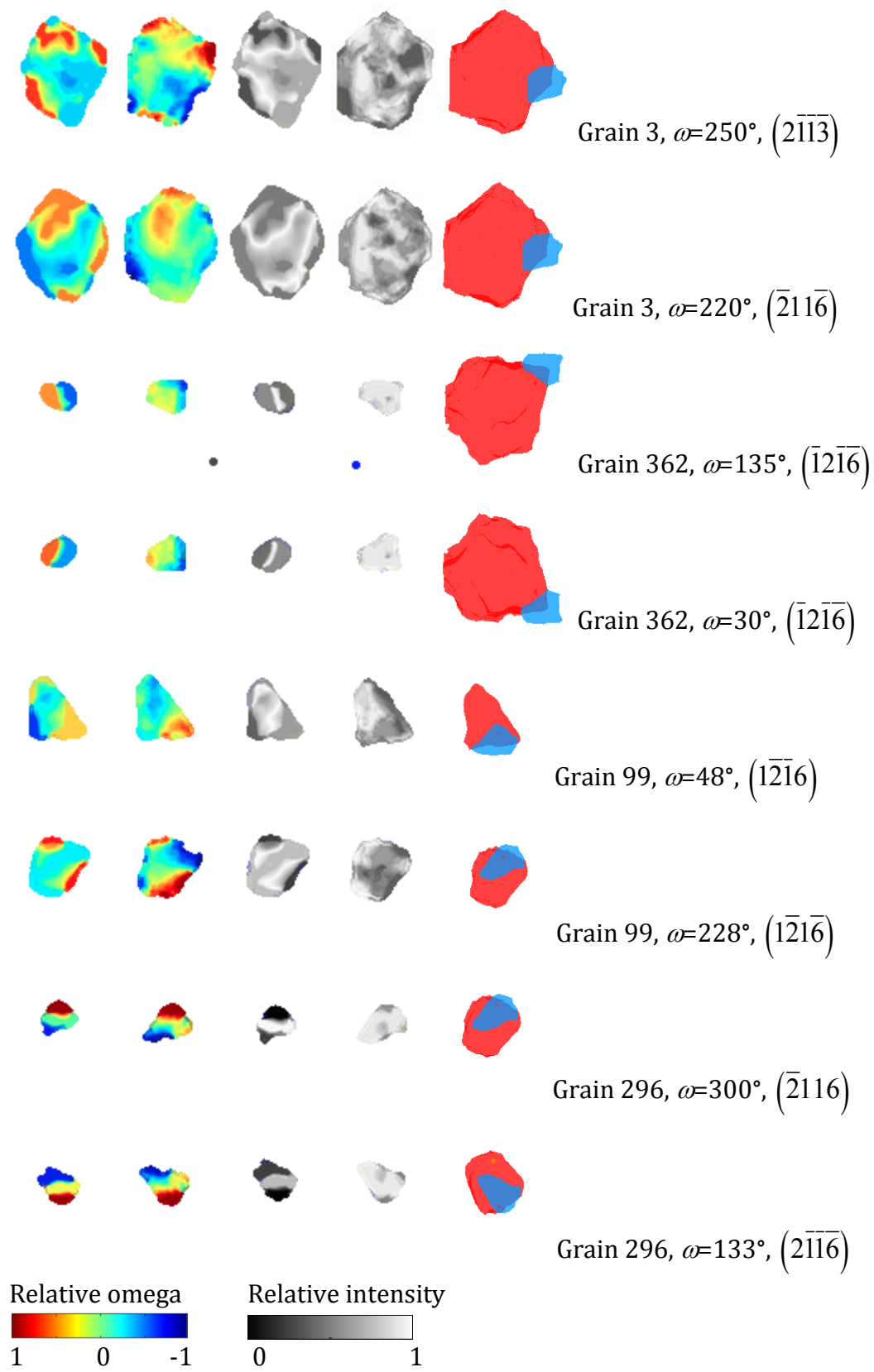


**Figure 15: Further examples of the comparison between measured and predicted diffraction image intensity; column 1) measured, column 2) prediction considering local strains and lattice rotation, column 3) measured (same as (column 1), scaled in relative intensity to remove sign), column 4) prediction considering lattice rotation only. Data is shown for 2 pairs of grains (3-362 and 99-296), sharing each a boundary predicted to be in compression. The relative positions of grain 3 (red) relative to 362 (blue) and the relative positions of grain 99 (red) relative to 296 (blue) are shown in column 5 by their projected images.**

Figure 13 shows only one example of a visual comparison between the predicted and observed diffraction spot images for one diffraction spot for one grain. In an effort to quantify the data from numerous image pairs, we selected the measured and predicted diffraction images of 34 grains that were adjacent to 17 large boundaries facets ( $>750 \mu\text{m}^2$ ) that were predicted to be highly stressed (i.e. above 200 MPa in absolute magnitude): 8 boundaries were in compression and 9 in tension. The predicted and measured diffraction images produced by each of these grains have been compared (rejecting those diffraction images which are almost two dimensional due to the insufficient intensity in the original data). Linear regression was applied to quantify the differences between the measured and predicted relative lattice rotation values ( $\omega$ ) for all the pixels in each diffraction image. The averaged coefficient of correlation (R) for the grains in compression is 0.23 with a standard of deviation 0.10 (here R=1 indicates a perfect fit). In tension, the corresponding coefficient of correlation is 0.16 with a standard deviation of 0.16. The correlation is no better than fair, although the agreement is worse for tensile grains, possibly due to some cracking, which is currently not modelled.

#### **4.4.8.2 Calculated stresses on cracked boundaries**

Here we plot the predicted stresses (in 3D) on the identified 21 cracked boundaries after cooling (Figure 16a) and subsequent loading in compression (Figure 16b). It can be seen that, as discussed earlier, with thermal loading alone their average stress was close to zero, although an average compressive stress of 120 MPa developed under

load. Further, these views fully locate the position of the cracked boundaries (towards one side of the sample).

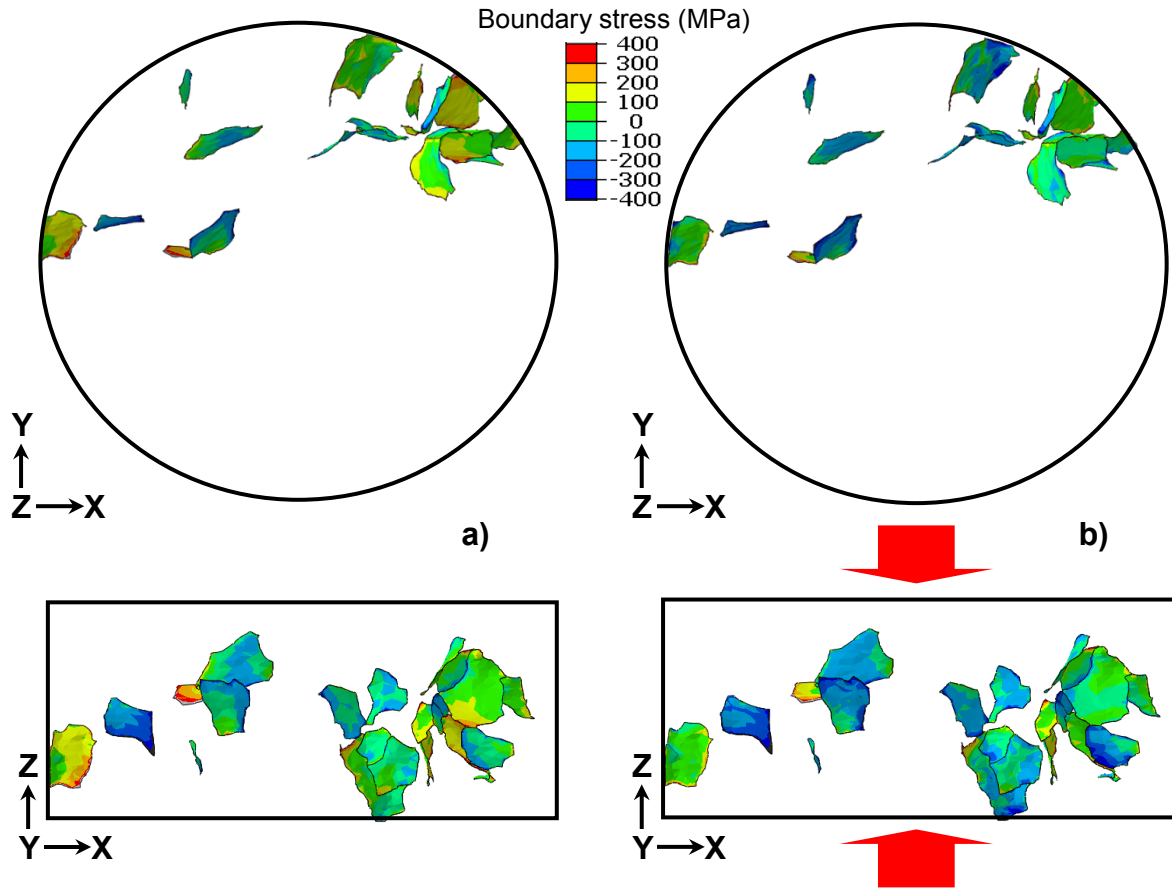


Figure 8: Calculated stress on observed cracked boundaries: a) after cooling and b) after such cooling with subsequent loading in compression (350MPa) along the Z axis (red arrows). The top views in the figure are the top views of the sample while the bottom views represent the side views of the sample.

#### 4.4.8.3 Simulation of diffraction spots from deformed grains

Based on the deformations calculated using the finite element crystal plasticity model (FE-CPS), the diffraction patterns for each grain were simulated independently and compared to the observed ones. Taking the reconstructed 3D shape of each grain, each voxel was assigned a local strain and orientation state ( $\epsilon_i$ ) from nearest neighbour interpolation of the FE-CPS results, and orientations of the diffracting plane normals are determined. The rotation angle ( $\omega$ ) at which diffraction occurs from a specific (hkl)

plane normal can be found for each voxel by applying Bragg's law. Once the omega angles and plane normal orientations for a given (hkl) reflection are known, the scattering and diffraction vectors and the path of the diffracted beam from each voxel can be calculated, and the intersection with the detector plane  $\mathbf{p}_i$ . Once this intersection is known for the undeformed state ( $\mathbf{p}_i^*$ ), it can be approximated for any deformed state using the Jacobian:

$$\mathbf{p}_i = \begin{bmatrix} x \\ y \\ \omega \end{bmatrix}_i \quad \mathbf{p}_i = \mathbf{p}_i^* + \frac{\partial \mathbf{p}_i}{\partial \varepsilon_i} \Delta \varepsilon_i \quad \text{Eq. (1)}$$

To facilitate the simulation, kinematical diffraction was assumed which allows that the diffraction spots to be approximated as a sum of the diffracted beam intensities from all the individual voxels. In other words, phase effects in the incoming and diffracted beam and therefore the interaction between the voxels were neglected. Self-absorption of the sample and extinction of the beam across diffracting grains were also neglected. All voxels are assumed to have the same scattering efficiency, contributing the same intensity to the diffracted beam. The resulting intensity observed at a given position on the detector is given by the following equation, where  $\Psi$  describes the interpolation of the projected intensities over the eight nearest detector pixels (in x, y,  $\omega$ ) to  $\mathbf{p}_i$ .

$$I_{(x,y,\omega)} = \sum_{(i)} I_i \cdot \Psi_{(\mathbf{p}_i)} \quad \text{Eq. (2)}$$

These approximations can be justified for deformed metallic crystals and have been successfully used to create grain maps of polycrystals using diffraction contrast tomography [40].

#### **4.4.9 References associated to publication 4**

- [1] Babout L, Marrow T], Engelberg D, Withers PJ. X-ray microtomographic observation of intergranular stress corrosion cracking in sensitised austenitic stainless steel. MATERIALS SCIENCE AND TECHNOLOGY 2006;22:1068.
- [2] Yousef SG, Rodel J, Fuller ER, Zimmermann A, El-Dasher BS. Microcrack evolution in alumina ceramics: Experiment and simulation. JOURNAL OF THE AMERICAN CERAMIC SOCIETY 2005;88:2809.

- [3] Kuszyk JA, Bradt RC. Influence of Grain Size on Effects of Thermal Expansion Anisotropy in MgTi<sub>2</sub>O<sub>5</sub>. JOURNAL OF THE AMERICAN CERAMIC SOCIETY 1973;56:420.
- [4] Vedula VR, Glass SJ, Saylor DM, Rohrer GS, Carter WC, Langer SA, Fuller ER. Residual-stress predictions in polycrystalline alumina. JOURNAL-AMERICAN CERAMIC SOCIETY 2001;84:2947.
- [5] Randle V. 'Special' boundaries and grain boundary plane engineering. Scripta Materialia 2006;54:1011.
- [6] Rohrer GS, Saylor DM, El Dasher B, Adams BL, Rollett AD, Wynblatt P. The distribution of internal interfaces in polycrystals. Zeitschrift fur Metallkunde 2004;95:197.
- [7] Marrow TJ, Gonzalez D, Aswad M, Quinta da Fonseca J, Withers PJ. In-situ observation and modelling of intergranular cracking in polycrystalline alumina. Key Engineering Materials 2011;465:560.
- [8] Watanabe T. APPROACH TO GRAIN BOUNDARY DESIGN FOR STRONG AND DUCTILE POLYCRYSTALS. Res Mechanica: International Journal of Structural Mechanics and Materials Science 1984;11:47.
- [9] Davies P, Randle V. Grain boundary engineering and the role of the interfacial plane. MATERIALS SCIENCE AND TECHNOLOGY;17:615.
- [10] Jones R, Randle V, Engelberg D, Marrow TJ. Five-parameter grain boundary analysis of a grain boundary-engineered austenitic stainless steel. Journal of Microscopy 2009;233:417.
- [11] Rahimi S, Engelberg DL, Duff JA, Marrow TJ. In situ observation of intergranular crack nucleation in a grain boundary controlled austenitic stainless steel. JOURNAL OF MICROSCOPY-OXFORD 2009;233:423.
- [12] Dillon SJ, Miller H, Harmer MP, Rohrer GS. Grain boundary plane distributions in aluminas evolving by normal and abnormal grain growth and displaying different complexions. International Journal of Materials Research 2010;101:50.
- [13] Kim MJ, Kim SM, Yoon DY. Singular Grain Boundaries in Alumina Doped with Silica. JOURNAL OF THE AMERICAN CERAMIC SOCIETY 2004;87:507.

- [14] Grah M, Alzebdeh K, Sheng PY, Vaudin MD, Bowman KJ, Ostojca-Starzewski M. Brittle intergranular failure in 2D microstructures: Experiments and computer simulations. *ACTA MATERIALIA* 1996;44:4003.
- [15] Espinosa HD, Zavattieri PD. A grain level model for the study of failure initiation and evolution in polycrystalline brittle materials. Part I: Theory and numerical implementation. *Mechanics of Materials* 2003;35:333.
- [16] Sfantos GK, Aliabadi MH. A boundary cohesive grain element formulation for modelling intergranular microfracture in polycrystalline brittle materials RID D-1029-2010. *International Journal for Numerical Methods in Engineering* 2007;69:1590.
- [17] Sands CM, Henderson RJ, Chandler HW. A three dimensional computational model of the mechanical response of a dual-phase ceramic. *COMPUTATIONAL MATERIALS SCIENCE* 2007;39:862.
- [18] Fritzen F, Boehlke T, Schnack E. Periodic three-dimensional mesh generation for crystalline aggregates based on Voronoi tessellations. *Computational Mechanics* 2009;43:701.
- [19] Spanos G, Rowenhorst DJ, Lewis AC, Geltmacher AB. Combining serial sectioning, EBSD analysis, and image-based finite element modeling. *Mrs Bulletin* 2008;33:597.
- [20] Simonovski I, Cizelj L, Marrow TJ, Quinta da Fonseca J, King A. Towards modelling intergranular stress-corrosion cracks using experimentally obtained grain topologies. *Proceedings of PVP2009 2009;2009 ASME Pressure Vessels and Piping Division Conference*.
- [21] Simonovski I, Cizelj L. Automatic parallel generation of finite element meshes for complex spatial structures. *COMPUTATIONAL MATERIALS SCIENCE* 2011;50:1606.
- [22] Fang Y, Ravi-Chandar K, White KW. Influence of surface residual stress state on crack path evolution in polycrystalline alumina RID D-9246-2011. *JOURNAL OF THE AMERICAN CERAMIC SOCIETY* 2002;85:1783.
- [23] Rowenhorst DJ, Lewis AC, Spanos G. Three-dimensional analysis of grain topology and interface curvature in a  $\beta$ -titanium alloy. *ACTA MATERIALIA* 2010;58:5511.
- [24] Masato E. Three-dimensional Characterization and Analysis of Steel Microstructure by Serial Sectioning. *Tetsu to Hagane* 2004;90:183.

- [25] Bhandari Y, Sarkar S, Groeber M, Uchic MD, Dimiduk DM, Ghosh S. 3D polycrystalline microstructure reconstruction from FIB generated serial sections for FE analysis. *COMPUTATIONAL MATERIALS SCIENCE* 2007;41:222.
- [26] Uchic MD, Groeber MA, Dimiduk DM, Simmons JP. 3D microstructural characterization of nickel superalloys via serial-sectioning using a dual beam FIB-SEM. *Scripta Materialia* 2006;55:23.
- [27] Groeber M, Ghosh S, Uchic MD, Dimiduk DM. A framework for automated analysis and simulation of 3D polycrystalline microstructures. Part 2: Synthetic structure generation. *ACTA MATERIALIA* 2008;56:1274.
- [28] Jones JL, Hoffman M, Vogel SC. Orientation-dependent lattice strains in lead zirconate titanate under mechanical compression by in situ neutron diffraction RID A-8361-2008. *Physica B-Condensed Matter* 2006;385:548.
- [29] Jones JL. The use of diffraction in the characterization of piezoelectric materials RID A-8361-2008. *Journal of Electroceramics* 2007;19:69.
- [30] Quinta da Fonseca J, Oliver EC, Bate PS, Withers PJ. Evolution of intergranular stresses during in situ straining of IF steel with different grain sizes. *Materials Science and Engineering: A* 2006;437:26.
- [31] Gonzalez D, Kelleher JF, Quinta da Fonseca J, Withers PJ. Macro and intergranular stress responses of austenitic stainless steel to 90° strain path changes. *Materials Science and Engineering: A* 2012;546:263.
- [32] Larson BC, Yang W, Ice GE, Budai JD, Tischler JZ. Three-dimensional X-ray structural microscopy with submicrometre resolution. *Nature* 2002;415:887.
- [33] Poulsen HF, Margulies L, Schmidt S, Winther G. Lattice rotations of individual bulk grains - Part I: 3D X-ray characterization. *Act. Mater.* 2003;51:3821.
- [34] Johnson G, King A, Honnicke MG, Marrow J, Ludwig W. X-ray diffraction contrast tomography: a novel technique for three-dimensional grain mapping of polycrystals. II. The combined case. *J. of App. Crystall.* 2008;41:310.
- [35] Lienert U, Almer J, Jakobsen B, Pantleon W, Poulsen HF, Hennessy D, Xiao C, Suter RM. 3-Dimensional Characterization of Polycrystalline Bulk Materials Using High-Energy Synchrotron Radiation. *MATERIALS SCIENCE FORUM* 2007;539-543:2353.

- [36] Jakobsen B, Poulsen HF, Lienert U, Pantleon W. Direct determination of elastic strains and dislocation densities in individual subgrains in deformation structures RID A-4131-2012. *ACTA MATERIALIA* 2007;55:3421.
- [37] Ustundag E, Rogan RC, Daymond MR, Tamura N, Margulies L, Poulsen H. Multiscale study of internal stress and texture in ferroelectrics RID C-1258-2009. In: Denis S, Hanabusa T, He BP, Mittemeijer E, Nan J, Noyan IC, Scholtes B, Tanaka K, Xu KW, editors. *Residual Stresses VII, Proceedings*, vol. 490-491. Zurich-Uetikon: Trans Tech Publications Ltd, 2005. p.28.
- [38] Herbig M, King A, Reischig P, Proudhon H, Lauridsen EM, Marrow J, Buffière J-Y, Ludwig W. 3-D growth of a short fatigue crack within a polycrystalline microstructure studied using combined diffraction and phase-contrast X-ray tomography. *ACTA MATERIALIA* 2011;59:590.
- [39] King A, Johnson G, Engelberg D, Ludwig W, Marrow J. Observations of intergranular stress corrosion cracking in a grain-mapped polycrystal. *SCIENCE* 2008;321:382.
- [40] Ludwig W, Reischig P, King A, Herbig M, Lauridsen EM, Johnson G, Marrow TJ, Buffiere JY. Three-dimensional grain mapping by x-ray diffraction contrast tomography and the use of Friedel pairs in diffraction data analysis. *Review of Scientific Instruments* 2009;80.
- [41] McDonald SA, Schneider LCR, Cocks ACF, Withers PJ. Particle movement during the deep penetration of a granular material studied by X-ray microtomography. *Scripta Materialia* 2006;54:191.
- [42] Ludwig W, King A, Reischig P, Herbig M, Lauridsen EM, Schmidt S, Proudhon H, Forest S, Cloetens P, Roscoat SRd, Buffière JY, Marrow TJ, Poulsen HF. New opportunities for 3D materials science of polycrystalline materials at the micrometre lengthscale by combined use of X-ray diffraction and X-ray imaging. *Materials Science and Engineering: A* 2009;524:69.
- [43] Randle, Owen G. Mechanisms of grain boundary engineering. *ACTA MATERIALIA* 2006;54:1777.

- [44] Choi JH, Kim DY, Hockey BJ, Wiederhorn SM, Handwerker CA, Blendell JE, Carter WC, Roosen AR. Equilibrium shape of internal cavities in sapphire. *JOURNAL OF THE AMERICAN CERAMIC SOCIETY* 1997;80:62.
- [45] Bay B, Smith T, Fyhrie D, Saad M. Digital volume correlation: Three-dimensional strain mapping using X-ray tomography. *Experimental Mechanics* 1999;39:217.
- [46] Shackelford JF, Alexander W. *CRC materials science and engineering handbook*: CRC Press, 2001.
- [47] Wachtman JB, Tefft WE, Lam DG, Stinchfield RP. Elastic Constants Of Synthetic Single-Crystal Corundum At Room Temperature. *Journal Of The American Ceramic Society* 1960;43:334.
- [48] ABAQUS Documentation. In: Abaqus I, editor. Providence, Rhode Island, 2006.
- [49] Hull FC. Plane section and spatial characteristics of equiaxed  $\beta$ -brass grains. *Materials Science and Technology* 1988;4:778.
- [50] Kreher W, Pompe W. *Internal stresses in heterogeneous solids*: Akademie-Verlag, 1989.
- [51] Aswad MA, Marrow TJ. *Intergranular crack nucleation in polycrystalline alumina*. Dresden, Germany, 2010.
- [52] He W, Ma W, Pantleon W. Microstructure of individual grains in cold-rolled aluminium from orientation inhomogeneities resolved by electron backscattering diffraction. *Materials Science and Engineering A* 2008;494:21.
- [53] Gonzalez D, King A, Simonovski I, Quinta da Fonseca J, Withers PJ. Modelling and Measurement of Plastic Deformation and Grain Rotation in 3D at the Grain-to-Grain Level. *Proceedings of the 1st World Congress on Integrated Computational Materials Engineering (ICME)*, 2011. p.107.
- [54] Pantleon W. Resolving the geometrically necessary dislocation content by conventional electron backscattering diffraction. *Scr. Mater.* 2008;58:994.

**END OF PUBLICATION 4**

# 5 Conclusions and future work

## 5.1 Overall conclusions

The conclusions in this dissertation have largely been extracted in each individual research case (including the annexes). Some of these conclusions are compiled here. As the conclusions for each of the publications and supplementary research are indeed interrelated, these are referred in the text of this section when relevant.

Previous to Publication 1, some residual stress measurements have been compared with CPFEM results in annex 6.9. In this case the residual stress across the section of a bent bar is well predicted and indication of the residual intergranular stress is anticipated. Publication 1 shows that, when averaged over several grains, the residual elastic strains can be reasonably well predicted even following complex loading paths. In such work three different 90° strain path changes have been studied. At the macroscale, the measurements revealed transient softening, only partially consistent with the predictions. Therefore, at this scale, Bauschinger effect on reloading that is only partially captured by the model. Only in the case of C<sub>2</sub>T<sub>3</sub> was any significant permanent softening observed. Low levels of permanent softening are consistent with previous work on single phase stainless steels. At the meso-scale (as defined in the introduction of this thesis), measurements of the elastic response of different  $\{hkl\}$  grain families were performed by neutron diffraction. These results revealed an even earlier onset of yield for strain paths reloaded in compression while a strain path reloaded in tension showed good agreement with corresponding predictions. Further results in publication 1 demonstrate some characteristics of plasticity in polycrystals. For instance, modelling results show that intergranular strains are introduced in the pre-strain but these soon become over-written by intergranular strains characteristic of the reloading such that no permanent softening is predicted. Additionally, it is important to note that the current model does not include an inherent Bauschinger

style permanent softening in the constitutive laws governing slip. It is quite possible that this would need to be invoked to explain any permanent softening encountered for larger pre-strains. This opportunity for improvement will be explained in more detail in the “further results” section.

In publication 2, cohesive elements in the grain boundary regions have been incorporated in order to calculate normal stresses to grain boundaries generated by elastic and plastic anisotropy during deformation and following unloading. This work was inspired by elastic simulations in bi-crystals (annex 6.7). It was found that, after 0.5% applied strain, stresses normal to grain boundaries introduced by plastic anisotropy dominate over the normal stresses introduced by elastic anisotropy. This is in line with results from Publication 1 (Figure 5) where it was seen that plastic deformation overwrote the previous internal strain characteristic to a give strain path. Further, stresses at triple junctions were predicted very high in magnitude (whether tensile or compressive). Some discussions were extracted in this respect. Finally, predictions of the magnitudes of the residual grain boundary stresses at soft-hard grain combinations were carried out, since these have been observed to fail. The results revealed the stress to be unrelated to the amount of plastic strain in the vicinity of the boundary and whether it was higher or lower than the average plastic strain. Finally, the relationship between the variability of residual grain boundary stresses and the grain boundary orientation was explored. Previous work has revealed some particular grain combinations that enhance intergranular stresses. In contrast with these results, the grain boundary orientation was statistically found to be independent to the residual grain boundary stresses.

In publication 3, diffraction contrast tomography (DCT) was used to map the 3D grain arrangement of an aluminium polycrystal. This was the basis of a microstructurally faithful mesh for crystal plasticity finite element modelling (CPFEM). The sample was then monitored by DCT during incremental uniaxial compression. Changes in the diffracted spots during deformation were interpreted in terms of crystal re-orientation and orientation spread within grains. Reorientation within grains of  $\sim \pm 1^\circ$  has been

observed after 1.2% compressive strain as predicted by the model. However, on a grain-to-grain basis, agreement is relatively poor. These poor results may be attributed to the simplicity of the model or to the fact that the boundary conditions employed in the model are likely to be somewhat different to those in the experiment. It is indeed very difficult to deform such a small sample in an idealised manner. Future developments of this approach might use in-situ tomographic observations, with well-defined mechanical loading quantified by digital volume correlation (DVC). Other opportunities for improvement are possible and these are discussed in more detail in the next section (further work section).

In publication 4, an image-based FE model of a reconstructed alumina polycrystal (using DCT) has been developed. Cohesive elements have been placed at the grain boundaries to accurately extract grain boundary stresses. The reconstructed grain orientations were used to implement the anisotropic crystal elastic stiffness constants and thermal expansion coefficients. This analysis was done using linear elasticity, neglecting any possible plasticity that could occur in the material. The purpose is to simulate the stresses formed upon cooling from an elevated temperature (i.e. sintering temperature). The stresses calculated at grain boundaries aligned with the basal plane are highest, in agreement with experiments and thermal lattice anisotropy. Higher tensile stresses are apparent when both grains have such common boundary orientation. Unlike findings in previous work, the average grain boundary stresses were insensitive to the relative grain-to-grain crystal misorientation. The predicted effect of crystal lattice strains and rotations on diffraction, due to the modelled thermal stresses, showed some agreement with the observed X-ray diffraction images of individual grains. Analogous to publication 3, well-defined mechanical loading quantified by digital volume correlation (DVC) may be used in future to feed realistic boundary conditions into the FE model.

Overall, it is worth noting that many intra-granular mechanisms are not captured by the current model (e.g. dislocation pile-ups or slip transfer) meaning that local stresses may be poorly predicted at boundaries in plastic models. Further improvements may be

achieved by model coupling with Discrete Dislocation Dynamics (DDD) models. In this regard, statistical (at a larger scale) experimental vs. simulation comparisons show a better agreement than local comparisons. For example, the strong effect of the neighbourhood at redistributing local stresses has been shown (publication 2) in fully developed plasticity. Again in fully developed plasticity, another example can be found in the measurements and predictions of local rotation maps plotted in publication 3 which show poor agreement. However, the magnitude of the reorientation within grains ( $\sim \pm 1^\circ$ ) is predicted as observed. Further, the agreement between predicted and modelled grain-averaged GOS in publication 3 is much more satisfactory. The agreement between predicted and measured rotations with respect to the average orientation following rolling (6.10) is also statistically satisfactory.

A further example on the local stress redistribution as a result of the neighbourhood in the polycrystal can be found in publications 4 and in the supplementary research associated to publication 2 (annex 6.5). The partial disagreement between predicted and measured diffraction images in publication 4 could be, at least in part, attributed to the fact that cracking has not been modelled. It is probable that these agreements will improve when considering cracking because a cracked boundary would redistribute stresses in neighbouring grains. This redistribution of local stresses has also been shown in the supplementary research associated to publication 2 using a Kroner-type approximation (annex 6.5). Indeed publication 2 demonstrated the dominance of plastic anisotropies at boundary stresses. It is therefore essential to note that annex 6.5 and publication 2 differ in nature to those in publication 4, since the later considers only linear elasticity. Yet the local redistribution of stresses is present in both.

Choices of geometry (using truncated octahedra) for simulating the grains in the aggregate have also been explored in annex 6.8. Publication 1 was, in fact, first attempted with truncated octahedra but somehow poorer neutron diffraction simulation results were obtained as discussed in the publication. Publication 1 was therefore carried out using Voronoi tessellation. Publication 1 was also carried out using Voronoi tessellation in order to obtain a range of grain boundary orientations and

study the effect of these angles on the grain boundary residual stresses, as exposed above. A further limitation in 3D models is the computational cost. Ideally, very dense meshes of a very large number of grains using “good” (e.g. quadratic interpolation) elements should be used. Some of these meshing effects have been explored in publication 2 and section 6.10. In denser meshes used in section 6.10, a broader misorientation distribution around the three axes indicates the better accommodation of the constraints by the neighbourhood. Similarly, in publication 2, the finer the meshes used, the lower the grain boundary stress variability.

## **5.2 Further work**

### ***5.2.1 Slip-reversal***

Perhaps the most challenging and required model implementation in the near future is the incorporation of backstress at the slip level, i.e. making reverse slip easier on activated slip systems. This effect has been known to contribute to the Bauschinger effect of the aggregate. For example, for 304 stainless steel, we have tested the reloading yield stresses in different directions of a cold-rolled sample (Figure 5.1). Further, kinematical hardening at the slip level is believed to play a key role following strain path changes.

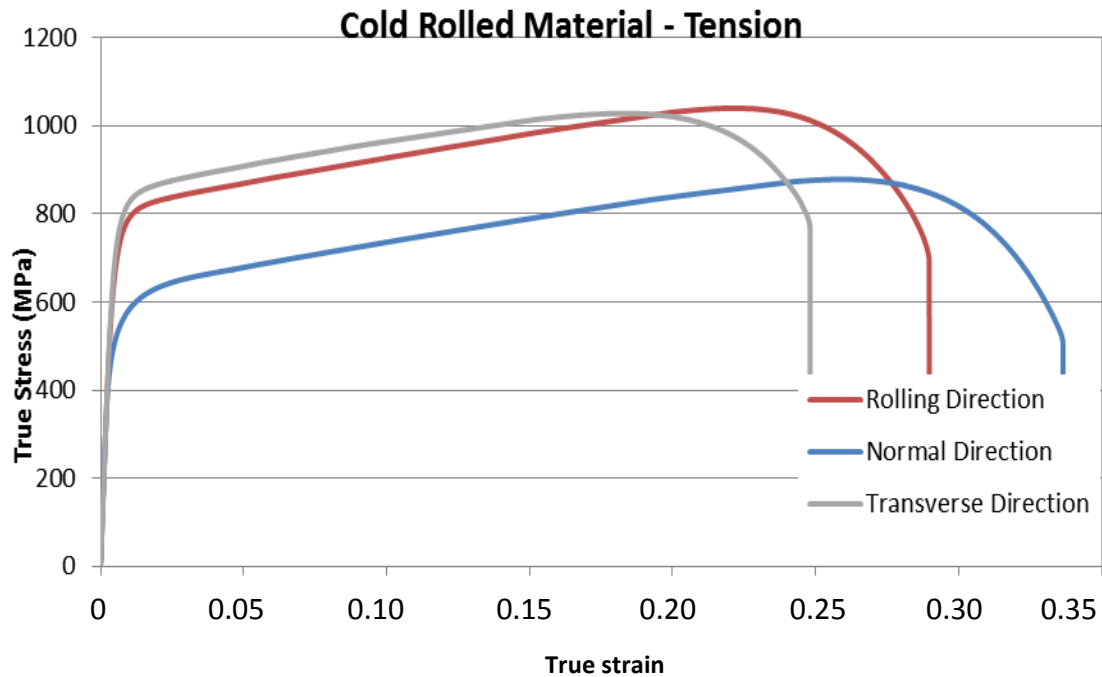


**Figure 5.1. Stress-strain curves following reloading of cold-rolled 304 stainless steel in three different directions: rolling direction, normal direction and transverse direction. The curves show a clear difference in yield stress for different directions (especially the transverse direction). Courtesy of David Wright (University of Manchester, UK)**

Back-stress has been simulated at the crystal slip level (Barbe et al., 2001). This approach is based on a macroscopic Armstrong-Frederick non-linear kinematic hardening and has been extended at the crystal level. The back stress rate term is a function of the plastic strain rate itself. Such approach has been demonstrated successful in simulating 3D aggregates.

Alternatively, the effect of strain softening in the opposite direction to the slip direction can be simulated without the knowledge of the back stress tensor. A strategy implemented by Lorentzen and co-workers (2002) considers that, as the hardening on a slip system that is loading is increased, the hardening coefficient on the opposite slip system, i.e. the same slip plane but opposite slip direction, is decreased by the same amount. This is a polycrystal plasticity model equivalent to the classical macroscopic kinematic hardening law. The main difference with macroscopic kinematic hardening is

that this describes a shift of the entire yield surface. In this case, however, the opposite slip direction is moved but the yield surface in other slip directions is unaffected. However, this is perhaps more representative of the “true” material, since it correlates with the reversal of dislocations on a given slip plane.

It would be possible to implement the slip-based kinematic hardening into an Abaqus material subroutine (UMAT) that simulates elasto-viscoplastic deformation via slip (Huang, 1991). Although the calculation of the back-stress tensor is possible, this latter approach would be easier to implement. The initial state variables controlling hardening in each slip direction would need to be twinned with those acting in the opposite sense of direction. This is possible since the knowledge of the Cauchy stress tensor allows resolving stresses and their sign, according to a convenient sign criterion.

### ***5.2.2 Further work on grain boundary stresses***

It is necessary to conduct experiments that can reveal stresses at boundaries to validate current models. An opportunity is open through Focused Ion Beam (FIB), in which the displacements caused by the relaxation after a sectioning proximate to the boundary can be incorporated into elasticity laws to reveal the stress state previous to the sectioning. Recent work shows that this technique can be used to infer stresses at the grain size level (Winiarski et al., 2011, Winiarski and Withers, 2012).

### ***5.2.3 Fatigue and SCC***

There are multiple future opportunities using CPFEM that arise from discussions in section 2.6. For instance, the experimentally observed nucleation sites in low cycle fatigue have been predicted as the regions of highest accumulated slip (Dunne et al., 2007). The research could then be extended to fatigue under complex loading paths. Further, the 3D path of an observed stress corrosion crack can be imported into a 3D CPFEM model containing damage-evolution boundary elements (e.g. cohesive elements

at the grain boundaries) (Simonovski and Cizelj, 2012). Then the damage-evolution properties would be adjusted according to the susceptibility/resistance of certain boundaries to SCC (see Annex 6.1)

#### ***5.2.4 Further work aluminium***

Further work could be performed in this project in the deformed state (Figure 4.9, central and right columns). Electron channeling contrast imaging of sectioned grains in the Bragg condition could be used to quantitatively characterize the dislocation density or the developed in-grain structures such as cell structures<sup>15</sup> (Gutierrez-Urrutia and Raabe, 2012). The link between these and the GOS or the average grain could be investigated. Similarly, predicted and measured average grain rotations could be plotted across a section of the aggregate (see Figure 4.9). This would enable us to visualize the level of agreement depending on the spatial arrangement of the grains i.e. grains with well-predicted average rotations could be grouped together in space.

#### ***5.2.5 Further work alumina***

The model could be extended to fracture simulation, since the interface elements used allow damage evolution with the extreme case of the total loss of stiffness at the boundary (crack). In this regard, a Griffith-type fracture criterion has been incorporated to simulate cracking in polycrystalline alumina (Yousef et al., 2005).

---

<sup>15</sup> As pure aluminium has a very high SFE, cell-walls structures are formed even at low strain (Landau et al. 2009)

## 6 Annexes

In this section some supplementary material is presented. In the first annex a summary of the recent findings on boundary susceptibility in SCC is presented. Such findings (Marrow et al., 2006, King et al., 2008) could be incorporated into models of observed cracks in 3D (section 5.2.3). In the second and third annexes, the methodology for averaging orientations and random crystal orientation assignments are respectively described.

Here, additional non-published research is disclosed. Firstly, we analyse the stresses developed in the vicinity of the grain boundary of an elastically anisotropic bicrystal. Secondly, we demonstrate the capability of sub-modelling in a bent bar i.e. the modelling at different length scales. Further, the intergranular stresses developed within individual grain families following 4 point bending and relaxation. Finally, we show CPFEM predictions of the statistical deviations of local rotations with respect to the average grain orientation. These results are then compared against EBSD measurements.

### **Co-authorship**

The virtual experiences in sections 4.1.1 and 4.1.2 have been fully carried out by myself. In sections 4.1.3 and 4.1.4, I have performed the simulations while the experimental data (ND, DHD and EBSD) has been provided by co-authors in references (Smith et al., 2009).

## 6.1 Annex: boundary character in SCC

1) Orientation of the *boundary plane*  $\{hkl\}$  with respect to its lattice. The low index planes are resistant. For instance, the plane (111) it is considered as a low index plane.

2) *Coincidence Site Lattice* (CSL or  $\Sigma$ ) is inversely proportional to the number of common atoms between the two lattices at the GB. Boundaries with  $\Sigma 11$  or lower tend to be resistant (e.g  $\Sigma 3$  or twins boundaries). Only boundaries with  $\Sigma > 29$  have been classified as susceptible boundaries.

3) Boundary *misorientation*, being those below  $9.4^\circ$  identified as resistant<sup>16</sup>.

A highly corrosion-susceptible boundary may be linked to a high boundary energy, where formation of chromium carbides is easier. This involves chromium depletion at the boundary, which may be enhanced by cold work. Read and Shockley (Read and Shockley, 1950) found that the boundary energy increases as the misorientation angle increases up to  $15^\circ$ , being the tilt accommodated by edge or screw dislocations. Rohrer (2004) has reported low boundary energy occurring in low index boundary planes. The relationships between the boundary energy and the CSL (Humphreys and Hatherly, 2004) are not simple, although some advances have been done (Badiyan and Shekhovtsov, 2006).

## 6.2 Annex: Random crystal orientation assignments

In order to assign local random orientations to each of the crystals of the aggregate we concluded that the most feasible way is to consider the centre of an sphere as the origin of the coordinate system  $(x, y, z)$  and select a random point on the sphere to define the

---

<sup>16</sup> Note that these groups are somewhat interrelated. For example, most of the  $\Sigma 3$  (resistant boundaries) have also a low  $\{hkl\}$  index (111) because that is how they naturally grow. The  $\Sigma 3$  with a  $\{hkl\}$  index other than (111) are not resistant.

first axis. After this selection, another random selection (second axis) needs to be performed between 0 and  $2\pi$  around the first axis. Clearly, the latter selection simply consists of a random number to be picked within 0 and  $2\pi$ . One could assume the former selection by simply assigning a point's spherical coordinates to a proportional random number. However, this would lead to weighting towards the poles, meaning that a correction to “non-weighted” the natural effect is needed. To better describe this non-random first point selection, consider a random selection of the angles in the vertical direction in the red grid in Figure 6.1 (left). Clearly this selection is uniform in units of angles but it is not in units of

Top view                      Side view                      Top view                      Side view

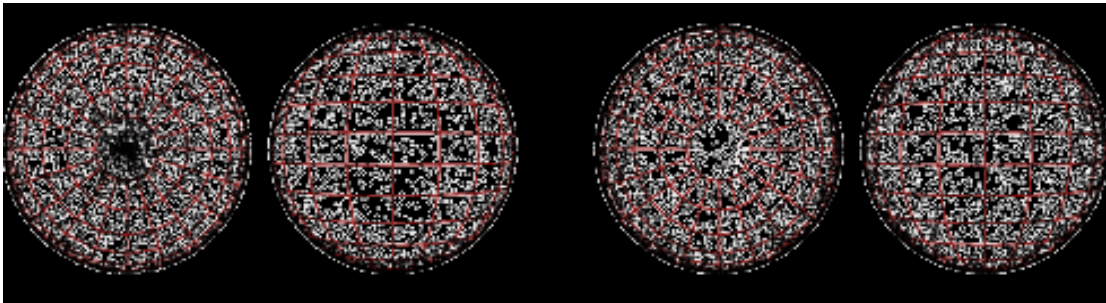


**Figure 6.1 Left) showing the incorrectly distributed points, Right) showing the correctly distributed points (Weisstein, 2012).**

area,  $d\delta$ , which become smaller near the poles. Thus, if not correction is applied, the population density near the poles is expected to be greater since the expected occurrence in these units of area it is the same as the rest but the unit of area is smaller. The corrected angles can be found as (Weisstein, 2012) a function of two random numbers,  $u$  and  $v$ , (both between 0 and 1) to define two axis ( $\mathbf{x}$  and  $\mathbf{y}$ ) by the two angles,  $\theta$  and  $\phi$ , the first one corrected and the second one proportional to  $2\pi$ :

$$\phi = \arccos(2v - 1) \tag{Eq. 6.2.1}$$

$$\theta = 2u\pi \tag{Eq. 6.2.2}$$

After such a correction is applied, any view of the sphere with a sufficiently large number of picked points should show a similar distribution, because of the infinite symmetry planes in a sphere (see Figure 6.1 (right)). The third axis of the material orientation is directly defined by the cross product vector between the first two vectors.

### **6.3 Annex: averaging orientations in crystals**

Barton and Dawson (2001) suggested a Newton-Raphson based method to average orientations. However crystal symmetry was not dealt with. Years later, the arithmetic average of quaternions was presented as not suitable when dealing with crystal symmetry (Cho et al., 2005).

For example, suppose the two orientations in Figure 6.2 to be averaged when cubic crystal lattice is present. The upper row gives the result when using the quaternions arithmetic mean to average the orientations (e.g. (Pantleon, 2008)). Clearly this does not represent the true average, instead the mean is either of the two orientations because of the crystal symmetry (lower row in Figure 6.2).

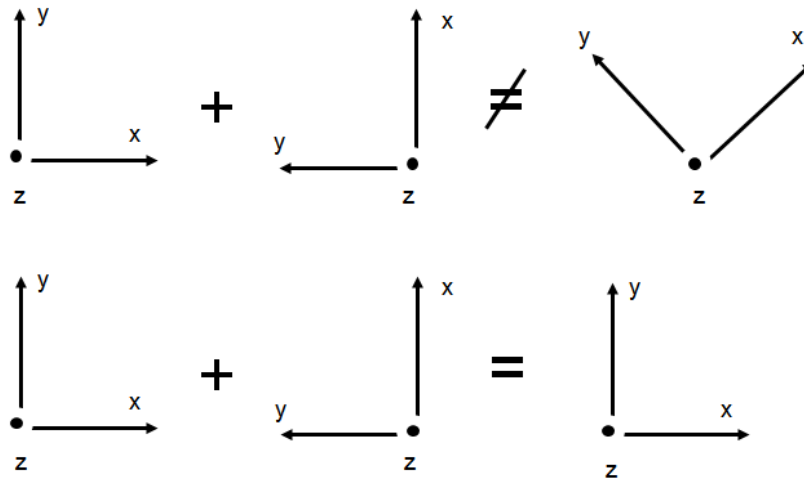


Figure 6.2. The upper row represents the arithmetic mean orientation when computed using quaternions and symmetry is neglected. The lower row represents the correct mean when cubic symmetry is present, which is equivalent to any of the two initial orientations

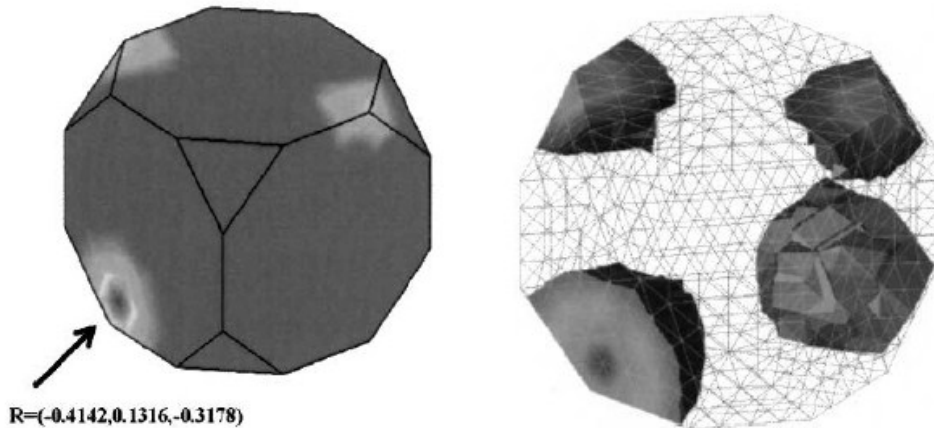


Figure 6.3. Brass texture component,  $\{144.74, 45, 270\}$  in Bunge Euler angles is represented on the truncated cubic fundamental region in Rodrigues' space. The Brass component lies on the symmetry plane: (a) filled region and (b) transparent region. (Cho et al., 2005)

To illustrate this further, we can consider a typical Brass texture component in Rodrigues space (similarly in quaternions space) in Figure 6.3. Such texture component lies on the symmetry plane. Therefore, pairs of points belonging to that fundamental region can have small disorientation angles, yet appearing far apart in space. This is inconvenient for computing the arithmetic average so the fundamental zone or

disorientation zone is not appropriate for calculating the mean orientation of a set of points. Crystal symmetry can be used to place all the orientations close to one another and minimize the misorientations between them, but it is not helpful to confine the cloud to any particular copy of the fundamental zone, because we do not want the cloud to be divided by a symmetry plane, as shown in Figure 6.3.

In order to deal with symmetry, a position criterion (Cho et al., 2005) was developed to average orientations. However, such method has only been applied for 2D measurements (we need 3D for the model). Moreover, this method is path dependent since the final result depends on the path chosen in a 2D grid. Alternatively, the geometrically central orientation could be taken as the mean orientation (Kamaya et al., 2005). Nevertheless, the mean orientation can become sensitive to local rotations or local texture.

In view of the complexity of averaging orientations with crystal symmetry, we have used a *Hill Climbing* procedure. We have chosen the quaternion that minimizes the sum of the misorientations from the trial quaternion to each of the other local orientations of the grain. We have considered (of course), for each point, the quaternion with the minimum rotation according to its symmetry. We have taken our trial orientations as each of the points of the grain where the orientation is known. This method is considerably computationally intense (because of its repetitive nature) and is schematically presented in Figure 6.4.

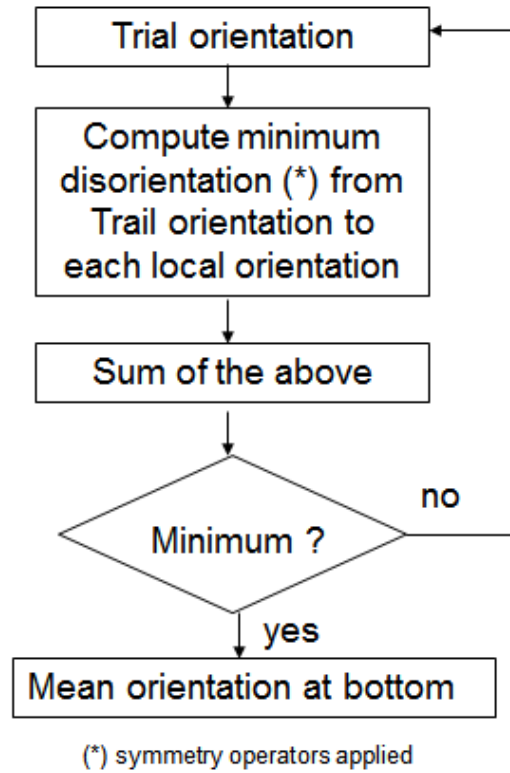


Figure 6.4. The Hill Climbing procedure used in the current research to determine the grain averaged orientation

## 6.4 Supplementary research associated with publication 1

In the remaining of the results and discussions section, some supplementary research is presented. Some key pre-processing and post-processing methods are first described. Further, some discussions on intragranular features as well as the particularity of the  $C_2C_1$  path using the Prager kinematic hardening description macroscopic are analysed.

### 6.4.1 Pre-processing

The Voronoi diagram is the nearest-neighbour map for a set of points. Each region contains those points that are nearer to one input site than to any other input site. Meshing geometries containing relatively very small features can be problematic (Quey

et al., 2011). In the case of the ABAQUS C3D10M elements (quadratic), the poor mesh quality (rather coarse) results in some elements becoming too distorted. Very small edges have been suppressed in the Voronoi structure to avoid distortion when using such elements (see Figure 6.5). Special attention has been paid to boundaries consisting of 3 small edges. Boundaries belonging to these edges have not been merged in an effort not to lose the boundary. In cases where the small edges could not be removed, a local mesh refinement has been applied (Figure 6.6).

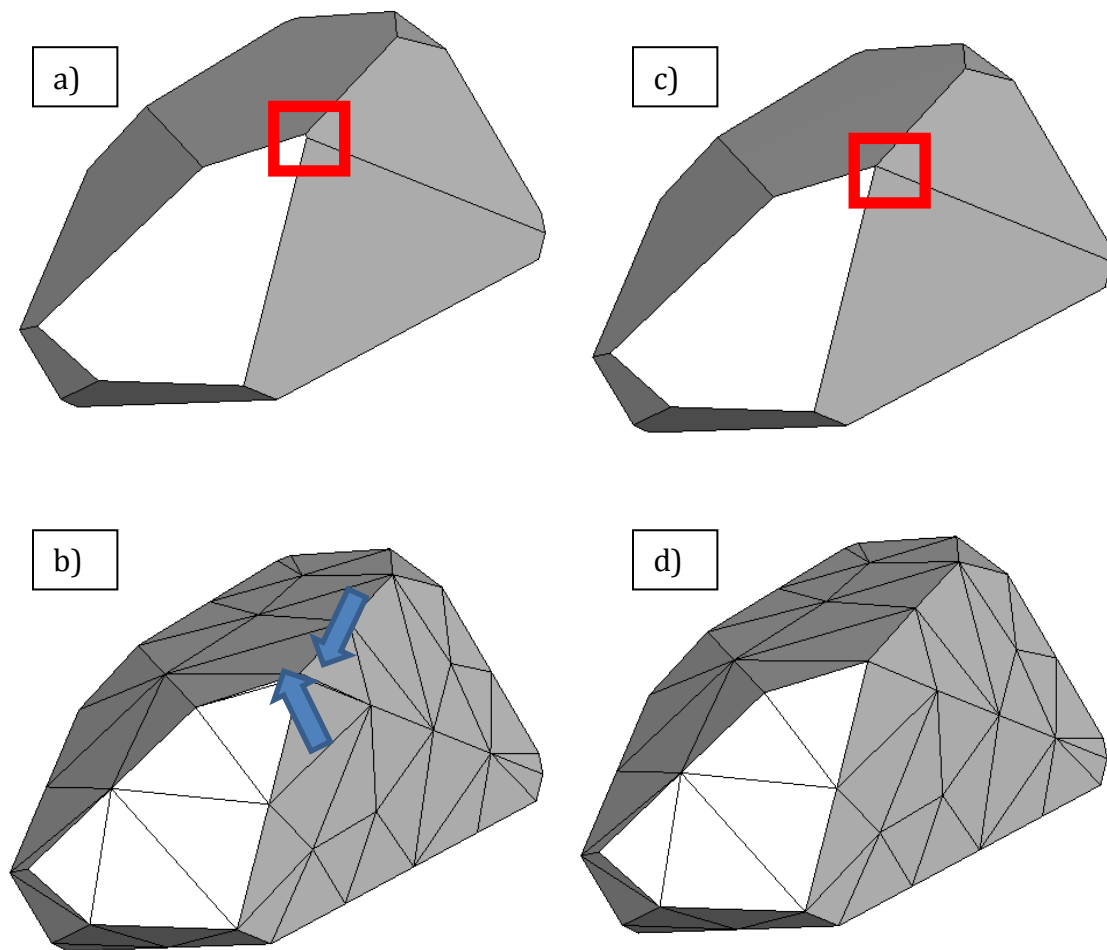


**Figure 6.5. Grain showing the removal of relatively small edges (a) to avoid distorted elements (marked with arrows in (b)). Grain after edge removal (c), and final mesh (d).**

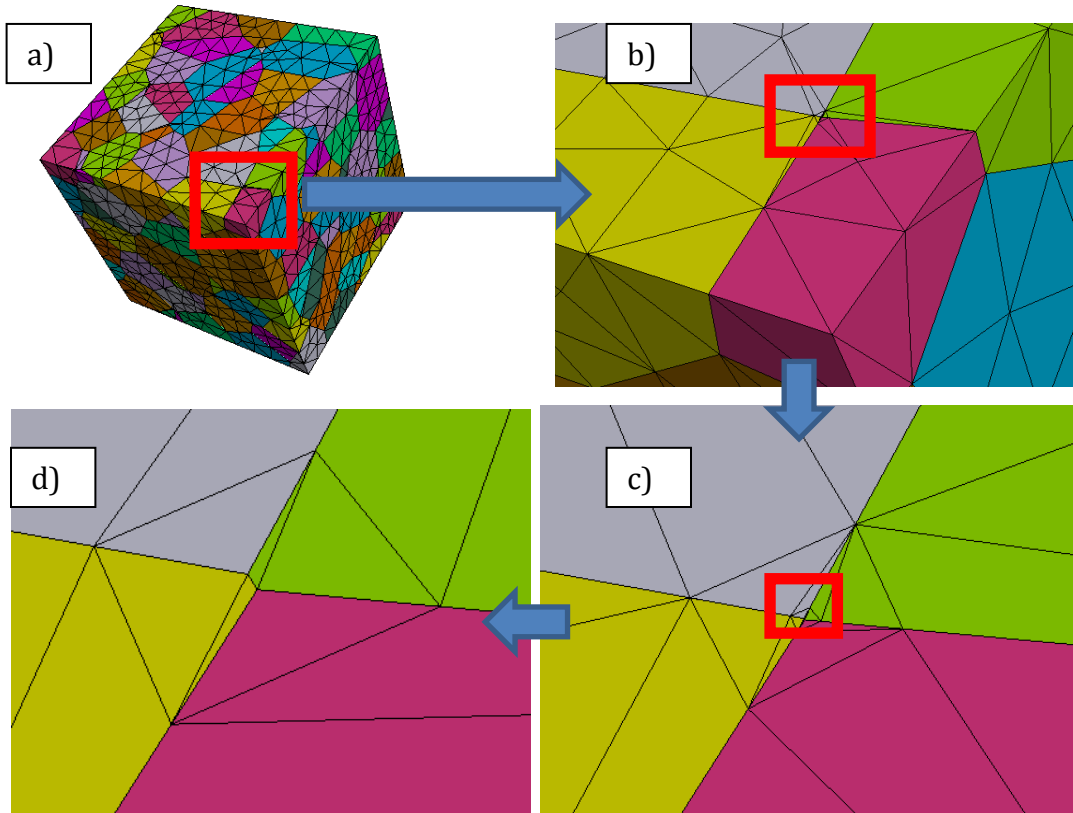


Figure 6.6. Resulting local mesh refinement (using ABAQUS C3D10M elements) to avoid element distortion. The RVE is shown in a) whereas close-up views are shown in b), c) and d).

### 6.4.2 Post-processing

A post-processing code has been written in Python and C++ to obtain the elastic strains for different families of crystallographic planes, as would be measured by neutron diffraction. Although not presented here, simulations of elastic strains using grains shaped as truncated octahedra (section 4.1.2) were also carried out. Surprisingly, agreement between neutron diffraction measurements and model predictions was found to be poorer than for the 3D Voronoi case.

### 6.4.3 Intragranular features

Recent ND studies have revealed a slight decrease of the peak width upon unloading in 304 stainless steel (Ahmed, 2011). This suggests softening during unloading by slip

reversal. The incorporation of kinematic hardening at the slip level in the model has been recommended in the conclusions in this work. However, accurate predictions may be more challenging than softening a slip plane on its reverse slip direction. The Bauschinger effect may be inherently anisotropic at the crystal scale. Dislocation boundaries accommodated in specific planes (Huang and Hansen, 1997) and the angle formed between the strain measurement direction and the loading axis play an important role in the peak broadening asymmetry (Pantleon et al., 2004). This suggests a source of short-range internal stresses that may alter the elastic strains within grains of each family.

#### ***6.4.4 Permanent softening at the macroscale***

In this section we use continuum plasticity to explain the low reloaded yield for the  $C_2C_1$  path, which is in consistency with its lower  $\alpha$  and our experiment. This is, of course, an approximation of reality since promoted slip reversal and dislocation annihilation will occur only in active slip systems, changing the macroscopic cylindrical yield surface shape.

A crystal accommodates the displacements imposed by its neighbours by slip and lattice rotations. This is achieved not only by movement of dislocations but also by creation of new dislocations which harden the material. This type of hardening would, in principle, harden the material equally in all subsequent reloading directions. Therefore, the elastic region increases uniformly upon subsequent strain paths. A hardening model can be used to describe this behaviour: isotropic hardening, in which the radius of the cylinder of plastification increases. This type of hardening has been claimed to be associated with the formation of stable dislocation structures, such as cell walls (Zang et al., 2011). In the (unrealistic) case that a material did not show any BE, its hardening may be described by pure isotropic hardening.

Prager (1956) first proposed a model to describe the Bauschinger effect: *kinematic hardening*, which has been claimed to arise from the motion of stable dislocations (Zang

et al., 2011). An internal stress tensor ( $\mathbf{x}$ ) or *backstress* was assumed to superpose the applied stress, changing the effective yield strength. As a result, kinematic hardening implies a translation of the cylinder of plastification (Dunne and Petrinic, 2005). This translation can be represented by a directional stress or backstress vector which is present upon loading reversal. Years later, some other popular variants of kinematic hardening have been proposed (Armstrong and Frederick, 1966, Chaboche, 1986), which have been reported to better capture the transient and permanent macroscopic stress strain responses.

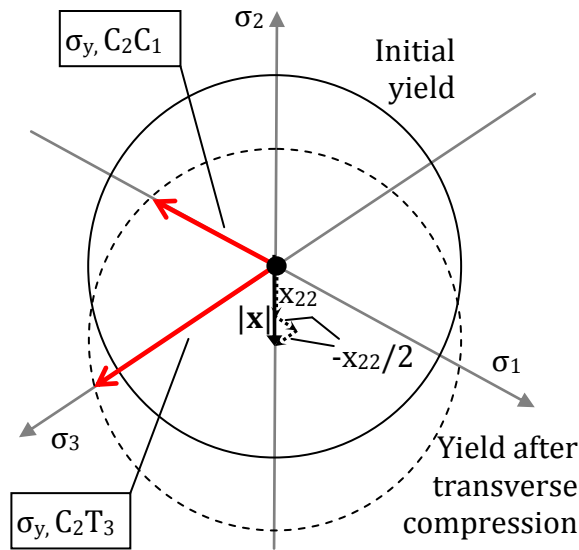


Figure 6.7. Resulting yield strengths  $\sigma_y(C_2C_1)$  and  $\sigma_y(C_2T_3)$  as a result of the yield surface translation represented on the deviatoric plane or  $\Pi$  plane (Hill, 1998). The magnitude of the backstress tensor is represented as  $|\mathbf{x}|$ . After compression in a transverse direction, the yield strength at  $90^\circ$  to this direction (in the axial or the other transverse direction) is reduced for compression but increased for tension (red arrows), when purely kinematic hardening and no shape change are assumed.

If isotropic hardening is neglected for the time being, pre-straining will translate the elastic domain in one direction. This would be evident as a lowering in yield strength in the directions perpendicular to the pre-strain, in addition to the conventional Bauschinger effect ( $180^\circ$  strain path changes). Prager assumed a linear proportionality between the increment of backstress and the increment of plastic strain. Based on this

theory, we note that like plastic strain, uniaxial loading creates not only a uniaxial component of  $\mathbf{x}$ , but also the other direct components. Assuming a material that macroscopically obeys the Von Mises criterion, Figure 6.7 shows the final yield surface as well as the resulting yield strengths  $(\sigma_y, C_2C_1)$  and  $(\sigma_y, C_2T_3)$  in the directions transverse to the prestrain. The yield strength for the  $T_3C_1$  strain path, although not shown for the sake of clarity, is equivalent in magnitude to  $(\sigma_y, C_2T_3)$ .

The uniaxial component of backstress,  $x_{22}$ , as a function of the uniaxial prestrain and the backstress magnitude,  $|\mathbf{x}|$ , are addressed next. Firstly we can examine the components of the backstress tensor,  $d\mathbf{x}$ , as a function of the uniaxial prestrain (Dunne and Petrinic, 2005). We consider the incremental plastic strain tensor for uniaxial loading in the 2-direction:

$$d\boldsymbol{\varepsilon}^p = \begin{pmatrix} -\frac{1}{2}d\varepsilon_{11}^p & 0 & 0 \\ 0 & d\varepsilon_{11}^p & 0 \\ 0 & 0 & -\frac{1}{2}d\varepsilon_{11}^p \end{pmatrix} \quad (\text{Eq. 6.4.1})$$

We have taken the increment in kinematic hardening ( $d\mathbf{x}$ ) to be proportional to the increment of plastic strain ( $d\boldsymbol{\varepsilon}^p$ ):

$$d\mathbf{x} = \frac{2}{3}cd\boldsymbol{\varepsilon}^p \quad (\text{Eq. 6.4.2})$$

where  $c$  is a material constant. This is called Prager linear hardening.  $d\boldsymbol{\varepsilon}^p$  is deviatoric because of the incompressibility condition. Therefore  $d\mathbf{x}$  is also a deviatoric quantity according to Eq. 4.2. For uniaxial loading in the 2-direction we may then write:

$$d\mathbf{x} = d\mathbf{x}' = \begin{pmatrix} -\frac{1}{2}dx_{11} & 0 & 0 \\ 0 & dx_{11} & 0 \\ 0 & 0 & -\frac{1}{2}dx_{11} \end{pmatrix} \quad (\text{Eq. 6.4.3})$$

Combining equations Eq. 4.1, Eq. 4.2 and Eq. 4.3 we find that:

$$dx_{11} = \frac{2}{3}cd\epsilon_{11}^p \quad (\text{Eq. 6.4.4})$$

The *magnitude* or *norm* of the backstress vector,  $|\mathbf{x}|$ , is shown in Figure 6.7 by construction and defined as:

$$|\mathbf{x}| = \left[ \left( \begin{array}{ccc} x_{11} & 0 & 0 \\ 0 & -\frac{1}{2}x_{11} & 0 \\ 0 & 0 & -\frac{1}{2}x_{11} \end{array} \right) : \left( \begin{array}{ccc} x_{11} & 0 & 0 \\ 0 & -\frac{1}{2}x_{11} & 0 \\ 0 & 0 & -\frac{1}{2}x_{11} \end{array} \right) \right]^{1/2} = \left| \frac{3}{2}x_{11} \right| \quad (\text{Eq. 6.4.5})$$

Since the axis of the cylinder is perpendicular to the  $\Pi$  plane in Figure 6.7, the yield strengths  $(\sigma_y, C_2C_1)$  and  $(\sigma_y, C_2T_3)$  are accurately represented in magnitude. This is consistent with the lower yield observed in the experiment for the  $C_2C_1$  than for the other two equivalent strain paths studied.

## 6.5 Supplementary research associated with publication 2

In this section we first address further relationships between stresses at boundaries in soft-hard grain combinations. Secondly, sensitivity results on the unloaded state that are briefly described in the publication are further examined. Finally, in order to gain a better insight of the results, the histograms of stresses of parallel and orthogonal boundaries in the unloaded state are presented.

### 6.5.1 Stresses at grain boundaries between soft and hard grains

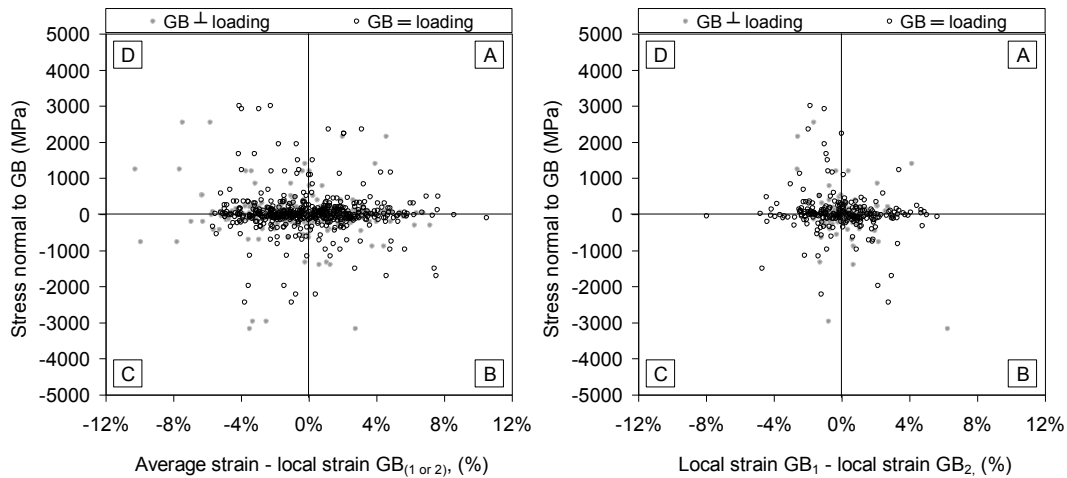


**Figure 6.8. Stress normal to boundaries versus the difference between a) the averaged plastic strain of the aggregate and the local plastic strain in the vicinity of the grain boundary; b) the plastic strains at each side of the grain boundary. All the results correspond to the unloaded state after 10% uniaxial strain. All the strains are resolved in the normal direction to the GB for comparison with Kroner approximation. The values are presented for boundaries approximately orthogonal and approximately parallel to the loading direction.**

Here discussions on section 3.4.2 of the main publication are recaptured. Figure 6.8a shows the relationship between the grain boundary stress and the differences of averaged and local plastic strains, all variables resolved direction normal to the boundary planes. For each boundary, the averaged plastic strain is calculated from the whole aggregate. The local plastic strain is taken as the elements in contact with the boundary for each grain. Thus, each boundary produces two local regions and consequently two values in the horizontal axis in Figure 6.8a. Two sets of boundaries are examined: parallel boundaries to the loading direction estimating that boundaries with  $\varphi$  higher than  $75^\circ$  are parallel and, orthogonal boundaries estimating that grain boundaries with  $\varphi$  lower than  $30^\circ$  are orthogonal. Following discussion derived from Eq. 8 (in publication 2), a boundary assumed to be parallel may exhibit tension if the local normal strain is higher than average whilst it may exhibit compression if the local normal strain results lower than that averaged for the aggregate. This means that, if the

present Eshelby-based approximation was somewhat applicable to randomly oriented polycrystals, the stress values in parallel GBs would show a tendency towards quadrants D and B (Figure 6.8a). Similarly, a tendency for orthogonal boundaries towards quadrants A and C would be noticed for plastically harder (than average), and plastically softer boundaries respectively. Such tendencies are clearly not observed; even when small boundaries, that present highly extreme stresses, are neglected. This may be explained, as previously discussed, by the strong influence of the neighbours acting over long distances within the polycrystal.

Although not shown, the results were further examined by considering the averaged strain as that of the two whole adjacent grains to the boundary in place of the aggregate averaged strain. The purpose was to consider a “more local” average strain. Again, this did not show any correlation between differences of plastic strain and calculated stress. We further considered the differences between the local normal plastic strains at each side of the grain boundary in an effort to relate these to normal stresses (Figure 6.8b). This test seems reasonable since damage is highly related to severe local strain heterogeneity (Bieler et al., 2009). Once again, such local strain difference failed to correlate with the predicted stresses, regardless of the orientation of the boundary.

### ***6.5.2 Effect of excluding small grain boundaries***

In the main publication it was clearly shown the stress variability shown in relatively small boundaries. It is, however, less clear whether the pronounced effect of the small boundaries arises from their small size or from the lack of integration points on such boundaries. In this section we study the effect of excluding small grain boundaries (e.g. Figure 6.9) on the relationship between boundary stress and grain boundary angle. Figure 6.10 shows the reduction of the extreme predicted stresses for all the angle intervals as the boundary-size exclusion increases in the fully anisotropic model.

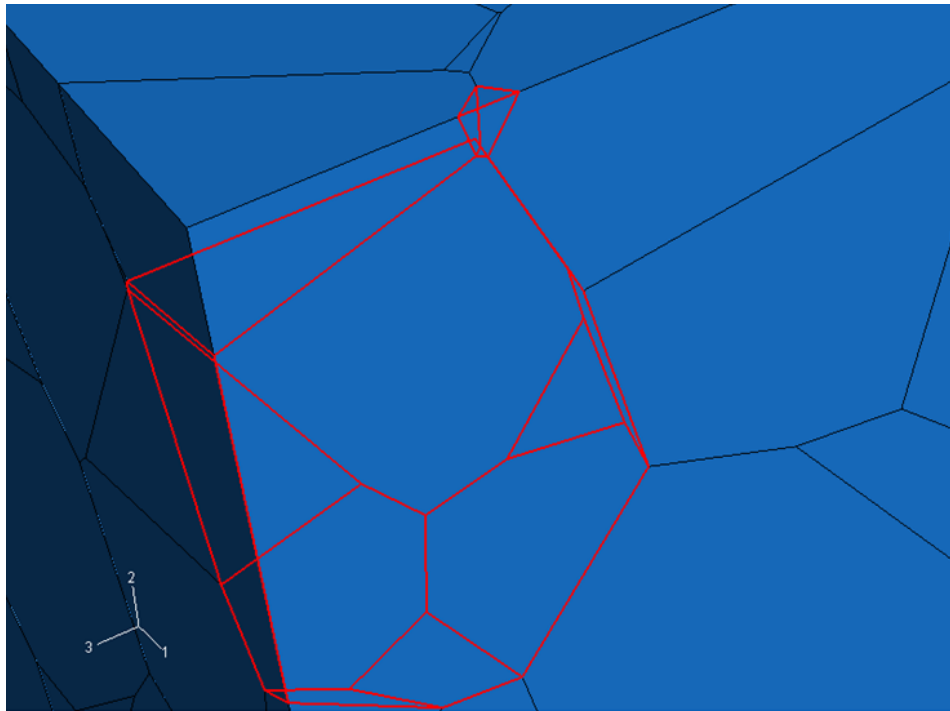


**Figure 6.9. Example of a relatively small boundary (circled in white) where stresses show a much greater variability than other boundaries.**

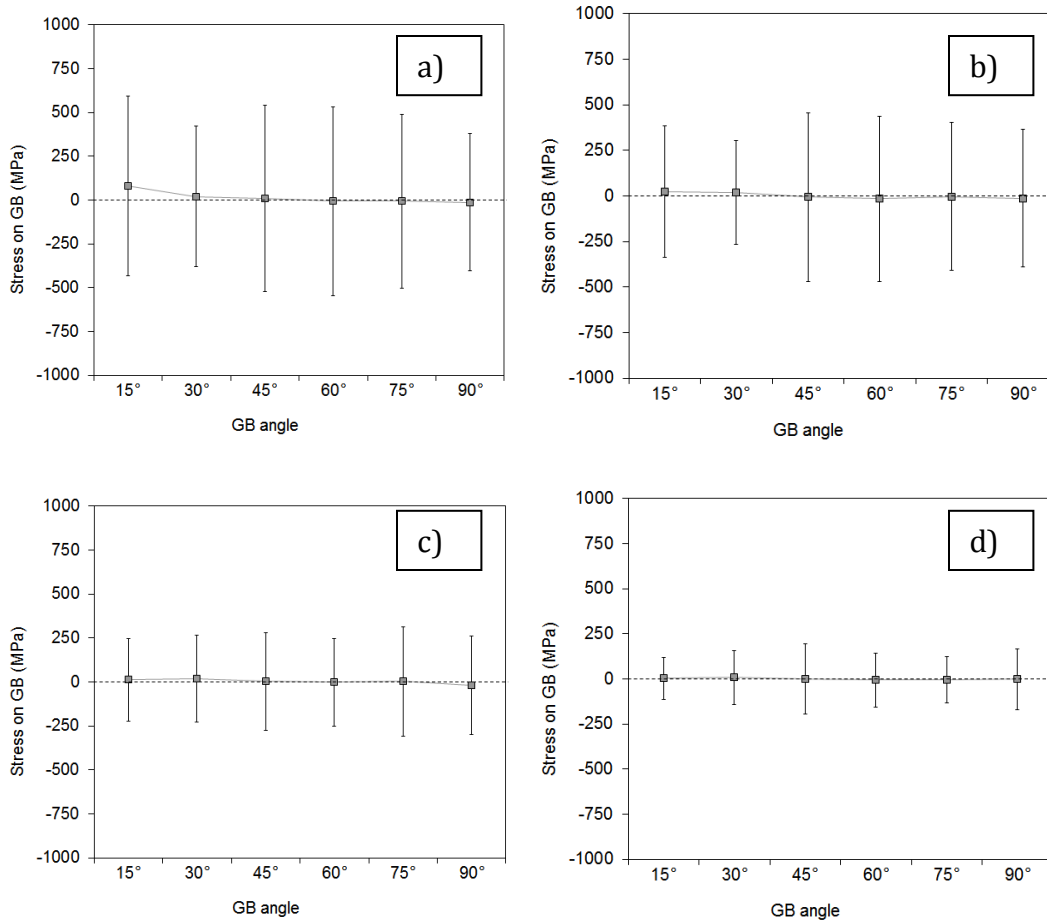


**Figure 6.10.** Average grain boundary stress for each grain boundary angle interval (solid squares) with the exclusion of the smallest: a) 70 boundaries (1 cohesive element each boundary), b) 109 boundaries (2 cohesive elements or less each boundary), c) 200 boundaries (4 cohesive elements or less each boundary), d) 400 boundaries (11 cohesive elements or less each boundary). Error bars show the standard error for each grain boundary angle interval.

### 6.5.3 Distribution of stresses at parallel and orthogonal boundaries

Here we further investigate the distribution within angle intervals when all boundaries are included. Namely, the 0°-15° (orthogonal) and 75°-90° (parallel) intervals are studied. The results are presented in Figure 6.11 and Figure 6.12 respectively. The distributions appear to follow a Gaussian distribution without any noticeable difference between parallel and orthogonal boundary sets.

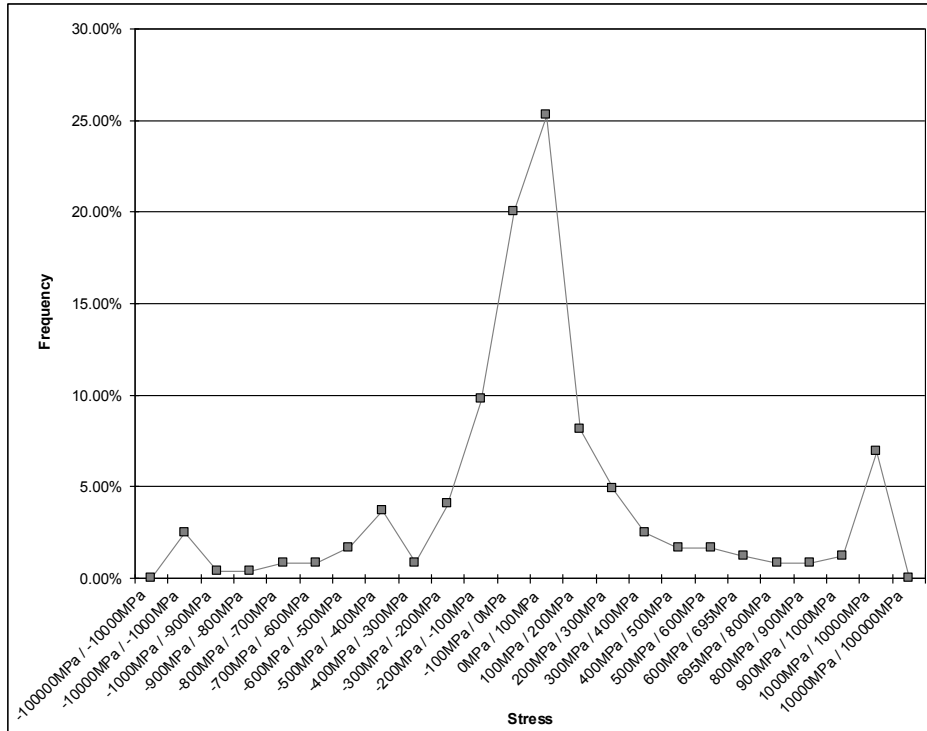


**Figure 6.11. Histogram of stresses normal to boundaries whose boundary planes normal form an angle lower than 15° with the loading direction (orthogonal) in the fully anisotropic model. The results correspond to the unloaded state after 10% uniaxial strain.**

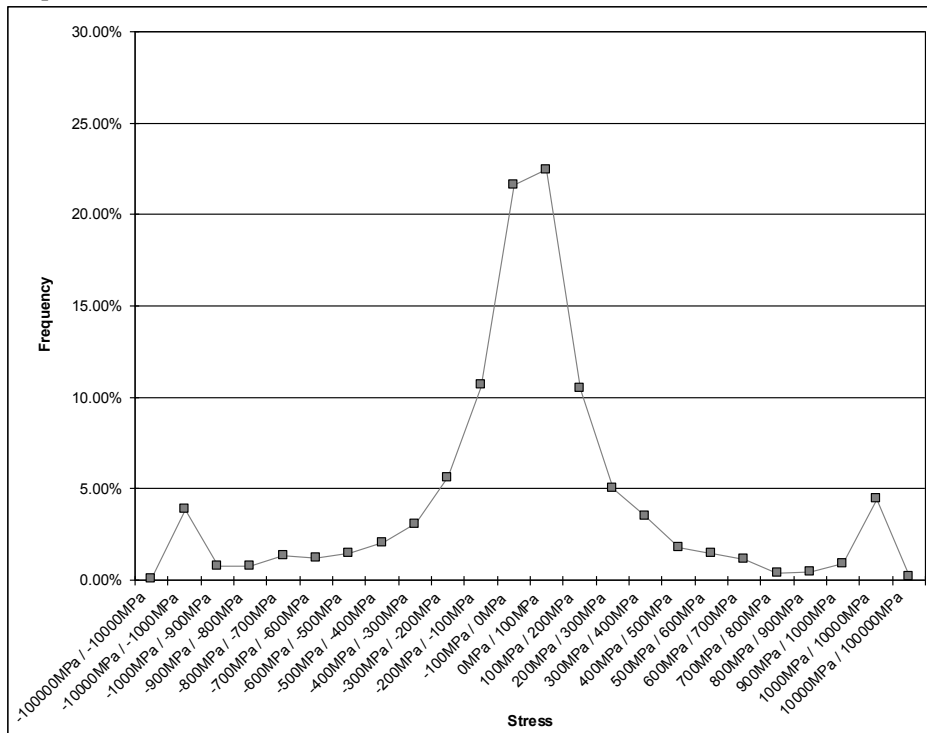


**Figure 6.12. Histogram of stresses normal to boundaries whose boundary planes normal form an angle higher than 75° with the loading direction (parallel) in the fully anisotropic model. The results correspond to the unloaded state after 10% uniaxial strain.**

## **6.6 Supplementary research associated with publication 3**

Here we first address the lattice rotation maps as annealed, as deformed and as the difference of these two (shown in publication 4). Moreover, we demonstrate the poor correlation of the measured and predicted GOS when the grain volume does not enter the correlation.

### ***6.6.1 Lattice rotation maps***

In the text it is commented: “...the grains for the undeformed sample showed distortion (probably due to residual strain during grain growth)”. Figure 6.13 shows the measured distortions before and after deformation. It is reasonable to link the observed initial misorientations with the non-trivial dislocation density in well annealed crystals  $10^{10} \text{ m}^{-2}$  ((Honeycombe, 1984), p. 88) because the recrystallization is driven by the stored energy of these dislocations (Carpenter and Elam, 1920). Another source of distortion may arise from the effect of the grain boundary energy which influences grain growth.

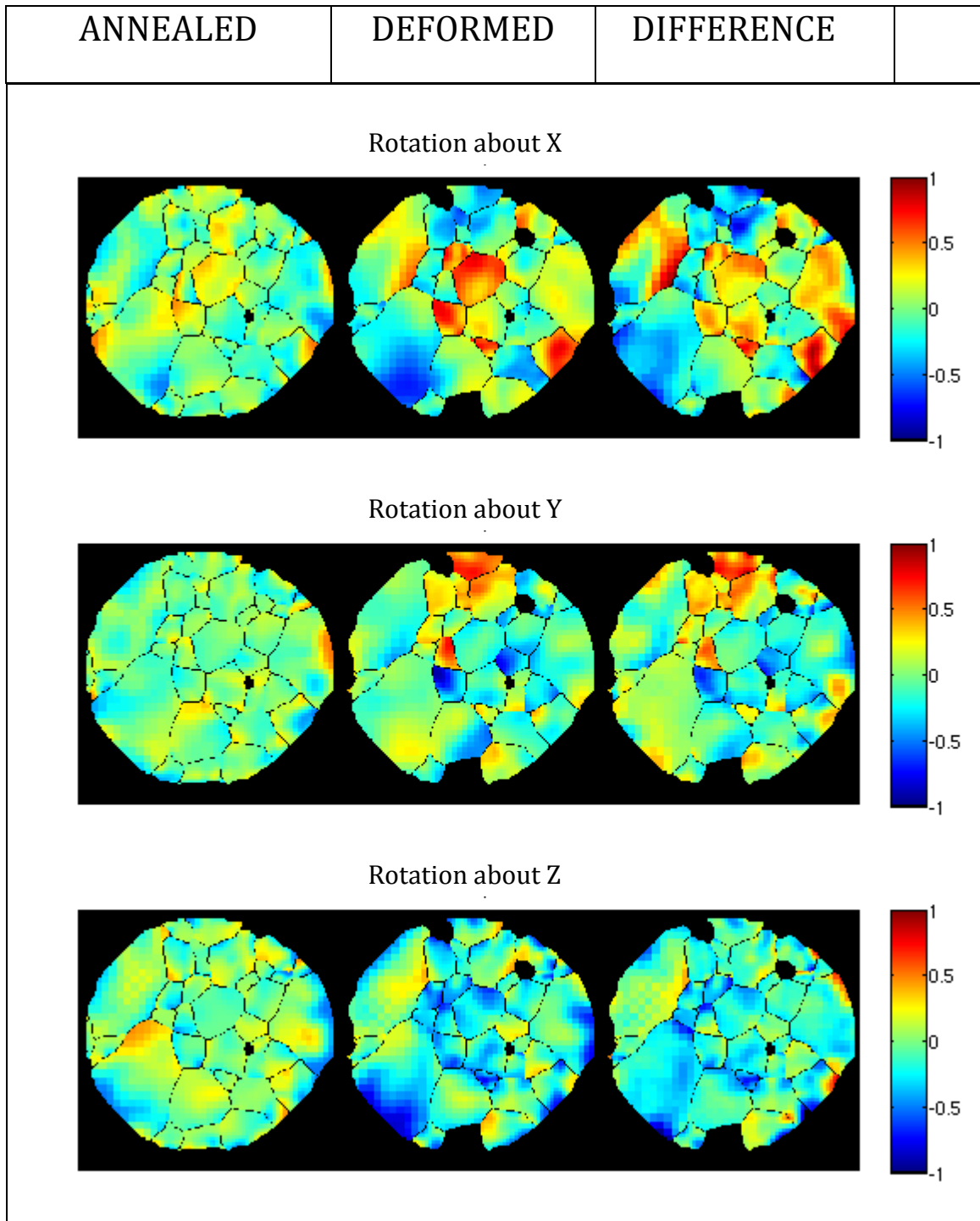


Figure 6.13. Local rotations about the grain average orientation, resolved about the X, Y and Z axes (in deg.). The rotations after annealing, subsequent deformation and the difference between these are shown in the left, central and right columns respectively.

### 6.6.2 Grain orientation spread

In Figure 6.14, the predicted and measured mean orientation spreads are plotted; in this case without dividing each by the grain volume. The correlation in this case is very weak. The observed in-grain misorientation is much larger for larger grains. When the grain volume enters the correlation (Figure 3 in the main paper), the strong dependence of the grain volume on the in-grain misorientation is very clear. This may be due to the fact that interior regions of the grain solidify first than outer regions, generating larger misfits in larger grains.

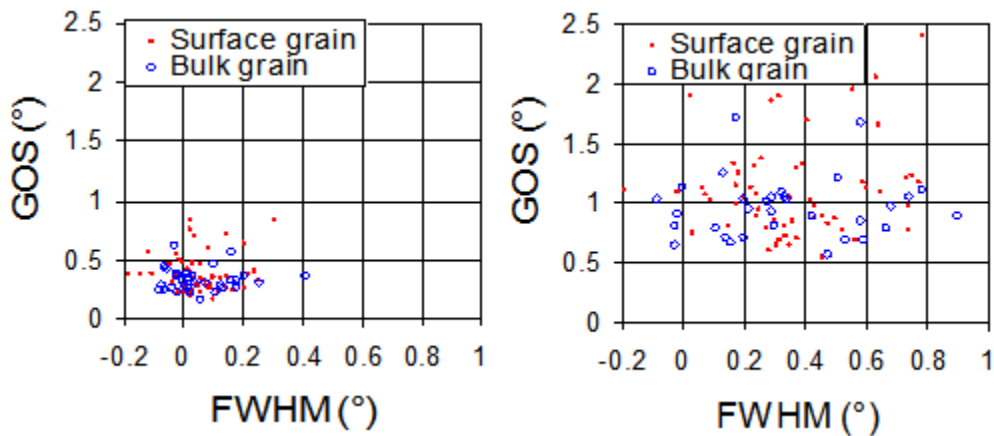


Figure 6.14. Measured diffraction blob spread by DCT versus Grain Orientation Spread (GOS) by CPFEM as loaded in compression at; a) 1.2% strain, b) 4.4% strain

## 6.7 Elastic bi-crystal simulations

A grain boundary is likely to raise stresses in its surroundings due to the deformation incompatibility due to elastic and plastic anisotropies. The grain boundary misorientation has been shown to influence the deformation close to the boundary in a plastically deformed aluminium bicrystal (Zaefferer et al., 2003). In this section, this fundamental question is envisaged via CPFEM considering only elastic anisotropy. This

study is somewhat simple but has served as a motivation for investigating the effects of elastic anisotropy in a polycrystal (publication 2). Attention is focused on the variability of stress caused by elastic anisotropy. The single crystal elastic constants used are those for 316 stainless steels:  $C_{11}=205$ ,  $C_{12}=138$  and  $C_{44}=126$  GPa (Ledbetter, 1984).

The boundary conditions applied are shown in Figure 4.11a. Two constraints have been set as follows: 1) restrictions of movement only in the loading direction of the square surface below the cube 2 with the wall and 2) restriction of movement in directions **1** and **2** plus rotation around direction **3** at Point A. These restrictions have been intentionally set to let the Poisson contraction, avoiding artificial stress risers because of the constraint. As shown in Figure 4.11a, a pressure of 100 MPa has been applied to act normal to the (squared) boundary of the bicrystal. This load is significantly below the uniaxial general yield of the polycrystal ( $\sim 200$ MPa) so it is expected that the bicrystal is deforming elastically throughout the simulation.

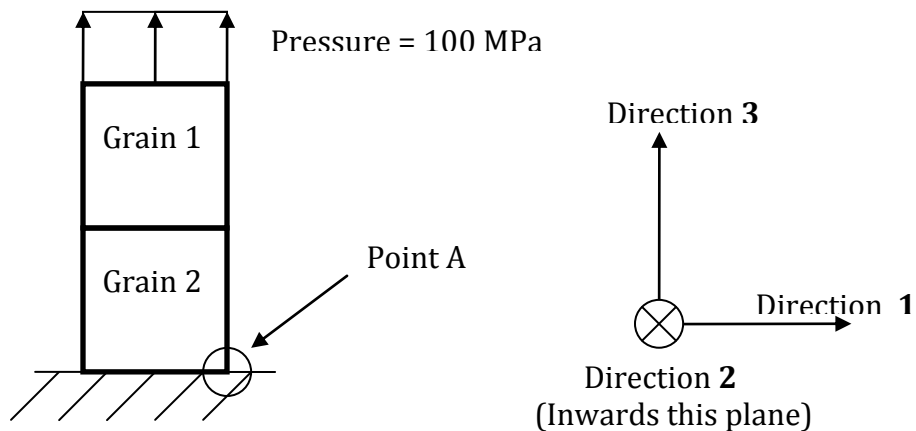


**Figure 6.1. Elastic simulation of a bicrystal showing: a) layout of the model and b) the definition of the coordinate system employed.**

Each cube is composed of 250 C3D20R ABAQUS elements. A C3D20R ABAQUS element is composed of 8 Gauss points and 20 nodes. Four simulations were run assigning different material orientations to cube 2 (or grain 2) while the orientation of cube 1 (or grain 1) was always the sample coordinates (Figure 4.11). The reference system is as

described in Figure 4.11b. The direction cosines of the directions **1** and **2** of cube 2 (in the sample coordinates) were  $\langle 1\ 0\ 0 \rangle$  and  $\langle 0\ 1\ 0 \rangle$  for the first simulation;  $\langle 0.447\ 0\ 0.894 \rangle$  and  $\langle 0\ 1\ 0 \rangle$  for the second;  $\langle 0.707\ 0\ 0.707 \rangle$  and  $\langle 0\ 1\ 0 \rangle$  for the third; and,  $\langle 0.577\ -0.577\ 0.577 \rangle$  and  $\langle 0.408\ 0.817\ 0.408 \rangle$  for the fourth simulation. The corresponding misorientation angles are 0, 26.56, 45 and 56.6 degrees respectively. The Von Mises stresses obtained for the simulation with 45 degrees are shown in Figure 4.12. The maximum stress at the nodes is shown to be  $\sim 150$  MPa. Closer examination of the values registered at the Gauss points showed a slightly lower value of maximum Von Mises stress (137 MPa). This is attributed to the node extrapolation across the element.

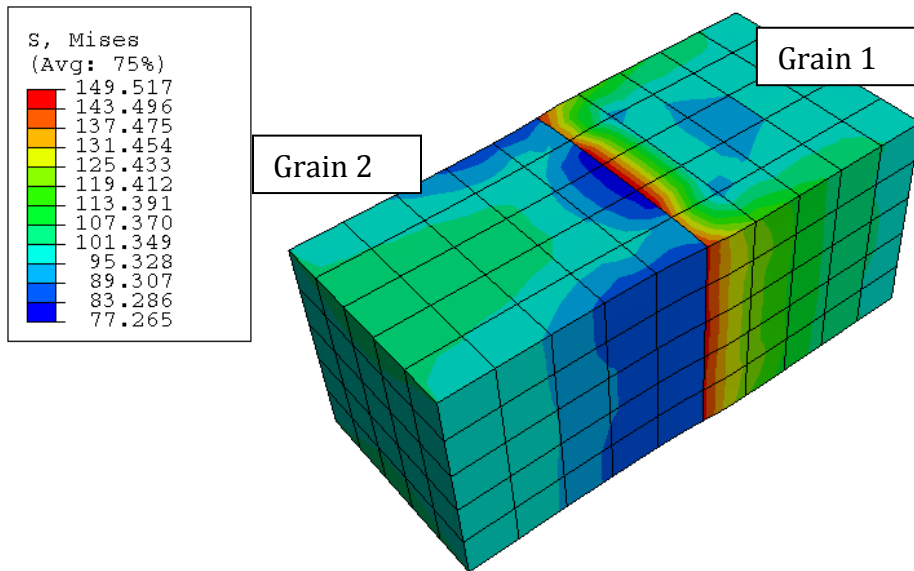


**Figure 4.12. Calculated Von Mises stress (MPa) for a bi-crystal with a misorientation of 45 degrees.**

A summary of the maximum Von Mises stress at the nodes in the vicinity of the grain boundary as a function of the misorientations are plotted in Figure 4.13. As expected, the Von Mises stress ratio (defined as the maximum stress over the average stress) is shown to increase up to 1.7 for a misorientation of 56.6 degrees.

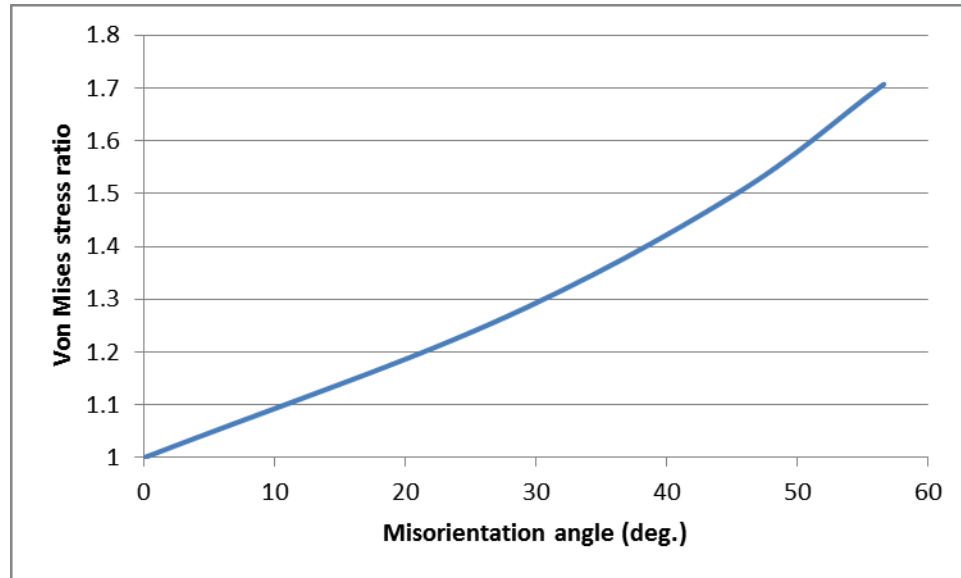


**Figure 4.13. Maximum Von Mises stress computed at the nodes in the vicinity of the grain boundary in a bi-crystal as a function of the misorientation angle.**

## 6.8 Submodelling using truncated octahedra

It is possible to use one way coupling (here also called submodelling) in which the displacements calculated in a global model are passed onto an aggregate of grains. Submodelling can be used to use crystal plasticity in a complex macroscopic stress state (e.g. near a crack tip or a plastically affected zone). In Figure 4.14, a submodel (or RVE) has been placed near the tensile surface of a bar subjected to 4 point bending.

Simulating grains as truncated octahedra is fairly popular as it produces a 3D space filling tessellation (Jivkov et al., 2007, Quey et al., 2011, Delannay et al., 2006). A Python script has been written for generating grains as truncated octahedra. We have used such a microstructure as a submodel, which is a particular case of a 3D Voronoi tessellation in which the Voronoi seeds form a BCC lattice. The procedure to assign initial random orientations in the crystals is described in annex 6.2. Such procedure has been used in the remaining of this research whenever random orientation assignment is a target.

Each octahedron was meshed with 24 elements ABAQUS C3D20R elements. These elements are 20-nodes-quadratic-bricks with 8 integration points. This is a reduced integration element. It was chosen to avoid volumetric locking (a refusal of the element to deform as the set of equations becomes over-constrained), associated to Poisson's ratio approaching  $\nu=0.5$  which is the case of plasticity (Bower, 2008). By contrast, the system of equations may include a weakly constrained deformation mode. This results in an unwanted deformation mode known as 'hourglassing' because of its unauthentic characteristic shape.

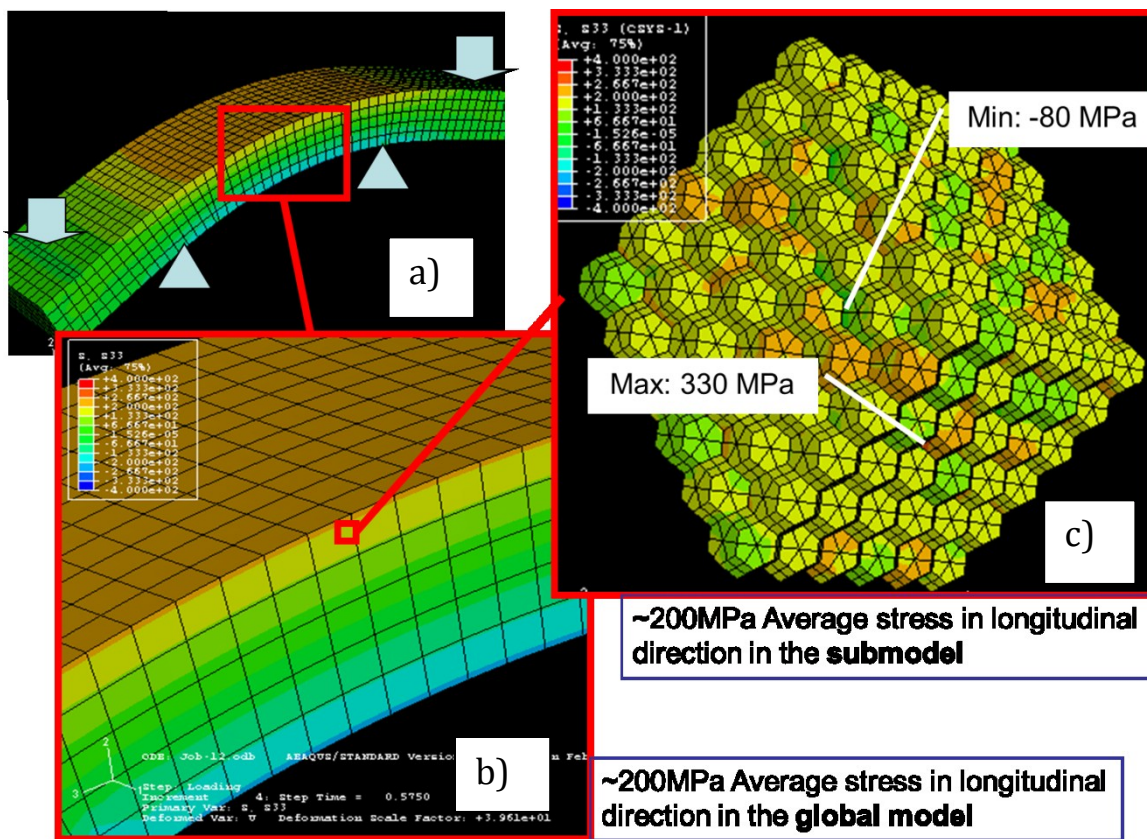


Figure 4.14. Logitudinal stress (MPa) developed in a simulated 4 point bending test (loaded), showing: a) the boundary conditions in the global model, b) region in the global model where the submodel is placed, and c) the submodel made of 216 grains shaped as truncated octohedra. The average longitudinal stress in the global model and the submodel (~200MPa) differ from the local stresses simulated in the submodel.

## **6.9 Modelling intergranular residual stress after 4 point bending**

### **6.9.1.1 Scope of the study**

This study reports a straight forward but elegant analysis that simulates the averaged stress of individual diffraction peaks and the grain-to-grain stress variability within them. This in itself is not new but provides an indicator of the grain-to-grain stress variability as compared to other measurement techniques. Several previous studies have measured the strain response for averaged grain families each of which has the same orientation but different geometry and different neighbours (e.g. (Daymond, 2005)). Very few, however have measured the averaged strains for individual grains (Lienert et al., 2004) or subgrains (Jakobsen et al., 2007). Here, the aim is to provide an indicator of the maximum stress variation if one particular diffraction peak was to be selected for neutron diffraction measurements.

### **6.9.1.2 Modelling approach**

We have modelled the mesh shown in Figure 4.2, using C3D10M elements and random orientations as explained in annex 6.2. We have assigned the material properties by calibrating a uniaxial loading test of a 316 stainless steel (as done in publications 1 and 2). Although sub-modelling is possible (see section 4.4.2), this would require running as many simulations as different positions of the aggregate through the thickness studied. Instead, the stress-strain curve was projected through the thickness taking the elastic limit at 3mm from the neutral fibre (depth). The subsequent loading was assumed only elastic, by subtracting a stress proportional to the depth. The subtracted stress was chosen so the area enclosed by the stress results zero at each side of the neutral fibre. This ensures momentum equilibrium in the out plane axis upon unloading. For a given depth, the unloading is assumed equal for all the individual grains.

### **6.9.1.3 Experimental**

The residual stress field induced by the elastic-plastic bending has been measured by ND and Deep Hole Drilling (DHD) (Smith et al., 2009). The DHD technique introduces a reference hole through the thickness of the component (Stefanescu et al., 2004, Leggatt et al., 1996, Smith et al., 2009). The displacements of the hole in the radial and vertical directions are measured after a cylinder, coaxial to the reference hole, is extracted from the component. This distortion allows determination of the residual stresses field using elasticity laws (section 2.4.1), setting the shear strains containing the cylindrical-hole to be zero.

### **6.9.1.4 Results and discussions**

The measured and predicted residual stress are presented in Figure 4.15. The residual stress profile clearly follows the usual stress profile for 4 point bending (Davis et al., 1988). The results illustrate the average stress for the {200} and {111} grain families and the possible variations in stress within each family.

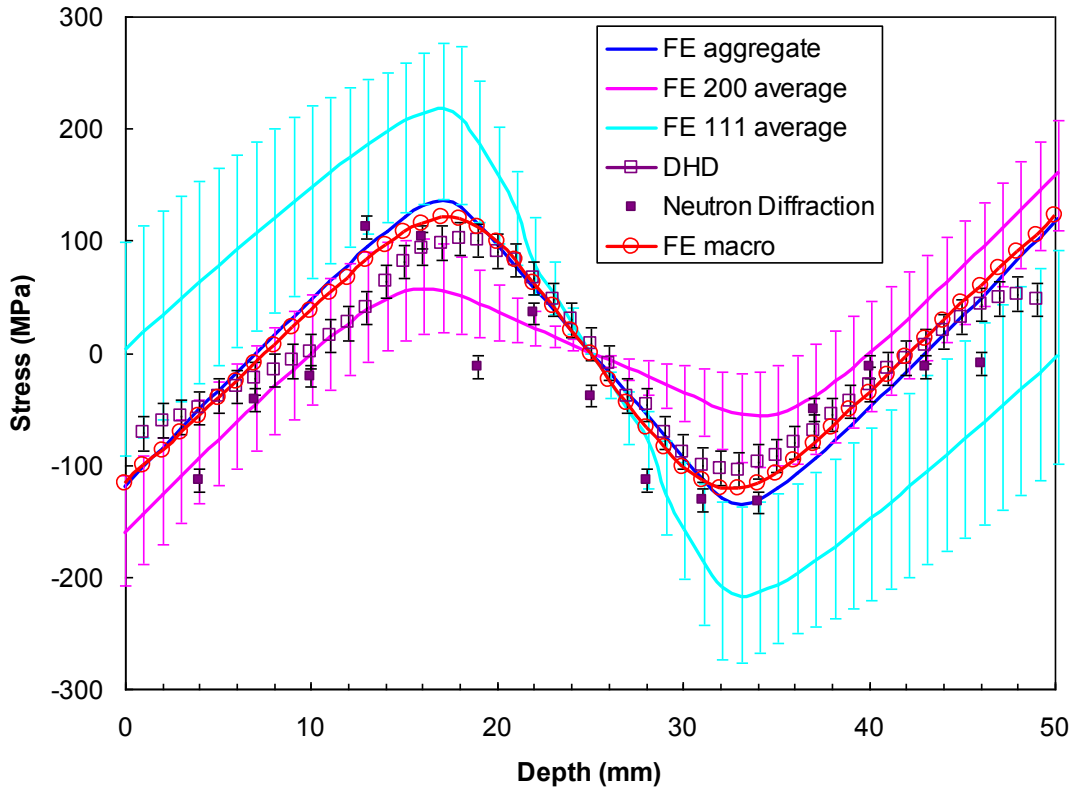


Figure 4.15. Predicted and measured macro-scale longitudinal residual stresses in an elastic-plastically bent rectangular beam, including the extent of possible variations due to lattice orientation. The error bars show the maximum and minimum stresses for the {200} and {111} lattice planes (Smith et al., 2009).

These results are in close agreement with previous experimental and modelling work (Lienert et al., 2004). For 2% applied strain, the measured {440} lattice strains of 20 individual (bulk) grains in a copper polycrystal revealed a standard deviation of  $\sim 6\%$  from the average axial lattice strain. Corresponding CPFEM predictions were in agreement with these observations (Lienert et al., 2004)

## 6.10 Intragranular rotations after cold-rolling stainless steel

### 6.10.1.1 Introduction

It was discussed in publication 1 that the strain history (e.g. strain paths) can play a crucial role in sensitising/desensitising metals to various damage mechanisms. The heterogeneity (or mosaicity) of lattice rotation with respect a reference orientation as deformation progresses is measurable (see the techniques in publication 3). This work presents the results of a numerical study aimed at exploring the mechanical aspects of cold rolling through the use of crystal plasticity finite element analysis. Specifically the work is aimed at quantifying the heterogeneity of crystal lattice rotations. Meaning that, the distribution of rotations within the grains is investigated.

The CPFEM technique is highly applicable to investigate these aspects since it simulates the development of plastic strain through the consideration of the local slip systems operative within individual crystals including the effect of neighbouring grains. As discussed in the literature review, CPFEM simulates the behaviour of a Representative Volume Element (RVE) of material and is able to calculate stress, total strain and rotations under various conditions and combinations of loading. Rotations distributions can then be assessed statistically to provide quantification of rotation around specific axes.

### 6.10.1.2 Methodology

#### *6.10.1.2.1 Collection of EBSD data*

Here we present the methodology employed for gathering the EBSD data to be compared against the CPFEM results. EBSD measurements have been performed in 304 austenitic stainless steel (grain size  $\sim 160 \mu\text{m}$ ). In the current work, deformation twins are ignored by taking a rather large EBSD step size. Therefore mainly the orientations of the parent grain are considered because deformation twins were very narrow. EBSD data points have been collected in two planes: the RD-ND plane and the RD-TD plane (see Figure 4.16). Measurements on both planes have been performed at a  $5 \mu\text{m}$  step

size. On the RD-ND plane, data has been collected from 270 grains. The total point count is 46251 for all grains. The point count per grain averages 171. As for the RD-TD plane, data has been collected from 441 grains. The total number of points is 39092 for all grains. The point count per grain averages 89.

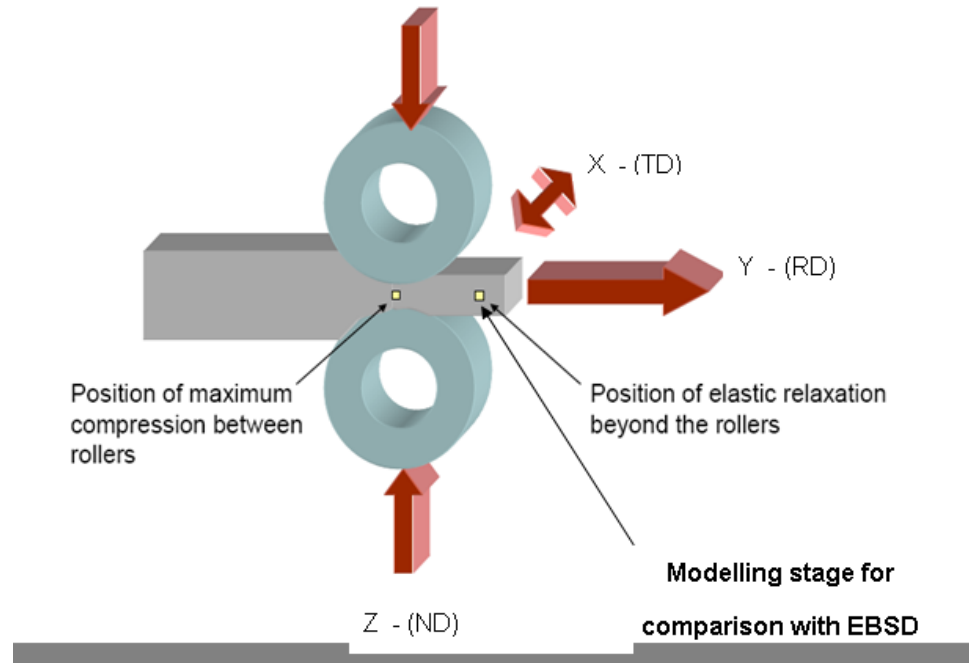


**Figure 4.16. Schematic illustration of the rolling process. Showing points of maximum compression and elastic relaxation. Relevant directions in the rolling process are shown: the normal direction (ND), the rolling direction (RD) and the transverse direction (TD).**

#### 6.10.1.2.2 Model description

The grains constituting the RVE of the polycrystal are represented by a finite element mesh. The elements used in this work are composed of 20 nodes and contain 8 Gauss points. Each element is assigned the properties of a single crystal and a crystallographic orientation. The RVE must contain a representative aggregate of grains, such that the global mechanical behaviour of the RVE is equivalent to that of the bulk. The actual orientations measured by EBSD (almost perfectly random) were used as the initial orientations for the simulations.

### 6.10.1.2.3 Constitutive laws and model calibration

The CPFEM approach used here differs slightly from that used in the rest of this work. An initial guess of resolved shear stress at Gauss points is determined by considering the Schmid factor of the slip system. This allows the calculation of the slip strain increments (plastic) using a predictor and therefore the updated elastic strain increments because the total strain increment is known. This elastic-plastic decomposition is possible under the infinitesimal elastic strain assumption (finite increments of elastic strain of 1% or less). The stress tensor can then be derived from the elastic strain increment and an internal iteration takes place to refine the initial value of resolved shear stress. Next, an implicit (non-linear) implementation is used where equilibrium is determined at the end of each time increment. Strain and rotation increments are given by the terminal strain rate and spin multiplied by that increment time. Details about the procedure along with some examples can be found in (Bate, 1999). Further examples of simulations can be found (Quinta da Fonseca et al., 2006, Utsunomiya et al., 2004). Plastic deformation is assumed to occur by slip (i.e. 12 slip systems here), which is assumed to be rate sensitive according to:

$$\frac{\dot{\gamma}}{\dot{\gamma}_0} = \left( \frac{\tau}{\tau_0} \right)^{1/m} \quad (\text{Eq. 4.6})$$

where  $\dot{\gamma}$  is the slip rate,  $\dot{\gamma}_0$  is the nominal reference slip rate,  $\tau$  is the resolved shear stress and  $\tau_0$  is the instantaneous slip resistance in any given slip system. The rate sensitivity,  $m$ , has a small positive value (typically 0.02) for all slip systems. As slip continues, the resistance to slip ( $\tau_0$ ) increases. This hardening behaviour is modelled using a modified Voce law, which describes a power law decay of the hardening rate from an initial to a final rate. It is given by:

$$\Theta = \Theta_{IV} + \Theta_0 \left[ \left| 1 - \frac{\tau}{\tau_s} \right|^\alpha \operatorname{sgn} \left( 1 - \frac{\tau}{\tau_s} \right) \right] \quad (\text{Eq. 4.7})$$

where  $\Theta_0$  is the initial hardening rate,  $\Theta_{IV}$  is the stage IV or final hardening rate and  $\tau_s$  is a saturation slip resistance. The parameters in table 1 were found to match the

stress-strain curve of the 304 stainless steel used in this work. The initial slip resistance was assumed to be 92 MPa for all slip systems.

**Table 4. Constants used in the present work to match the measured macroscopic stress-strain curve**

$C_{11}$	$C_{12}$	$C_{44}$	$\alpha$	$m$	$\Theta_0$	$\Theta_{IV}$	$\tau_s$
(GPa)	(GPa)	(GPa)			(MPa)	(MPa)	(MPa)
205	139.7	130.3	3.7	0.02	1300	170	230

#### 6.10.1.2.4 Simulation of rolling

The simulation of rolling requires that the maximum compression is applied to the RVE (to simulate the material condition between the rollers) following which elastic relaxation must be simulated (to simulate the material condition away from the rollers). This was undertaken in two stages (shown in Figure 4.16). In Stage 1 a compressive strain is applied to the RVE (20 % reduction in the ND or **Z** direction), whilst the TD (or **X**) is constrained. The material is therefore subjected to expand only along the RD (or **Y**), according to the incompressibility condition postulated in continuum plasticity. In Stage 2 all the boundary conditions are removed to allow elastic relaxation.

#### 6.10.1.2.5 Post-processing

In the introduction, it was mentioned that rotations distributions can be assessed statistically to provide quantification of rotation around specific axes. Here we describe such procedure in detail. The steps we have carried out can be listed as follows:

- 1<sup>st</sup> - To obtain an *average orientation* for each grain
- 2<sup>nd</sup> - Once an average orientation has been approved, the minimum *misorientation quaternion* between the average and the local orientation ( $\Delta\mathbf{q}$ ) is calculated, according to symmetry (24 operators for cubic materials)
- 3<sup>rd</sup> - To *decompose each misorientation quaternion* ( $\Delta\mathbf{q}$ ) around the sample axes (x, y, z) following the procedure in (Pantleon, 2008)

While the 2<sup>nd</sup> and 3<sup>rd</sup> step are well established and almost direct, the average orientation is less straight forward when *crystal symmetry* is present and deserves more discussion (Annex 6.3)

### 6.10.1.3 Results and discussions

#### 6.10.1.3.1 EBSD Results

Our results showed a broader distribution on the RD-ND plane than those on the RD-TD plane. This may be attributed to the higher averaged point-count-per-grain for the RD-TD plane (171), as opposed to the RD-ND plane (89). Statistically it is likely that, in the former, more points are close to the grain boundaries where deformation heterogeneity is maximum. In the remaining, we take the average distribution (in each direction) of both planes and name it “EBSD data”.

#### 6.10.1.3.2 CPFEM vs. EBSD

In this section we focus on the direct comparison between measurements (averaged for RD-TD and RD-ND data planes) and model predictions. For this we have used the methodology for averaging orientations and decomposing the in-grain rotations (with respect to its average), as described earlier.

We have simulated the cold-rolling deformation of 1000 grains (10x10x10). Each grain is assumed to enclose a perfect cubic volume when undeformed. We have used two models in order to quantify the effect of the mesh density. In the first model, each grain is composed of one element (8 Gauss points). In the second model, each grain is composed of 8 elements (64 Gauss points). Figure 4.17 shows the EBSD data along with model predictions for both meshes.

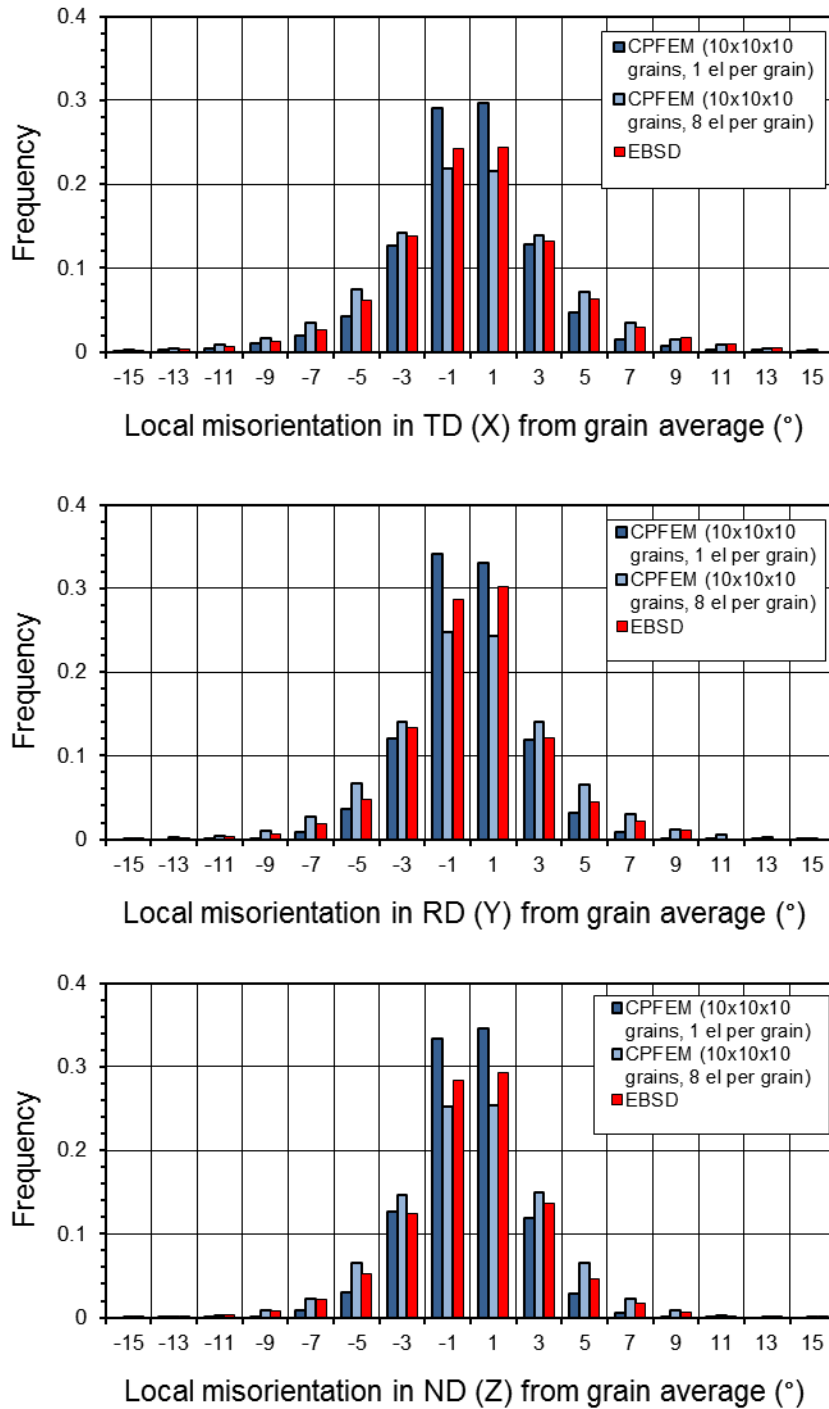


**Figure 4.17. In-grain rotations (with respect to its average) as measured by EBSD and as predicted by two models with different mesh density, decomposed about the: a) X axis (TD), b) Y axis (RD) and c) Z axis (ND). The results correspond to 20 % reduction in the ND or Z direction.**

Clearly, in both models rotation about the transversal direction ( $\mathbf{X}$ ) shows a broader distribution with respect to the others. In passing, it is worth stating that both measured planes by EBSD also showed a broader distribution around  $\mathbf{X}$  (not shown). This feature is therefore well captured by the model. It is also noticeable the broadening of the denser model (8 elements per grain) as opposed to the model where each grain is considered as a single element. This is expected since more elements mean more nodes and more Gauss points to accommodate the boundary conditions imposed by neighboring grains.

#### 6.10.1.3.3 Strain bands

Slip bands (within grains) have been observed and linked to initiation of SCC in cold-rolled 304L stainless steel in a 360°C PWR environment (Couvant et al., 2004). At a less small scale, strain bands running across grains are known to appear under deformation. Slip bands may develop in a region containing a strain band across grains, further enhancing strain localization and possibly damage. Local slip bands have been seen to oxidize more and to be locally more strained when located on macroscopic shear bands (The effect of strain localization on SCC Susceptibility R&T 002, 2012). While slip bands are not simulated by CPFEM, macroscopic strain bands can be captured (Barbe et al., 2009).

Figure 4.18 shows the total strain map of the RVE resolved in the three reference directions:  $\varepsilon_{RD}$ ,  $\varepsilon_{TD}$  and  $\varepsilon_{ND}$ . For each plot, the colour scale has been selected as the macroscopic  $\pm 0.1$  strain, giving a constant amplitude range of 0.2 strain. The intention is to visualize the relative heterogeneities and shear bands in the three strain directions. Consistent with experimental work, strain localisation is predicted to occur in strain bands, being more pronounced in the RD-ND plane. They seem to occur at a slightly lower angle than 45° with the RD (see Figure 4.19). By inspection of the deformed mesh, they presumably started forming at 45° and might have become inclined towards the rolling direction following the 20% thickness reduction.

Rolling, as described here (see section 4.4.4.2.4), is essentially a plain strain deformation at the macroscale. Clearly, the variability of strain resolved in the normal direction (Figure 4.18c) is lower than in the other two directions (Figure 4.18a and Figure 4.18b). This is in connexion with a somewhat plain strain condition associated to rolling, and so are the predictions and measurements showing a broader local misorientation distribution about the TD.

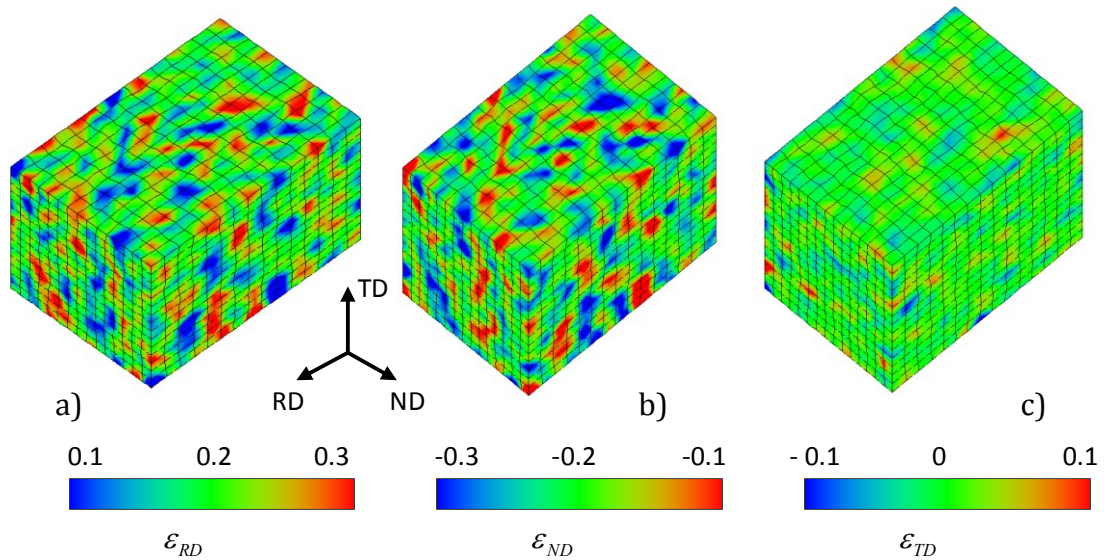


**Figure 4.18.** Strain map of the RVE resolved (a) in the rolling direction,  $\epsilon_{RD}$ , (b) in the transverse direction,  $\epsilon_{TD}$ , and (c) and in the normal direction,  $\epsilon_{ND}$ . All strains have been plotted using a colour scale in the same strain amplitude range (0.2) to compare strain heterogeneities in the 3 directions.

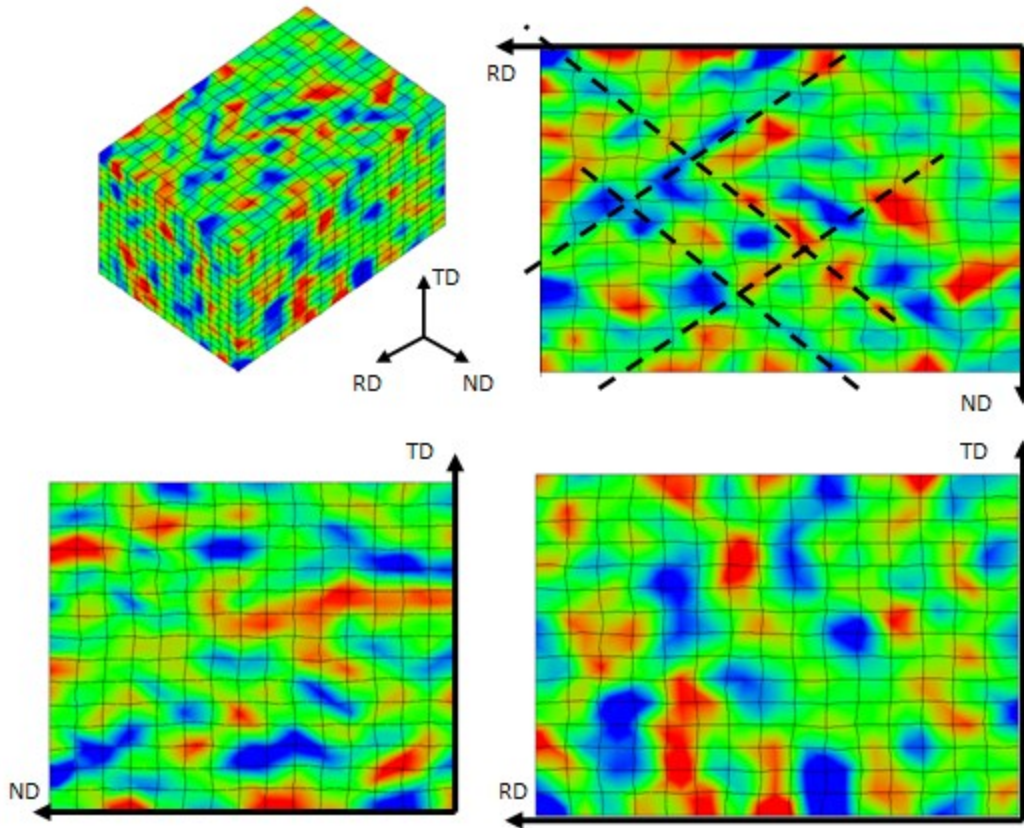


Figure 4.19. Strain map (resolved in the rolling direction,  $\varepsilon_{RD}$ ) of three faces of the RVE, showing differences in strain bands formation for different planes. Strain bands are predicted to be more pronounced in the RD-ND plane (dashed lines). Strain ranges from 0.1 (blue) to 0.3 (red).

#### 6.10.1.4 Conclusions

- Local lattice rotations have been collected in the (20% thickness reduction) cold-rolled 304 stainless steel, by EBSD, on the RD-ND and the RD-TD plane.
- Corresponding 3D CPFEM cold-rolling simulations have been performed in two different models using: a coarse mesh density (one element per grain); and a fine mesh density (eight elements per grain). Both models contain, however, a RVE of 1000 grains. The effectively random orientations measured by EBSD have served as an input for the model simulations.

- A Hill Climbing procedure has been implemented in order to calculate the grain-averaged orientation of each grain. Then we have calculated the misorientation of each local point to the grain-averaged orientation and decomposed such rotation about the three sample axes: RD, TD and ND.
- The local misorientation distribution about the three sample axes (to the grain-averaged orientation) of the measured RD-TD and the RD-ND planes differ slightly, being the latter broader.
- The model using the denser mesh shows a broader misorientation distribution around the three axes. This can be attributed to the larger number of elements defining each grain, because they can accommodate better the constraints by the neighbourhood.
- Both: model predictions and measurements show a broader local misorientation distribution about the TD.
- Strain outputs have been mapped and the heterogeneity of strain forming bands can be noticed. Such strain bands are predicted to be better defined on the RD-ND plane. Strain heterogeneity in the TD is considerably weaker than in the other two directions.

---

**REFERENCES**

2006. ABAQUS Documentation. *In: ABAQUS, I. (ed.)*. Providence, Rhode Island.
- ABDOLVAND, H. 2012. Multi-scale modeling and experimental study of deformation twinning in hexagonal close-packed materials. Queen's University, Canada.
- ABDOLVAND, H., DAYMOND, M. R. & MAREAU, C. 2011. Incorporation of twinning into a crystal plasticity finite element model: Evolution of lattice strains and texture in Zircaloy-2. *International Journal of Plasticity*, 27, 1721-1738.
- ABRIVARD, G., BUSSO, E. P., CAILLETAUD, G. & FOREST, S. 2007. Modeling of Deformation of FCC Polycrystalline Aggregates Using a Dislocation-based Crystal Plasticity Model. *AIP Conference Proceedings*, 908, 661-666.
- ACHARYA, A. 2008. A Counterpoint to Cermelli and Gurtin's Criteria for Choosing the 'Correct' Geometric Dislocation Tensor in Finite Plasticity. *In: REDDY, B. D. (ed.) IUTAM Symposium on Theoretical, Computational and Modelling Aspects of Inelastic Media*. Springer Netherlands.
- AHMED, I. I. 2011. *The influence of material factors, including cold work, on the susceptibility of stainless steels to stress corrosion cracking*. University of Manchester.
- AHMEDABADI, P., KAIN, V., GUPTA, M., SAMAJDAR, I., SHARMA, S. C., BHAGWAT, P. & CHOWDHURY, R. 2011. The role of niobium carbide in radiation induced segregation behaviour of type 347 austenitic stainless steel. *Journal of Nuclear Materials*, 415, 123-131.
- ALANKAR, A., MASTORAKOS, I. N. & FIELD, D. P. 2009. Development of a 3D crystal plasticity model that tracks dislocation density evolution. *Solid State Phenomena*, 160, 57-57.
- ANDERSON, T. L. 2005. *Fracture Mechanics: Fundamentals and Applications, Third Edition*, CRC Press.
- ARMSTRONG, P. J. & FREDERICK, C. O. 1966. A mathematical representation of the multiaxial Bauschinger effect. *Berkeley Nuclear Laboratories*, GEGB report RD/B/N731.

## References

---

- ARSENAULT, R. J., BEELER, J. R., ESTERLING, D. M. & COMMITTEE, A. S. M. I. M. S. D. S. S. 1988. *Computer simulation in materials science: papers presented at the 1986 ASM Materials Science Seminar, 4-5 October, 1986, Lake Buena Vista, Florida*, ASM International.
- ASARO, R. 1983. Crystal Plasticity. *Journal of Applied Mechanics-Transactions of the Asme*, 50, 921-934.
- ASARO, R. J. & RICE, J. R. 1977. *Strain Localization in Ductile Single Crystals*, Division of Engineering, Brown University.
- ASHBY, M. F. 1970. The deformation of plastically non-homogeneous materials. *Philosophical Magazine*, 21, 399-399.
- BADIYAN, E. E. & SHEKHOVTSOV, O. V. 2006. On the Nature of the Low Energy of Special Twist Grain Boundaries. *Physics of Metals*, 102, 196-200.
- BARBE, F., DECKER, L., JEULIN, D. & CAILLETAUD, G. 2001. Intergranular and intragranular behavior of polycrystalline aggregates. Part 1: F.E. model. *Int. J. of Plas.*, 17, 513-536.
- BARBE, F., QUEY, R., MUSIENKO, A. & CAILLETAUD, G. 2009. Three-dimensional characterization of strain localization bands in high-resolution elastoplastic polycrystals. *Mechanics Research Communications*, 36, 762-768.
- BARTON, N. R. & DAWSON, P. R. 2001. A methodology for determining average lattice orientation and its application to the characterization of grain substructure. *Metallurgical and Materials Transactions a-Physical Metallurgy and Materials Science*, 32, 1967-1975.
- BATE, P. 1999. Modelling deformation microstructure with the crystal plasticity finite-element method. 357, 1589-1601.
- BAUSCHINGER, J. 1881. Ueber die Veränderung der Elasticitätsgrenze und des Elasticitätsmoduls verschiedener Metalle. *Civiling N.F.*, 27, 289-348.
- BAUSCHINGER, J. 1886. On the Change of the Elastic Limit and Hardness of Iron and Steels through Extension and Compression, through Heating and Cooling, and through Cycling. *Mitteilung aus dem Mechanisch, Technischen Laboratorium der K. Technische Hochschule in München 13, Part 5*, 31.

## References

---

- BENHAM, P. P., CRAWFORD, P. R. J. & ARMSTRONG, D. C. G. 1996. *Mechanics of Engineering Materials*, Prentice Hall.
- BHATTI, R. & WITHERS, P. J. 2008. Unpublished results.
- BIELER, T. R., EISENLOHR, P., ROTERS, F., KUMAR, D., MASON, D. E., CRIMP, M. A. & RAABE, D. 2009. The role of heterogeneous deformation on damage nucleation at grain boundaries in single phase metals. *Int. J. of Plas.*, 25, 1655-1683.
- BOAS, W. & HARGREAVES, M. E. 1948. On the Inhomogeneity of Plastic Deformation in the Crystals of an Aggregate. *Proceedings of the Royal Society of London. Series A. Mathematical and Physical Sciences*, 193, 89-97.
- BONET, J. & WOOD, R. D. 1997. *Nonlinear Continuum Mechanics for Finite Element Analysis*, Cambridge University Press.
- BOWER, A. F. 2008. *Applied Mechanics of Solids - Chapter 8: Theory of FEA -8.6 Special Elements* [Online]. Available: [http://solidmechanics.org/text/Chapter8\\_6/Chapter8\\_6.htm](http://solidmechanics.org/text/Chapter8_6/Chapter8_6.htm) [Accessed].
- BRITTON, T. B., LIANG, H., DUNNE, F. P. E. & WILKINSON, A. J. 2009. The effect of crystal orientation on the indentation response of commercially pure titanium: experiments and simulations. *Proceedings of the Royal Society A: Mathematical, Physical and Engineering Sciences*, 466, 695-719.
- BROWN, L. M. 2003. Slip bands, ellipsoids, pile-ups and cracks. *Transactions of the Royal Society of South Africa*, 58, 103-103.
- BUCHANAN, GW. 1995. *Finite Element Analysis*. Schaum's Outline Series. McGraw-Hill.
- BUSSO, E. P., MEISSONNIER, F. T. & O'DOWD, N. P. 2000. Gradient-dependent deformation of two-phase single crystals. *Journal of the Mechanics and Physics of Solids*, 48, 2333-2361.
- CALLISTER, W. D. 2006. *Materials Science and Engineering: An Introduction*, John Wiley & Sons.
- CARPENTER, H. C. H. & ELAM, C. F. 1920. Crystal Growth and Recrystallization in Metals. *J. Inst. Met.*, 24, 83-131.
- CHABOCHE, J. L. 1986. Time-independent constitutive theories for cyclic plasticity. *International Journal of Plasticity*, 2, 149-188.

- 
- CHO, J.-H., ROLLETT, A. D. & OH, K. H. 2005. Determination of a mean orientation in electron backscatter diffraction measurements. *Metallurgical and Materials Transactions A*, 36, 3427-3438.
- CLAUSEN, B. 1997. *Characterisation of polycrystal deformation by numerical modelling and neutron diffraction measurement*. Risø National Laboratory.
- CLYNE, T. W. & WITHERS, P. J. 1995. *An Introduction to Metal Matrix Composites*, Cambridge University Press.
- COTTRELL, A. 1953. *Dislocations and plastic flow in crystals*, Oxford, Clarendon Press.
- COUVANT, T., LEGRAS, L., VAILLANT, F., BOURSIER, J. M. & ROUILLON, Y. Year. EFFECT OF STRAIN PATH ON STRESS CORROSION CRACKING OF AISI 304L STAINLESS STEEL IN PWR PRIMARY ENVIRONMENT AT 360°C. In, 2004 Nice, France.
- CRISFIELD, M. A. 1996. *Non-Linear Finite Element Analysis of Solids and Structures*, Wiley.
- CULLITY, B. D. & STOCK, S. R. 2001. *Elements of X-ray Diffraction*.
- DANG VAN, K. 1993. Macro-micro approach in high-cycle multiaxial fatigue. *Advances in multi-axial fatigue*, 120-130.
- DAVIS, J. R., SEMIATIN, S. L. & METALS, A. S. F. 1988. *ASM Metals Handbook, Vol. 14: Forming and Forging*, ASM International.
- DAYMOND, M. R. 2005. A combined finite element and self-consistent model; Validation by neutron diffraction strain scanning. *MATERIALS SCIENCE FORUM*, 495-497, 1019-1024.
- DAYMOND, M. R., TOMÉ, C. N. & BOURKE, M. A. M. 2000. Measured and predicted intergranular strains in textured austenitic steel. *Acta Mater.*, 48, 553-564.
- DELANNAY, L., JACQUES, P. J. & KALIDINDI, S. R. 2006. Finite element modeling of crystal plasticity with grains shaped as truncated octahedrons. *International Journal of Plasticity*, 22, 1879-1898.
- DEMIR, E. 2008. Taylor-based model for micro-machining of single crystal fcc materials including frictional effects—Application to micro-milling process. *International Journal of Machine Tools and Manufacture*, 48, 1592-1598.
- DIETER, G. E. 1988. *Mechanical metallurgy*, McGraw-Hill.

## References

---

- DIETZEL, W. & TURNBULL, A. 2007. *Stress Corrosion Cracking*, GKSS-Forschungszentrum.
- DUNNE, F. & PETRINIC, N. 2005. *Introduction to Computational Plasticity*.
- DUNNE, F. P. E., WILKINSON, A. J. & ALLEN, R. 2007. Experimental and computational studies of low cycle fatigue crack nucleation in a polycrystal. *INTERNATIONAL JOURNAL OF PLASTICITY*, 23, 273-295.
- DYE, D., STONE, H. J. & REED, R. C. 2001. Intergranular and interphase microstresses. *Current Opinion in Solid State and Materials Science*, 5, 31-37.
- ELBER, W. 1970. Fatigue crack closure under cyclic tension. *Engineering Fracture Mechanics*, 2, 37-45.
- ESHELBY, J. D. 1957. The Determination of the Elastic Field of an Ellipsoidal Inclusion, and Related Problems. *Proceedings of the Royal Society of London. Series A. Mathematical and Physical Sciences*, 241, 376-396.
- FAGAN, M. J. 1992. *Finite Element Analysis: Theory and Practice*. Longman.
- FATHALLAH, R., SIDHOM, H., BRAHAM, C. & CASTEX, L. 2003. Effect of surface properties on high cycle fatigue behaviour of shot peened ductile steel. *MATERIALS SCIENCE AND TECHNOLOGY*, 19, 1050-1056.
- FLECK, N. A., MULLER, G. M., ASHBY, M. F. & HUTCHINSON, J. W. 1994. Strain gradient plasticity: Theory and experiment. *Acta Metallurgica et Materialia*, 42, 475-487.
- FRENKEL, J. 1926. Zur theorie de elastizitatsgrenze und der festigkeit. *Kristallinischer Korper. Phys.*, 37, 572-603.
- GRIFFITH, A. A. 1921. The Phenomena of Rupture and Flow in Solids. *Philosophical Transactions of the Royal Society of London. Series A, Containing Papers of a Mathematical or Physical Character*, 221, 163-198.
- GURTIN, M. E. 2002. A gradient theory of single-crystal viscoplasticity that accounts for geometrically necessary dislocations. *Journal of the Mechanics and Physics of Solids*, 50, 5-32.
- GUTIERREZ-URRUTIA, I. & RAABE, D. 2012. Dislocation density measurement by electron channeling contrast imaging in a scanning electron microscope. *Scripta Materialia*, 66, 343-346.

## References

---

- HILL, R. 1998. *The mathematical theory of plasticity*, Oxford University Press.
- HIRTH, J. 1972. The influence of grain boundaries on mechanical properties. *Metallurgical and Materials Transactions B*, 3, 3047-3067.
- HONEYCOMBE, R. W. K. 1984. *The Plastic Deformation of Metals*.
- HOSFORD, W. F. 2005. *Mechanical Behavior of Materials*, Cambridge University Press.
- HUANG, X. & HANSEN, N. 1997. Grain orientation dependence of microstructure in aluminium deformed in tension. *Scripta Materialia*, 37, 1-7.
- HUANG, Y. 1991. A user-material subroutine incorporating single crystal plasticity in the ABAQUS finite element program, Mech Report 178. In: HUANG, Y. (ed.). Division of Engineering and Applied Sciences, Harvard University, Cambridge, Massachusetts.
- HUGHES, D. A., HANSEN, N. & BAMMANN, D. J. 2003. Geometrically necessary boundaries, incidental dislocation boundaries and geometrically necessary dislocations. *Scripta Materialia*, 48, 147-153.
- HULL, D. & BACON, D. J. 1984. *Introduction to Dislocations*, Butterworth-Heinemann.
- HUMPHREYS, F. J. & HATHERLY, M. 2004. *Recrystallization and related annealing phenomena*, Elsevier.
- INGLIS, C. 1913. Stresses in a Plate due to the Presence of Cracks and Sharp Corners. *Transactions of the Institution of Naval Architects*, 55, 219-230.
- JAKOBSEN, B., POULSEN, H. F., LIENERT, U. & PANTLEON, W. 2007. Direct determination of elastic strains and dislocation densities in individual subgrains in deformation structures RID A-4131-2012. *Acta Materialia*, 55, 3421-3430.
- JIVKOV, A. P., STEVENS, N. P. C. & MARROW, T. J. 2007. Modelling Intergranular Stress Corrosion Cracking in Simulated Three-Dimensional Microstructures. *Key Engineering Materials*, 345-346, 1019-1022.
- KAIN, V., CHANDRA, K., ADHE, K. N. & DE, P. K. 2004. Effect of cold work on low-temperature sensitization behaviour of austenitic stainless steels. *Journal of Nuclear Materials*, 334, 115-132.
- KAMAYA, M., WILKINSON, A. J. & TITCHMARSH, J. M. 2005. Measurement of plastic strain of polycrystalline material by electron backscatter diffraction. *Nuclear Engineering and Design*, 235, 713-725.

## References

---

- KARAMINEZHAAD, M., SHARAFI, S. & DALILI, K. 2006. Effect of molybdenum on SCC of 17-4PH stainless steel under different aging conditions in chloride solutions. *JOURNAL OF MATERIALS SCIENCE*, 41, 3329-3333.
- KASSNER, M. E., NEMAT-NASSER, S., SUO, Z. G., BAO, G., BARBOUR, J. C., BRINSON, L. C., ESPINOSA, H., GAO, H. J., GRANICK, S., GUMBSCH, P., KIM, K. S., KNAUSS, W., KUBIN, L., LANGER, J., LARSON, B. C., MAHADEVAN, L., MAJUMDAR, A., TORQUATO, S. & VAN SWOL, F. 2005. New directions in mechanics. *Mechanics of Materials*, 37, 231-259.
- KEAVY, M.A. 2008. Finite element with elastomers.
- KELLEHER, J. F. 2006. *Residual stress in railway rails*, University of Manchester.
- KELLEHER, J. F., LOPEZ-CRESPO, P., YUSOF, F. & WITHERS, P. J. 2010. The Use of Diffraction to Study Fatigue Crack Tip Mechanics. In: AKINIWA, Y., AKITA, K. & SUZUKI, H. (eds.) *Mechanical Stress Evaluation by Neutrons and Synchrotron Radiation*. Stafa-Zurich: Trans Tech Publications Ltd.
- KELLY, A., GROVES, G. W. & KIDD, P. 2000. *Crystallography and Crystal Defects*, John Wiley & Sons.
- KING, A., JOHNSON, G., ENGELBERG, D., LUDWIG, W. & MARROW, J. 2008. Observations of intergranular stress corrosion cracking in a grain-mapped polycrystal. *SCIENCE*, 321, 382-385.
- KOCKS, U. F., TOMÉ, C. N., WENK, H.-R. & MECKING, H. 2000. *Texture and anisotropy: preferred orientations in polycrystals and their effect on materials properties*, Cambridge University Press.
- KORSUNSKY, A. M., DINI, D., DUNNE, F. P. E. & WALSH, M. J. 2007. Comparative assessment of dissipated energy and other fatigue criteria. *INTERNATIONAL JOURNAL OF FATIGUE*, 29, 1990-1995.
- KORSUNSKY, A. M., JARNES, K. E. & DAYMOND, M. R. 2004. Intergranular stresses in polycrystalline fatigue: diffraction measurement and self-consistent modelling. *ENGINEERING FRACTURE MECHANICS*, 71, 805-812.

- 
- KRONBERG, M. L. 1957. Plastic deformation of single crystals of sapphire: Basal slip and twinning. *Acta Metallurgica*, 5, 507-524.
- KRÖNER, E. 1958. Berechnung der elastischen Konstanten des Vielkristalls aus den Konstanten des Einkristalls. *Zeitschrift für Physik A Hadrons and Nuclei*, 151, 504-518.
- KRÖNER, E. 1960. Allgemeine Kontinuumstheorie der Versetzungen und Eigenspannungen. *Archive for Rational Mechanics and Analysis*, 4, 273-334.
- KRÖNER, E. 1961. Zur plastischen verformung des vielkristalls. *Acta Metallurgica*, 9, 155-161.
- KRÖNER, E. 2001. Benefits and shortcomings of the continuous theory of dislocations. *International Journal of Solids and Structures*, 38, 1115-1134.
- LANDAU, P., SHNECK, R. Z., MAKOV, G. & VENKERT, A. 2009. Evolution of dislocation patterns in fcc metals. *IOP Conference Series: Materials Science and Engineering*, 3, 012004-012004.
- LEDBETTER, H. M. 1984. Monocrystal Polycrystal Elastic-Constants Of A Stainless-Steel. *Physica Status Solidi A-Applied Research*, 85, 89-96.
- LEGGATT, R. H., SMITH, D. J., SMITH, S. D. & FAURE, F. 1996. Development and Experimental Validation of the Deep Hole Method for Residual Stress Measurement. *The Journal of Strain Analysis for Engineering Design*, 31, 177-186.
- LEMAITRE, J. & CHABOCHE, J.-L. 1994. *Mechanics of Solid Materials*, Cambridge University Press.
- LIANG, H. & DUNNE, F. P. E. 2009. GND accumulation in bi-crystal deformation: Crystal plasticity analysis and comparison with experiments. *International Journal of Mechanical Sciences*, 51, 326-333.
- LIENERT, U., HAN, T., ALMER, J., DAWSON, P., LEFFERS, T., MARGULIES, L., NIELSEN, S., POULSEN, H. & SCHMIDT, S. 2004. Investigating the effect of grain interaction during plastic deformation of copper. *Acta Materialia*, 52, 4461-4467.
- LIU, Q. & HANSEN, N. 1995. Geometrically necessary boundaries and incidental dislocation boundaries formed during cold deformation. *Scripta Metallurgica et Materialia*, 32, 1289-1295.

## References

---

- LORENTZEN, T., DAYMOND, M. R., CLAUSEN, B. & TOMÉ, C. N. 2002. Lattice strain evolution during cyclic loading of stainless steel. *Acta Materialia*, 50, 1627-1638.
- LOZANO-PEREZ, S., YAMADA, T., TERACHI, T., SCHRÖDER, M., ENGLISH, C. A., SMITH, G. D. W., GROVENOR, C. R. M. & EYRE, B. L. 2009. Multi-scale characterization of stress corrosion cracking of cold-worked stainless steels and the influence of Cr content. *Acta Materialia*, 57, 5361-5381.
- MA, A., ROTERS, F. & RAABE, D. 2006. Studying the effect of grain boundaries in dislocation density based crystal-plasticity finite element simulations. *International Journal of Solids and Structures*, 43, 7287-7303.
- MA, A., ROTERS, F. & RAABE, D. 2007. A dislocation density based constitutive law for BCC materials in crystal plasticity FEM. *Computational Materials Science*, 39, 91-95.
- MANONUKUL, A. & DUNNE, F. P. E. 2004. High- and low-cycle fatigue crack initiation using polycrystal plasticity. *Proceedings of the Royal Society of London Series A-Mathematical Physical and Engineering Sciences*, 460, 1881-1903.
- MARROW, T. J., BABOUT, L., JIVKOV, A. P., WOOD, P., ENGELBERG, D., STEVENS, N., WITHERS, P. J. & NEWMAN, R. C. 2006. Three dimensional observations and modelling of intergranular stress corrosion cracking in austenitic stainless steel. *Journal of Nuclear Materials*, 352, 62-74.
- MARTINEZ, M. L., BORLADO, C. R., MOMPEAN, F. J., PENG, R. L., DAYMOND, M. R., RUIZ, J. & GARCIA-HERNANDEZ, M. 2002. Neutron strain scanning in straightened eutectoid steel rods. *Applied Physics A: Materials Science & Processing*, 74, s1679-s1682-s1679-s1682.
- MCDOWELL, D. 2008. Viscoplasticity of heterogeneous metallic materials. *Materials Science and Engineering: R: Reports*, 62, 67-123.
- MCDOWELL, D. L. & DUNNE, F. P. E. 2010. Microstructure-sensitive computational modeling of fatigue crack formation. *International Journal of Fatigue*, 32, 1521-1542.
- MCGUIRE, M. F. 2008. *Stainless Steels for Design Engineers*, ASM International.

- MEYERS, M. A., BENSON, D. J., VOHRINGER, O., KAD, B. K., XUE, Q. & FU, H. H. 2002. Constitutive description of dynamic deformation: physically-based mechanisms. *Materials Science and Engineering a-Structural Materials Properties Microstructure and Processing*, 322, 194-216.
- MOCHIZUKI, M. 2007. Control of welding residual stress for ensuring integrity against fatigue and stress-corrosion cracking. *NUCLEAR ENGINEERING AND DESIGN*, 237, 107-123.
- MUGHRABI, H. 1983. Dislocation wall and cell structures and long-range internal stresses in deformed metal crystals. *Acta Metallurgica*, 31, 1367-1379.
- MUGHRABI, H. 2006. Deformation-induced long-range internal stresses and lattice plane misorientations and the role of geometrically necessary dislocations. *Philosophical Magazine*, 86, 4037-4037.
- NABARRO, F. R. N. 1947. Dislocations in a simple cubic lattice. *Proc. Phys. Soc.*, 59, 256-256.
- NEEDLEMAN, A. & ASARO 1985. Overview no. 42 Texture development and strain hardening in rate dependent polycrystals. *Acta Metallurgica*, 33, 923-953.
- NEMAT-NASSER, S. 2004. *Plasticity: A Treatise on Finite Deformation of Heterogeneous Inelastic Materials*, Cambridge University Press.
- NYE, J. F. 1953. Some geometrical relations in dislocated crystals. *Acta Metallurgica*, 1, 153-162.
- NYE, J. F. 1985. *Physical Properties of Crystals: Their Representation by Tensors and Matrices*, Oxford University Press, USA.
- OLIVER, E. C. 2004. *The generation of internal stresses in single and two phase materials*.
- OLIVER, E. C., DAYMOND, M. R. & WITHERS, P. J. 2004. Interphase and intergranular stress generation in carbon steels. *Acta Materialia*, 52, 1937-1951.
- OROWAN, E. 1934. Zur Kristallplastizitat. *Z. Phys.*, 89, 605-659.
- OROWAN, E. 1959. *Causes and effects of internal stresses*, Elsevier Publishing Company, New York.
- PANTLEON, W. 2008. Resolving the geometrically necessary dislocation content by conventional electron backscattering diffraction. *Scr. Mater.*, 58, 994-997.

## References

---

- PANTLEON, W., POULSEN, H., ALMER, J. & LIENERT, U. 2004. In situ X-ray peak shape analysis of embedded individual grains during plastic deformation of metals. *Materials Science and Engineering A*, 387-389, 339-342.
- PEIERLS, R. 1940. The size of a dislocation. *Proc. Phys. Soc.*, 52, 34-34.
- PETRIC, Z. 2010. Generating 3D Voronoi tessellations for material modeling. Jozef Stefan Institute. Tech. report.
- PI, H., HAN, J., ZHANG, C., TIEU, A. K. & JIANG, Z. 2008. Modeling uniaxial tensile deformation of polycrystalline Al using CPFEM. *Journal of University of Science and Technology Beijing, Mineral, Metallurgy, Material*, 15, 43-47.
- POLANYI, M. 1934. *Z. Phys.*, 89, 660-660.
- PRAGER, W. 1956. A new method of analyzing stress and strain in work-hardening plastic solids. *J. Appl. Mech.*, pp. 493-502-pp. 493-502.
- QIN, B. & BHADSHIA, H. 2008. Plastic strain due to twinning in austenitic TWIP steels. *MATERIALS SCIENCE AND TECHNOLOGY*, 24, 969-973.
- QUEY, R., DAWSON, P. R. & BARBE, F. 2011. Large-scale 3D random polycrystals for the finite element method: Generation, meshing and remeshing. *Computer Methods in Applied Mechanics and Engineering*, 200, 1729-1745.
- QUINTA DA FONSECA, J., OLIVER, E. C., BATE, P. S. & WITHERS, P. J. 2006. Evolution of intergranular stresses during in situ straining of IF steel with different grain sizes. *Materials Science and Engineering: A*, 437, 26-32.
- RAQUET, O., HERMS, E., VAILLANT, F., COUVANT, T. & BOURSIER, J. M. 2006. SCC of cold-worked austenitic stainless steels in PWR conditions. *Proceedings of the 12th International Conference on Environmental Degradation of Materials in Nuclear Power Systems-Water Reactors*, 1049-1059/1059.
- READ, W. T. & SHOCKLEY, W. 1950. Dislocation Models of Crystal Grain Boundaries. *Physical Review*, 78, 275-289.
- REUSS, A. 1929. Berechnung der Fließgrenze von Mischkristallen auf Grund der Plastizitätsbedingung für Einkristalle. *ZAMM - Journal of Applied Mathematics and Mechanics / Zeitschrift für Angewandte Mathematik und Mechanik*, 9, 49-58.
- RICE, J. R. 1968. *A path independent integral and the approximate analysis of stress concentration by notches and cracks.*

- 
- RIVEROS, G. A. 2006. Numerical Evaluation of Stress Intensity Factors (KI) J-Integral Approach. US Army Corps of Engineers.
- ROHRER, G. S., SAYLOR, D. M., EL DASHER, B., ADAMS, B. L., ROLLETT, A. D. & WYNBLATT, P. 2004. The distribution of internal interfaces in polycrystals. *Zeitschrift fur Metallkunde*, 95, 197-214.
- ROTTERS, F., EISENLOHR, P., HANTCHERLI, L., TJAHJANTO, D. D., BIELER, T. R. & RAABE, D. 2010. Overview of constitutive laws, kinematics, homogenization and multiscale methods in crystal plasticity finite-element modeling: Theory, experiments, applications. *Acta Materialia*, 58, 1152-1211.
- RÜHLE, M. & METALLFORSCHUNG, M.-P.-I. F. 2002. *European White Book on Fundamental Research in Materials Science*, Max-Planck-Institut für Metallforschung.
- SACHS, G. 1928. Zur Ableitung einer Fließbedingung. *Z. Ver. Deu. Ing.*, 72-734.
- SCHWEITZER, P. A. 2010. *Fundamentals of Corrosion: Mechanisms, Causes, and Preventative Methods*, CRC Press.
- SHAFFER, J. B., KNEZEVIC, M. & KALIDINDI, S. R. 2010. Building texture evolution networks for deformation processing of polycrystalline fcc metals using spectral approaches: Applications to process design for targeted performance. *International Journal of Plasticity*, 26, 1183-1194.
- SHAH, K. P. 2012. *The Hand Book on Mechanical Maintenance* [Online]. Available: <http://practicalmaintenance.net/?p=1135> [Accessed].
- SHIBATA, T. 1983. Stochastic approach to the effect of alloying elements on the pitting resistance of ferritic stainless steels. *Transactions ISIJ*, 23, 785-788.
- SHILKROT, L. E., MILLER, R. E. & CURTIN, W. A. 2004. Multiscale plasticity modeling: coupled atomistics and discrete dislocation mechanics. *Journal of the Mechanics and Physics of Solids*, 52, 755-787.
- SIMONOVSKI, I. & CIZELJ, L. 2011a. Automatic parallel generation of finite element meshes for complex spatial structures. *Computational Materials Science*, 50, 1606-1618.
- SIMONOVSKI, I. & CIZELJ, L. 2011b. Computational multiscale modeling of intergranular cracking. *Journal of Nuclear Materials*, 414, 243-250.

## References

---

- SIMONOVSKI, I. & CIZELJ, L. 2012. Towards modeling intergranular stress corrosion cracks on grain size scales. *Nuclear Engineering and Design*.
- SMITH, D. J., FLEWITT, GOUDAR, HODGSON, HADIDI, M., TRUMAN, WITHERS, P. J., KEAVEY, M., CLITHEROE, S., GONZALEZ, D. & KELLEHER, J. F. 2009. Multiscale Approaches to Enhance Materials Performance: Residual Stress and Microstructural Issues. University of Bristol & University of Manchester.
- SONG, X., ZHANG, S. Y., DINI, D. & KORSUNSKY, A. M. 2008. Inter-granular residual stresses in polycrystalline aggregates: finite element modelling and diffraction post-processing. *STRESS EVALUATION IN MATERIALS USING NEUTRONS AND SYNCHROTRON RADIATION*, 571-572, 271-276.
- SPANOS, G., ROWENHORST, D. J., LEWIS, A. C. & GELTMACHER, A. B. 2008. Combining serial sectioning, EBSD analysis, and image-based finite element modeling. *Mrs Bulletin*, 33, 597-602.
- STEFANESCU, D., TRUMAN, C. E. & SMITH, D. J. 2004. An Integrated Approach for Measuring Near-Surface and Subsurface Residual Stress in Engineering Components. *The Journal of Strain Analysis for Engineering Design*, 39, 483-497.
- SURESH, S. 1998. *Fatigue of Materials*.
- SZCZEPINSKI, W. 1979. *Introduction to the Mechanics of Plastic Forming of Metals*, Springer.
- TAYLOR, C. J., ZHAI, T., WILKINSON, A. J. & MARTIN, J. W. 1999. Influence of grain orientations on the initiation of fatigue damage in an Al-Li alloy. *JOURNAL OF MICROSCOPY-OXFORD*, 195, 239-247.
- TAYLOR, G. I. 1934. *Proc. R. Soc.*, A145, 362-362.
- TAYLOR, G. I. 1938. Plastic strain in metals. *J. Inst. Met.*, 24, 62-307.
- TEODOSIU, C. 1982. *Elastic models of crystal defects*, Editura Academiei.
- UNGAR, T., MUGHRABI, H., RÖNNPAGEL, D. & WILKENS, M. 1984. X-ray line-broadening study of the dislocation cell structure in deformed [001]-orientated copper single crystals. *Acta Metallurgica*, 32, 333-342.
- UTSUNOMIYA, H., SUTCLIFFE, M. P. F., SHERCLIFF, H. R., BATE, P. S. & MILLER, D. B. 2004. Three-dimensional topography of the matt surface in aluminium pack rolling. *International Journal of Mechanical Sciences*, 46, 1083-1096.

- 
- VARMA, S. K., KALYANAM, J., MURR, L. E. & SRINIVAS, V. 1994. EFFECT OF GRAIN-SIZE ON DEFORMATION-INDUCED MARTENSITE FORMATION IN 304-STAINLESS-STEEL AND 316-STAINLESS-STEEL DURING ROOM-TEMPERATURE TENSILE TESTING. *Journal of Materials Science Letters*, 13, 107-111.
- VENABLES, J. A. 1964. The electron microscopy of deformation twinning. *Journal of Physics and Chemistry of Solids*, 25, 685-692.
- VOIGT, W. 1889. Ueber die Beziehung zwischen den beiden Elasticitätsconstanten isotroper Körper. *Annalen der Physik*, 274, 573-587.
- VON MISES, R. 1928. Mechanik der plastischen Formänderung von Kristallen. *Z. Angew. Math. Mech.*, 8, 161-185.
- WANG, X. & WANG 2005. Inter- and intragranular stresses in cyclically-deformed 316 stainless steel. *Materials science & engineering. A, Structural materials*, 399, 114-119.
- WANG, Z. G., ZHANG, Z. F., LI, X. W., JIA, W. P. & LI, S. X. 2001. Orientation dependence of the cyclic deformation behavior and the role of grain boundaries in fatigue damage in copper crystals. *Materials Science and Engineering A*, 319-321, 63-73.
- WATANABE, T. 1993. Grain boundary design and control for high temperature materials. *Materials Science and Engineering: A*, 166, 11-28.
- WEISSTEIN, E. W. 2012. *Sphere Point Picking -- from Wolfram MathWorld* [Online]. Available: <http://mathworld.wolfram.com/SpherePointPicking.html> [Accessed].
- WINIARSKI, B., SCHAJER, G. S. & WITHERS, P. J. 2011. Surface Decoration for Improving the Accuracy of Displacement Measurements by Digital Image Correlation in SEM. *Experimental Mechanics*, 52, 793-804.
- WINIARSKI, B. & WITHERS, P. 2012. Micron-Scale Residual Stress Measurement by Micro-Hole Drilling and Digital Image Correlation. *Experimental Mechanics*, 52, 417-428.
- WITHERS, P. J. & BHADESHIA, H. 2001. Overview - Residual stress part 1 - Measurement techniques. *Materials Science and Technology*, 17, 355-365.
- WONG, S. L. & DAWSON, P. R. 2010. Influence of directional strength-to-stiffness on the elastic-plastic transition of fcc polycrystals under uniaxial tensile loading. *Acta Materialia*, 58, 1658-1678.

## References

---

- YALCINKAYA, T., BREKELMANS, W. A. M. & GEERS, M. G. D. 2011. Deformation patterning driven by rate dependent non-convex strain gradient plasticity. *Journal of the Mechanics and Physics of Solids*, 59, 1-17.
- YOUSEF, S. G., RODEL, J., FULLER, E. R., ZIMMERMANN, A. & EL-DASHER, B. S. 2005. Microcrack evolution in alumina ceramics: Experiment and simulation. *JOURNAL OF THE AMERICAN CERAMIC SOCIETY*, 88, 2809-2816.
- ZAEFFERER, S., KUO, J. C., ZHAO, Z., WINNING, M. & RAABE, D. 2003. On the influence of the grain boundary misorientation on the plastic deformation of aluminum bicrystals. *Acta Materialia*, 51, 4719-4735.
- ZANG, S. L., GUO, C., THUILLIER, S. & LEE, M. G. 2011. A model of one-surface cyclic plasticity and its application to springback prediction. *International Journal of Mechanical Sciences*, 53, 425-435.
- ZEHETBAUER, M. & SEUMER, V. 1993. Cold work hardening in stages IV and V of F.C.C. metals—I. Experiments and interpretation. *Acta Metallurgica et Materialia*, 41, 577-588.
- ZHANG, M., BRIDIER, F., VILLECHAISE, P., MENDEZ, J. & MCDOWELL, D. L. 2010. Simulation of slip band evolution in duplex Ti-6Al-4V. *Acta Materialia*, 58, 1087-1096.
- ZIENKIEWICZ, O. C. 1977. *The Finite Element Method*, McGraw Hill Higher Education.